



# III-V-on-Si nanowire-based solar cells for tandem applications

Capucine Tong

## ► To cite this version:

Capucine Tong. III-V-on-Si nanowire-based solar cells for tandem applications. Micro and nanotechnologies/Microelectronics. Université Paris-Saclay, 2023. English. NNT : 2023UPAST044 . tel-04194165

**HAL Id: tel-04194165**

**<https://theses.hal.science/tel-04194165>**

Submitted on 2 Sep 2023

**HAL** is a multi-disciplinary open access archive for the deposit and dissemination of scientific research documents, whether they are published or not. The documents may come from teaching and research institutions in France or abroad, or from public or private research centers.

L'archive ouverte pluridisciplinaire **HAL**, est destinée au dépôt et à la diffusion de documents scientifiques de niveau recherche, publiés ou non, émanant des établissements d'enseignement et de recherche français ou étrangers, des laboratoires publics ou privés.

# III-V-on-Si nanowire-based solar cells for tandem applications

*Cellules solaires à base de nanofils III-V sur Si pour  
des applications tandem*

## Thèse de doctorat de l'université Paris-Saclay

École doctorale n° 575, Electrical, Optical, Bio-physics and Engineering (EOBE).  
Spécialité de doctorat : Electronique, Photonique et, Micro-Nanotechnologies.  
Graduate School : Sciences de l'ingénierie et des systèmes.  
Réfèrent : Faculté des sciences d'Orsay.

Thèse préparée dans les unités de recherche **C2N (Université Paris-Saclay, CNRS)** et  
**IPVF (Institut Polytechnique de Paris)**  
sous la direction de **Stéphane COLLIN**, directeur de recherche, et le co-encadrement  
de **Andrea CATTONI**, chargé de recherche.

Thèse soutenue à Palaiseau, le 31 mars 2023, par

**Capucine TONG**

## Composition du Jury

Membres du jury avec voix délibérative

### **Maria TCHERNYCHEVA**

Directrice de recherche, C2N, CNRS, Université Paris-Saclay

Présidente

### **Ray LAPIERRE**

Professeur, McMaster University, Canada

Rapporteur & Examineur

### **Charles CORNET**

Professeur, Institut FOTON, INSA-Rennes

Rapporteur & Examineur

### **Erik BAKKERS**

Professeur, Eindhoven University of Technology, Pays-Bas

Examineur

### **Jean DECOBERT**

Ingénieur de recherche, III-V Lab, Palaiseau

Examineur



**Titre :** Cellules solaires à base de nanofils III-V sur Si pour des applications tandem

**Mots clés :** Photovoltaïque, III-V, nanofils, épitaxie, cellules solaires, tandem

**Résumé :** Les cellules solaires tandem combinant une cellule à base de semiconducteurs III-V et une cellule en silicium (Si) offrent une voie prometteuse pour dépasser la limite de rendement des cellules traditionnelles à simple jonction en Si (29,4%). Grâce à leurs faibles diamètres, les nanofils (NFs) permettent de contourner élégamment les problèmes liés au désaccord de maille et aux différences d'expansion thermique, lors de la croissance directe de couches III-V sur Si. L'objectif de cette thèse est de fabriquer une cellule solaire à haut rendement constituée de NFs en GaAs, et ultimement de NFs en GaAsP, crus directement sur Si par épitaxie par jets moléculaires. Tout d'abord, la préparation du substrat de Si patterné a été optimisée pour obtenir de façon reproductible des réseaux ordonnés de NFs en GaAs, avec des taux de verticalité quasi-parfaits. Notre cellule record à base de NFs à jonctions GaAs/GaInP radiales a démontré un Voc élevé de 0,65 V et un rendement de près de 3,7%, à l'état de l'art des cellules solaires à NFs à base de jonctions en GaAs radiales, crues sur Si. La caractérisation avancée de ces réseaux de NFs a

indiqué de bonnes propriétés opto-électroniques, avec une séparation des quasi-niveaux de Fermi de 0,84 eV à 1 soleil, et nous avons identifié des voies d'amélioration importantes. L'augmentation du dopage de type n dans la coquille des NFs pourrait être une des pistes d'amélioration. Dans ce contexte, nous avons étudié par cathodoluminescence l'efficacité et l'homogénéité de l'incorporation du tellure dans des NFs en GaAs auto-catalysés. Enfin, des cellules solaires à base de NFs à jonctions GaAs/GaAsP/GaP axiales ont été fabriquées pour la première fois dans notre groupe. Des caractérisations de luminescence ont indiqué des propriétés opto-électroniques prometteuses, tandis que des simulations électroniques ont permis d'attribuer l'origine des performances limitées à des barrières d'énergie au niveau du contact de type n. En conclusion, ce travail de thèse a contribué à des avancées technologiques significatives, et les caractérisations avancées ainsi que les résultats de simulation présentés ont mis en lumière le potentiel et les défis des cellules solaires à base de NFs III-V sur Si.

**Title :** III-V-on-Si nanowire-based solar cells for tandem applications

**Keywords :** Photovoltaics, III-V, nanowires, epitaxy, solar cells, tandem

**Abstract :** Tandem PV technologies combining a III-V semiconductor cell over a silicon (Si) cell offer a promising pathway to exceed the efficiency limit of single junction Si solar cells (29.4%). Owing to their small diameters, nanowires (NWs) allow to mitigate the lattice constant and thermal coefficient mismatch issues associated with the direct growth of high-quality III-V layers on Si. The goal of this PhD work is to fabricate a high-efficiency solar cell consisting of first GaAs NWs, and ultimately GaAsP NWs, directly grown on Si by molecular beam epitaxy. First, the patterned Si substrate preparation process was optimized to obtain ordered GaAs NW arrays with near-perfect and reproducible vertical yields. Our champion core-shell GaAs/GaInP NW solar cell demonstrated a high Voc of 0.65 V, and an efficiency of almost 3.7%, at the state-of-the-art of radial junction GaAs NW solar cells grown on Si. The calibrated photoluminescence characterization of

these NW arrays indicated good optoelectronic properties, with a quasi-Fermi level splitting of 0.84 eV at 1 sun, and we identified significant room for device improvement. Increasing the n-type doping level in the NW shell could be one way of enhancing device performance. To this end, we used cathodoluminescence to study the incorporation efficiency and homogeneity of tellurium in self-catalyzed GaAs NWs. Finally, GaAs/GaAsP/GaP axial junction NW solar cells were fabricated for the first time in our group. Luminescence characterization indicated promising optoelectronic properties. Using electronic simulation, we attributed the limited performances to energy barriers at the n-type contact. Overall, this PhD work contributed to significant technological advances, and the detailed characterization experiments and simulation results presented shed light on the potential and challenges of III-V-on-Si NW-based solar cells.

*"Science, in the immediate, produces knowledge and, indirectly, means of action."*  
*Albert Einstein, 1949*



# Acknowledgements

J'aimerais tout d'abord remercier tous les membres du jury pour avoir accepté d'évaluer mon travail. Merci aux rapporteurs Charles Cornet et Ray Lapierre pour avoir lu mon manuscrit, et pour vos retours très détaillés et constructifs. Merci également à Maria Tchernycheva, Erik Bakkers et Jean Decobert de m'avoir fait l'honneur d'accepter de prendre part à ce jury et pour les riches échanges.

J'aimerais ensuite remercier mes encadrants de thèse, le duo de choc Stéphane et Andrea. Merci de m'avoir fait confiance et de m'avoir donné l'opportunité de faire une thèse sur les cellules solaires, un sujet qui me tenait beaucoup à coeur. Merci Andrea pour m'avoir tant appris sur les résultats qui peuvent découler d'une simple curiosité scientifique, et sur l'importance de la persévérance dans tout projet de recherche. Merci Stéphane pour la transmission de méthodes de travail rigoureuses, qui je suis sûre seront très utiles dans mon futur emploi, quel qu'il soit. Enfin, j'aimerais également vous remercier tous les deux pour vos qualités humaines. Je pense que votre bienveillance et enthousiasme quotidien constituent une force de l'équipe SUNLIT, notamment en des périodes difficiles de confinements, et je suis sûre que ce sont des qualités qui constitueront une des forces de ton futur groupe Andrea au Politecnico di Milano.

Ensuite j'aimerais remercier des personnes que je considère comme ayant été des mentors : Amaury, pour les expériences en lien avec l'hyperspectrale, mais pas que: merci aussi pour les nombreuses discussions sur l'interprétation de mes résultats EQE ou IV, et pour celles sur des sujets divers et variés comme l'empreinte carbone de l'endive. Merci Romaric, pour m'avoir transmis ta passion pour le projet nanofils, et pour m'avoir prodiguée des conseils précieux en début de thèse sur les voies à explorer. Merci également de m'avoir accordée ta disponibilité alors que tu étais toi-même en fin de thèse, et d'avoir été patient dans la transmission de ton savoir à la jeune doctorante novice que j'étais à l'époque. En termes de patience, j'aimerais également remercier celles de Thomas et Anton. Merci Thomas pour m'avoir dévoilée les secrets de la CL, et pour tes histoires rigolotes de rugbyman qui animaient souvent le bureau D118. Anton, merci infiniment, pour m'avoir enseignée l'opération de la MBE Riber32. Merci d'avoir été là toutes ces fois où j'ai eu peur de faire, ou d'avoir fait, une bêtise sur ce grand bâti capricieux.

Dans la lignée des maîtres épitaxieurs, j'aimerais également remercier Jean-Christophe et Laurent du côté C2N, et Maxime et Amadéo du côté IPVF. Merci à vous tous pour m'avoir transmis un petit peu de votre expertise, et pour toutes les maintenances fastidieuses qui permettent le bon fonctionnement des bâtis.

Ensuite, j'aimerais remercier les doctorants avec qui j'ai partagé cette expérience de thèse, intégralement ou en partie : Guillaume, Olivier, Anatole, Sophie, Margot, Marie, Javid, Tiphaine, et bien évidemment Salim et Bérengère; avec qui j'ai également partagé l'épreuve de la rédaction. Je suis ravie d'avoir partagé avec vous cette semaine de rédaction intense à la montagne, je pense que je n'avais jamais autant travaillé tout en prenant le temps de faire du sport et de cuisiner des bons petits plats fait-maison... J'ai hâte qu'on soit tous docteurs pour fêter ça dignement ! Carlos, Thomas V, Jules, Amaury, la fin est encore un peu loin pour vous, mais je vous souhaite le meilleur pour la fin de votre thèse. Je souhaite également une excellente fin de thèse à mes amis de Londres: Mayching, Daniel, Jasper, Maxime et Marcus, en thèse dans différents labos du monde.

Anne, Emile, Xavier et Frédéric, merci pour ces bons moments musicaux partagés les mercredi, jeudi, ou vendredi midis, enfin quand l'amphi était libre quoi finalement ! Je suis ravie d'avoir fait votre connaissance grâce à la musique, et très fière de tout ce qu'on a pu accomplir malgré un mélange d'instruments original et des niveaux assez hétéroclites. J'espère sincèrement que vous

---

continuerez ces sessions musicales, et qu'on aura l'occasion peut-être même de rejouer ensemble dans le futur. Dans la lignée des gens dont je me suis rapprochée un petit peu grâce à la musique et à notre passion commune pour les comédies musicales, j'aimerais également faire une petite dédicace à Anatole et Olivier, j'ai hâte pour les prochains événements du groupe HSM !

Dans la grande famille du badminton de Massy, j'aimerais remercier en particulier les Fit-mintoniens : Marc, Mehdi, Thibaud, Pierre et François. Merci pour tous ces bons moments partagés, sportifs, festifs, et autres. Ça me touche beaucoup que vous ayez assisté à ma soutenance de thèse. Dans les autres personnes qui m'ont permis d'oublier momentanément le travail dans des soirées, repas, sorties culturelles, voyages vélo ou appels vidéo, j'aimerais remercier Jade, Marie, Margaux, Camille, Clément, Mélodie et Sébastien, 我永远的搭档, et évidemment les membres de ma coloc préférée : Guillaume, Antoine, Charlotte, Eric et Margaux. Nos chemins divergent à présent, mais je suis sûre que nous continuerons à nous retrouver pour danser jusqu'au bout de la nuit, ou pédaler jusqu'à Saint-Louis (oui j'ai choisi cette ville alsacienne pour la rime). Quant à nos chemins à nous Guillaume, ils semblent plutôt converger, je suis impatiente de voir ce que le futur nous réserve !

Pour finir j'aimerais remercier la famille, à commencer peut-être avec Marie et Stéphane. Merci de m'avoir accueilli à bras ouvert dans votre grande famille, votre présence à ma soutenance m'a beaucoup touchée. Et enfin, j'aimerais remercier les fils conducteurs de ma vie : mes parents et mon frère. Si j'en suis là aujourd'hui c'est en grande partie grâce à vous, à votre soutien indéfectible malgré la distance, et à vos conseils qui m'ont régulièrement aidé à réaliser mon plein potentiel. Maman et Guillaume, un grand merci d'avoir fait le trajet pour pouvoir assister physiquement à ma soutenance (on essaiera de compenser votre empreinte carbone plus tard...). Je suis très heureuse d'avoir pu partager cette journée spéciale avec vous. Après presque 3 ans de pandémie, j'ai hâte que nous nous retrouvions enfin tous ensemble en famille cet été !

# Contents

<b>List of Acronyms</b>	<b>3</b>
<b>General Introduction</b>	<b>5</b>
<b>1 Theory and Methods</b>	<b>10</b>
1.1 Physics of solar cells	11
1.1.1 Basic principles	11
1.1.2 Semiconductors and junctions	13
1.2 PV technologies	15
1.2.1 Existing PV technologies and their limitations	15
1.2.2 Advantages of III-V-on-Si tandem solar cells and their challenges	16
1.2.3 Potential of III-V nanowires/Si	17
1.3 Characterization of III-V NW solar cells	20
1.3.1 Characterization of as-grown NWs	20
1.3.2 Hyperspectral photoluminescence	23
1.3.3 Characterization of processed NW arrays	25
1.4 Chapter conclusions	26
<b>2 Growth of Vertical GaAs Nanowire Arrays on Silicon</b>	<b>27</b>
2.1 Molecular beam epitaxy (MBE) for NW growth	28
2.1.1 Epitaxial growth of semiconductor NWs	28
2.1.2 Principle and components of MBE	30
2.1.3 MBE set-ups used in this work	32
2.1.4 State-of-the-art of GaAs NW arrays grown on Si	33
2.2 Towards 100% vertical GaAs NWs grown on Si with tuneable diameter	37
2.2.1 Optimizing the patterned substrate preparation for near-perfect yields	37
2.2.2 NW diameter variation with mask hole size	43
2.3 Chapter conclusions	48
<b>3 GaAs/GaInP Core-Shell Nanowire Solar Cell with State-of-the-art Voc and Quasi-Fermi Level Splitting</b>	<b>51</b>
3.1 Experimental methods	52
3.1.1 Growth of GaAs/GaInP core-shell NW arrays on Si	52
3.1.2 NW solar cell fabrication	54
3.2 Optoelectronic properties of the NW solar cell	55
3.2.1 Current-voltage (J-V) characteristics	55
3.2.2 External quantum efficiency (EQE) response	56
3.2.3 Nanowire absorption modelling	58
3.3 Absolute photoluminescence (PL) and quasi-Fermi level (qFl) splitting analysis	59
3.3.1 Hyperspectral PL maps and average PL spectra	60
3.3.2 Investigating the mismatch between qFl splitting and $qVoc$	60
3.4 Modelling hole transport at the p-type contact	62
3.4.1 Simplified 1D cell structure modelled using SCAPS	62
3.4.2 A hole concentration-dependent potential barrier in the VB	63
3.4.3 Impact of the GaP/Si VB offset	65
3.5 Chapter conclusions	66

<b>4</b>	<b>Investigating Te as an Alternative n-type Dopant for GaAs Nanowires</b>	<b>67</b>
4.1	Doping control in NWs	68
4.1.1	Doping related challenges in GaAs NWs	68
4.1.2	Characterizing carrier concentration in NWs	69
4.2	Experimental methods	71
4.2.1	Epitaxial growth of Te-doped GaAs thin films and NWs	71
4.2.2	Characterization	72
4.3	Electron concentration determination in GaAs:Te thin film references	74
4.4	Electron concentration mapping in GaAs:Te nanowires	76
4.4.1	NWs grown at 640°C (Te-NW1)	76
4.4.2	NWs grown at 620°C (Te-NW2)	77
4.4.3	Comparison	78
4.5	Chapter conclusions	80
<b>5</b>	<b>New Generation of Nanowire Solar Cells: GaAs/GaAsP Axial Heterojunctions</b>	<b>83</b>
5.1	Axial vs. radial NW junctions	84
5.1.1	Light absorption	84
5.1.2	Charge carrier separation and collection	84
5.1.3	Passivation	85
5.1.4	Evaluation of axial and radial junction NW solar cell performances	85
5.2	Investigating the optoelectronic properties of GaAs/GaAsP axial junction NWs	86
5.2.1	Growth recipe of the GaAs/GaAsP axial junction NWs	86
5.2.2	Growth recipe of the reference samples	87
5.2.3	Surface passivation assessment using luminescence	87
5.3	Axial junction NW solar cell fabrication process	92
5.3.1	<i>Ex-situ</i> removal of the Ga droplets	92
5.3.2	An organic/inorganic hybrid material for NW planarization	93
5.3.3	Improving the NW/ITO contact	94
5.4	Performances of our first axial junction NW solar cells	96
5.4.1	Current-voltage (J-V) characteristics	96
5.4.2	External quantum efficiency (EQE) response	97
5.4.3	Modeling electron transport at the n-type contact	99
5.5	Chapter conclusions	103
<b>6</b>	<b>Conclusion and Perspectives</b>	<b>105</b>
<b>A</b>	<b>Impact of the RIE etching parameters on the Si/SiO<sub>2</sub> interface</b>	<b>109</b>
<b>B</b>	<b>Communication and Recognition</b>	<b>113</b>
<b>C</b>	<b>Summary in French / Résumé en langue française</b>	<b>115</b>
	<b>Bibliography</b>	<b>125</b>

# List of Acronyms

**BCB** benzocyclobutene.

**BEP** beam equivalent pressure.

**CB** conduction band.

**CCD** charge-coupled device.

**CCP-RIE** capacitively coupled plasma-reactive ion etching.

**CL** cathodoluminescence.

**DI** deionized.

**EBIC** electron beam induced current.

**EBL** electron-beam lithography.

**EDX** energy-dispersive X-ray spectroscopy.

**EQE** external quantum efficiency.

**FET** field-effect transistor.

**FF** fill factor.

**FIB** focused ion beam.

**FTIR** Fourier-transform infrared spectroscopy.

**FWHM** full width at half maximum.

**ITO** indium tin oxide.

**LED** light-emitting diode.

**LPE** liquid-phase epitaxy.

**LT** low temperature.

**MBE** molecular beam epitaxy.

**ML** monolayer.

**MOCVD** metal-organic chemical vapour deposition.

**NA** numerical aperture.

**NIL** nanoimprint lithography.

**NW** nanowire.

**OPTP** optical pump-terahertz probe.

**ORMOSIL** organically-modified silica.



**PCE** power conversion efficiency.

**PECVD** plasma-enhanced chemical vapour deposition.

**PL** photoluminescence.

**PNW** patterned NW substrate nomenclature.

**PV** photovoltaic.

**qFl** quasi-Fermi level.

**RHEED** reflection high energy electron diffraction.

**RT** room temperature.

**RTA** rapid thermal annealing.

**SAG** selective area growth.

**SCR** space charge region.

**SEM** scanning electron microscope.

**STEM** scanning transmission electron microscope.

**TEM** transmission electron microscope.

**UHV** ultra-high vacuum.

**VB** valence band.

**VLS** vapour-liquid-solid.

**VPE** vapour-phase epitaxy.

**VS** vapour-solid.

**WZ** wurtzite.

**ZB** zinc blende.

# General Introduction

Earth's average surface temperature and climate have changed considerably throughout history. During the last ice age 20 000 years ago, the average global temperature was 6°C cooler than today [Tierney et al., 2020]. While these past changes occurred on geological timescales, the global warming observed since the industrial revolution in the 18<sup>th</sup> century is taking place at an unprecedented speed: the Earth's average surface temperature has increased at an average rate of +0.08°C/decade since 1880, and over twice that rate (+0.18°C/decade) since 1981, giving rise to disruptive consequences and amounting to one of the greatest challenges humans have ever faced [Dryzek et al., 2011]. In this general introduction, I first explain the crucial role of solar photovoltaics for not only the global energy transition, but also to reduce air pollution and provide affordable electricity access worldwide. Then, I introduce the main motivation and goals of this PhD thesis.

## The energy transition, a major challenge for the 21<sup>st</sup> century

Since the 1850s, the average global temperature has already increased by 1.1°C, unequivocally due to greenhouse gas emissions resulting from human activities [IPCC, 2013]. While many countries have committed to limiting global warming to 1.5°C compared to pre-industrial levels (Paris Agreement 2015), scientists from the Intergovernmental Panel on Climate Change (IPCC) forecast an increase of 1.4°C to 4.4°C by 2100, depending on the emissions scenario considered [IPCC, 2020]. Due to over 60% of the world electricity still being generated by the combustion of fossil fuels, electricity production alone accounted for about 26% of global CO<sub>2</sub> emissions in 2021 [Climate TRACE, 2022]. With an electricity demand predicted to nearly double in 2050 due to further electrification of the energy system [International Energy Agency, 2021b], a shift towards renewables and other low emissions sources of electricity is imperative.

In 2020, renewables accounted for almost 30% of the electricity supply (3% solar photovoltaics). To fulfill the targets set by the 26<sup>th</sup> Conference of the Parties (COP26) and achieve net zero greenhouse gas emissions by 2050 [UN Climate Change Conference UK, 2021], the share of renewables in the electricity mix has to increase to 88 % (33 % solar photovoltaics) by 2050.

## Photovoltaics: a renewable energy solution

The sun is the source of nearly all energy on Earth and its heat and light are at the origin of life. The sun's energy can be harnessed in different ways, through the burning of accumulated plant matter (fossil fuels, biomass), the use of air currents created by heated air and the Earth's rotation (windmills, wind turbines) or the accumulation of rainwater in dams from water evaporated elsewhere by the sun.

Photovoltaics (PV) get their name from the process of converting sunlight (photons) into electricity (electrons) through the photovoltaic effect discovered in 1839 by Edmond Becquerel [Becquerel, 1839]. This simple and elegant method of harnessing the sun's energy was exploited by scientists at Bell Laboratories to demonstrate the first practical photovoltaic device in 1954, with a power conversion efficiency of 6% [Chapin et al., 1957]. Their cell was made of silicon (Si), the second most abundant element in the Earth's crust and the basis for most electronics today. It is such that the time period encompassing the late 20<sup>th</sup> century to the early 21<sup>st</sup> century is sometimes referred to as the "Silicon Age" (also known as the Digital Age) [Dabrowski and Müssig, 2000; Siffert and Krimmel, 2013]. For several decades, the high cost of PV technologies have prevented

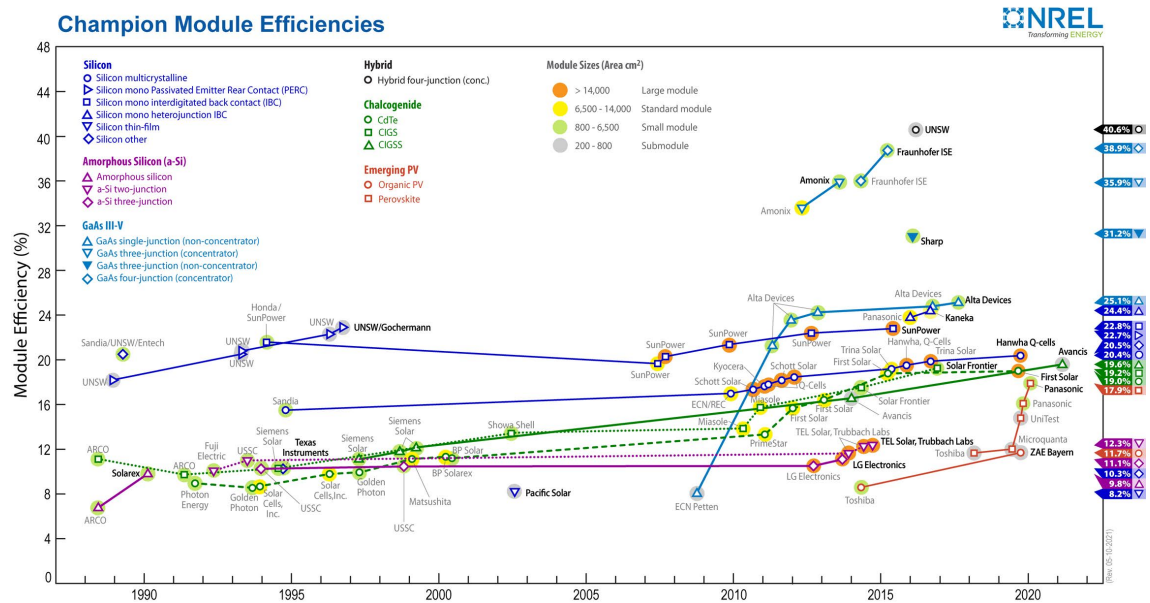


Figure 1: Champion photovoltaic module efficiency chart from the National Renewable Energy Laboratory (NREL).

them to be considered for large scale power generation, and they were only used in niche applications such as space. As illustrated in Figure 1 and Figure 2, Si solar cell technologies have since undergone significant cost-efficiency improvements, with prices falling to 0.18 €/Wp (2020), and highest module efficiencies reaching 24.4% [Fraunhofer Institute for Solar Energy Systems, 2021].

Solar PV is thus already one of the cheapest sources of electricity in the world, overtaking carbon

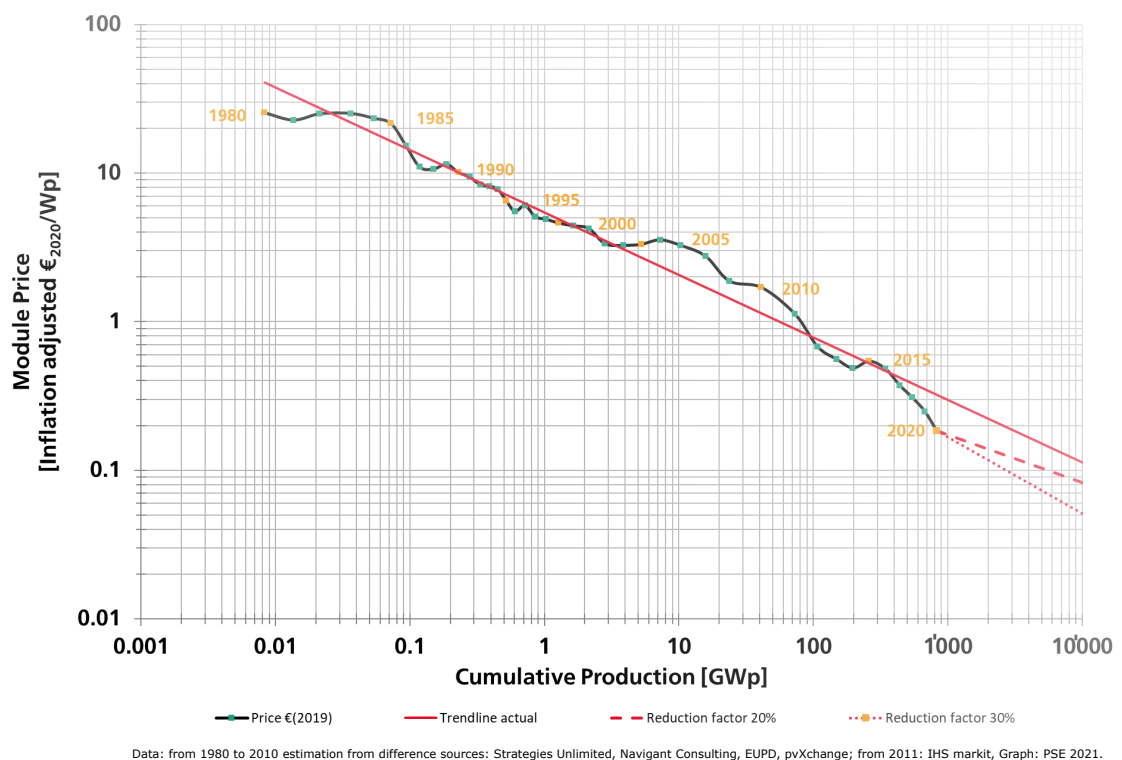


Figure 2: Photovoltaics price learning curve, encompassing all commercially available PV technologies (> 95% Si-based). Reprinted from [Fraunhofer Institute for Solar Energy Systems, 2021]

intensive fossil fuels, and emitting over 25 times less CO<sub>2</sub> equivalent per kWh of electricity produced than an oil or coal power station [Perez-Lopez et al., 2020]. However, the current commercially available Si-based PV technologies (> 95% of the modules sold today) will soon be limited by their maximum theoretical power conversion efficiency of about 29% [Niewelt et al., 2022]. This is due to the inherent absorption properties of silicon. As illustrated in Figure 3, Si cell technologies can only absorb a small portion of the solar spectrum. Research and development in novel cell architectures are thus required to increase the proportion of the solar spectrum exploited by PV technologies. Only the latter will enable higher power conversion efficiencies at ever falling costs, and help achieve net zero greenhouse gas emissions as soon as possible in order to limit global warming effects.

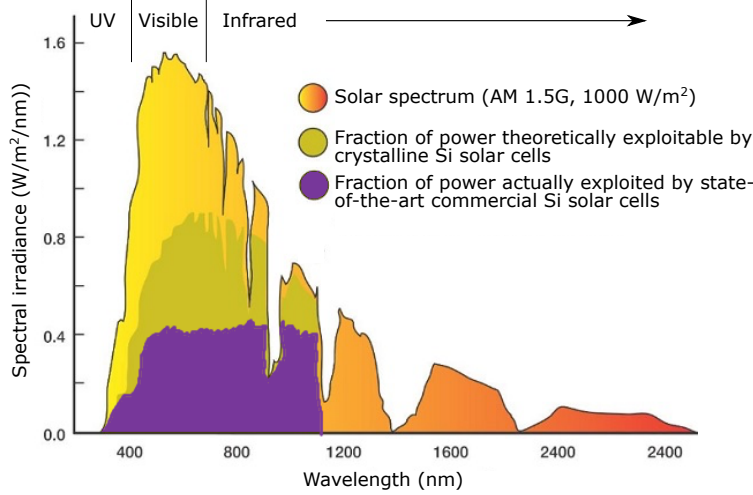


Figure 3: Standard AM 1.5G solar spectrum universally used to characterize terrestrial flat-plate PV modules. The fraction of power theoretically exploitable by crystalline Si solar cells is shown in mustard, while the fraction of power actually exploited by commercialized Si cells is shown in purple.

## Aim of this PhD work, and manuscript outline

In order to increase the fraction of solar power exploited by solar cells to produce electricity, different PV materials can be stacked on top of each other, each optimized to absorb a specific portion of the solar spectrum. When two materials are stacked together, we talk about a tandem solar cell. Considering the maturity of the silicon PV technology and the superior properties of III-V semiconductors, III-V-on-silicon (III-V/Si) solar cells appear as a very promising tandem device configuration for high-efficiency PV devices. However, the fabrication of III-V/Si tandem cells is currently challenged by the use of expensive III-V substrates, and the difficult integration of III-Vs on Si due to lattice and thermal expansion coefficient mismatches. The direct growth of high structural quality III-V nanowires (NWs) on mismatched Si substrates presents an elegant way to overcome these challenges. The success of this strategy relies on the precise control of the NWs grown on Si(111) substrates, their crystal structure, doping, junction formation, passivation, and opportune contacts.

The ultimate goal of the research carried out in this PhD work is hence to fabricate a high-efficiency tandem solar cell, consisting of GaAsP NWs with an optimal bandgap of 1.7 eV, directly grown on a bottom planar Si solar cell. However, given the difficulty to control the composition of ternary compounds in NW structures, the aim of this PhD work was firstly to develop a robust selective-area growth method for GaAs-based NWs grown on inactive Si(111) substrates, by molecular beam epitaxy (MBE).

Chapter 1 (Theory and Methods) serves as an introduction to the physics required to understand the operation of solar cells, and the processes occurring in them on a microscopic scale. An

overview of the existing PV technologies is then given to highlight the interest and motivation behind the development of nanowire-based III-V-on-Si tandem solar cells. Finally, the characterization techniques used to assess the properties and performances of the NW arrays grown in this PhD work are presented.

[Chapter 2](#) focuses on the fundamentals of NW growth by MBE and presents the set-ups used in this PhD work for NW synthesis. The parameters influencing the epitaxial growth of regular GaAs NW arrays on Si are also discussed using results from the literature. Finally, the substrate preparation optimizations which allowed us to achieve near-perfect NW vertical yields and controllable NW diameter are presented.

Secondly, the aim of this PhD work was to fabricate functional nanowire solar cells using the optimized GaAs NW arrays.

[Chapter 3](#) presents the second generation of NW solar cells developed in our group, which are based on GaAs/GaInP NWs with radial heterojunctions. The state-of-the-art performances obtained thanks to previous optimizations are first reported. Then, an in-depth investigation of the cells' optoelectronic properties, including a first-time quantification of the quasi-Fermi level splitting in NW array solar cells, is presented. Optical and electronic simulations carried out are also discussed to provide insights into the main absorption and electrical losses, as well as guidelines to design and fabricate higher-efficiency devices. In particular, improvements at the n-type contact were found to be necessary to favor electron extraction.

[Chapter 4](#) first introduces the importance of doping control in NWs, and highlights the difficulties in achieving high n-type doping levels in GaAs NW shells using the commonly used Si dopant. The advanced characterization methods typically used to assess carrier concentration in NWs are then presented, emphasizing the advantages of cathodoluminescence (CL). Next, the room temperature and low temperature CL methods developed in our group to quantify electron concentrations in Si-doped GaAs are validated on planar tellurium (Te)-doped GaAs samples from Tampere University. These methods are consequently used to study the impact of the NW growth temperature on the Te dopant incorporation efficiencies in GaAs NWs, in order to investigate the use of Te as an alternative n-type dopant in GaAs NWs.

[Chapter 5](#) first assesses the advantages and disadvantages of radial vs. axial NW junctions, in terms of light absorption, charge carrier separation and collection, passivation and practical NW solar cell performance. It then presents the preliminary results obtained on the optoelectronic properties of GaAs/GaAsP axial junction NWs in which the catalyst droplet has not been consumed *in-situ*. Next, the optimizations carried out on the NW solar cell fabrication process are reported, before showing the performances of the very first axial junction NW solar cells fabricated in our group. These performances are then discussed in light of electrical simulations.

## Contributions

During my PhD, I had the opportunity of collaborating and working with different colleagues from the two laboratories in which I carried out my research, namely the IPVF and the C2N. Here, I would like to clarify their contributions, as well as mine, to the results presented in this manuscript.

The patterned Si substrates used in this project were mostly prepared by Andrea Cattoni, researcher at the C2N and leader of the project. This was mainly due to his expertise on the subject, and the use of electron beam lithography as well as hydrofluoric (HF) acid, both of which I could not be trained for as a non-permanent researcher. I however helped with the SiO<sub>2</sub> mask layer deposition by PECVD, and the pattern transfer step using RIE etching. Andrea also acquired the FTIR spectra shown in [subsection 2.2.1](#), and developed the Marangoni substrate drying process presented in the same section. The results presented in [Appendix A](#) were obtained prior to the start of this PhD thesis, by Marco Faustini and Andrea.

I conducted all the NW growths presented herein using two different MBE reactors (Riber32 and Compact21), and subsequently observed them using SEM. The samples presented in [Chapter 3](#) and [Chapter 4](#) are however exceptions. The radial junction NW solar cells from [Chapter 3](#) were

grown and fabricated by the previous PhD student on this project, Romaric de Lépinau, with whom I had the chance to work with during the first few months of my PhD. While he did the microscopy characterization of the as-grown NW arrays from [subsection 3.1.1](#), I did all the following optoelectronic characterization of the solar cells. This includes the current-voltage, EQE and PL measurements presented in [Section 3.3](#). Amaury Delamarre, researcher at the C2N, showed me how to use the hyperspectral PL set-up and analyze the resulting data. In addition, he helped with some of the PL acquisitions. I also carried out the electronic simulations presented in [Section 3.4](#) and [subsection 5.4.3](#) using the SCAPS software. However, the absorption simulations presented in [subsection 3.2.3](#) were conducted by Andrea.

The Te-doped GaAs samples presented in [Chapter 4](#) were grown by collaborators from the Optoelectronics Research Center at Tampere University in Finland. They also performed the electron microscopy observations, as well as Hall reference measurements, and PL characterization of the thin film samples. I performed all the CL measurements presented in [Chapter 4](#), with the help of former PhD student, Thomas Bidaud, who trained me on the set-up and showed me how to analyze the resulting data.

I carried out the luminescence measurements (PL and CL) on the axial junction NWs presented in [Chapter 5](#). However, the ORMOSIL solution used to planarize these NW arrays was developed by Andrea. I then participated in the optimization of the planarization process, and fabricated our first axial junction NW solar cells using photolithography, sputtering, and contact evaporation. Finally, I performed the current-voltage and EQE characterizations of these axial junction NW solar cells.

# Chapter 1

## Theory and Methods

### Chapter Contents

---

<b>1.1</b>	<b>Physics of solar cells</b>	<b>11</b>
1.1.1	Basic principles	11
	The photovoltaic effect	11
	Characteristics of an operational solar cell	11
	The equivalent circuit	12
1.1.2	Semiconductors and junctions	13
	Crystal structure	13
	Energy bands and energy gap	14
	Doping: the p-n junction	14
<b>1.2</b>	<b>PV technologies</b>	<b>15</b>
1.2.1	Existing PV technologies and their limitations	15
1.2.2	Advantages of III-V-on-Si tandem solar cells and their challenges	16
1.2.3	Potential of III-V nanowires/Si	17
	NW properties	19
	III-V NW solar cell performances	19
<b>1.3</b>	<b>Characterization of III-V NW solar cells</b>	<b>20</b>
1.3.1	Characterization of as-grown NWs	20
	Electron microscopy	20
	Cathodoluminescence	20
1.3.2	Hyperspectral photoluminescence	23
	Hyperspectral imager set-up	23
	Absolute calibration procedure	24
1.3.3	Characterization of processed NW arrays	25
	Current-voltage measurements using a solar simulator	25
	External quantum efficiency (EQE)	25
<b>1.4</b>	<b>Chapter conclusions</b>	<b>26</b>

---

This chapter serves as an introduction to the physics required to understand the operation of solar cells, and the processes occurring in them on a microscopic scale. An overview of the existing PV technologies will also be given to highlight the interest and motivation behind the development of nanowire-based III-V-on-Si tandem solar cells. Finally, the characterization techniques used to assess the properties and performances of the III-V nanowire arrays grown in this PhD work will be presented.

## 1.1 Physics of solar cells

This section offers a brief overview of solar cell and semiconductor physics involved in the results that will be presented in the rest of this PhD manuscript. For detailed consideration of solar cell and semiconductor physics, standard textbooks and reference works by [Nelson, 2003; Sze and Ng, 2007a; Würfel and Würfel, 2016; Smets et al., 2016] are recommended.

### 1.1.1 Basic principles

#### The photovoltaic effect

The process by which a photovoltaic (PV) device converts electromagnetic radiation into electricity is known as the photovoltaic effect [Becquerel, 1839]. In most applications, the radiation is sunlight and the building block of the devices are called solar cells. Light shining on a solar cell produces both a current and a voltage to generate electric power. This process requires a material in which the absorption of light (photons) gives rise to electron-hole pairs, which can be efficiently separated and extracted to an external circuit to do electrical work. The main figure of merit used to assess a solar cell performance is its power conversion efficiency (PCE). The latter is defined as the fraction of incident power density ( $P_{in}$ ) converted into electricity. The experimental parameters which enable the determination of the PCE (also denoted  $\eta$ ) include the short-circuit current density ( $J_{SC}$ ), open-circuit voltage ( $V_{OC}$ ) and fill factor (FF), following:

$$\eta = \frac{J_{SC}V_{OC}FF}{P_{in}}. \quad (1.1)$$

These parameters are typically measured under standard test conditions in order to compare different solar cell technologies (cell temperature of 25°C, incident power density of 1000 W m<sup>-2</sup>, AM 1.5G spectrum, see Figure 3).

#### Characteristics of an operational solar cell

The **short-circuit current** ( $I_{SC}$ ) corresponds to the photocurrent generated by a solar cell when its external voltage is zero (i.e. the cell is short-circuited). It depends on the area of the solar cell (the short-circuit current density ( $J_{SC}$ ) is commonly used to remove this dependence), the power and spectrum of the incident light source, the absorption and reflection of the solar cell, and the minority-carrier collection probability. To relate the  $J_{SC}$  to the incident spectrum, the cell's external quantum efficiency (EQE) is thus required, which gives the probability that an incident photon of wavelength  $\lambda$  will deliver one electron to the external circuit:

$$J_{SC} = q \int_{\lambda_1}^{\lambda_2} \phi_{AM1.5G}(\lambda) EQE(\lambda) d\lambda. \quad (1.2)$$

Here  $q$  is the electronic charge, and  $\phi_{AM1.5G}(\lambda)$  is the AM1.5G spectral photon flux density in the wavelength range of interest  $\lambda_1 - \lambda_2$  (units of photon s<sup>-1</sup> m<sup>-2</sup> nm<sup>-1</sup>).

The **open-circuit voltage** ( $V_{OC}$ ) is the maximum voltage available from a solar cell, and corresponds to the difference of electrical potential between the solar cell terminals at zero net current. It is a measure of the amount of carrier recombination in the device, and can be defined by the following equation (in the one-diode model approximation):

$$V_{OC} = \frac{nkT}{q} \ln\left(\frac{I_{ph}}{I_0} + 1\right). \quad (1.3)$$

$I_{ph}$  and  $I_0$  correspond to the photogenerated and dark saturation currents, respectively, while  $n$  is the ideality factor,  $k$  the Boltzmann constant, and  $T$  the cell temperature. Note that  $V_{OC}$  increases logarithmically with light intensity (ideally directly proportional to  $I_{ph}$ ).

The **fill factor** (FF) is defined as the ratio of the maximum power ( $P_{max}$ ) to the product of  $I_{SC}$  and  $V_{OC}$ :

$$FF = \frac{P_{max}}{I_{SC}V_{OC}} = \frac{I_{mpp}V_{mpp}}{I_{SC}V_{OC}}. \quad (1.4)$$



It is directly affected by series and shunt resistances in the device.

Figure 1.1 shows the current-voltage (I-V) characteristics of an ideal solar cell under illumination and in the dark. As solar cells convert light into electricity, it might seem strange to measure them in the dark. However, dark current-voltage measurements in which carriers are injected into the circuit with electrical means rather than with light, provide complementary information on the cell properties [Honsberg and Bowden, 2019]. Figure 1.1 follows the standard PV sign convention which defines the  $I_{SC}$  as positive [Nelson, 2003]. Nevertheless, the I-V curves presented in the rest of this manuscript were flipped to follow the passive sign convention (with negative  $I_{SC}$ ). In fact, when a voltage is applied to a solar cell the latter actually works as a passive component. However, for ease of understanding, the absolute value of  $I_{SC}$  and  $J_{SC}$  will be referred to in the discussions. The power-voltage characteristics of the cell under illumination are also shown in grey in Figure 1.1, from which we can see that the solar cell produces power between 0 and  $V_{OC}$  ( $P > 0$ ). At  $V < 0$ , the illuminated cell acts as a photodetector which consumes power to generate a photocurrent. At  $V > V_{OC}$ , the cell operates in the same regime as light-emitting diodes (LEDs) and consumes power to emit light. Graphically, the FF corresponds to the ratio between the areas of the inner and outer rectangles (dashed) in Figure 1.1.

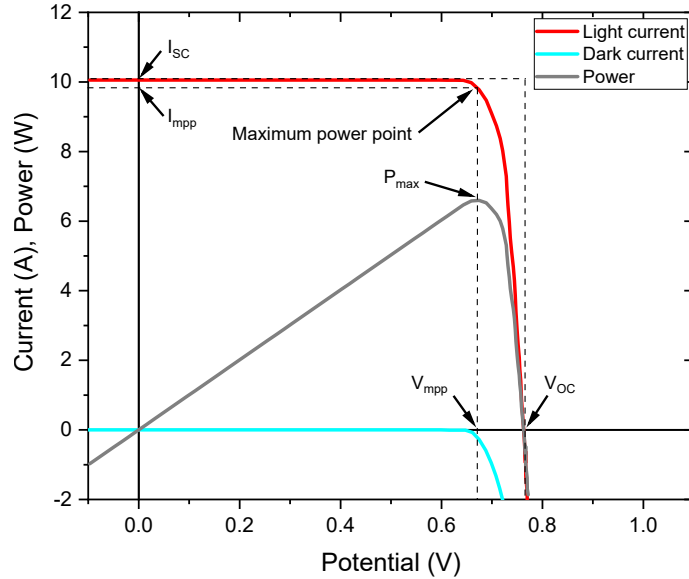


Figure 1.1: Current-voltage characteristics of an ideal solar cell under illumination (red) and in the dark (blue). The power-voltage characteristics of the cell under illumination are shown in grey. The maximum power point is reached at  $(V_{mpp}, I_{mpp})$ , and the FF can be obtained by calculating the ratio between the areas of the inner and outer rectangles (dashed).

### The equivalent circuit

To understand the current-voltage behavior of a solar cell, it is useful to create a model which is electrically equivalent. An ideal solar cell can be modelled by a current source in parallel with a diode. However, in reality series and shunt resistance components ( $R_{series}$  and  $R_{shunt}$ , respectively) also need to be taken into account, as illustrated in Figure 1.2.

The non-ideal current-voltage behavior of a solar cell can then be described by the following equation:

$$I = I_{ph} - I_0 \left( \exp\left(\frac{q(V + IR_{series})}{nkT}\right) - 1 \right) - \frac{V + IR_{series}}{R_{shunt}}, \quad (1.5)$$

where  $n$  here is the ideality factor quantifying how closely the cell follows the behavior of an ideal diode.

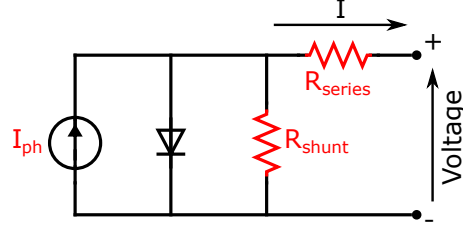


Figure 1.2: Equivalent electrical circuit of a non-ideal solar cell.

Solar cells rely on the photovoltaic effect to convert sunlight into electricity, with a power conversion efficiency which depends on the cell's  $J_{SC}$ ,  $V_{OC}$  and FF. The latter can be obtained from current-voltage measurements.

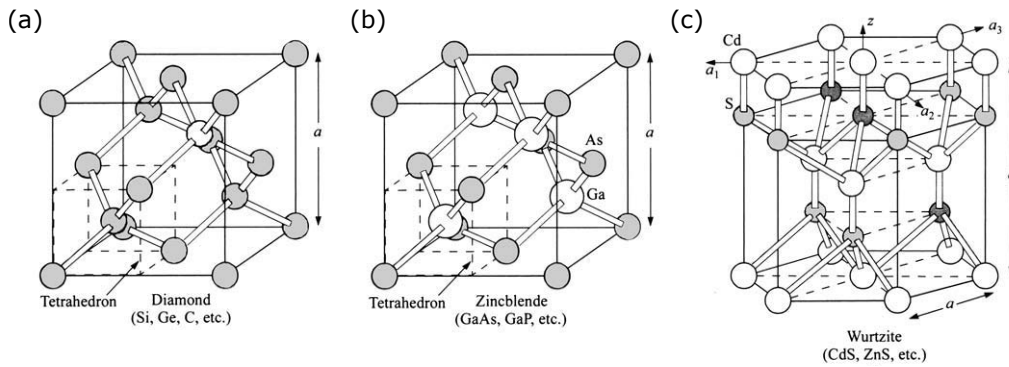
### 1.1.2 Semiconductors and junctions

A variety of materials can satisfy the requirements of PV energy conversion, but the great majority of solar cells use semiconductor materials in the form of a p-n junction. Semiconductor materials can be pure elements, like the most commonly used crystalline silicon (Si), or compounds such as gallium arsenide (GaAs). The latter is composed of elements from groups III and V of the periodic table, making it part of the III-V semiconductors group which will be of particular interest herein.

#### Crystal structure

Most common semiconductors are crystalline solids in which there is an ordered arrangement of atoms determining their physical properties. Many important semiconductors have diamond or zinc blende (ZB) lattice structures (illustrated in Figures 1.3a and b, respectively), in which each atom is surrounded by four equidistant nearest neighbours lying at the corners of a tetrahedron [Sze and Ng, 2007a]. While in a diamond lattice like the one making up Si, all the atoms are the same, in a ZB structure like the one making up GaAs, one sublattice is Ga and the other one As. GaAs can also crystallize in the wurtzite (WZ) structure illustrated in Figure 1.3c, which consists of two interpenetrating hexagonal close-packed lattices. While bulk GaAs crystals and planar thin films crystallize only in the ZB structure, the formation probability of both ZB and WZ phases can be similar in GaAs nanowires (NWs), often resulting in axial polytype heterostructures which usually deteriorate the NW device performance [Senichev et al., 2018].

The distance between atoms in a crystal lattice determines the lattice parameter, which is of primordial importance in the epitaxial growth of a crystal layer over a substrate of different composition. In fact, strain and crystal defects can be introduced when the lattice parameters of the different materials are not matched.

Figure 1.3: (a) Diamond, (b) zinc blende (ZB), and (c) wurtzite (WZ) crystal structures, with  $a$  being the lattice constant. Adapted from [Sze and Ng, 2007a].

## Energy bands and energy gap

For any given material, there are two distinct energy bands in which electrons may exist: the valence band (VB) and the conduction band (CB) [Ashcroft and Mermin, 1976]. These bands can either overlap (conductors), or be separated by a more or less wide forbidden energy gap known as the bandgap (insulators and semiconductors, respectively). The bandgap ( $E_g$ ) is one of the most important parameters in semiconductor physics, and can be defined by the minimum amount of energy required to excite a bound electron from the VB into a free-state in the CB to conduct electricity. The excitation of an electron to the CB leaves behind a positively charged hole.

The bandgap determines the wavelengths of light that a semiconductor can absorb and emit. In fact, only photons with energies above  $E_g$  can be absorbed to generate electron-hole pairs. However, since electrons and holes tend to occupy energy levels at the bottom of the CB and the top of the VB, respectively, photons with energies much higher than  $E_g$  will release their excess energy as heat. This energy loss process is known as thermalization. The other main energy loss process in solar cells comes from the non-absorption of photons that have energies lower than the bandgap. Building on these reflections, Shockley and Queisser analyzed the maximum theoretical efficiency of single-junction PV devices using the thermodynamic principle of detailed balance [Shockley and Queisser, 1961; Tiedje et al., 1984]. Figure 1.4a shows the maximum theoretical efficiency of single-junction solar cells as a function of bandgap, in the limits of the assumptions of the Shockley-Queisser (SQ) model [Guillemoles et al., 2019].

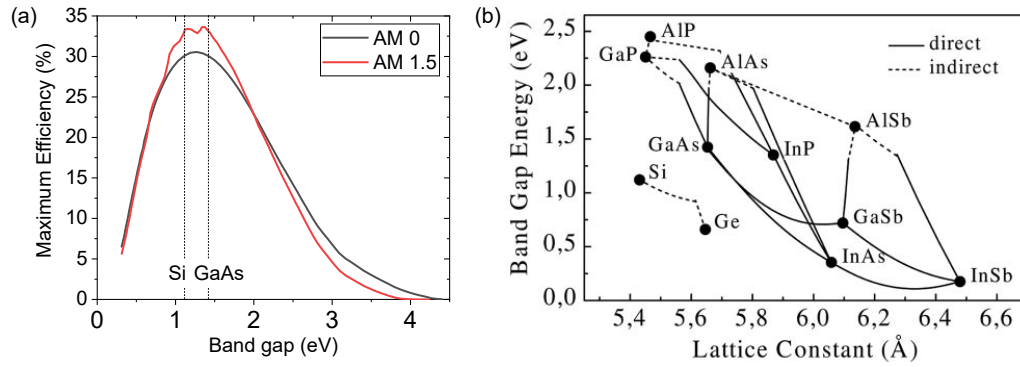


Figure 1.4: Impact of semiconductor bandgap on (a) the maximum theoretical efficiency of single-junction solar cells under a 1-sun illumination within the limits of the SQ model, and (b) the lattice parameter (reprinted from [Bett et al., 1999]).

From Figure 1.4a, we can see that a range of bandgaps are available for optimum cell efficiency. One of the many advantages of III-V compound semiconductors is actually their highly tunable bandgap, many of them which are direct, as illustrated in Figure 1.4b. In fact, semiconductors can have either a direct or an indirect bandgap. In semiconductors with a direct bandgap (such as GaAs), the maximal energy state in the VB and the minimal energy state in the CB have the same crystal momentum. On the other hand, in indirect bandgap semiconductors (such as Si), a change in crystal momentum via the intervention of phonons is required for an electron to move from the maximal energy state in the VB to the minimal energy state in the CB. These differences bear significant consequences on light absorption and charge carrier recombination processes, with indirect bandgap materials not absorbing light as efficiently as ones with direct bandgap. Nevertheless, the conducting properties of both types of semiconductors can be altered in useful ways by introducing impurities into the crystal structure.

## Doping: the p-n junction

Doping consists in introducing impurities which will vary the concentration of electrons and holes in a semiconductor in order to modulate its electrical properties. The introduction of atoms with one more (less) valence electron than the host lattice results in n-type (p-type) doping. When two oppositely doped regions are brought together, a semiconductor p-n junction is created. While other ways of separating electron and hole carriers in a solar cell exist, the p-n junction is the most common one. The latter is also the elementary component of most modern electronic devices,

making its working principles very well-documented [Seeger, 2004; Sze and Ng, 2007b].

At thermodynamic equilibrium, the large difference in carrier concentration between the n- and the p-type regions causes diffusion of electrons from the n- to the p-type regions and holes from the p- to the n-type regions. Due to this diffusion process, the region close to the junction becomes depleted of charge carriers, giving rise to a space charge region (SCR), in which an electric field is formed by the charge of the ionized donor and acceptor atoms remaining in the respective regions. This internal electric field forces the charge carriers to move in a direction opposite to the concentration gradient. However, at thermodynamic equilibrium, these drift and diffusion currents cancel out such that no net current flows in the solar cell, as illustrated in Figure 1.5a by the constant Fermi level ( $E_F$ ).

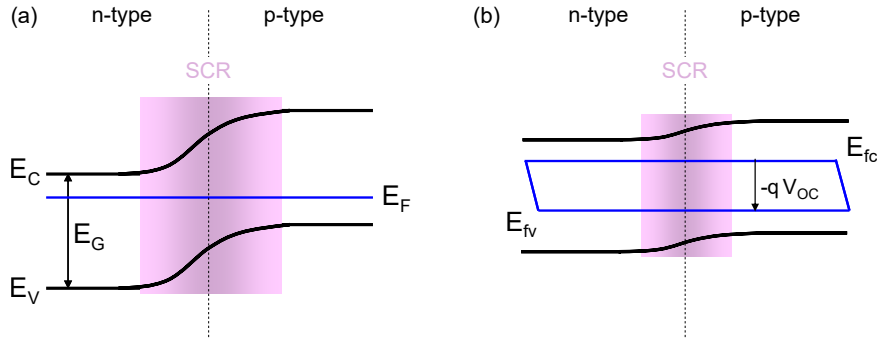


Figure 1.5: Energy-band diagram of a p-n junction (a) at equilibrium (in the dark, no external applied bias), and (b) at open-circuit voltage under illumination.

Under illumination, additional electron-hole pairs are generated in a p-n junction and the concentration of minority carriers strongly increases (electrons in the p-type region and holes in the n-type region). In such out-of-equilibrium semiconductors, the electron and hole populations are described by their quasi-Fermi levels,  $E_{fc}$  and  $E_{fv}$ , respectively. Figure 1.5b shows the energy band diagram of a p-n junction at open-circuit voltage under illumination, in which the electrostatic potential barrier across the junction has been lowered by an amount  $qV_{OC}$ . This is analogous to a solar cell under illumination but not connected to an external load.

When the n- and p-doped semiconductors are of the same material we talk about homojunctions. Heterojunctions on the other hand, combine different materials and thus present the advantage of having a bandgap variation which when optimized can favor charge carrier extraction. The limitation in heterojunctions comes however from the strain and defects introduced at the interface due to lattice-mismatch between the different materials.

The majority of solar cells are based on a semiconductor p-n junction, the properties of which depend primarily on the semiconductor crystal structure, bandgap, and doping level. Heterojunctions usually outperform homojunctions due to better energy band alignments, but in order to grow dissimilar materials on top of each other without introducing strain or defects, lattice matching is required. III-V semiconductors present the advantage of having widely tunable composition (hence lattice constant and bandgap), allowing them to be easily integrated into heterostructures.

## 1.2 PV technologies

### 1.2.1 Existing PV technologies and their limitations

The PV market is currently dominated by **crystalline Si** technologies which make up 95% of the PV market share [Fraunhofer ISE, 2022]. The record efficiency for lab-size Si cells and PV modules is 26.8% [LONGi, 2022], and 24.4% [Kaneka Corporation, 2016], respectively. Although these technologies are mature and hence cost-effective, they are fast approaching the maximum

efficiency limit of 29.4% for Si solar cells [Niewelt et al., 2022].

**Chalcogenide thin film** solar cells (mainly CIGS and CdTe) account for the remaining PV market share, with record lab cell efficiencies at 23.4% and 22.1%, for CIGS and CdTe, respectively, and record module efficiencies at 19.2% and 19.5% for CIGS and CdTe, respectively [Green et al., 2022]. Despite their lower maturity, thin film technologies present several advantages over the traditional Si devices, including better light absorption (hence thinner cell layers), flexibility, lower carbon footprint [Bosmans et al., 2021], and potentially lower cost [Efazl et al., 2021]. However, the widespread use of CIGS and CdTe thin film solar cells is still limited by concerns regarding the efficiency of commercial modules.

**III-V semiconductors** currently make up the most efficient single-junction solar cells owing to their excellent light absorption properties (29.1% for GaAs [Kayes et al., 2011]). Furthermore, their widely tunable composition and optical characteristics enable their direct integration into heterostructures and multi-junction cells. The latter will be further discussed in the next section. Nevertheless, the high-cost of III-Vs have so far limited their use to niche applications such as space and high-concentration systems.

**Perovskite** solar cells are a relatively new PV technology which has shown remarkable progress in recent years, with efficiencies increasing from 3.8% in 2009 to over 25% today [Green et al., 2022]. However, despite the benefits of cheap production and simple manufacturing process, the commercialization of perovskite solar cells is still hindered above all by low stability [Qiu et al., 2021].

Other less performant PV technologies include **organic** (18.2%), **dye-sensitized** (12.3%) and **amorphous Si** (10.2%) solar cells [Green et al., 2022].

Today's PV market is largely dominated by the crystalline Si technology, with a record module efficiency of 24.4%. However, their power conversion efficiency is fast approaching its physical limit, and other PV technologies, or combination of PV technologies, will be required to achieve conversion efficiencies beyond 30%.

## 1.2.2 Advantages of III-V-on-Si tandem solar cells and their challenges

Tandem solar cells present a path to exceed the efficiency limits of single-junction devices by stacking two p-n junctions made of different semiconductor materials. In fact, as the p-n junctions have different bandgaps, they can each be optimized to absorb a specific portion of the broad solar spectrum. Typically, the top cell absorbs high energy photons (it has a wider bandgap) and the bottom cell absorbs low energy photons (narrower bandgap). There are two main designs for tandem solar cells. Figure 1.6a illustrates the two-terminal (2T) architecture, while Figure 1.6b presents the four-terminal (4T) architecture. In a 2T tandem design, the sub-cells are connected monolithically in series, meaning that only two external electrical contacts are required, but the top and bottom cells must be current-matched. The 4T design implies connecting each sub-cell separately to an external circuit, requiring four contacts for one tandem cell. Although the 4T configuration allows for greater design flexibility, it also increases the module-level cell interconnection complexity, explaining why at present, 2T tandem configurations have been preferably used in all industry-scale solar cell architectures [VanSant et al., 2021].

As mentioned in the previous section, solar cells based on III-V semiconductors currently outperform all other single-junction PV technologies, so their combination with the mature and low-cost Si technology could hold great promise for high-efficiency solar cells. Figure 1.6 shows the maximum efficiency achievable for a tandem device under the AM 1.5G spectrum, in either a 2T tandem configuration (c), or a 4T one (d). We can see that for an industrially scalable 2T tandem configuration with a bottom cell bandgap of 1.12 eV (Si), a maximum PCE of above 45% can be achieved using an optimal top cell with bandgap 1.7 eV. Coming back to Figure 1.4b, indeed a wide range of III-V compound semiconductor systems have a direct bandgap of 1.7 eV (namely  $\text{GaAs}_{0.75}\text{P}_{0.25}$ ,  $\text{In}_{0.6}\text{Ga}_{0.4}\text{P}$  and  $\text{Al}_{0.2}\text{Ga}_{0.8}\text{As}$ ). However, none of them are lattice-matched with Si.

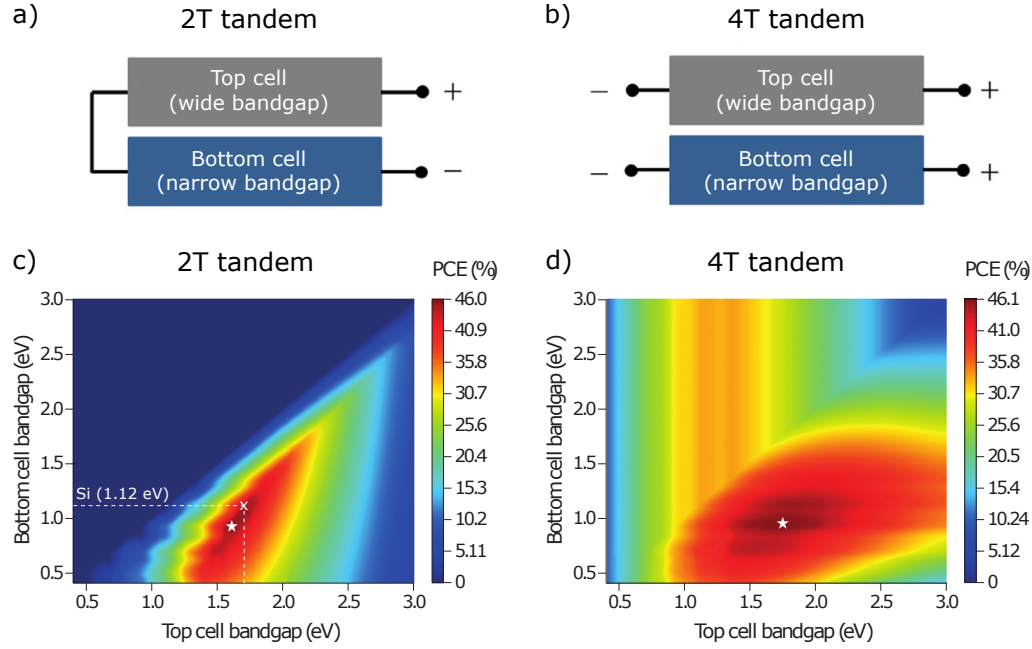


Figure 1.6: Schematic illustration of (a) a two-terminal (2T), and (b) a four-terminal (4T), tandem solar cell configuration. Theoretical maximum power conversion efficiency (PCE) achievable for (c) a 2T, and (d) a 4T, tandem configuration, as a function of the bandgap of the top and bottom cells. The dashed lines trace the maximum efficiency achievable for a tandem cell in which a Si bottom cell is combined with a top cell possessing an optimal bandgap of 1.7 eV. The star indicates the maximum PCE. Adapted from [Cheng and Ding, 2021; Eperon et al., 2017].

Three methods are currently employed to integrate III-V and Si sub-cells: heteroepitaxial growth, wafer bonding, and mechanical stacking. Heteroepitaxial growth on Si is the most cost-effective approach, but it is challenged by the lattice and thermal expansion coefficient mismatches between the III-V and the Si materials, limiting the record efficiency to 25.9% for a GaInP/GaAs/Si triple-junction solar cell [Feifel et al., 2021]. Wafer bonding consists in first growing the III-V layers on lattice-matched III-V substrates, and then transferring them to the Si bottom cell. The record efficiency achieved by such a wafer-bonded approach is 35.9% (triple-junction, 2T) [Green et al., 2022], and demonstrates the potential of silicon-based tandem photovoltaics. However, this method requires very expensive wafer surface preparation, making it difficult to implement industrially. Mechanical stacking relaxes the requirements on the Si wafer surface preparation, typically through the use of a 4T tandem configuration (record efficiency of also 35.9% for a triple-junction device), but just like in the wafer-bonding approach, it involves the removal of expensive III-V substrates, preventing implementation at an industrial scale.

Stacking different PV materials, each optimized to absorb a specific portion of the solar spectrum, holds great promise for high-efficiency solar cells. Considering the maturity of the Si PV technology and the superior properties of III-V semiconductors, III-V-on-Si solar cells appear as a very appealing tandem device configuration. In fact, efficiencies above 35% have already been demonstrated for III-V-on-Si triple-junction solar cells fabricated using the wafer bonding or mechanical stacking approach. However, the costly processes involved in these approaches can hardly be extended to an industrial level.

### 1.2.3 Potential of III-V nanowires/Si

Nanowires (NWs) are high aspect-ratio structures with a diameter on the order of nanometers, and unique properties.



Table 1.1: Summary of recently reported III-V NW array solar cell performances, as measured under 1-sun illumination. Two tandem-on-Si NW solar cells are also reported. The best performing GaAs planar solar cell is indicated for comparison. A question mark (?) indicates missing information and a hyphen (-) expresses the absence of a growth or process step.

Reference	Material	Substrate	Geometry (dopants)	Growth method (epitaxy technique)	Passivation	Planarization	Eff. (%)	V <sub>oc</sub> (V)	J <sub>sc</sub> (mA/cm <sup>2</sup> )	FF
[Wood, 2017]	GaAsP (top cell in tandem)	Si	Radial p-i-n (Be, Te)	Self-catalyzed (MBE)	AlInP	BCB	0.75	0.507	4.54	0.322
[Boulanger et al., 2016]	GaAs	Si	Radial p-i-n (Be, Te)	Self-catalyzed (MBE)	AlInP	BCB	3.3	0.39	18.2	0.465
[Dastjerdi et al., 2016]	GaAs	Si	Radial p-i-n (Be, Te)	Self-catalyzed (MBE)	AlInP	BCB	4.1	0.45	22.8	0.40
[Yao et al., 2015]	GaAs (top cell in tandem)	Si	Axial n-i-p (Si, Zn)	SAG (MOCVD)	-	BCB	6.44	0.518	21.5	0.581
[Mukherjee et al., 2021]	GaAs	Si	Axial p-i-n (Be, Te)	Self-catalyzed (MBE)	-	SU-8	7.74	0.62	21.2	0.59
[Nakai et al., 2013]	GaAs	GaAs	Radial p-n (Zn, Si)	SAG (MOCVD)	InGaP	BCB	4.01	0.50	12.7	0.65
[Mariani et al., 2013]	GaAs	GaAs	Radial n-i-p (Sn, Zn)	SAG (MOCVD)	InGaP	BCB	7.43	0.57	18.9	0.69
[Yao et al., 2014]	GaAs	GaAs	Axial n-i-p (Si, Zn)	SAG (MOCVD)	-	BCB	7.58	0.565	21.08	0.637
[Aberg et al., 2016]	GaAs	GaAs	Axial p-i-n (Zn, Sn)	Au-catalyzed (MOCVD)	AlGaAs	BCB	15.3	0.906	21.3	0.792
[Yoshimura et al., 2013]	InP	InP	Radial p-n (Zn, Si)	SAG (MOCVD)	AlInP	BCB	6.35	0.457	23.4	0.596
[Otmes et al., 2018]	InP	InP	Axial p-i-n (Zn, Sn)	Au-catalyzed (MOCVD)	SiOx	BCB	15.0	0.73	26.64	0.77
[Van Dam et al., 2016]	InP	InP	Axial p-n (?, ?)	Etch-down (?)	SiOx	BCB	17.8	0.765	29.3	0.794
This work	GaAs/InGaP	Si	Radial p-i-n (Be, Si)	Self-catalyzed (MBE)	InGaP	BCB	3.68	0.65	14.2	0.40
[Wood, 2017]	GaAsP/Si	Si p-n	Tandem Radial p-i-n (Be, Te)	Self-catalyzed (MBE)	AlInP	BCB	3.51	1.16	7.65	0.396
[Yao et al., 2015]	GaAs/Si	Si n-p	Tandem Axial n-i-p (Si, ?)	SAG (MOCVD)	-	BCB	11.4	0.956	20.64	0.578
[Kayes et al., 2011]	GaAs	GaAs	Planar	VS (MOCVD)	-	-	29.1	1.127	29.78	0.867

## NW properties

Compared to their planar counterparts, III-V NWs offer many advantages for silicon-based tandem PV devices. First, vertically-oriented III-V NWs have been shown to be able to absorb light from an area larger than their physical cross-sections [Garnett et al., 2011; Anttu and Xu, 2013; Lapierre et al., 2013; Krogstrup et al., 2013], allowing to harvest more photons with less expensive III-V material. This enhanced absorption is due to resonant absorption mechanisms occurring in NWs, which can also result in anti-reflection properties when the geometrical NW array parameters are optimized [van Dam, 2016; Ghahfarokhi et al., 2016].

NWs can further reduce the III-V/Si tandem solar cell cost by enabling direct single-crystal growth on inexpensive Si substrates. In fact, the strain typically induced by the lattice-mismatch between the III-V and Si materials can be effectively relaxed through the NW sidewalls due to the small NW diameters, avoiding the formation of crystal defects [Mårtensson et al., 2004; Chuang et al., 2007; Kavanagh, 2010]. This enables a broader range of top cell absorption energies than is possible with planar layers in a tandem solar cell configuration.

## III-V NW solar cell performances

Promising efficiencies above 30% can be expected for such tandem solar cells consisting of III-V NWs directly grown on Si [Lapierre, 2011; Huang et al., 2012]. However, a number of unresolved issues must be addressed before they can be used in commercial devices. Table 1.1 reports the performances of state-of-the-art III-V NW array solar cells, directly grown on both III-V and Si substrates. We can see that a lot of research efforts have been focused on GaAs NWs. This is because GaAs is one of the most studied III-V semiconductor materials, and as a binary compound its composition can be more easily controlled than the ternary compounds required to achieve an optimal top cell bandgap of 1.7 eV. GaAs, with its bandgap of 1.42 eV, was thus used as a proof-of-concept material for the NW solar cells developed in the framework of this PhD work. The performances of InP NW solar cells are also shown in Table 1.1 for reference as they currently hold the record efficiency of 17.8% for III-V NW solar cells [Van Dam et al., 2016], although the latter was obtained by a top-down fabrication method.

As seen from Table 1.1, the best GaAs NW solar cells grown on Si are currently still largely outperformed by ones grown on GaAs (7.74% [Mukherjee et al., 2021] vs. 15.3% [Aberg et al., 2016]), and planar thin films (29.1% [Kayes et al., 2011]). The difference with GaAs NWs grown on GaAs substrates stems mainly from the use of gold (Au) as foreign catalyst for the vapour-liquid-solid (VLS) growth of GaAs NWs on GaAs substrates. In fact, the use of foreign catalysts allows for independent tuning of the growth parameters and hence higher growth reproducibility and facilitated growth optimization. However, Au is not compatible with Si-based technologies as it creates deep recombination centers and readily diffuses in bulk Si. To avoid degraded Si bottom cell performance in a tandem configuration, self-catalyzed or selective-area growth of GaAs is thus preferred. The mechanisms involved in NW growth will be discussed in detail in Chapter 2. The only two III-V NW/Si tandem solar cells reported so far are presented in Table 1.1. A clear benefit in terms of  $V_{OC}$  can be observed, and an encouraging efficiency of 11.4% was obtained by [Yao et al., 2015] despite an unoptimized Si bottom cell and unpassivated GaAs NWs with suboptimal bandgap value for a tandem on Si.

The GaAs-based NW p-n junctions can be formed in the axial or the radial direction, each with their specific advantages and disadvantages (see Chapter 5). Table 1.1 reveals that axial junction NW solar cells currently demonstrate higher performances than radial junction ones. However, both are still limited by low  $V_{OC}$  and FF due to issues arising from NW doping, passivation and contacting, all of which will be addressed to some extent in this PhD manuscript.



Due to their small diameters and geometry, III-V NWs offer many advantages for a tandem on Si solar cell configuration compared to their planar counterparts. However, despite rapid development in the field in the past decade, the record efficiency of III-V NW solar cells directly grown on inactive Si substrates is still below 10%. This is because many challenges regarding NW synthesis and device fabrication still need to be overcome to fully exploit the potential of NW solar cells.

### 1.3 Characterization of III-V NW solar cells

The nanoscale dimensions of NWs complexify the characterization of their properties. In this section, I briefly describe the techniques that were used to characterize the as-grown NWs, as well as processed NW solar cells presented in this manuscript.

#### 1.3.1 Characterization of as-grown NWs

##### Electron microscopy

After growth, NW arrays were systematically observed using a standard scanning electron microscope (SEM) to measure the NW dimensions and calculate the vertical yield. The latter corresponds to the percentage of mask holes filled with a single vertical NW, and is a figure of merit for regular NW array growth that will be used extensively in [Chapter 2](#).

The crystal structure of selected individual NWs, mechanically transferred to a copper grid, was observed using a transmission electron microscope (TEM). The TEM results presented in [Chapter 3](#) were obtained using a FEI Titan THEMIS operating at 200 kV at the C2N (more details in [\[de Lépinau, 2020\]](#)). Insights on the chemical composition of the NWs were gained by energy-dispersive X-ray spectroscopy (EDX) measurements using a Bruker Super X detector. The TEM results presented in [Chapter 4](#) were collected by collaborators at Tampere University in Finland.

##### Cathodoluminescence

Cathodoluminescence (CL) is an advanced spectroscopy technique based on the analysis of photons emitted from a material bombarded by a focused beam of electrons. It is a contactless technique with high spatial resolution, which allows the study of the crystal structure, surface passivation, defect and doping levels in nanoscale materials.

- **CL set-up and working principles:**

A cathodoluminescence microscope manufactured by Attolight (model Allalin 4027 Chronos) and located at the C2N was used in this PhD work. A schematic of the latter can be found in [Figure 1.7](#), from which three distinct ensembles are distinguishable, namely the electron emission system (grey), the light collection optics (yellow), and the dispersion and detection systems (red). The sample is securely mounted on a piezoelectric hexapod-like positioning system. A liquid helium flow cryostat allows to work on a broad temperature range (10 K - 350 K) while keeping an outstanding mechanical stability. Time-resolved measurements can also be performed in this CL equipment thanks to the use of a pulsed laser triggering the electron beam and a streak-camera for the time-resolved acquisition. However, these components have not been included in [Figure 1.7](#) as only the continuous operation mode was employed in this project.

The CL emission system is composed of a Schottky field emission gun and electron magnetic lenses which accelerate the electrons at a voltage of typically 6 kV. The electron beam current is controlled by the gun lens (typically a few nA) and the aperture (typically 100  $\mu\text{m}$ ). Once the sample is placed in the focal plane of the optical collection path, the electron beam can be finely adjusted. Focus (through the objective lens) and astigmatism (through deflector and stigmator) are fine-tuned to obtain the best SEM image quality.

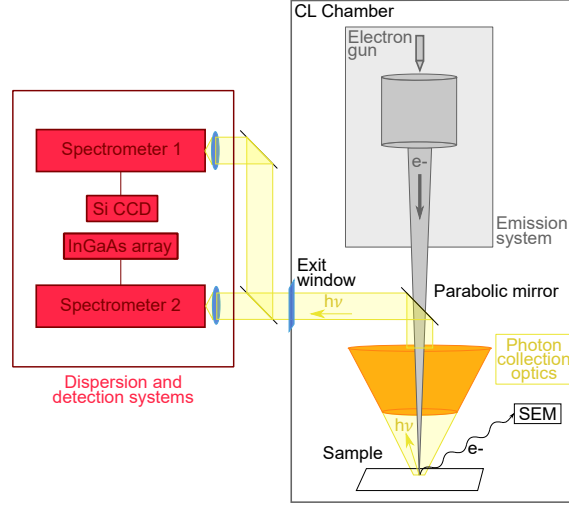


Figure 1.7: Schematics of the cathodoluminescence set-up used. Three distinct ensembles can be distinguished: the emission system (grey), the light collection optics (yellow), and the detection and dispersion systems (red). The time-resolved system is not shown here as it was not used in this PhD work. Adapted from [Bidaud, 2021].

Photons emitted by the sample are collected by a reflective objective and finally focused by an achromatic doublet on the entrance slit of a Horiba iHR320 spectrometer equipped with a Peltier-cooled Andor Newton Si charge-coupled device (CCD) (1024 x 256 pixels, 26  $\mu\text{m}$  pixel width, 0.53 nm/pixel spectral dispersion). This configuration is suited for CL signals in the 300–1100 nm luminescence range, fully compatible with the typical emissions of GaAs-based semiconductors. All CL spectra presented herein were corrected for the diffraction efficiency of the grating and the sensitivity of the CCD camera, and have a spectral resolution of roughly 1.5 nm (3 pixels).

One of the main advantages of the CL characterization technique is its spatial resolution, enabled by the scanning electron beam. In fact, by scanning the sample surface in an X-Y pattern and collecting the light emitted from each excitation position, a hyperspectral map of the sample can be obtained (2D image with a luminescence spectrum at each pixel). However, while the electron beam spot diameter is only about 10 nm, the volume of interaction between the impinging electrons and the sample is larger. In fact, CASINO simulations [Drouin et al., 2007; Chen et al., 2017] showed that for a GaAs slab excited in the aforementioned conditions, 75% and 95% of the carriers are generated in a pear-shaped excitation volume within a radius/depth of approximately 30/95 nm and 110/185 nm, respectively. Moreover, it is important to keep in mind that while the electron beam excitation is localized, emitted light can be collected from a much larger area. This is because electrogenerated carriers can diffuse in the sample before radiatively recombining some distance away from the excitation spot. The spatial resolution of the CL measurements is thus generally governed by the carrier diffusion lengths, which can be of several micrometers in high-quality, well-passivated III-V materials. In NWs however, the high surface/volume ratio and presence of defects limit carrier diffusion, especially at low temperature. Paradoxically, while this is undesired from a device perspective, it is beneficial to improve the CL spatial resolution.

A more detailed description of the CL set-up used and its working principles can be found in [Chen, 2018; Bidaud, 2021].

#### • CL spectra analysis:

As mentioned previously, the emission of light from a semiconductor contains crucial information on its optical and transport properties. Its relevance for NW doping characterization is shown in Chapter 4, and the aim here is to explain how the CL spectra were fitted to determine the electron concentration in GaAs NWs, at both room temperature (RT) and low temperature (LT). The explanation below is based on previous work from our group [Chen et al., 2017, 2021b].

**At room temperature**, the excitons are practically dissociated and shallow donors and acceptors are totally ionized. Band-to-band recombination of excess carriers is hence the most important mechanism, facilitating the modeling of the luminescence spectra at RT. The precise analysis of the RT luminescence lineshape is performed using the generalized Planck law and an absorption model for doped GaAs. The generalized Planck law defines the emitted photon flux  $\phi(\hbar\omega)$  as:

$$\phi(\hbar\omega) = \frac{A(\hbar\omega)}{4\pi^2\hbar^3c^2} \frac{(\hbar\omega)^2}{\exp(\frac{\hbar\omega - (E_{fc} - E_{fv})}{k_B T}) - 1}. \quad (1.6)$$

Here  $\hbar\omega$  is the photon energy,  $A$  the absorptivity,  $c$  the speed of light in vacuum,  $k_B$  the Boltzmann constant,  $T$  the absolute temperature, and  $E_{fc}$  and  $E_{fv}$  the electron and hole quasi-Fermi levels, respectively. The absorptivity in a homogeneous slab of thickness  $d$  is:

$$A(\hbar\omega) = (1 - R)[1 - \exp(-\alpha(\hbar\omega)d)], \quad (1.7)$$

where  $R$  is the reflectivity on the front surface, and  $\alpha$  the absorption coefficient of GaAs. The latter is obtained by using a model with parabolic bands, convoluted with an Urbach tail (low-energy exponential decay representing sub-bandgap absorption), and taking into account the probability of finding available states in the conduction and valence bands that match the energy  $\hbar\omega$ . This joint probability of occupation is typically lowered when many carriers occupy the bands, for instance in the case of high doping. In general,  $d$  can be regarded as a characteristic length over which carriers are generated, travel and recombine radiatively [Katahara and Hillhouse, 2014].

The RT CL spectra of n-doped GaAs can then be fitted with the generalized Planck law using the least-squares method to determine the bandgap  $E_g$ , the electron Fermi level  $E_{fc}$ , and the Urbach tail  $\gamma$ . The hole Fermi level  $E_{fv}$  is fixed at several  $k_B T$  above the VB edge, while the temperature  $T$  and the thickness  $d$  are fixed at 300 K and 150 nm, respectively. For all GaAs doping levels, a value of  $14800 \text{ cm}^{-1}$  at  $\hbar\omega = 1.6 \text{ eV}$  is used for the ideal absorption coefficient  $\alpha_{ideal}$ , since at energies above, the absorption coefficient is rather independent of the doping level. The fitted  $E_{fc}$  can then be related to the electron concentration  $n$  through a theoretical relation corrected for the nonparabolicity of the CB:

$$n = N_c [\mathcal{F}_{1/2}(\frac{E_{fc} - E_c}{k_B T}) - \frac{15\beta k_B T}{4E_g} \mathcal{F}_{3/2}(\frac{E_{fc} - E_c}{k_B T})]. \quad (1.8)$$

Here  $N_c$  is the effective density of the CB, taken as  $4.2 \times 10^{17} \text{ cm}^{-3}$ ,  $\mathcal{F}_j$  is the Fermi integral of order  $j$ , and  $\beta$  is the nonparabolicity factor taken as -0.83 for n-GaAs at RT [Blakemore, 1982]. Since for low-doped samples ( $< 5 \times 10^{17} \text{ cm}^{-3}$ ) accurate electron Fermi levels cannot be accurately extracted from the luminescence analysis, the aforementioned method provides a quantitative determination of high electron concentrations only ( $1 \times 10^{18} - 1 \times 10^{19} \text{ cm}^{-3}$ ).

**At low temperature**, the luminescence tends to be dominated by defects and exciton recombination. As thermal broadening is practically suppressed at LT, the electron concentration  $n$  can be obtained directly by fitting the full width at half maximum (FWHM) of the LT luminescence spectra following a phenomenological formula first established by [De-Sheng et al., 1982], and revisited by our group using previous experimental results:

$$FWHM(\text{eV}) = (3.75 \pm 0.21) \times 10^{-14} \times n^{2/3}. \quad (1.9)$$

Here the electron concentration  $n$  is in  $\text{cm}^{-3}$ , and  $\pm 0.21$  indicates the 95% confidence interval of the fitted parameter. This empirical relation can be used to determine electron concentrations in the range of about  $4 \times 10^{17} - 1 \times 10^{19} \text{ cm}^{-3}$ .

Both the RT and LT CL spectra analysis methods described above will be used to determine the electron concentration in Te-doped GaAs NWs in Chapter 4.

The dimensions and vertical yield of as-grown NW arrays can be systematically analyzed using standard SEM, while the crystal structure and chemical composition of selected individual NWs can be investigated using TEM and EDX. As a contactless characterization technique with high spatial resolution, CL enables the determination of the electron concentration in individual GaAs NWs at both RT and LT, by fitting the lineshape of the CL spectrum recorded. Electron concentrations between  $1 \times 10^{18}$ – $1 \times 10^{19} \text{ cm}^{-3}$  and  $4 \times 10^{17}$ – $1 \times 10^{19} \text{ cm}^{-3}$  can be determined at RT and LT, respectively.

### 1.3.2 Hyperspectral photoluminescence

Photoluminescence (PL) is similar to CL as it also consists in analyzing the light emitted by an excited semiconductor in order to gain information on its optical and transport properties. However, in PL the excitation source is composed of photons rather than electrons, typically originating from a monochromatic laser or LED source. PL thus presents a lower spatial resolution than CL, but it allows the characterization of both as-grown and processed NW arrays. The photogeneration of carriers in PL also translates into a quasi-Fermi level splitting which can be related to the emitted photon flux according to the generalized Planck law presented in Equation (1.6). In PL, the absorptivity  $A$  corresponds to the absorption probability of an incident photon of energy  $\hbar\omega$  on a surface element. In this PhD work, a home-made hyperspectral imager set-up located at the IPVF and calibrated in absolute units was used for PL measurements.

#### Hyperspectral imager set-up

Hyperspectral imaging of a luminescence signal refers to the acquisition of a luminescence spectrum for each pixel of a 2D image. As illustrated in Figure 1.8, the excitation light source used in the hyperspectral imaging set-up located at the IPVF is a laser or LED beam, spread through a diffuser to ensure wide-field illumination. The solar cells themselves, via a  $J_{SC}$  measured at 1-sun illumination, are generally used as power-meters to measure the intensity of the excitation light. An objective with numerical aperture (NA) 0.6 is then used to focus the illumination on the sample surface. The light emitted from the sample is collected through the same objective, and selectively transmitted upwards using a beam splitter.

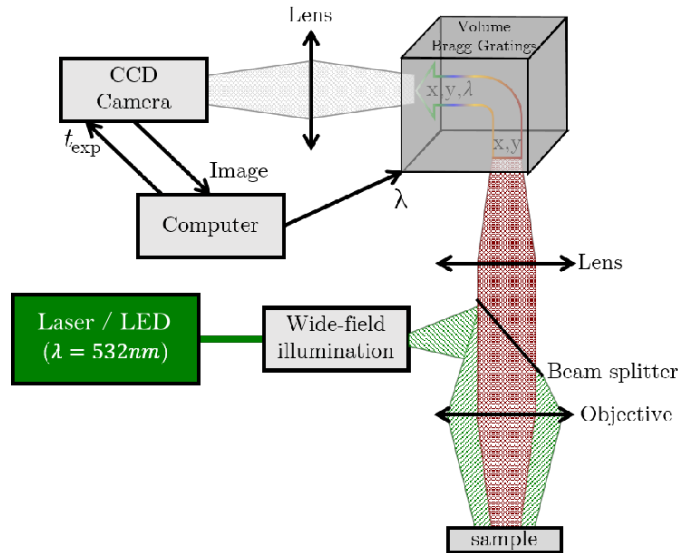


Figure 1.8: Schematics of the hyperspectral PL imaging set-up used, with here a green excitation light source and a sample emitting red luminescence. Reprinted from [Bercegol, 2020].

In order to separate the spectral components of the emitted luminescence, a 2D spectral filter based on volume Bragg gratings is used. The latter forms a 2D image acquired by the CCD camera. Exposing the CCD camera to the luminescence signal for a given exposure time for each position

of the grating (hence for each selected wavelength) then yields a 3D data cube ( $x$ - $y$ - $\lambda$ ). This data cube needs to be rectified by the acquisition software before being exploited to obtain spectrally-resolved images with a minimal spectral resolution of 2 nm and a typical spatial resolution of 1  $\mu\text{m}$  (determined by the numerical aperture of the objective).

A more detailed description of the hyperspectral PL imaging set-up used and its working principles can be found in [Bercegol, 2020; Fournier, 2021].

### Absolute calibration procedure

The acquired 3D data gives a number of counts, per pixel area, per wavelength step  $\delta\lambda$  of the acquisition. In order to obtain spectrally-resolved PL images in absolute units ( $\text{photon s}^{-1} \text{nm}^{-1} \text{m}^{-2} \text{sr}^{-1}$ ), a series of calibrations are required. The thorough calibration procedure is explained in [Delamarre, 2013], while its main steps are described below.

- **Spectral accuracy:** The grating's spectral accuracy is verified by shining two lasers of known wavelengths (783.6 nm and 1062.2 nm) into the objective.
- **Dark image subtraction:** For every data set, two cubes are acquired and rectified, one in the illuminated condition ( $I_{illum}$ ) and one in the “dark” condition ( $I_{dark}$ ), with similar experimental parameters (especially the same exposition time  $t_{exp}$ ). During the dark cube acquisition, the sample is not illuminated. This allows the correction of the camera read and dark current noises, as well as potential parasitic illumination from the surroundings by subtracting the dark signal from the one acquired in the illuminated condition:

$$I(x, y, \lambda) = \frac{I_{illum}(x, y, \lambda) - I_{dark}(x, y, \lambda)}{t_{exp}}. \quad (1.10)$$

- **Correction of the set-up response:** Spatial and spectral sensitivity variations of the set-up also need to be taken into account. In order to reconstruct the initial luminescence spectrum, a white lamp with known spectrum is used. Its light is guided through an integrating sphere placed at the sample position to ensure spatially homogeneous light emission. The hyperspectral set-up then records a cube of the lamp's luminescence ( $I_{lamp}$ ), which is to be compared to the lamp's reference spectrum ( $I_{ref}$ ) to give the set-up response ( $R_{setup}$ ):

$$R_{setup}(x, y, \lambda) = \frac{I_{ref}(\lambda)}{I_{lamp}(x, y, \lambda)}. \quad (1.11)$$

- **Converting counts to photons:** A laser coupled into an optical fiber at the sample position and directed towards the objective is used to calibrate the photon flux emitted by the investigated sample. The laser photon flux (number of photons per second,  $n_{photons}$ ) is first deduced from its power ( $P_{laser}$ ) measured with a power-meter:

$$n_{photons} = \frac{\text{Laser energy}}{\text{Energy of 1 photon}} = \frac{P_{laser}}{\frac{hc}{\lambda}}. \quad (1.12)$$

Here  $\lambda$  is the laser wavelength,  $h$  the Planck constant, and  $c$  the speed of light in vacuum. On the other hand, the product of the set-up response ( $R_{setup}$ ) and the hyperspectral cube of laser emission ( $I_{laser}$ ), summed over the space and narrow laser bandwidth, results in a corresponding number of counts per second ( $n_{counts}$ ). Given that the photon flux coming out of the optical fiber is entirely collected by the set-up due to its small solid angle of emission compared to the collection angle of the microscope objective, a counts to photons ratio ( $R_{ctp}$ ) can then be defined as:

$$R_{ctp} = \frac{n_{photons}}{n_{counts}} = \frac{n_{photons}}{\sum_{x,y,\lambda} R_{setup}(x, y, \lambda) I_{laser}(x, y, \lambda)}. \quad (1.13)$$

- **Spatial calibration:** One pixel of the CCD camera images a sample surface that we note  $S_{pixel}$ . The latter can be determined using a sample with characteristic dimensions. The size of a pixel will vary depending on the objective used.

- **Solid angle normalization:** A Lambertian emission profile is assumed for the sample's photoluminescence, however only a fraction of it is collected by the objective, depending on its numerical aperture  $NA$ . The collection solid angle is given by  $\Omega = \pi NA^2$ . The output cube is divided by  $\Omega$  to be expressed in  $\text{sr}^{-1}$ .

Putting everything together, a PL cube with absolute physical units ( $\text{photon s}^{-1} \text{nm}^{-1} \text{m}^{-2} \text{sr}^{-1}$ ) can be obtained as follows:

$$I_{abs}(x, y, \lambda) = \frac{I_{illum}(x, y, \lambda) - I_{dark}(x, y, \lambda)}{t_{exp}} \cdot R_{setup}(x, y, \lambda) \cdot R_{ctp} \cdot \frac{1}{\delta\lambda \cdot S_{pixel} \cdot \Omega}. \quad (1.14)$$

A home-made hyperspectral imager set-up located at the IPVF allows the collection of a 3D data set containing the PL spectrum at each point of a 2D image, calibrated in absolute physical units. Hyperspectral PL measurements acquired with this set-up were used to determine the quasi-Fermi level splitting and spatial inhomogeneities in GaAs/GaInP core-shell NW arrays (see [Chapter 3](#)).

### 1.3.3 Characterization of processed NW arrays

After processing the NW arrays, functional solar cells can be obtained. The figures of merit for the assessment of a solar cell performance have been previously presented in [subsection 1.1.1](#). The latter can be measured using a solar simulator and an external quantum efficiency set-up.

#### Current-voltage measurements using a solar simulator

The electrical performances ( $J_{SC}$ ,  $V_{OC}$ , FF, and PCE) of the NW solar cells were measured at the C2N using a Keithley 2601B source measure unit in a four-probe configuration at room temperature, in the dark and under a 1-sun illumination. The latter is provided by a Newport 94011A-ES solar simulator equipped with an AM1.5G filter. Its power was calibrated to  $1000 \text{ W m}^{-2}$  using a known Si reference cell at  $25^\circ\text{C}$ .

#### External quantum efficiency (EQE)

As briefly explained in [subsection 1.1.1](#), the EQE measures the probability for an incident photon of generating an electron that will be collected at the solar cell contacts. The measurement of the EQE (at 0 V) allows the determination of the cell's  $J_{SC}$  through integration with the AM1.5G spectrum ([Equation \(1.2\)](#)), in a more accurate way than when a solar simulator is used. This is because  $J_{SC}$  determination from EQE has the advantage of being independent of the spectral shape of the light source. The EQE can also be expressed as a convolution of the position and wavelength-dependent normalized carrier generation rate ( $G^n(\lambda, z)$ ), and the position and voltage-dependent collection function ( $\eta_c(z, V)$ ), as follows [[Scheer and Schock, 2011](#)]:

$$EQE(\lambda, V) = \int G^n(\lambda, z) \eta_c(z, V) dz. \quad (1.15)$$

EQE measurements under potential bias can thus yield valuable information on carrier collection in a solar cell.

A Xenon light source coupled with a Horiba Triax monochromator is used for EQE measurements at the C2N. The illumination spot has a diameter that can be tuned between tens of nm and a few mm using different microscope objectives (and diaphragms), and is focused at nearly normal incidence on the investigated sample surface. EQE measurements always start by a wavelength scan over the spectral range of interest (300–1000 nm for GaAs, 5 nm interval) performed on a reference Si photodiode. Knowing its spectral sensitivity allows to determine the number of incident photons from the measurement of the current. Then, the investigated solar cell is placed at the same position as the reference diode, and is electrically contacted using four-point probes

connected to a Keithley source measure unit. The photocurrent recorded under the same illumination conditions then gives a number of collected electrons. The EQE of the cell can be deduced from the ratio between the number of collected electrons and the number of incident photons.

## 1.4 Chapter conclusions

In this chapter, the physics behind the working principles of solar cells based on a semiconductor p-n junction were introduced. The figures of merit used to assess the performance of PV devices were also given, and used to compare different existing technologies.

While Si-based PV technologies currently dominate the market, the higher performance of III-V materials were highlighted. I stressed the importance of tandem solar cell architectures to achieve power conversion efficiencies beyond 30%, with in particular the III-V/Si configuration having great potential for high-efficiency devices. However, cost-related issues, as well as ones associated with lattice constant and thermal expansion coefficient mismatches were exposed as reasons behind the so far limited large-scale development of III-V/Si solar cells. I then presented the unique properties of NWs, which offer many advantages for Si-based tandem PV devices. However, the reported performance of state-of-the-art III-V NW solar cells showed that a number of unresolved issues must be addressed before their potential can be fully exploited.

To improve the performance of NW solar cell devices it is important to characterize them thoroughly. In [Section 1.3](#), I thus presented the advanced characterization techniques employed in this PhD work. Electron microscopy techniques such as SEM and TEM were used to analyze the dimensions, vertical yield and crystal structure of as-grown NWs. The CL methods developed in the group and used to quantify the carrier concentration in individual NWs were also explained. I then detailed the principles of the hyperspectral PL set-up which can be used to investigate the optoelectronic properties of both as-grown and processed NW arrays. Finally, the solar simulator and EQE set-ups used to measure the performance of functional NW solar cells were also presented.



## Chapter 2

# Growth of Vertical GaAs Nanowire Arrays on Silicon

### Chapter Contents

<b>2.1</b>	<b>Molecular beam epitaxy (MBE) for NW growth</b>	<b>28</b>
2.1.1	Epitaxial growth of semiconductor NWs	28
	Fundamentals of VLS and VS growth mechanisms	28
	Main epitaxial growth methods	29
2.1.2	Principle and components of MBE	30
	Growth rate and flux ratio calibration by RHEED	31
2.1.3	MBE set-ups used in this work	32
2.1.4	State-of-the-art of GaAs NW arrays grown on Si	33
	Pre-growth (substrate) parameters influencing the NW vertical yield	34
	Growth parameters influencing the NW vertical yield	34
<b>2.2</b>	<b>Towards 100% vertical GaAs NWs grown on Si with tuneable diameter</b>	<b>37</b>
2.2.1	Optimizing the patterned substrate preparation for near-perfect yields	37
	A robust silicon substrate cleaning procedure	37
	Depositing high-quality dielectric layers for good mask selectivity	37
	Mask patterning process	39
	New drying method for pristine and homogeneous substrate surface	41
2.2.2	NW diameter variation with mask hole size	43
	Standard NW growth recipe	43
	NW morphology evolution with mask hole size	44
	NW vertical yield variation with mask hole size	47
<b>2.3</b>	<b>Chapter conclusions</b>	<b>48</b>

The eagerly pursued integration of defect-free III-V materials on silicon can be achieved by using epitaxially grown NWs. In this chapter, the fundamentals of NW growth by molecular beam epitaxy (MBE) will be introduced, along with the MBE set-ups used in this PhD work. The parameters influencing the epitaxial growth of regular GaAs NW arrays on Si will then be discussed using results obtained from the literature. Finally, the substrate preparation optimizations which allowed us to achieve near-perfect NW vertical yields and controllable NW diameter will be presented.



## 2.1 Molecular beam epitaxy (MBE) for NW growth

### 2.1.1 Epitaxial growth of semiconductor NWs

The term epitaxy, from the Greek roots *epi* (above) and *taxis* (an ordered manner), refers to the process of growing new crystalline layers of a well-defined orientation relative to the underlying crystalline substrate. A wide range of materials can be grown by epitaxy (oxides, metals, organics, etc.), but its main commercial applications are in the semiconductor industry. In fact, the highly controlled epitaxial growth environment allows for the deposition of crystal layers with extremely low impurity levels and controlled material composition and doping, as required for the fabrication of semiconductor devices such as transistors, diodes, lasers, and solar cells. In the case of homoepitaxy, the epitaxial layer is made of the same exact material as the substrate, while in heteroepitaxy, the epitaxial layer is of a different composition. High-quality layers are difficult to obtain in heteroepitaxy when there is a mismatch in the lattice constants and thermal expansion coefficients of the substrate and the grown layer.

Semiconductor NWs can be prepared by either a top-down or bottom-up approach. In the top-down approach, bulk material is selectively removed by lithographic techniques to form NWs. The variety of substrates on which the NWs can be formed is hence limited in this approach by the lattice constants and thermal expansion coefficients of the substrate and the grown layer. In addition, the material selectively removed in between the NWs is usually lost in the process, reducing the cost-efficiency of this approach. In the bottom-up approach however, NWs can be directly grown on dissimilar substrates (such as silicon for III-V NWs), with relatively little material loss.

To grow 1D nanostructures such as NWs perpendicular to the substrate, the addition of material during the growth process must occur only along one direction [Zhang et al., 2016]. This is most commonly achieved by using the vapour-liquid-solid (VLS) growth mechanism, but can also occur via vapour-solid (VS) growth.

#### Fundamentals of VLS and VS growth mechanisms

Semiconductor NW growth occurs predominantly via the VLS growth method, which was first demonstrated in 1964 by Wagner and Ellis with the growth of sub-micrometer Si whiskers using a gold catalyst [Wagner and Ellis, 1964]. In fact, in VLS growth, a liquid metal droplet is used to catalyze the growth of high-quality NWs, whose position and diameter are determined by the location and size of the droplet on the substrate. The droplet can be composed of either one of the growth constituents (self-catalyzed growth approach), or of a foreign element such as gold. In the case of gold, the droplets can be localized on the substrate using lithography techniques, or randomly positioned through the deposition and subsequent heating of a gold film. However, due to the well-known incompatibility of gold with Si technology [Lang et al., 1980; Tavendale and Pearton, 1983], the growth of III-V nanowires on Si substrates is usually promoted by the group III metal, which sits at the top of the NW and acts as a material collector during growth, as illustrated by the blue arrows in Figure 2.2. Upon supersaturation of the group V element within the droplet, precipitation of the semiconductor material begins at the triple phase line [Glas et al., 2007], ultimately resulting in fast one-dimensional crystal growth [Fontcuberta i Morral et al., 2015; Zhang et al., 2016]. During NW synthesis by the VLS mechanism, some radial growth also occurs concurrently through the VS mechanism due to atom incorporation via the NW sidewalls [Oehler et al., 2018]. This is illustrated in Figure 2.1, and in Figure 2.2 by the brown arrows, and will be further explained in the next paragraph. Typically, NWs with a diameter of 20-200 nm and a length of up to several microns can be obtained by the VLS growth mechanism using modern epitaxy techniques such as molecular beam epitaxy (MBE) and metal-organic chemical vapour deposition (MOCVD) [Dubrovskii, 2014].

NWs can also be grown entirely by a catalyst-free (VS) process, in a manner similar to thin film growth, typically through selective area growth (SAG) [Motohisa et al., 2004; Ikejiri et al., 2007; Kim et al., 2018]. In SAG, the nucleation sites are defined by a template method (see Figure 2.2) involving the deposition of amorphous films on the substrate surface (typically SiO<sub>2</sub> or SiN), and their subsequent patterning using lithography techniques. Although several works have demonstrated excellent control of NW properties using SAG [Yao et al., 2015], no consensus has however been reached regarding the exact growth mechanisms involved. In particular the complete absence of catalyst droplet during SAG is still debated [Gao et al., 2016], and in both MBE and

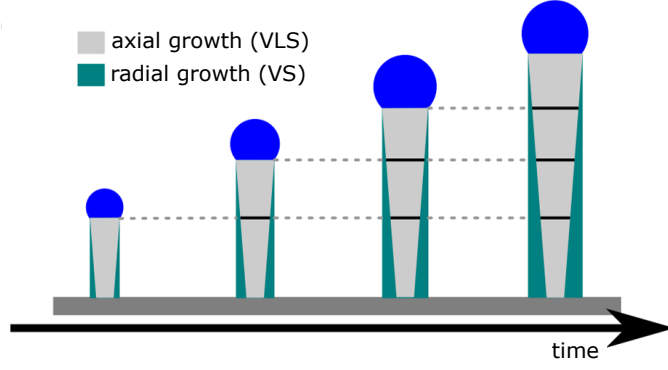


Figure 2.1: Schematics of the NW morphology evolution resulting from simultaneous axial (VLS) and radial (VS) growth. Black lines indicate example marker layers used in the morphology evolution study. Reprinted from [Oehler et al., 2018].

MOCVD, VS growth has been found to result in a higher number of stacking faults in the NWs as compared to VLS [Güniat et al., 2019]. As a consequence, it is common to grow self-catalyzed III-V NW arrays on patterned substrates, especially for the formation of radial structures, in which a NW core is first synthesized via the VLS mechanism and after droplet consumption, the axial elongation is replaced by radial (shell) growth via the VS mechanism [Colombo et al., 2009; Couto et al., 2012; Vettori et al., 2019]. This is illustrated in Figure 2.2. The subsequent radial NW growth is enabled by the dependence of the crystal growth velocity on crystallographic orientation [Güniat et al., 2019], and is further dictated by the group III atoms' diffusion characteristics along the NW sidewalls. The different NW core and shell growth mechanisms also result in varying dopant incorporation pathways, which can affect the doping profile along the growth direction. This will be discussed in more detail in Chapter 4.

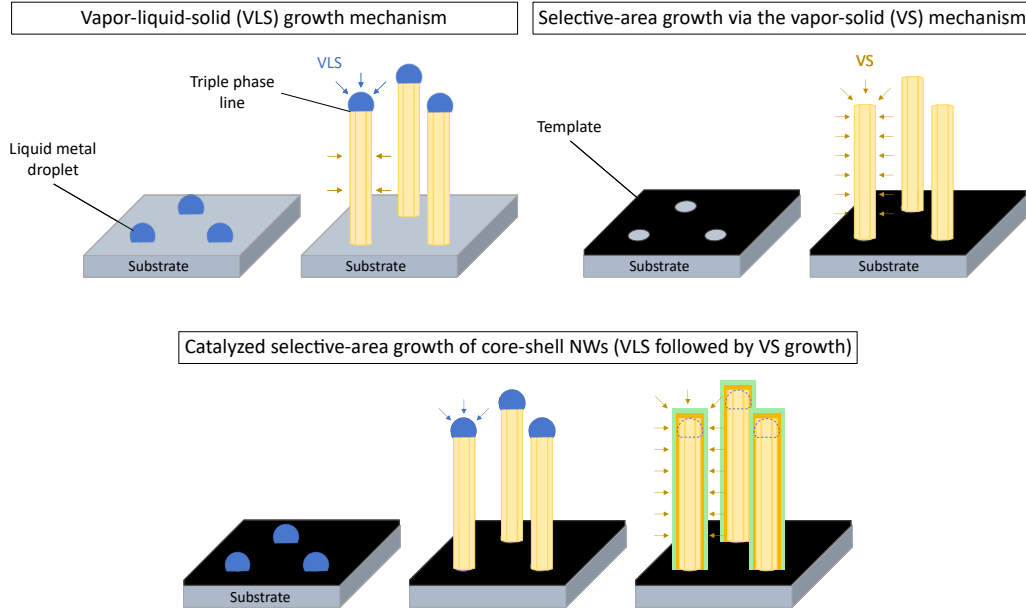


Figure 2.2: Mechanisms of VLS, selective-area (VS), and catalyzed selective-area growths. The arrows indicate the main atom incorporation pathways.

### Main epitaxial growth methods

Several epitaxial growth techniques exist and can be classified according to the phase (liquid or vapor) of the material used to form the solid epitaxial layer. The first epitaxial growth technique used to produce complex electronic devices was liquid-phase epitaxy (LPE) [Capper et al., 2007; Pohl, 2013]. Nowadays, more sophisticated methods based on vapour-phase epitaxy (VPE) are

used for the growth of electronic and optoelectronic devices, with the most prominent ones being metal-organic chemical vapour deposition (MOCVD) and molecular beam epitaxy (MBE) [Copper et al., 2007].

- **Metal-organic chemical vapour deposition (MOCVD)**  
MOCVD is a chemical vapor deposition method which occurs in a pressure regime comprised between 15–750 Torr, and uses complex and often toxic metal-organic and hydride sources rather than elemental sources. In MOCVD, a carrier gas (typically hydrogen) is required to transport the reactants to the substrate surface, where they react chemically to form epitaxial layers at high growth rates (typically around 5  $\mu\text{m}/\text{h}$ , but growth rates beyond 100  $\mu\text{m}/\text{h}$  have been demonstrated [Lang et al., 2018, 2020]). As a consequence, MOCVD is eligible for industrial-scale epitaxial films production.
- **Molecular beam epitaxy (MBE)**  
MBE growth is a physical vapor deposition method which occurs in an ultra-high vacuum (UHV) environment (base pressure  $1 \times 10^{-10}$  Torr), resulting in highly directional elemental beams and exceptional material purity. However, the high vacuum requirements of the MBE means less setup variability, long maintenance periods and greater cost. Epitaxial growth rates are typically on the order of 1  $\mu\text{m}/\text{h}$ . As a consequence, MBE is often used for lab-scale demonstrations of new device concepts [Farrow, 1995; Pelzel, 2013], as it is the case in the framework of this PhD work.

NWs are most often grown by the VLS mechanism in which a liquid droplet acts as catalyst. Such growth can occur at random positions, or in an ordered manner on substrates patterned with a dielectric mask. The latter enables the growth of regular NW arrays with reproducible characteristics. Such catalyzed selective-area growth can be used to form core-shell NW structures when the axial VLS growth is followed by radial VS growth after droplet consumption. The most prominent epitaxial growth methods include MOCVD and MBE, each with their own advantages and disadvantages. Nevertheless, MBE is more suited for lab-scale demonstrations of new device concept, such as the ones presented in this PhD work.

### 2.1.2 Principle and components of MBE

MBE was developed during the 1960s as a thin film growth technique for GaAs-based structures [Orton and Foxon, 2015]. It involves the generation of atomic or molecular fluxes (*molecular beam*)

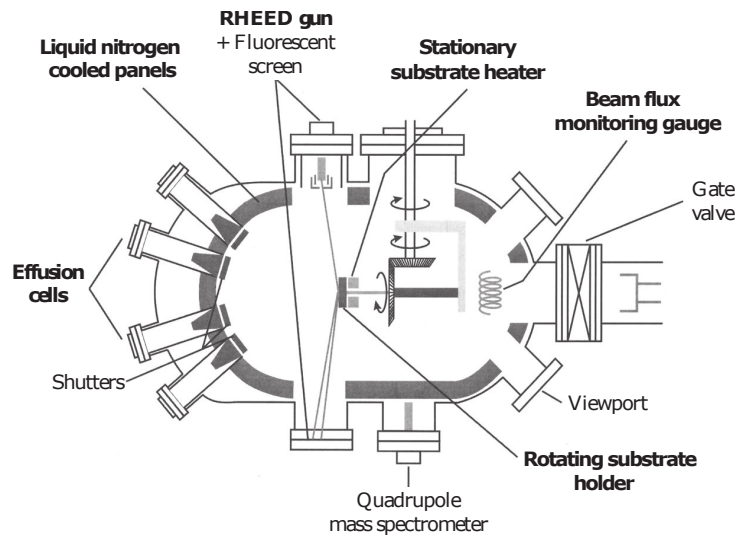


Figure 2.3: Schematic diagram of a typical MBE growth chamber. The key components are highlighted in **bold** and explained in the main text. Adapted from [Orton and Foxon, 2015]

directed towards the substrate which react at its surface to form a single-crystal layer with well-defined crystalline orientation with respect to the substrate (*epitaxy*, see [subsection 2.1.1](#)).

In solid-source MBE, elementary sources in their ultra-pure solid form are contained in individual **Knudsen effusion cells** (crucibles with heating filaments, cooling system, and orifice shutter), as depicted in [Figure 2.3](#). In order to grow single-crystal layers, the effusion cells are heated up to an appropriate temperature at which the elements undergo sublimation. The gaseous elements then travel from the effusion cells to the substrate surface where they condense and react with each other to form a crystalline layer. Uniform growth is enabled by mounting the substrate on a **rotating holder** placed in front of a **stationary heater**. As previously mentioned, MBE systems operate under UHV environments to ensure negligible unintentional impurity levels in the epitaxially grown layer. These demanding vacuum conditions are achieved in the MBE by primary, secondary and cryogenic pumps, as well as **liquid-nitrogen cooled cryopanel**s. The UHV growth environment also enables *in-situ* monitoring of both the growth rate and structural quality of the growing film through the use of **reflection high energy electron diffraction (RHEED)**. As the absolute molecular beam fluxes (number of atoms per unit area per unit time) cannot be measured directly, a **beam flux monitoring ionization gauge** placed at the substrate position is used to monitor instead the system-dependent beam equivalent pressures (BEPs), which after calibration gives a reading that is proportional to the absolute molecular beam flux and hence growth rate.

### Growth rate and flux ratio calibration by RHEED

The crystalline quality and morphology of NWs depend strongly on the growth rate and group V to group III flux ratio (referred to herein as V/III ratio) used during growth. RHEED intensity oscillations provide a fast and accurate *in-situ* growth rate determination method for 2D materials. However, the growth rate of NWs cannot be measured directly, and 2D equivalents are typically given as references. In a RHEED system, a beam of electrons generated by an electron gun strikes the sample surface at grazing incidence ( $1-3^\circ$ ), and diffracts from atoms at the topmost layers of the sample. A small fraction of these diffracted electrons interfere constructively at specific angles and form diffraction patterns on a fluorescent screen placed opposite the electron gun, as depicted in [Figure 2.3](#). These diffraction patterns depend on the surface features of the sample, and the intensity of individual diffraction spots fluctuate in a periodic manner as a result of the varying surface coverage (roughness) during monolayer (ML) growth. As illustrated in [Figure 2.4](#), when the sample surface is atomically flat, the intensity of the diffracted pattern is maximal. When a ML starts to grow, the surface coverage (roughness) increases, resulting in a reduction of the RHEED signal intensity, until the ML is complete. Therefore, when epitaxial growth occurs ML by ML, the time required to grow a ML is given by the period of the RHEED signal oscillation, and its

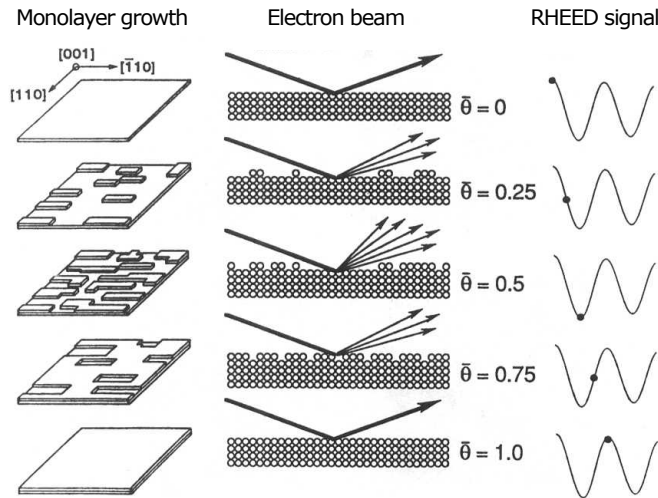


Figure 2.4: Real space representation of the formation of a single monolayer, monitored by RHEED oscillations.  $\bar{\theta}$  gives the fractional layer coverage. Reprinted from [[Ohring, 2001](#)].

inverse corresponds to the growth rate in ML/s. A ML of GaAs corresponds to the thickness of one full layer of Ga and one full layer of As atoms. Knowing the crystal lattice parameter of GaAs thus allows the growth rate to be converted from ML/s to nm/s, and even to atoms/cm<sup>2</sup>/s (flux).

When III-V semiconductor growth is carried out under an excess of group V elements, the growth rate is said to be *group III limited*. On the contrary, when growth occurs under an excess of group III elements, the growth rate is said to be *group V limited*. Growth in a group V limited regime is however not sustainable as group III droplets form rapidly on the surface, degrading the sample. Figure 2.5a shows the variation of the planar GaAs growth rate with varying Ga cell temperatures in a group III (Ga) limited regime, as determined from RHEED intensity oscillations on a GaAs(100) substrate. Figure 2.5b shows the transition between a group III (Ga) limited regime and a group V (As) limited regime at a fixed Ga cell temperature of 963°C and a varying As flux (adjusted with the As valve opening). The latter enables the determination of the stoichiometry point, at which the V/III ratio is 1, i.e. the atomic fluxes of Ga and As are equal. The typical growth rates of GaAs and GaP NWs grown in this PhD work are 0.71 ML/s (2 Å/s) and 0.66 ML/s (1.8 Å/s), respectively, with a typical V/III ratio of 1.2, calibrated using the aforementioned method.

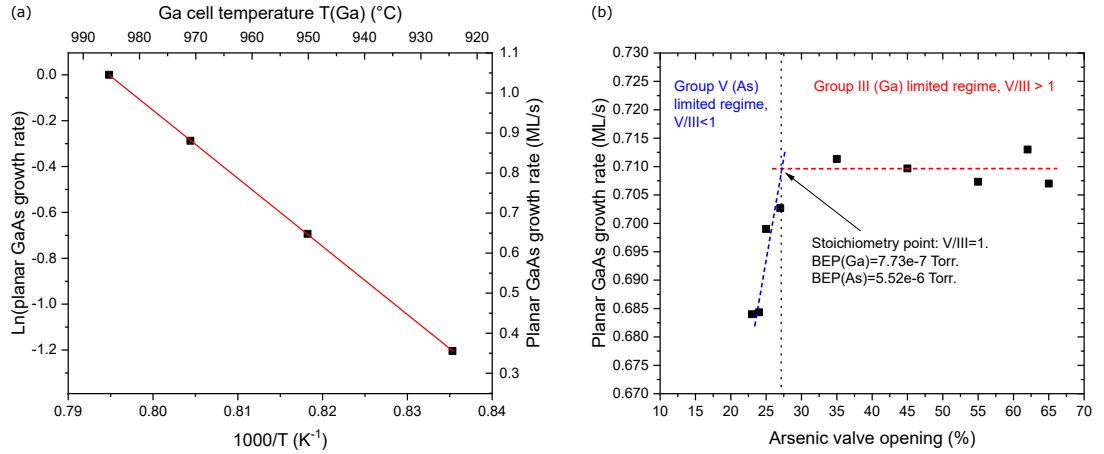


Figure 2.5: Evolution of the planar GaAs growth rate on a GaAs(100) substrate at 600°C, with respect to (a) Ga cell temperatures following an Arrhenius law in Ga limited conditions, and (b) the As flux (adjusted with the As valve opening) at a constant Ga cell temperature of 963°C, as measured by RHEED intensity oscillations. The transition between the As limited regime and the Ga limited regime gives the stoichiometry point at which the V/III ratio is 1, i.e. the atomic fluxes of Ga and As are equal.

MBE machines are complex systems operating under ultra-high vacuum conditions. Atomic or molecular fluxes are typically generated by effusion cells, and directed towards the substrate to react at its surface in order to form an epitaxial layer. The growth rate and structural quality of the growing layer can be assessed *in-situ* using RHEED. The beam fluxes are typically also carefully monitored using an ionization gauge, to ensure desired flux ratios (here V/III ratio) during growth.

### 2.1.3 MBE set-ups used in this work

Two solid-source MBE set-ups were used for the NW growths presented in this PhD manuscript, namely a Compact21 reactor located at the IPVF and a Riber32 reactor located at the C2N. This is mainly due to the move of the former during the PhD project.

The Riber32 MBE set-up is a much older model, and has previously been used for the growth of Au-catalyzed NWs, unlike the Compact21 set-up which has only been used for self-catalyzed III-V NWs and planar layers. It is also smaller and more compact, with the source cells disposed on one side of the growth chamber over two rows, facing the substrate holder. Dissimilar to the Compact21



system, the substrate normal in the Riber32 set-up is not perpendicular to the XY-plane, and the cells' angles of incidence relative to the substrate normal are not identical, as illustrated in the schematics of Figures 2.6a and b. The different flux incidence angles in the two MBE systems can lead to different growth dynamics for NWs. Other differences that can be expected from the change of the MBE set-up are related to the sample temperature, which can slightly vary from one pyrometer/thermocouple reading to another, and the residual impurities in the MBE chamber due to the history of the machines, but these have not been studied here.

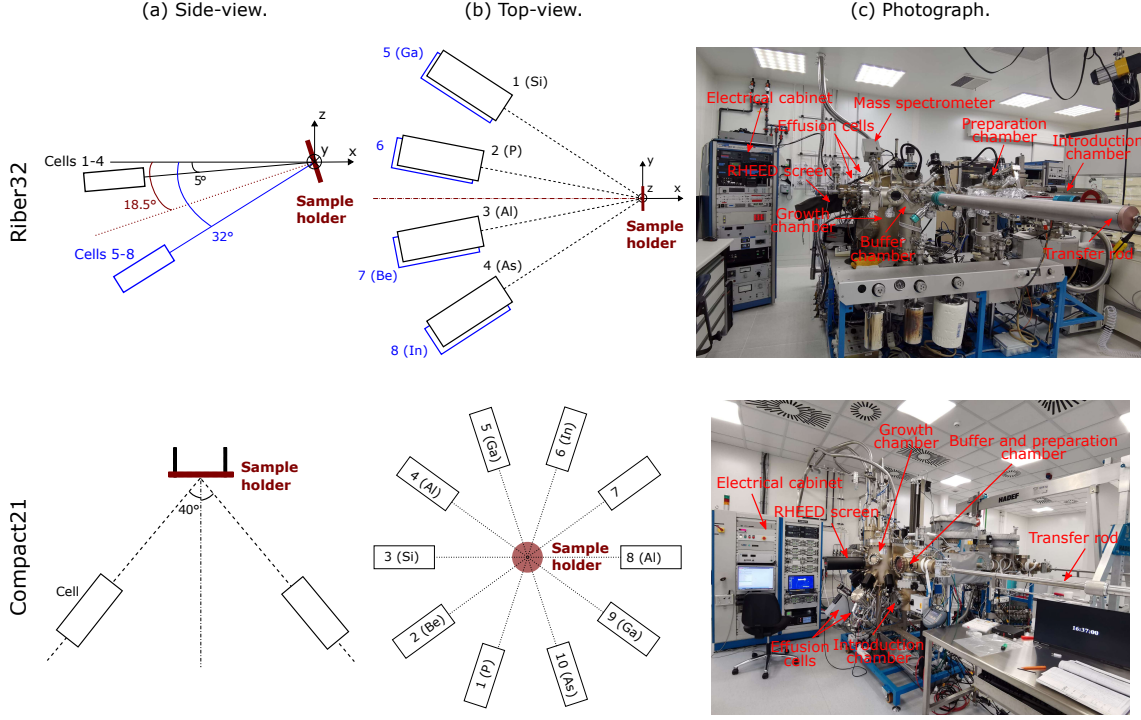


Figure 2.6: (a) Side-view and (b) top-view of the geometrical configuration of the source cells in the Riber32 and Compact21 MBE set-ups located at the C2N and the IPVF, respectively. Adapted from [de Lépinau, 2020]. (c) Photographs showing the components of the two MBE systems.

Two MBE set-ups were used for NW growth in this PhD work, namely a Compact21 reactor located at the IPVF, and a Riber32 reactor located at the C2N.

#### 2.1.4 State-of-the-art of GaAs NW arrays grown on Si

Given that to make large-area solar cells the uniformity of the NWs is critical, the literature review below focuses on regular NW array growth. In particular, it focuses on the self-catalyzed growth of GaAs NWs on patterned Si substrates. This is because GaAs is one of the most studied III-V semiconductors, and has been used extensively as a proof-of-concept material for NW devices. The key growth parameters of the state-of-the-art GaAs NW arrays reported in the literature in the past 10 years are presented in Table 2.1. All the Si substrates used in these growths have a  $\langle 111 \rangle$  orientation to follow the preferred GaAs NW growth direction [Zeng et al., 2020]. The figure of merit chosen to compare the GaAs NW arrays is the NW vertical yield, defined as the percentage of mask holes filled with a single vertical NW. In fact, one of the main challenges of GaAs NW growth on patterned Si substrates is to obtain high NW vertical yields in a reproducible manner [Barrigón et al., 2019]. Several studies have been dedicated to investigating the parameters controlling the NW vertical yield, and in fact 1/3 of the references cited in Table 2.1 contain explicitly the word “yield” in their title. As pre-growth (substrate preparation) and growth parameters can both impact the NW vertical yield, it is important to deconvolute their influence.

### Pre-growth (substrate) parameters influencing the NW vertical yield

The patterned substrate preparation directly determines the quality of the NW growth. The pre-growth parameters that will be discussed in the next paragraphs using Table 2.1 as support, are: the properties of the dielectric mask layer, its thickness and patterning technique, the mask hole diameters and interhole distance (pitch), and finally the cleanliness of the Si surface in the mask hole openings.

As previously mentioned, all the NW arrays reported in Table 2.1 are grown on  $\langle 111 \rangle$ -oriented Si substrates to follow the preferred GaAs NW growth direction. Most substrates are also p-doped to pursue p-n junction NW solar cell devices. As observed in Table 2.1, the most popular **dielectric material** used for self-assisted selective-area-growth of GaAs NWs is silicon oxide, either thermally grown, or deposited by plasma-enhanced chemical vapour deposition (PECVD). When comparing SiO<sub>2</sub> layers deposited by the two aforementioned methods, [Plissard et al., 2011] observed detrimental parasitic growth only on PECVD-deposited SiO<sub>2</sub>, and suggested that mask selectivity differences can arise due to the quality of the deposited layers. Hence, regardless of the deposition method used, it is important to optimize the dielectric layer quality to obtain the desired mask surface chemistry and diffusion properties. This will be further discussed in Section 2.2 using our experimental results.

The **dielectric mask thickness** is another important parameter for successful NW growth, and more precisely it is the mask hole aspect ratio (hole diameter/mask layer thickness) which was reported to play a prominent role in producing the most-suited Ga droplets for achieving high NW vertical yields [Vukajlovic-Plestina et al., 2019]. However, we can see from Table 2.1 that while the community seems to have converged to mask layer thicknesses between 10 and 30 nm after wet etching, the optimized **mask hole diameters** vary largely, from below 40 to above 200 nm, depending on the patterning method used. Many groups observed that increasing the hole diameter eventually resulted in the growth of multiple NWs in one hole, due to an increased collection area for Ga at the substrate, combined with unfavorable wetting of the droplets [Plissard et al., 2011; Zhang et al., 2014; Bahrami et al., 2020]. This is further discussed in the next subsection on the growth parameters influencing the NW vertical yield.

As seen from Table 2.1, the two dominating **lithography techniques** used for the SAG of NWs are electron-beam lithography (EBL) and nanoimprint lithography (NIL). The latter is typically preferred for large pattern sizes because it is faster than the sequential process used in EBL. However, it is still difficult to realize feature sizes as small as the ones achievable with EBL, although [Küpers et al., 2017] have demonstrated a conventional NIL process combined with an indirect pattern transfer (NIL-IPT) technique that can result in hole diameters below 50 nm.

The interhole distance (**pitch**) used in the different studies have been summarized in Table 2.1 as an indication, but actually its value was found to not have a significant impact on the NW vertical yield for pitches above 100 nm [Plissard et al., 2011; Russo-Averchi et al., 2015; Schroth et al., 2019; Wilson et al., 2021]. The pitch is rather chosen according to the final NW density required.

The **cleanliness of the Si surface** in the mask openings is also critical for the nucleation of GaAs NWs [Küpers et al., 2017], and the community has converged on the importance of a hydrofluoric acid (HF)-based chemical etch prior to MBE-loading to remove the native oxide formed on the Si surface in the mask openings. Most often however, a thin layer of native oxide forms again before the substrate is loaded into the UHV MBE chamber. Since III-V growth is inhibited on the oxide layer, its formation has been identified as the reason for the previously reported low reproducibility and yield for III-V NWs grown on Si substrates [Heiss et al., 2014]. It is now known that an *in-situ* high-temperature annealing carried out in the MBE chamber can thoroughly clean and free the patterned holes of native oxide, allowing high-yield GaAs NW growth on Si [Heiss et al., 2014; Zhang et al., 2014; Munshi et al., 2014; Vettori et al., 2019].

### Growth parameters influencing the NW vertical yield

The growth temperature and V/III flux ratio are growth parameters that have been shown to primarily control the NW dimensions and morphology, when they are kept within a reasonable range [Colombo et al., 2008; Paek et al., 2008; Plissard et al., 2010]. In the following paragraphs, the discussion will hence be focused on the impact of the Ga droplet formation inside the holes prior to growth (Ga pre-deposition step), and the influence of a GaP stem.

Table 2.1: State-of-the-art self-catalyzed GaAs NWs grown by MBE on patterned Si(111) substrates and their optimized pre-growth and growth parameters, as well as NW array characteristics. A question mark (?) indicates missing information, a star (\*) indicates values not given in the article but estimated from my own measurements on the pattern with the best NW vertical yield. A hyphen (-) expresses the absence of a growth step. Note that in [Zhang et al., 2014] the material grown is GaAsP.

Reference	Pre-growth parameters					Growth parameters					NW array characteristics				
	Mask	Mask thick. (nm)	Patterning method	Wet etch method	Mask hole diam. (nm)	Pitch (µm)	Annealing temp. (time) (°C (min))	Growth temp. (°C)	V/III ratio	Ga flux (ML/s)	Ga pre-dep. (ML)	GaP stem	NW length µm	NW base diam. nm	Max. yield (%)
[Plissard et al., 2011]	SiOx thermal	10	EBL	HF 1%, 1min	60	0.5, 1	-	630	1.8	1	45	No	1*	55*	95
[Heiss et al., 2014]	SiOx thermal	18	EBL	BHF 7:1	100	0.4	770 (30)	615	?	0.35	-	No	?	?	65
[Zhang et al., 2014]	SiOx thermal	30	NIL	HF 5%, 2min	50	1	900 (20)	630	3-20	?	(60 s)	GaAsP NWs	2*	100*	>90*
[Munshi et al., 2014]	SiOx thermal	40 (pre-etch)	NIL	HF 1%, 20s	100	1	690 (5)	630	?	0.6	30	No	2*	130*	80
[Russo-Averchi et al., 2015]	SiOx thermal + a-Si PECVD	20 + 15 (pre-etch)	EBL	BHF 7:1, 12s	90 (pre-etch)	0.4, 1.6	770 (30)	630	?	0.35	?	No	2.5*	90*	80
	SiOx PECVD	30 (pre-etch)	EBL	BHF 10:1, 20s	60 (pre-etch)	0.36	600 (10), H2 plasma	600	2	0.12	-	Yes	?	46	80
[Küpers et al., 2017]	SiOx thermal	20 (pre-etch)	NIL-IPT	HF 1%, 1min + boiling DI water	50	1.5	680 (10)	630	2.4	0.5	45	No	2.1*	160*	80
[Küpers et al., 2018]	SiOx thermal	15-20 (pre-etch)	EBL	HF 1%, 1min + boiling DI water	40-50 (pre-etch)	1	680 (10)	630	2.4	0.5	45	No	2.3*	140*	75
[Schroth et al., 2019]	SiOx thermal	20 (pre-etch)	EBL	HF 0.5%, 1min + boiling DI water	40 (pre-etch)	0.1-1	800 (30)	630	3	0.12	55	No	0.675	40	80*
[Vukajlovic-Plestina et al., 2019]	SiOx thermal	10	EBL	BHF, 2s	45 (pre-etch)	0.4	-	635	?	0.35	210	No	?	150*	90
[Vettori et al., 2019]	SiOx PECVD	19	EBL	HF 1%, 25s	50	0.5	615 (5)	600	2.3	0.5	108	No	1.2*	80*	85
[Bahrami et al., 2020]	SiOx thermal	16 (pre-etch)	FIB	HF 0.5%, 1min + boiling DI water	200-240	5	700 (10)	560-630	1-2	0.5-0.15	45	No	1-4	15-150	80
[Scaccabarozzi et al., 2020]	SiOx PECVD	14	EBL	Diluted HF	50	0.3	700 (-)	600	1.4	0.5	6	No	1.5*	70*	50
[Wilson et al., 2021]	SiOx PECVD	17	EBL	BHF 10:1, 20s	87 (pre-etch)	0.36-1	550 (10), H2 plasma	600	2	0.12	30	Yes	3-5	120-180	~100
[Mukherjee et al., 2021]	SiOx thermal	40 (pre-etch)	EBL	BOE	100 (pre-etch)	1	-	625	?	0.7	-	GaAsSb stem	2.1	150	95
This work	SiOx PECVD	10-20	EBL	HF 1%, 30s	20-100 (pre-etch)	0.2-1	750 (20)	600	1.2	0.71	128	Yes	0.1-2	60-170	~100



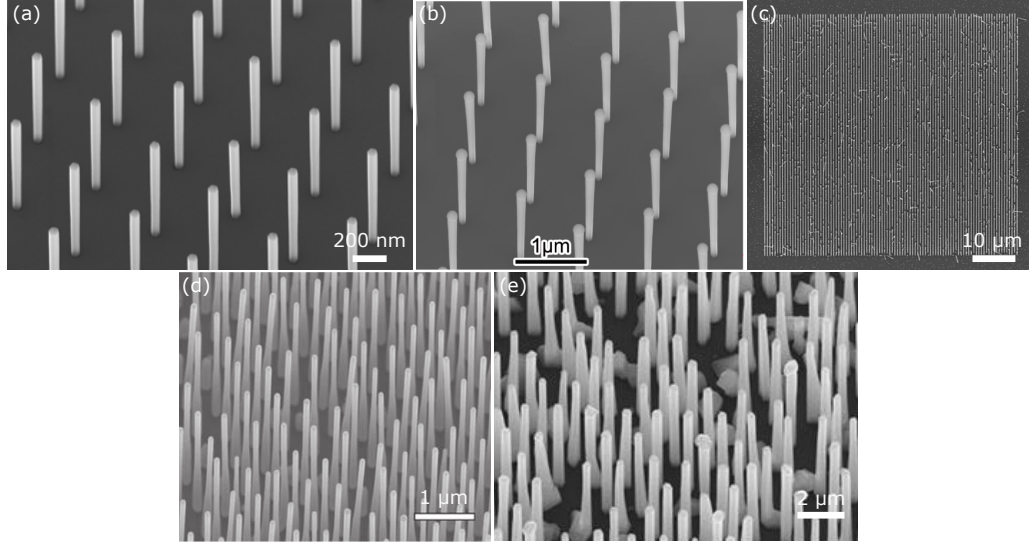


Figure 2.7: Regular GaAs NW arrays grown on Si(111) with vertical yields  $> 90\%$ , from (a) [Plissard et al., 2011], (b) [Zhang et al., 2014] (GaAsP NWs), (c) [Vukajlovic-Plestina et al., 2019], (d) [Wilson et al., 2021] (GaP stem) and (e) [Mukherjee et al., 2021] (GaAsSb stem). The corresponding pre-growth and growth parameters can be found in Table 2.1, along with the as-grown NW array characteristics.

In VLS NW growth, Ga droplets can form spontaneously without intentional pre-deposition, as in the studies in Table 2.1 for which a **Ga pre-deposition** step has not been indicated (“-” in the column “Ga pre-dep.”). However, many groups have reported that allowing Ga droplets to form in the mask openings prior to NW growth significantly improves the NW vertical yield, in particular when Ga completely fills the holes. In fact, all the studies that investigated the influence of the Ga pre-deposition on the NW yield observed an optimal pre-deposition duration that corresponded to a complete filling of the holes [Plissard et al., 2011; Munshi et al., 2014; Vukajlovic-Plestina et al., 2019]. Hole filling by the Ga droplet has been modeled [Zhang et al., 2014; Wilson et al., 2021], and a  $90^\circ$  contact angle between the droplet and the Si surface has been reported to favor NW growth perpendicular to the substrate [Matteini et al., 2016]. Hence, it is essential to calibrate the Ga droplet volume with respect to the hole dimensions, and this can be done by varying the duration for which Ga is evaporated at a given rate, without any group V flux (Ga pre-deposition time). Care needs to also be taken with the growth temperature, which can influence the Ga droplet dimensions above a certain threshold (around  $640^\circ\text{C}$  according to [Munshi et al., 2014]), due to substantial desorption of Ga adatoms on the substrate surface at high temperatures.

Finally, GaP NW arrays have been observed to consistently present higher vertical yields than GaAs arrays in the same growth conditions [Boulanger et al., 2016; Dastjerdi et al., 2016; Scaccabarozzi et al., 2020; de Lépinau, 2020]. The reasons behind this yield enhancement from GaAs to GaP have not yet been elucidated, but could be related to the fact that unlike GaAs, GaP is nearly lattice-matched to Si (see Figure 1.4b). However, GaAsSb NWs were also found to exhibit better vertical yields [Mukherjee et al., 2021], and it has a greater lattice-mismatch than GaAs on Si... Following these empirical observations, it has become common to initiate GaAs NW growth with a small stem of GaP or GaAsSb to enhance the NW vertical yield. SEM images of the NW arrays from Table 2.1 with a vertical yield above  $90\%$  are shown in Figure 2.7. A stem was used in two of the five growths shown (Figure 2.7d and e), while in one of them GaAsP NWs were grown (Figure 2.7b).

Taking into consideration the pre-growth and growth parameters previously discussed, we choose to grow GaAs NW arrays on p-Si(111) substrates covered by a  $\text{SiO}_2$  layer deposited by PECVD, and patterned with EBL. The mask hole diameters and pitch have been widely varied to optimize the Ga pre-deposition step which allows to achieve high NW vertical yields. For the same reason, the GaAs NW growth is initiated by a GaP stem. In the following section, the detailed substrate preparation method used for our NW samples will be presented, highlighting how we

managed to overcome issues of poor mask selectivity and sample inhomogeneity in order to achieve near-perfect NW vertical yields. Then, the growth parameters used for our GaAs NW arrays will be presented, accompanied by a discussion on the control of the NW diameter and morphology via mask hole diameter and V/III ratio optimization.

The figure of merit typically used to assess and compare the growths of regular NW arrays is the vertical yield. The latter can be impacted by many parameters. Among the pre-growth parameters influencing the NW vertical yield, we can find the mask material quality and thickness, the diameter of the mask holes, and the cleanliness of the Si surface in the mask openings. Among the growth parameters directly influencing the NW vertical yield, there is the Ga pre-deposition time, and the presence of a GaP or GaAsSb stem. All of these parameters have been studied in the literature in the aim of optimizing the NW vertical yield. However, despite significant research efforts, not many groups have been able to achieve NW vertical yields above 90%.

## 2.2 Towards 100% vertical GaAs NWs grown on Si with tuneable diameter

In order to fabricate highly efficient GaAs-based NW solar cells, the NW vertical yield first needs to be optimized. In this section, I will present the optimizations carried out on different steps of the substrate preparation process, which allowed us to achieve near-perfect vertical yields on two different solid-source MBE systems (presented in [subsection 2.1.3](#)).

### 2.2.1 Optimizing the patterned substrate preparation for near-perfect yields

Two-inch p-doped (B) Cz Si(111) wafers supplied by Siltronic were used for the NWs grown in this work, with a thickness of 250–300  $\mu\text{m}$  and a nominal resistivity of 0.01–0.02  $\Omega\text{cm}$ . Si surfaces are naturally prone to oxidation and contamination by organic and inorganic impurities [[Morita et al., 1990](#)], so a reliable cleaning procedure is critical to ensure the quality of the layers grown on top.

#### A robust silicon substrate cleaning procedure

The silicon wafer cleaning process previously developed in our group first starts with a 4 min oxygen plasma in a capacitively coupled plasma-reactive ion etching (CCP-RIE) chamber with a bias voltage of 190 V. On one hand, the high energy ions from the plasma mechanically break the molecular bonds of high molecular weight carbon impurities, and on the other hand, the oxygen species created in the plasma react with low molecular weight carbon contaminants to produce even smaller and more volatile species which easily evaporate from the surface [[Robinson et al., 2004](#); [Shun'ko and Belkin, 2007](#)]. The top few nanometers of the silicon wafer are also oxidized, trapping the remaining surface contaminants. The wafer is then immersed in a 5% HF solution which removes the oxidized silicon layer and the potential contaminants trapped inside, leaving the dangling bonds from the silicon surface saturated with hydrogen [[Angermann et al., 2000](#)]. In total, 3 cycles of oxidation/etching are performed to ensure an ultra-clean silicon wafer surface [[Madiomanana et al., 2015](#)] before dielectric mask deposition. This specific wafer cleaning procedure improved the wafer-to-wafer reproducibility and NW vertical yield significantly (systematically above 90%), as summarized in Figure 3.23 of the PhD manuscript of [[de Lépinau, 2020](#)].

#### Depositing high-quality dielectric layers for good mask selectivity

PECVD is used to deposit a thin layer of  $\text{SiO}_2$  (50–70 nm) on the clean silicon substrate, which will later on be patterned. At the beginning of my PhD, I struggled to obtain good NW vertical yields despite the previously presented robust Si wafer cleaning procedure, due to very poor mask selectivity (presence of Ga droplets not only in the mask openings but also on its surface). After investigation, we ascribed the poor mask selectivity to some carbon contamination in the PECVD

chamber, which could be avoided by pre-conditioning it before the dielectric layer deposition.

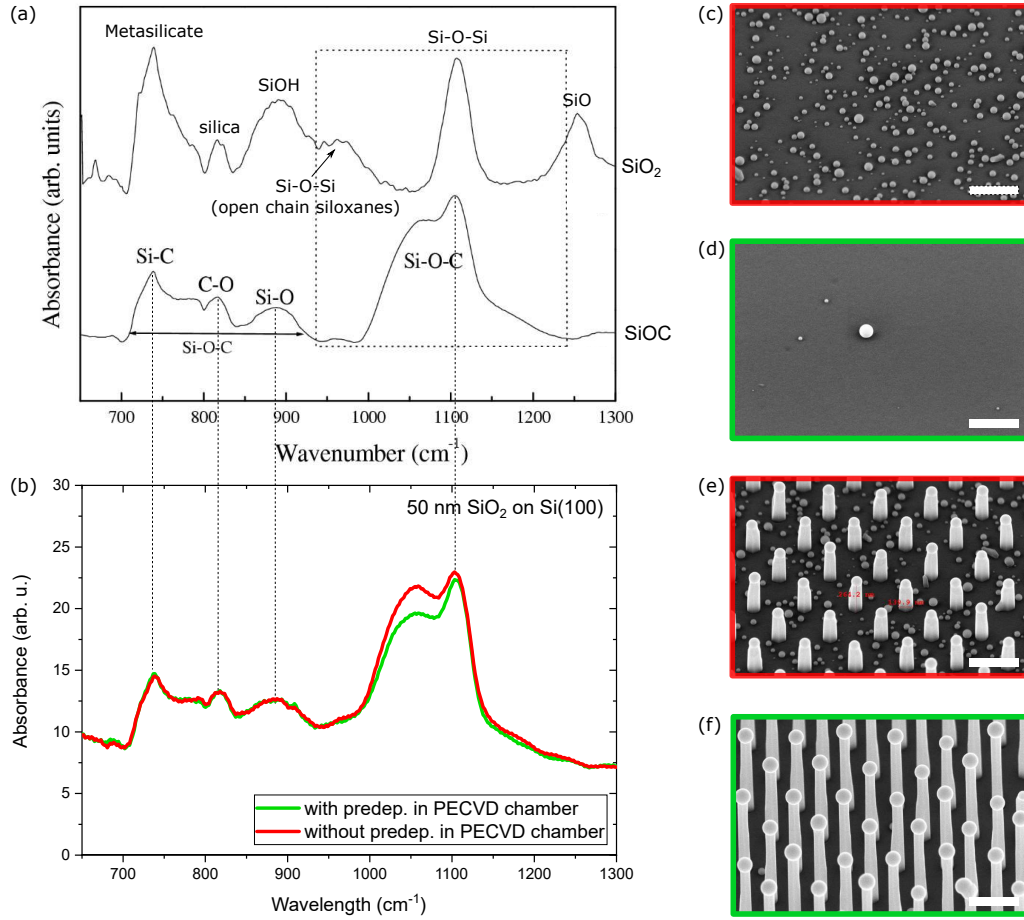


Figure 2.8: (a) FTIR spectra of  $\text{SiO}_2$  and  $\text{SiOC}$  films with identified bonds, adapted from [Oh and Choi, 2010]. (b) FTIR spectra of two 50 nm  $\text{SiO}_2$  layers deposited on  $\text{Si}(100)$  in a PECVD chamber, one with a silica pre-deposition of 6 min in the chamber (green), and one without pre-deposition (red). SEM images of the  $\text{SiO}_2$  surface outside mask openings after NW growth, for (c) a sample on which  $\text{SiO}_2$  was deposited without pre-deposition in the PECVD chamber, and (d) with pre-deposition. (e) and (d) corresponding NW arrays grown on patterned areas of the substrate (pitch 500 nm, nominal hole diameter 90 nm). Note that the growth duration differs for the two samples, resulting in NWs of different dimensions. Scale bar = 500 nm.

Figure 2.8a shows the Fourier-transform infrared spectroscopy (FTIR) spectra of  $\text{SiO}_2$  and  $\text{SiOC}$  films obtained by [Oh and Choi, 2010]. Figure 2.8b compares the FTIR spectra of a  $\text{SiO}_2$  layer deposited in our PECVD chamber after a 6 min silica pre-deposition prior to loading the Si substrate (green), to the one of a  $\text{SiO}_2$  layer directly deposited on a Si substrate (red). Both spectra show characteristic peaks of the  $\text{Si-O-C}$  bonds, revealing some carbon contamination in the PECVD chamber. However, the peaks are less pronounced in the FTIR spectrum of the  $\text{SiO}_2$  layer deposited after a 6 min silica pre-deposition (green), suggesting that the extent of carbon contamination in the PECVD chamber depends on its pre-conditioning. The SEM images in Figure 2.8 show the amount of parasitic Ga droplets outside mask openings after NW growth, on (c) a  $\text{SiO}_2$  mask directly deposited on the Si substrate (no pre-conditioning of the PECVD chamber) and (d) a  $\text{SiO}_2$  mask deposited after a pre-deposition in the PECVD chamber. A much higher selectivity can be observed for the  $\text{SiO}_2$  mask deposited after a pre-deposition in the PECVD chamber, as revealed by the significantly lower amount of parasitic Ga droplets present outside mask openings after NW growth. This is most likely due to less impurity atoms acting as nucleation sites on the  $\text{SiO}_2$  mask deposited after a pre-deposition in the PECVD chamber. Figures 2.8e and f show the SEM images of the corresponding NW arrays grown in the  $\text{SiO}_2$  mask openings. Again, many parasitic Ga droplets can be seen on the  $\text{SiO}_2$  mask deposited without any pre-deposition in the

PECVD chamber, and we can expect the presence of these Ga droplets, which act as material collector in the array, to disturb the thermodynamics and kinetics of VLS NW growth, as seen in Figure 2.8e. The detailed NW growth recipes for these samples can be found in subsection 2.2.2. Note that the growth duration differed for the two samples, resulting in NWs of different dimensions.

After having seen how the dielectric layer quality can impact the mask selectivity and hence NW growth, in the next sections I will present our substrate patterning process and demonstrate how important it is to thoroughly clean the mask surface before growth in order to obtain homogeneous samples with near-perfect NW vertical yields.

### Mask patterning process

After silica deposition, the substrates are coated with an electron-sensitive resist (495PMMA, 2%) and patterned in an electron-beam lithography (EBL) machine operating at 100 kV. Typical substrate designs include hexagonal hole patterns found in large squares and smaller matrices. The large squares (red in Figure 2.9), familiarly referred to as “spot patterns”, have sides ranging from 1-5 mm and are patterned by injecting a single electron dose at the center of each hole. The diameter of the holes depends on the injected electron dose (expressed in  $\mu\text{C cm}^{-2}$ ), while the interhole distance (pitch) is a direct input. The smaller matrices found in the pattern design are on the other hand composed of arrays with different pitches and hole diameters (see magnified schematic of the matrix in Figure 2.9), patterned pixel-by-pixel in the EBL machine with a beam step size of 1 nm to ensure that small circles can be defined. Despite longer patterning times, the hole dimension and edge definition are much better controlled using pixel-by-pixel patterning, which has previously been linked to higher NW vertical yields in the matrices [de Lépinau, 2020]. In the next section, I will demonstrate that by removing the native oxide in the mask openings and thoroughly cleaning its surface prior to MBE loading, near-perfect vertical yields can also be obtained in the large squares (spot patterns), enabling faster patterning of large areas needed for the fabrication of devices.

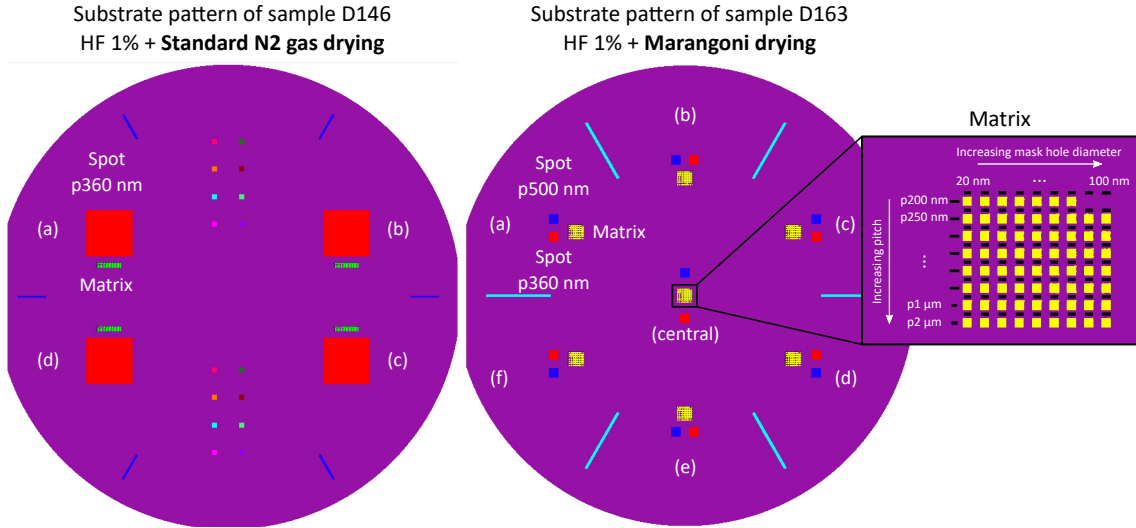


Figure 2.9: Schematics showing the substrate patterns of samples D146 (PNW314, standard  $N_2$  drying) and D163 (PNW318, Marangoni drying). Spot patterns undergo a single EBL exposure on a large-area of the substrate, while matrices are patterned pixel-by-pixel and contain several smaller patterns with varying pitches and nominal hole diameters, as indicated in the magnified schematic. The pitch is differentiated from the hole diameter by a letter ‘p’ in front of the numbers.

After EBL, the hexagonal hole pattern in the PMMA is transferred to the  $\text{SiO}_2$  mask by CCP-RIE at 7 mTorr, with a mixture of  $\text{SF}_6$  and  $\text{CHF}_3$  gases (flow rate ratio of 8:20) and a bias voltage of 190 V. The etching time is a crucial parameter for successful NW growth as it will determine the remaining mask thickness and patterned hole dimensions (see discussion in subsection 2.1.4). Care is also given here to not completely etch open the mask holes in order to avoid plasma-induced damage to the Si [Arora, 1987; Oehrlein, 1989]. As a clean silica mask surface is required to ensure



adsorbed Ga atom diffusion or re-emission during growth, a 4 min oxygen plasma is then carried out at a bias voltage of 300 V to remove any residual resist particles and carbon contamination left after the lithographic processing. The choice of the bias voltages used in both the  $\text{SF}_6\text{-CHF}_3$  and  $\text{O}_2$  RIE processes is explained in [Appendix A](#). Finally, the substrate is cleaned with an HF 1% solution for 30 s (then rinsed in deionized (DI) water and  $\text{N}_2$  dried), to remove the oxide layer before being loaded into the MBE chamber. However, as explained in [subsection 2.1.4](#), a thin layer of native oxide may form again in the mask openings before the substrate is loaded into the UHV MBE chamber [[van der Heide et al., 1989](#)], and an *in-situ* high-temperature annealing is required to thoroughly clean and free the patterned holes of native oxide. In all the NW growths presented in this PhD manuscript, a 20 min thermal annealing was carried out at  $750^\circ\text{C}$  prior to growth, enabling the high NW vertical yield seen in [Figure 2.10b](#).

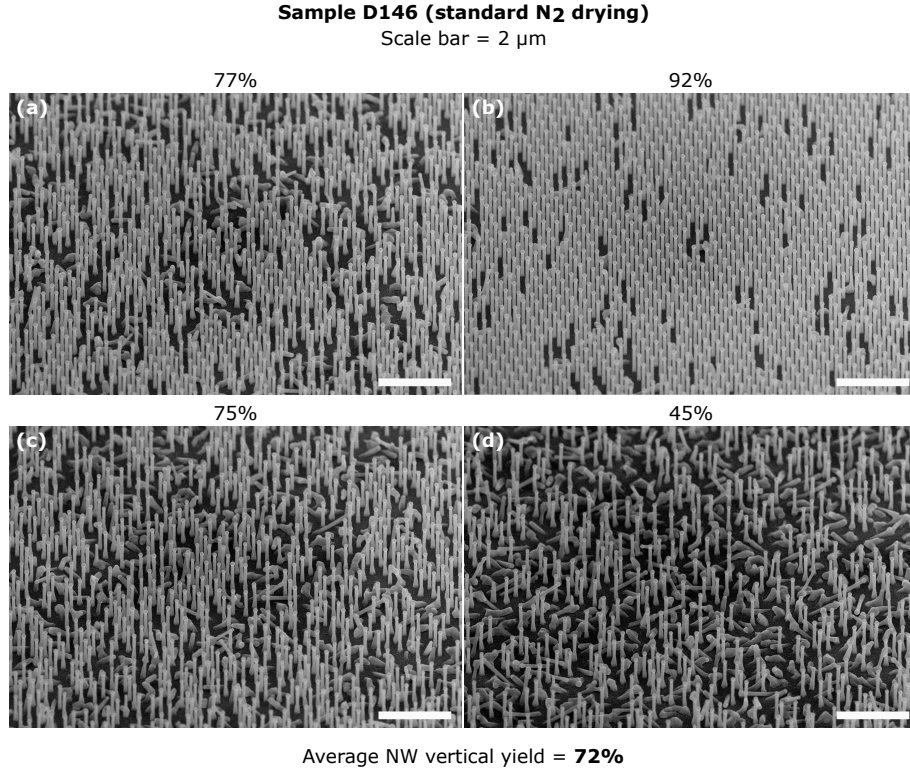


Figure 2.10: SEM images of the 4 spot patterns from sample D146 (standard  $\text{N}_2$  drying) with pitch 360 nm, corresponding to the red squares in [Figure 2.9](#) (left). Although having been exposed to the exact same preparation procedure, the 4 spot patterns demonstrate significantly different NW vertical yields, as indicated by the given percentages.

However, the above-mentioned efforts still did not allow high vertical yields to be obtained homogeneously across the sample surface, as observed from the SEM images of the 4 spot patterns from sample D146, whose substrate design is illustrated in [Figure 2.9](#) (left). In fact, although the 4 spot patterns were exposed to the exact same EBL process and subsequent substrate preparation and growth steps, very different NW growths were obtained in them, with vertical yields varying from 45-92% depending on the spot pattern. As we were bewildered by the significant sample inhomogeneity revealed by the repeated substrate pattern designs (which were chosen to facilitate subsequent device processing tests), we decided to investigate the origin of the substrate surface non-uniformity. Our first hypothesis was prompted by the traces observed by eye on some of the substrate surfaces after NW growth ([Figure 2.11](#)). These led us to suspect a correlation between the sample inhomogeneity and impurities which could have been introduced on the substrate surface during DI water rinsing after the final HF dip, and left there by the standard  $\text{N}_2$  flow drying.

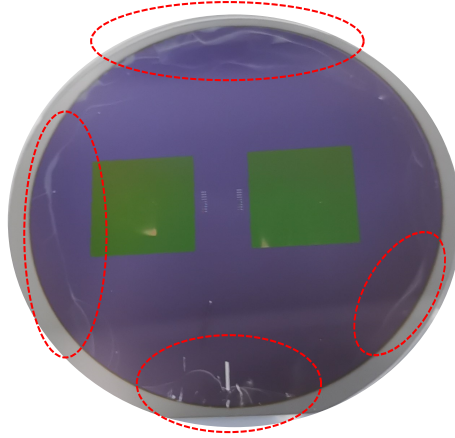


Figure 2.11: Photograph of a patterned Si substrate after NW growth, on which inhomogeneous traces can be seen by eye.

### New drying method for pristine and homogeneous substrate surface

To confirm the hypothesis stated above, which correlates the sample inhomogeneity to impurities from the rinsing water after the final HF dip, drying experiments taking advantage of the Marangoni effect were carried out. The Marangoni effect [Marangoni, 1865] describes the mass transfer along an interface between two phases due to a surface tension gradient, and it has been exploited to develop an extremely clean Si wafer drying process called Marangoni drying [Leenaars et al., 1990]. The schematics in Figure 2.12 show the experimental set-up used in Marangoni drying: a wafer is withdrawn from a rinse bath (water), while at the same time  $N_2$  gas with a trace of organic vapor is passed along its surface. The organic vapor comes from an organic solvent with a vapor pressure lower than the one of water, and stored in an aspirator bottle through which  $N_2$  gas is bubbled. The wafer surface is kept at a temperature greater than that of the rinse bath, so that the organic solvent vapor does not condensate on the wafer surface. Instead, it condensates on the surface of the water from the rinse bath, and remains there thanks to its lower surface tension, resulting in a surface tension gradient in the film wetting the substrate. This surface tension gradient causes a mass transfer along the interface between the solvent and the water (Marangoni flow), which forces the impurities to remain in the water (see magnified schematic in Figure 2.12).

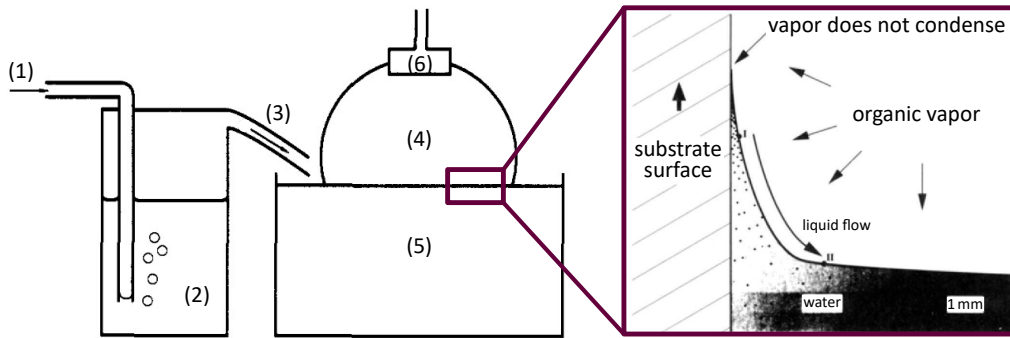


Figure 2.12: Schematic representation of the Marangoni drying experimental set-up and process, with (1)  $N_2$  flow, (2) bottle containing organic liquid, (3)  $N_2$  flow partly saturated with organic vapor, (4) silicon wafer, (5) water and (6) lever with clamp. Adapted from [Leenaars et al., 1990].

We adapted the set-up shown in Figure 2.12 to a dip-coating equipment in which the substrate withdrawal speed and atmosphere composition and temperature could be precisely controlled. Similarly to the experiments performed by [Leenaars et al., 1990], we used a 1 M NaCl bath to simulate a water rinse bath with impurities, and carried out tests on Si(100) substrates (covered with native oxide) using 3 different solvents and 3 different withdrawal speeds. The solvents investigated included isopropyl alcohol (IPA), methyl isobutyl ketone (MIBK), and 2-methoxyethanol,

with vapor pressures of 44 mbar, 21 mbar, and 8 mbar, respectively. The dip-coater chamber atmosphere was heated to an optimal temperature of 100°C to facilitate the drying process of the silicon oxide surface, which unlike silicon is hydrophilic. The substrate surfaces obtained after different Marangoni drying experiments were analyzed using an optical microscope and are shown in Figure 2.13. The dark traces correspond to the NaCl salts remaining on the substrate surface after Marangoni drying. We can see that the cleanest substrate surface is obtained after Marangoni drying with a  $N_2$ /2-methoxyethanol flow at a substrate withdrawal speed of 2 mm/s (draining regime). The higher ability of 2-methoxyethanol for forcing NaCl salts to remain in the water could perhaps be correlated to its vapor pressure of 8 mbar, which is far lower than the one of water (32 mbar) compared to the other two solvents.

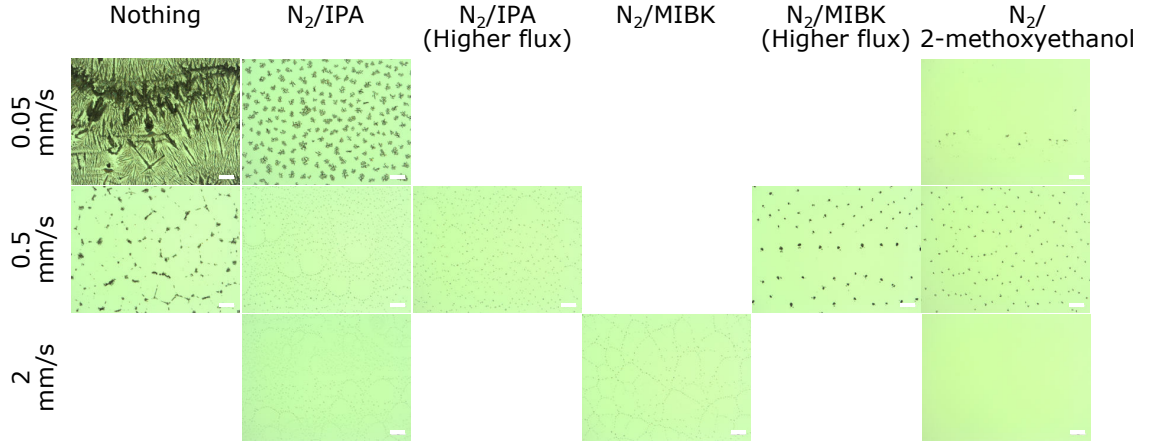


Figure 2.13: Optical microscopy images of Si(100) wafer surfaces obtained after Marangoni drying experiments in a dip-coating chamber at 100°C, using different solvents and substrate withdrawal speeds. Scale bar = 200  $\mu$ m.

The optimized Marangoni drying process described above ( $N_2$ /2-methoxyethanol, 2 mm/s) was used to prepare the patterned substrate of sample D163. As observed from the SEM images in Figure 2.14, near-perfect NW vertical yields were obtained homogeneously across 7 spot patterns, located on different areas of sample D163 (see red squares in Figure 2.9 (right)). The comparison with sample D146 (Figure 2.10), in which the patterned substrate was dried using a standard  $N_2$  flow is here striking, and emphasizes the importance of a pristine substrate surface for high quality NW growth. Note that the NWs in sample D163 are shorter than the ones in sample D146 due to a shorter growth duration (7 min vs. 12 min).

A specific Si wafer cleaning procedure consisting of 3 consecutive cycles of oxidation/etching, was previously observed to improve wafer-to-wafer reproducibility and NW vertical yield. The dielectric mask selectivity, which is also of critical importance to ensure good NW growth, has been here related to the quality of the dielectric mask layer. We observed that  $SiO_2$  layers deposited after a pre-deposition in the PECVD chamber resulted in significantly higher mask selectivity due to less carbon contamination. This highlights the importance of the pre-conditioning of the PECVD chamber. Nevertheless, despite these patterned substrate preparation optimizations, high NW vertical yields could not be obtained homogeneously across the sample surface. We suspected this to be related to impurities introduced on the substrate surface during water rinsing after the final HF dip, and left there by the standard  $N_2$  drying. As a consequence, we investigated a new drying method known as Marangoni drying. The cleanest substrate surface was obtained after Marangoni drying with a  $N_2$ /2-methoxyethanol flow at a substrate withdrawal speed of 2 mm/s. The latter allowed near-perfect NW vertical yields (average 99.5%) to be obtained homogeneously on 7 large-area patterns spread out across the sample surface.

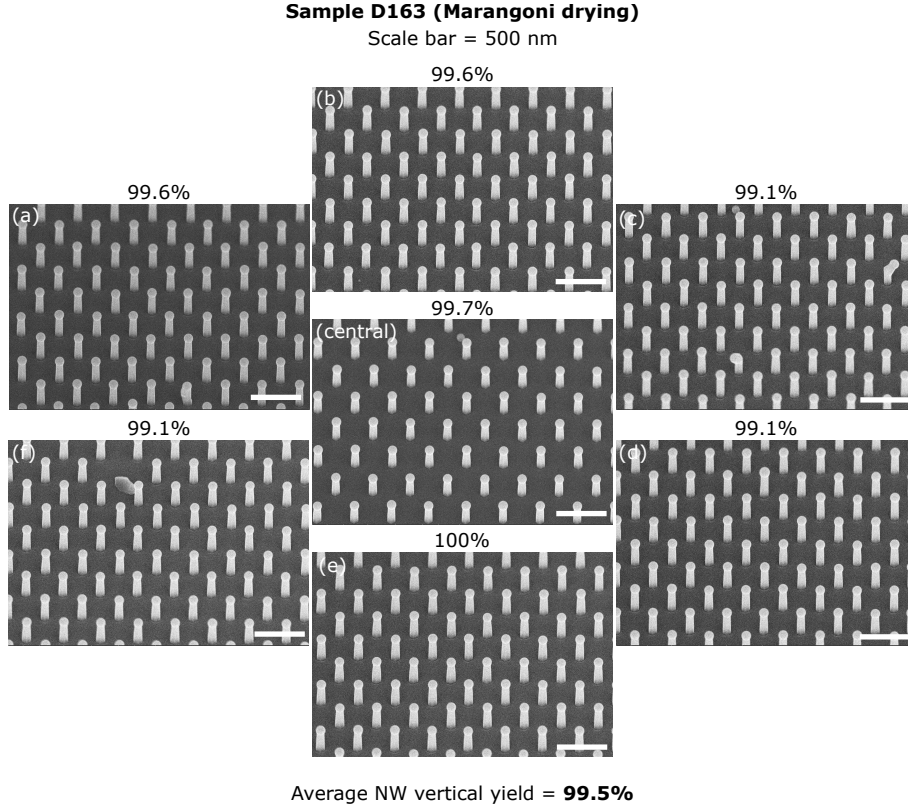


Figure 2.14: SEM images of the 7 spot patterns from sample D163 (Marangoni drying) with pitch 360 nm, corresponding to the red squares in Figure 2.9 (right). Near-perfect NW vertical yields are observed homogeneously across the 7 spot patterns, as given by the percentages which were calculated on larger areas (roughly  $100 \mu\text{m}^2$ ).

### 2.2.2 NW diameter variation with mask hole size

All the optimized patterned substrate preparation steps described in the previous section also allowed us to achieve near-perfect vertical yields across a wide-range of mask hole diameters in matrix patterns (see pattern design in Figure 2.9). In these matrices, the NW diameter was observed to depend on the mask hole diameter. This correlation could enable NWs of different diameters to be obtained in a single array, and hence maximize NW array absorption [Wu et al., 2017b,a].

#### Standard NW growth recipe

Once the patterned substrate has been prepared following the above-mentioned procedure, it is loaded into the MBE chamber and first outgassed in the preparation chamber at  $600^\circ\text{C}$  for 1h in order to desorb the water molecules. Then it is transferred to a rotating holder in the MBE growth chamber (10 rpm) for a 20 min *in-situ* high-temperature annealing at roughly  $750^\circ\text{C}$ , as monitored by an IRCON  $0.9 \mu\text{m}$  pyrometer. After annealing, the substrate temperature is brought down to the desired growth temperature of  $600^\circ\text{C}$ .

The self-catalyzed VLS growth of GaAs NWs is initiated by a 3 min Ga pre-deposition step in which a Ga flux corresponding to a two-dimensional GaAs equivalent growth rate of  $0.71 \text{ ML/s}$  ( $2 \text{ \AA/s}$ ), is used to localize the Ga droplets in the holes of the patterned substrate, as it was summarized in Table 2.1. A Be flux corresponding to a hole concentration in planar GaAs of  $6 \times 10^{18} \text{ cm}^{-3}$  is also introduced for p-type doping. After Ga pre-deposition, the phosphorous valve is opened to begin the growth of a Be-doped GaP segment at a  $\text{P}_2/\text{Ga}$  effective atomic flux ratio of 1.2. After 20 s of Be-doped GaP growth, the P valve is closed linearly while opening the one of As over the course of 30 s, resulting in a linearly graded GaP/GaAs transition which contributes to flatten the valence band offset between GaP and GaAs for solar cell device performance purposes [Boulanger



et al., 2016; Tong et al., 2022b]. The Be-doping is also introduced to anticipate the fabrication of functional p-n junctions. GaAs NWs are then grown under an  $\text{As}_4/\text{Ga}$  flux ratio of 1.2, and the same Be flux during 7 and 9 min, for samples 77407 and D163, respectively. Note that sample 77407 was grown in the MBE Riber32 set-up while D163 was grown in the MBE Compact21. Relatively short NW growth times were used in order to facilitate the NW dimensions measurements (no shadowing from neighboring NWs).

The recorded NW dimensions from matrix patterns of samples 77407 and D163, with a 250 nm pitch and nominal hole diameters varying from 20-100 nm, are summarized in Figure 2.15 and will be discussed below.

### NW morphology evolution with mask hole size

The table in Figure 2.15a indicates the pre-growth and growth parameters that differ for samples 77407 and D163. The NW diameters and lengths were measured on at least 10 NWs in a way that is illustrated in Figure 2.15b, except for the patterns with vertical yields below 50%, for which less NWs were measured. The plots in Figures 2.15c and d show the evolution of the NW diameter at the top and at the base, as well as NW length, with nominal mask hole diameter for samples 77407 and D163, respectively. SEM images of representative NWs from each array are shown above the plots. The corresponding vertical yields determined from areas greater than  $5 \mu\text{m}^2$  are also indicated. The full SEM images from which the representative NWs were extracted can be found in Figure 2.16. In sample D163, NWs from the 20 nm hole array were found to be missing due to unopened mask holes.

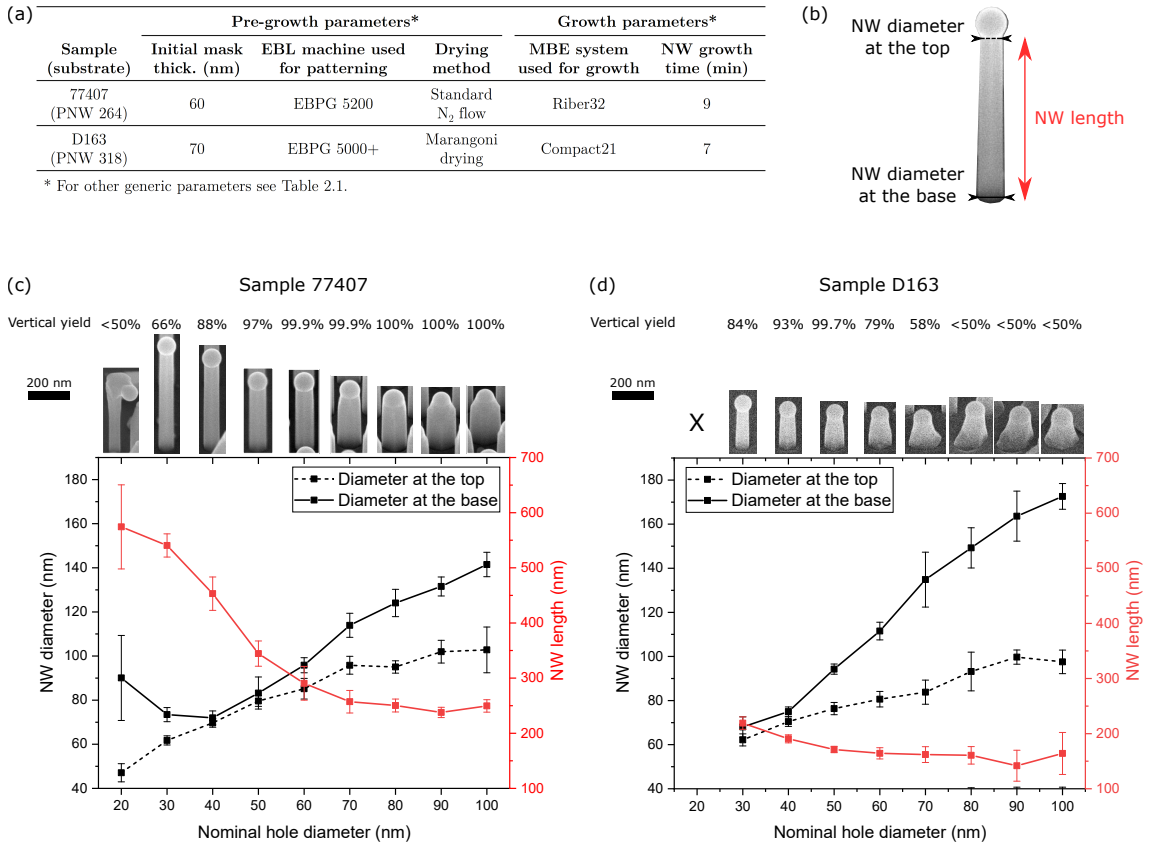


Figure 2.15: (a) Table summarizing the pre-growth and growth parameters which differ for samples 77407 and D163. (b) Illustration of each NW dimension's measuring method. (c) and (d) Evolution of the NW diameters (at the base and at the top) and NW length with nominal mask hole diameter in matrix patterns with a 250 nm pitch, for samples 77407 and D163, respectively. The SEM image of a representative NW from each array is shown at the top, along with the NW vertical yields calculated on areas  $> 5 \mu\text{m}^2$ . The complete SEM images from which the single NWs were extracted can be found in Figure 2.16.

As we can see from the plots in [Figure 2.15](#), NWs from sample 77407 (D163) have base diameters between 70-140 nm (70-170 nm), top diameters between 50-100 nm (60-100 nm), and lengths between 250-600 nm (140-220 nm). The significantly shorter NW lengths observed for sample D163 are a result of a shorter NW growth duration (7 min vs. 9 min, as indicated in [Figure 2.15a](#)), which also impacts the final NW top diameters. As previously mentioned in [subsection 2.1.1](#), some radial VS growth always occurs concurrently during VLS growth (see schematics in [Figure 2.1](#)). However, this mainly occurs after a NW length exceeding the Ga diffusion length on the NW sidewalls has been reached. For growth conditions similar to ours, the diffusion length of Ga adatom on the NW sidewalls has been found to be above 500 nm [[Dubrovskii et al., 2015](#); [Küpers et al., 2018](#)]. Considering the relatively short NW lengths obtained here ( $< 650$  nm), radial VS growth can thus be neglected, and the following discussion will be mainly focused on the relationship between the NW diameter and the catalyst droplet dynamics. The different growth conditions which may arise in the two MBE reactors used could also have an effect on the final NW morphologies, but we assume that the latter is negligible. Keeping these elements in mind, we will discuss the evolution of the NW diameters with mask hole size in the next paragraphs.

The slightly bigger base diameters obtained for the NWs from sample D163 could be related to bigger mask holes compared to sample 77407, resulting from an originally thicker mask layer (70 nm vs. 60 nm, as indicated in [Figure 2.15a](#)). In fact, despite the same electron beam dose used during EBL, slightly different proximity effect corrections were applied to take into account the samples' different mask layer thicknesses. This could result in marginally different real electron beam doses in the mask holes and hence different hole diameters. In addition, during pattern transfer from the PMMA to the mask using CCP-RIE, in order to obtain the same final mask layer thickness, the initially thicker mask of sample D163 had to be over-etched compared to the one of sample 77407. This should lead to a slightly different hole profile with somewhat bigger mask hole diameters for sample D163.

A clear correlation between mask hole and NW diameters can be seen from both [Figures 2.15c](#) and [d](#), in which the NW diameters increase with increasing mask hole size. This can be related to the fact that although the same Ga pre-deposition time and flux were used for all arrays of both samples, larger initial mask hole diameters lead to smaller initial Ga droplet contact angles, and hence larger NW base diameter. This statement is only true when the mask holes are free from any oxide layer, and the Ga droplet does not spill over the holes. In our growth conditions, mask hole diameters of initially 20–100 nm can lead to NW base diameters between 70–140 nm, for NW lengths below 650 nm. Looking at the state-of-the-art self-catalyzed GaAs NWs from the literature ([Table 2.1](#)), we can see that wide NW base diameters ( $> 100$  nm) are typically only obtained for NW lengths  $> 1\text{--}2\text{ }\mu\text{m}$ , that is after a considerable radial VS growth. The fact that we managed to obtain relatively wide NW base diameters with negligible radial VS contribution suggests that a tight control of the NW diameter can be achieved, using lithography techniques that allow the precise patterning of mask holes, and specific substrate cleaning and drying procedures like the ones we implemented. To the best of our knowledge, similar correlations between mask hole size and NW diameter have never been observed before. In the study by [[Wilson et al., 2021](#)], mask hole diameters between 57–101 nm resulted in NWs with base diameters varying between 120–160 nm, but with no specific trend (see [Figure 3a](#) from their article). In their study, for a pitch of 360 nm, the NW base diameter obtained from an 87 nm mask hole was found to be bigger than both the ones obtained from 71 nm and 101 nm mask holes. The absence of an observed correlation between the mask hole size and NW base diameter in the literature could be due to still unoptimized patterned substrate preparation in the community. In fact, we believe that native oxide previously remaining in our mask openings and formerly dirty mask surfaces have prevented us to notice clear trends in the past. However, the absence of an observed correlation between the mask hole size and NW base diameter in the literature could also be due the fact that typically longer NWs are grown. As a matter of fact, radial VS growth becomes significant for the growth of NWs longer than the Ga diffusion length on the NW sidewalls, which enlarges the NW base diameter and makes it difficult to directly correlate mask hole size and NW base diameter.

As the growth continues under constant fluxes, the NW diameter varies according to the morphology evolution of the droplet, which itself depends on the balance of Ga and group V (As or P) species reaching it. When less Ga atoms reach the droplet compared to the ones being incorporated

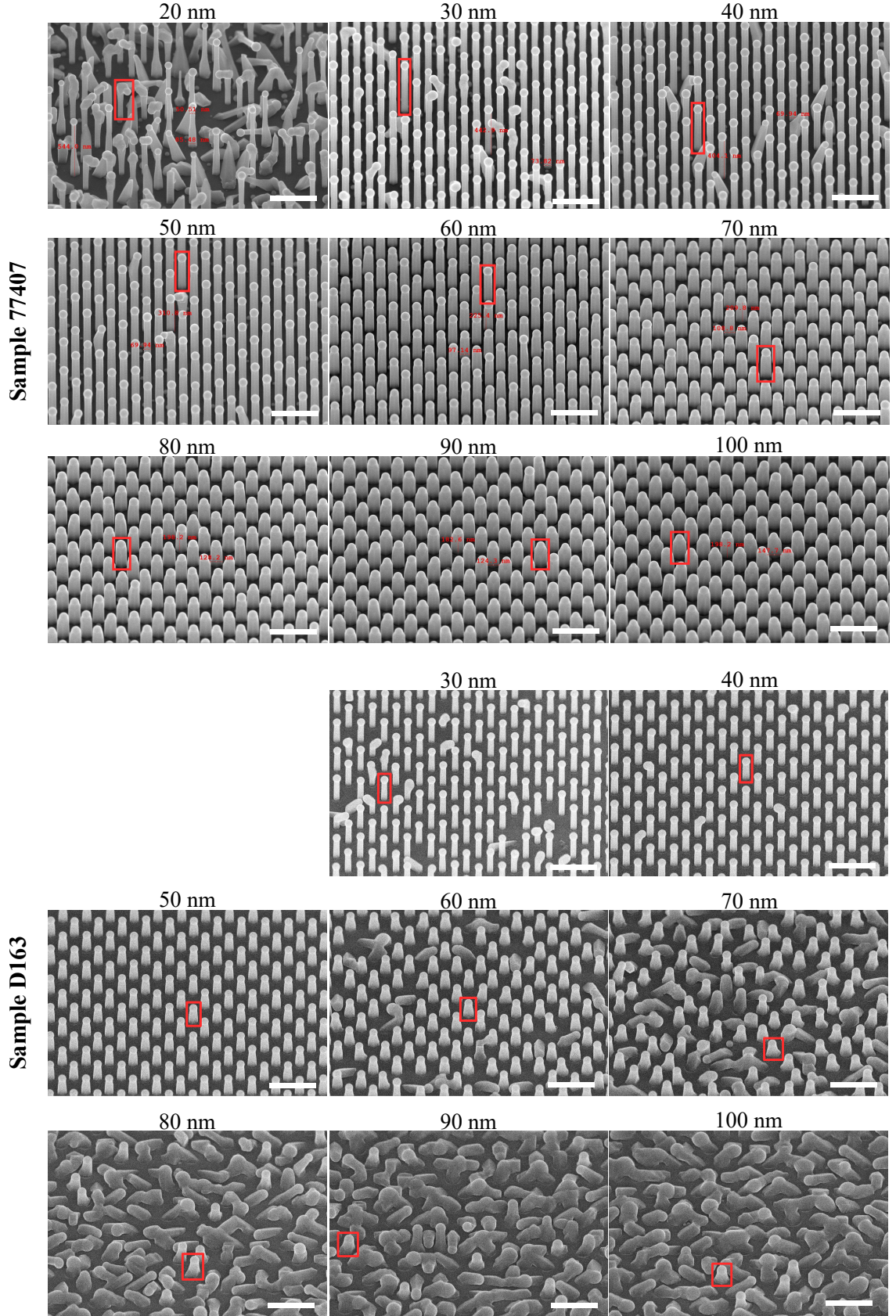


Figure 2.16: Tilted SEM images (45°) of the arrays containing the single NWs presented in [Figure 2.15](#). The pitch is 250 nm for all arrays, and the nominal mask hole diameter varies between 20–100 nm, as indicated above the SEM images. Scale bar = 500 nm.



in the NW for growth, the droplet will slowly shrink and lead to a positive NW tapering like the one observed in our NWs for nominal hole diameters  $> 70$  nm (Figure 2.16). In smaller holes, the Ga droplet can be expected to have an initially higher contact angle, resulting in smaller NW base diameters. When more Ga atoms reach the droplet compared to the ones being incorporated in the NW for growth, the droplet will slowly inflate and may even eventually fall off to one side. This is observed in our NWs for nominal hole diameters  $< 40$  nm (Figure 2.16). These observations are in agreement with previous work stating that the instantaneous NW diameter is governed by the size and morphology of the catalyst droplet [Gudiksen and Lieber, 2000; Priante et al., 2013; Dubrovskii et al., 2015]. From Figures 2.15a and b (dashed), less significant variation of the NW top diameter with respect to mask hole size can be observed in both samples 77407 and D163. This could be related to a self-equilibration effect of the NW diameter. In fact, under constant fluxes, the diameter of self-catalyzed NWs with initially widely distributed Ga droplet sizes (in holes of the same size), has been observed to eventually converge towards a critical value related to the size evolution of the droplet during growth [Dubrovskii et al., 2015]. Although this self-equilibration effect cannot be directly observed in our samples due to the growth time not being long enough to reach the size-uniform state, it could still explain the less significant variation of the NW top diameter with respect to mask hole size compared to the variation of the NW diameter at the base.

In order to obtain untapered NWs before reaching the size-uniform state, the growth conditions then need to be carefully tuned. First, the Ga pre-deposition time has to be adjusted to completely fill the holes in order to promote vertical NW growth (the variation of NW vertical yield in our NW arrays will be discussed in the next section). The V/III flux ratio then needs to be continuously adapted to the size of the droplet so that it neither shrinks nor inflates during NW growth, especially after the NW length exceeds the Ga diffusion length on the NW sidewalls, or shadowing effects are no longer negligible. This can be achieved by a two-step growth approach which decouples NW nucleation in the mask holes from NW elongation. In fact, [Küpers et al., 2018] managed to obtain untapered NWs with diameters of 45 nm at a length of 2.5  $\mu\text{m}$  in an array with a pitch of 1  $\mu\text{m}$ . Nevertheless, they emphasize that indeed for long NWs, a large part of the NW volume can result from radial VS growth, in which case the latter needs to be taken into account along with the droplet dynamics when optimizing the NW morphology. It is also interesting to notice that untapered NWs with different diameters can be obtained in a single growth run by varying the pitch [Dubrovskii et al., 2015] and taking advantage of the shadowing effect [Sibirev et al., 2012; Schroth et al., 2019]. However, it seems like the pitch needs to be varied significantly in order to obtain small changes in the NW diameter. In the study from [Dubrovskii et al., 2015], regular arrays of 50, 60, and 70 nm diameter NWs were obtained from pitches of 250, 500, and 1000 nm, respectively.

### NW vertical yield variation with mask hole size

As seen from Figures 2.15c and d, for sample 77407 (D163) very high NW vertical yields were obtained for arrays with nominal hole diameters varying between 40–100 nm (30–50 nm), which to our knowledge is unprecedented. In fact, near-perfect NW vertical yields were also obtained by [Wilson et al., 2021] for a hole diameter of 87 nm, but the yield was observed to dramatically decrease for slightly smaller or bigger hole dimensions (see Figure 2 in their article). For instance, they obtained NW vertical yields below 20% for a hole diameter of 57 nm. An optimal vertical yield of around 80% was also obtained by [Vettori et al., 2019] for a nominal hole diameter of 40 nm, but it rapidly decreased to below 60% for nominal hole diameters just below (30 nm) and above (50 nm), and reached a value lower than 10% for holes larger than 80 nm. So in comparison, we managed to obtain very high NW vertical yields in our NW arrays across a wide range of nominal hole diameters.

Nevertheless, our NW vertical yields were also observed to decrease when the hole size would deviate too much from the optimal one (with respect to the growth conditions). Curiously, lower NW vertical yields were obtained for sample D163 for which a Marangoni drying procedure was used after HF etching, than for sample 77407 for which standard  $\text{N}_2$  drying was employed. The exact reasons behind the yield differences between these two samples, and between the spot and matrix patterns of sample D163 (Figure 2.14) have not yet been elucidated. It may be that the substrate of sample 77407 was very clean even without the use of the Marangoni drying process, but that reproducibility issues at the time prevented us from obtaining the same results twice. However,

for both samples 77407 and D163, the NW vertical yield seems to be decreasing at smaller hole diameters mainly due to a change of NW growth direction during its elongation. Indeed, it looks like at some point during growth in small holes, the droplet becomes too big for the thin NW body and ends up falling on its side, driving growth in a different direction. This can be observed in the SEM images in Figure 2.16 when looking at the non-vertical NWs from sample 77407 (D163) with nominal hole diameters between 20–40 nm (30 nm). For bigger hole diameters, the decrease in NW vertical yield is only observed in sample D163, and seems to be mainly due to “crawling” NWs and some 2D crystal growth. This can be seen from the SEM images in Figure 2.16 for sample D163, nominal hole diameters between 60–100 nm. This defective growth could be attributed to poor seed configurations throughout the early stages of growth due to unoptimized Ga filling of the holes [de Lépinay, 2020], but the latter has not been investigated further here. We do believe however that the different vertical yield evolution obtained for samples 77407 and D163 are a result of slightly different effective hole aspect ratios resulting from different initial mask thicknesses, as explained in the previous section.

The optimization of our patterned substrate preparation process enabled the observation of a direct correlation between the mask hole size and NW diameter, for two samples grown in different MBE reactors. For both samples, the NW base diameter was observed to vary more significantly with mask hole size than the NW top diameter, probably due to a self-equilibration effect of the diameter of self-catalyzed NWs. Nevertheless, we managed to obtain NW base diameters that are much wider than the ones obtained in the literature given the NW lengths. This highlights the importance of precise mask hole patterning and cleaning in controlling the NW base diameter in a reproducible manner. The careful tuning of fluxes during growth could then enable untapered NW morphologies to be obtained before the size-uniform state is reached, but this was not investigated here.

Very high NW vertical yields were observed in both NW samples across a wide range of nominal hole diameters. However, the sample in which Marangoni drying was used did not show better yields in the matrix patterns than the sample for which a standard N<sub>2</sub> drying was carried out. The exact reasons behind these unexpected results still have to be further elucidated, but we believe that the slightly different effective hole aspect ratios resulting from different initial mask thicknesses in the two samples contributed to the different vertical yield evolution with mask hole size.

## 2.3 Chapter conclusions

The epitaxial growth of semiconductor NWs for solar cell applications is preferentially carried out by self-catalyzed selective-area growth, the fundamentals of which have been explained at the beginning of this chapter. I then presented the principle and components of the two MBE reactors used in this PhD work for NW growth, one located at the IPVF and one at the C2N. A review of the pre-growth and growth parameters influencing the NW vertical yield was then given based on the growth results obtained from state-of-the-art self-catalyzed GaAs NW arrays grown on Si(111) substrates. The NW vertical yield was used as a figure of merit throughout the chapter to assess the different NW array growths. Despite significant research efforts, not many groups have been able to achieve NW vertical yields above 90%, which is essential for fabricating high-efficiency NW devices with homogeneous properties.

In the second part of the chapter, I presented our patterned substrate preparation procedure. The relation between good mask selectivity and mask layer quality was exposed. In fact, carbon contamination in the PECVD chamber used to deposit the mask layer was observed to dramatically impact its selectivity. We managed to improve the latter by pre-conditioning the PECVD chamber. High NW vertical yields resulted from this mask layer quality optimization, but not homogeneously across the sample surface. We believe that the inhomogeneous NW growth may have been a result of impurities introduced on the substrate surface during DI water rinsing after the final HF dip, and

left there by the standard N<sub>2</sub> drying. In fact, the implementation of a Marangoni drying system allowed us to obtain near-perfect NW vertical yields homogeneously across several large-area spot patterns of the sample (average 99.5%). The optimization of our patterned substrate preparation process also enabled the observation of a direct correlation between the mask hole size and NW diameter, for two samples grown in different MBE reactors. This opens up new opportunities for the precise control of the diameter of self-catalyzed NWs. However, although very high NW vertical yields were obtained in the matrix patterns of both samples across a wide range of nominal hole sizes, the sample with Marangoni drying actually showed lower vertical yields compared to the sample for which standard N<sub>2</sub> drying was employed. We believe that this could be a result of the slightly different effective hole aspect ratios in the two samples, but it needs to be further investigated.



# Chapter 3

## GaAs/GaInP Core-Shell Nanowire Solar Cell with State-of-the-art Voc and Quasi-Fermi Level Splitting

### Chapter Contents

<b>3.1</b>	<b>Experimental methods</b>	<b>52</b>
3.1.1	Growth of GaAs/GaInP core-shell NW arrays on Si	52
	Patterned substrate preparation	52
	MBE growth recipe	52
	Characterization of as-grown NW arrays	52
3.1.2	NW solar cell fabrication	54
<b>3.2</b>	<b>Optoelectronic properties of the NW solar cell</b>	<b>55</b>
3.2.1	Current-voltage (J-V) characteristics	55
3.2.2	External quantum efficiency (EQE) response	56
	EQE under applied voltage bias	57
3.2.3	Nanowire absorption modelling	58
<b>3.3</b>	<b>Absolute photoluminescence (PL) and quasi-Fermi level (qFl) splitting analysis</b>	<b>59</b>
3.3.1	Hyperspectral PL maps and average PL spectra	60
3.3.2	Investigating the mismatch between qFl splitting and $qV_{oc}$	60
<b>3.4</b>	<b>Modelling hole transport at the p-type contact</b>	<b>62</b>
3.4.1	Simplified 1D cell structure modelled using SCAPS	62
3.4.2	A hole concentration-dependent potential barrier in the VB	63
3.4.3	Impact of the GaP/Si VB offset	65
<b>3.5</b>	<b>Chapter conclusions</b>	<b>66</b>

The first generation of NW solar cells fabricated in our group was based on GaAs NWs with radial homojunctions [de Lépinau, 2020]. In this chapter, I will present the second generation of NW solar cells fabricated in our group, which is based on GaAs/GaInP NWs with radial heterojunctions. The latter show better performances than the homojunction solar cells, mainly owing to more selective contacts. After reporting the state-of-the-art performances we managed to obtain due to previous optimizations, I will present an in-depth investigation of the cells' optoelectronic properties, in part through a first-time quantification of the quasi-Fermi level splitting in NW array solar cells. Optical and electronic simulations carried out will also be discussed to provide insights into the main absorption and electrical losses, as well as guidelines to design and fabricate higher-efficiency devices. The majority of the results presented in this chapter was published in [Tong et al., 2022b].



## 3.1 Experimental methods

### 3.1.1 Growth of GaAs/GaInP core-shell NW arrays on Si

#### Patterned substrate preparation

One-sixth of a two-inch p-Si(111) wafer with the characteristics described in [subsection 2.2.1](#) was used for the growth of the core-shell NWs presented in this chapter. The wafer surface was cleaned following the robust cleaning procedure described previously. A  $37 \pm 1$  nm thick SiO<sub>2</sub> layer was deposited via PECVD, before being patterned following the substrate preparation process detailed in [subsection 2.2.1](#) (hexagonal pattern with 500 nm pitch). The SiO<sub>2</sub> remaining inside the holes was removed by a 30 s dip in a 1 % HF solution. After rinsing with deionized water and drying with N<sub>2</sub>, the sample was stored overnight in a box filled with N<sub>2</sub> before being transported the next day to the Riber32 MBE chamber, which used to be located in the manufacturer's laboratory prior to its move to the IPVF. Marangoni drying was not used here because this sample was grown before the drying experiments presented previously in [subsection 2.2.1](#). Finally, the substrate was outgassed in the preparation chamber at 500-550°C until a pressure of  $3 \times 10^{-9}$  Torr was reached.

#### MBE growth recipe

Prior to growth, the substrate was held at 690°C for 10 min in the MBE growth chamber on a rotating holder (10 rpm), after which the growth temperature was stabilized at 620°C as monitored with a 0.9  $\mu$ m IRCON pyrometer. The growth procedure was initiated by a 1 min Ga pre-deposition with an equivalent thickness of 42 ML GaAs(100), and a Be flux of  $6 \times 10^{11}$  cm<sup>-2</sup> s<sup>-1</sup>. A Be-doped GaP stem (p-GaP) was grown during 80 s at a P<sub>2</sub>/Ga flux ratio of 1, before linearly closing the P valve while opening the one of As over 30 s. This results in a linearly graded GaP/GaAs transition which contributes to flatten the VB offset between GaP and GaAs [[Boulanger et al., 2016](#)]. The main Be-doped GaAs core segment (p-GaAs) was then grown under an As<sub>4</sub>/Ga flux ratio of 1.2, and the same Be flux during 12 min. The Ga flux during the GaP stem and GaAs core growths was set to correspond to a 2 Å/s growth rate on GaAs(100). The liquid Ga catalyst droplet was then consumed *in situ* during 20 min at the same temperature by shutting down the Ga flux and using an As<sub>4</sub> flux at 16% of its value during core growth. A nominally intrinsic GaAs shell (i-GaAs) was grown during 30 min at a substrate temperature of 590°C, under a Ga flux of 0.74 Å/s and an excess of As<sub>4</sub> (As<sub>4</sub>/Ga flux ratio of 7.1). The substrate temperature was finally set to 470°C for the 25 min growth of a Si-doped GaInP shell (n-GaInP), aiming at a planar growth rate of 1.1 Å/s, a planar composition of In<sub>0.58</sub> Ga<sub>0.42</sub>P and a planar doping level of  $6 \times 10^{18}$  cm<sup>-3</sup>. The NW structure was terminated by an n-type delta-doped GaInP capping layer (n<sup>+</sup>-GaInP). GaInP was grown during 32 s before stopping the Ga and In flux and providing an increased Si flux under excess P<sub>2</sub> for another 32 s, resulting in a Si surface concentration of  $1.4 \times 10^{12}$  cm<sup>-2</sup> in one atomic plane. This cycle was repeated 10 times, resulting in an equivalent GaInP layer grown during 5 min 35 s with an average planar Si concentration of  $1.7 \times 10^{19}$  cm<sup>-3</sup>.

#### Characterization of as-grown NW arrays

From the SEM image of the as-grown NW array shown in [Figure 3.1b](#), the NWs height and diameter could be determined as  $1800 \pm 130$  nm and  $220 \pm 20$  nm, respectively. The p-GaAs NW core diameter reported in [Figure 3.1a](#) was obtained from the measurement of NW cores previously grown in nearly identical conditions. The i-GaAs shell thickness was deduced by subtracting the p-GaAs NW core diameter from the total width of the As-containing region, as determined by cross section EDX ([Figure 3.2](#)). Similarly, the GaInP shell thickness was determined from the lateral extension of the (In,P)-containing regions of the cross-section EDX maps. Note that these EDX-determined shell thicknesses are rough estimates and significant errors are expected due to several factors. First, the diffusion dynamics of group III adatoms vary depending on the species and the growth temperature. Some regions in the shell may collect more or less material due to shadowing of surrounding NWs, resulting in non-uniform thickness. Furthermore, the NW core diameter was also found to vary between growths and after droplet consumption (typically within  $\pm 20$  nm). Finally, the geometrical surface orientation relative to the angle of the MBE cell leads to severe growth rate differences between the NW head and sidewall, as much as a factor of six, as measured using a scanning transmission electron microscope (STEM), see [Figure 3.2](#). On average

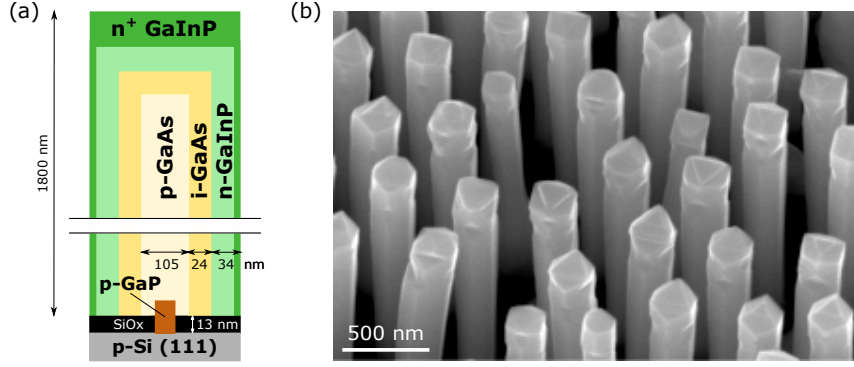


Figure 3.1: (a) Schematic of the dimensions of a core-shell GaAs/GaInP heterojunction NW with a delta-doped GaInP capping layer. (b) Tilted (35°) SEM overview of an as-grown GaAs/GaInP NW array with a 500 nm pitch.

the GaInP NW sidewalls were found to be richer in Ga [de Lépinau, 2020], which is why we corrected the nominal target Ga fraction to  $\text{Ga}_{0.42}\text{In}_{0.58}\text{P}$ , instead of using the theoretical GaAs-matched composition of  $\text{Ga}_{0.51}\text{In}_{0.49}\text{P}$ . However, as seen from the quantitative EDX analyses of the final Ga content in the GaInP shell (Figure 3.3), the latter still varies significantly across the NW axis, from on average 36% close to the NW foot to 50% towards the top of the NW, with major fluctuations in the tip segment. From the still important discrepancy with the GaAs-matched composition of  $\text{Ga}_{0.51}\text{In}_{0.49}\text{P}$ , a maximum lattice-mismatch of around 1% is expected between the GaAs NW core and GaInP NW shell [de Lépinau, 2020], which based on theoretical models from the literature [Raychaudhuri and Yu, 2006; Aifantis et al., 2007; Haapamaki et al., 2012; Salehzadeh et al., 2013] should be above the critical mismatch beyond which plastic relaxation occurs in our NWs. In fact, extended defects such as dislocations and twins are visible on the STEM image in Figure 3.2. Theoretical calculations from the literature suggest that plastic relaxation could be avoided if shells with a uniform thickness of 15 nm could be grown with a composition maintained within  $\pm 5\%$  of the GaAs-matched composition of  $\text{Ga}_{0.51}\text{In}_{0.49}\text{P}$  (misfit  $< 0.4\%$ ). Please note that the presented STEM-EDX analyses were obtained by the PhD student working on the project before me, and more details can be found in [de Lépinau, 2020].

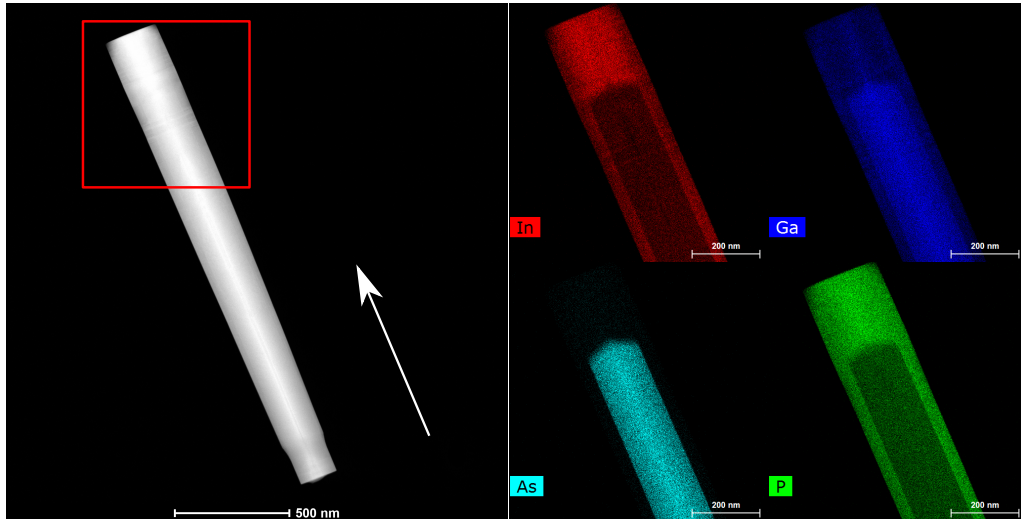


Figure 3.2: (left) STEM image taken with a high-angle annular dark field (HAADF) detector. The white arrow indicates the GaAs [111]B growth direction. (right) Corresponding In, Ga, As, and P elemental maps of the final NW section, indicated by the red square in the STEM image, obtained by EDX analysis. The core-shell heterostructure can be seen from the  $\langle 11\bar{2} \rangle$  zone-axis. Adapted from [de Lépinau, 2020], also published in [Tong et al., 2022b].

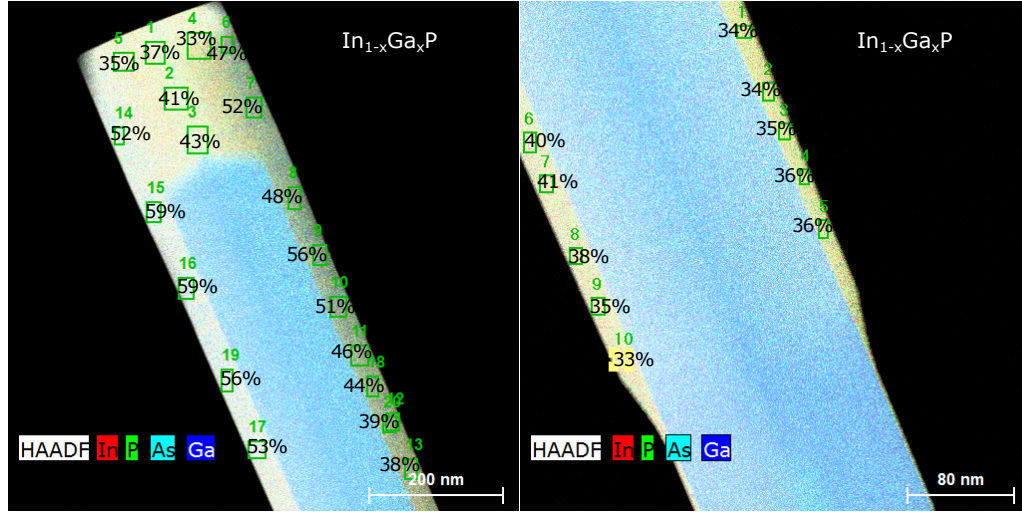


Figure 3.3: Combination image assembled from the HAADF image (black and white) and the corresponding In, Ga, As, P, elemental EDX maps (colour) from Figure 3.2. The values indicated in percentage are the chemical composition parameter  $x$  of the  $\text{In}_{1-x}\text{Ga}_x\text{P}$  shell for each selected zones (green rectangles). The left image is an overview of the final NW section, while the right image shows the bottom of the NW. Adapted from [de Lépinau, 2020], also published in [Tong et al., 2022b].

The doping levels were estimated in the core and shell of previous GaAs NW samples grown in similar conditions using CL spectroscopy by fitting the spectrum to a generalized Planck law, as described in our earlier work [Chen et al., 2021b,a]. The core p-type doping with Be is thus expected here to be close to  $p = 5 \times 10^{18} \text{ cm}^{-3}$ , whereas the shell n-type doping with Si is limited to  $n < 1 \times 10^{18} \text{ cm}^{-3}$  [Chen et al., 2021a], despite the use of the delta-doping technique [Schubert, 1990] in the outer-most NW shell [de Lépinau, 2020]. The size and carrier concentration of the p-GaP stem are difficult to measure. Estimations from growth parameters suggest a roughly 80 nm long and 40 nm wide p-GaP stem, with a doping concentration similar to the one in the p-GaAs core. Potential hole extraction barriers in the NW device arising from the introduction of this additional heterojunction at the foot of the NW are discussed in Section 3.4.

### 3.1.2 NW solar cell fabrication

The as-grown NWs were embedded in a benzocyclobutene (BCB) matrix for planarization. Plasma CCP-RIE etching and a dip in 1 % HF followed to reveal the NW heads. Photolithography was then used to deposit 150 nm of indium tin oxide (ITO) and Ti/Au contacts on specific areas of the sample to electrically connect NWs of the same cell, and ensure good mechanical and electrical contact with measurement probes. The back contact was formed by depositing a 300 nm Al layer on the back surface of the p-Si(111) wafer. The final device is made up of several circular cells with diameters ranging from 140  $\mu\text{m}$  to 1 mm. The champion cell (B276-18k-1c), which will be extensively characterized in the next sections, is shown in Figure 3.4a. It has an outer diameter of 600  $\mu\text{m}$  and an inner diameter of 440  $\mu\text{m}$ . After device characterization, a cross section view of the same cell was obtained by focused ion beam (FIB) milling and tilted SEM imaging (Figure 3.4b).

The Ga content in the shell of GaAs/GaInP core-shell NWs grown by MBE on patterned Si(111) was found to vary significantly along the NW axis. Quantitative STEM-EDX measurements of the Ga content in the GaInP NW shell enabled an estimation of the lattice-mismatch with the GaAs NW core, which is expected to be at the origin of the crystal defects observed in the NWs. Nevertheless, the GaAs/GaInP core-shell NWs were successfully processed into functional solar cell devices, whose characteristics will be analyzed in the next sections.

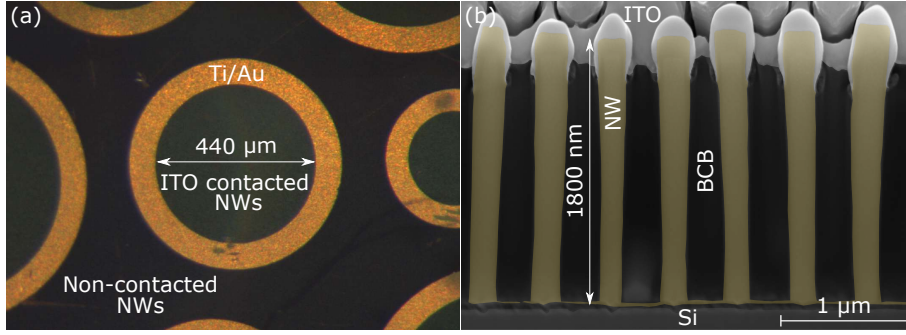


Figure 3.4: (a) Top view stereo microscope image of the champion NW solar cell presented in this chapter (B276-18k-1c). (b) Tilted (45°) SEM image of the cell, showing its different layers. The as-grown NWs are colored in yellow, while the Si substrate, BCB matrix and ITO are uncolored and can be easily distinguished.

## 3.2 Optoelectronic properties of the NW solar cell

### 3.2.1 Current-voltage (J-V) characteristics

The electrical performances of 13 NW solar cells from the aforementioned sample were measured under a 1-sun illumination (AM1.5G) using the solar simulator described in subsection 1.3.3. The recorded open-circuit voltage ( $V_{OC}$ ) and fill factor (FF) values are summarized in Figure 3.5. The short-circuit current ( $J_{SC}$ ) values exhibited were determined from EQE integration across the relevant wavelength range, as  $J_{SC}$  determination from EQE has the advantage of being independent of the spectral shape of the light source. The red star indicates the performances of the champion cell.

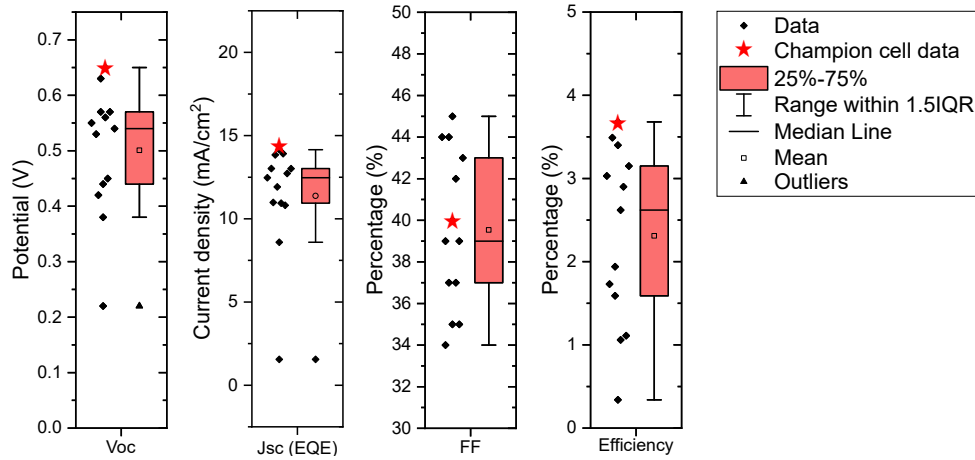


Figure 3.5: Box plots showing the  $V_{OC}$ ,  $J_{SC}$ , FF and efficiency values of 13 NW solar cells from the same sample. While the  $V_{OC}$  and FF were obtained from solar simulator measurements (1 sun, AM1.5G), the  $J_{SC}$  values exhibited were obtained from EQE integration. The latter were used to determine the efficiency values reported. The cell investigated in-depth in this chapter corresponds to the champion cell, whose performances are indicated by the red stars ( $V_{OC} = 0.65$  V,  $J_{SC} = 14.2 \text{ mA cm}^{-2}$ , FF = 40%,  $\eta = 3.68\%$ ).

The J-V characteristics of the champion cell in the dark and under a 1-sun illumination (AM1.5G) are shown in Figure 3.6a. A high  $V_{OC}$  of 0.65 V was obtained, along with a  $J_{SC}$  of  $14.2 \text{ mA cm}^{-2}$  (as determined from EQE integration across the relevant wavelength range, otherwise  $J_{SC(\text{solar simulator})} = 15.5 \text{ mA cm}^{-2}$ ), and a FF of 40%. As seen from Table 1.1, the resulting power conversion efficiency of 3.68% is at the state-of-the-art of solar cells with GaAs-based radial junction NWs grown on Si. However, it can also be noticed that the performances of this NW solar cell are still far behind the ones of the best GaAs thin film solar cell. The cross-over between the dark and the illuminated curves at 0.7 V suggests an electron barrier in the conduction band

which is reduced upon photodoping. The slope of the illuminated J-V curve near the short-circuit current point indicates either a voltage-dependent photocurrent (hence charge carrier collection function), or an illumination-dependent shunt path which drains a higher current under illumination. This will be further investigated in the next section when analyzing the cell's EQE response under applied forward and reverse biases. The semi-logarithmic plot of the J-V curve in the dark is shown in Figure 3.6b along with a one-diode model fit. A high and unfittable reverse-current can be observed, while the forward current was accurately fitted with a high ideality factor of 4 and a recombination parameter of  $J_0 = 4.1 \times 10^{-6} \text{ A cm}^{-2}$ . Satisfying shunt and series resistance of  $7.2 \times 10^3 \Omega \text{ cm}^2$  and  $0.17 \Omega \text{ cm}^2$ , respectively, were also obtained from the fit of the forward current.

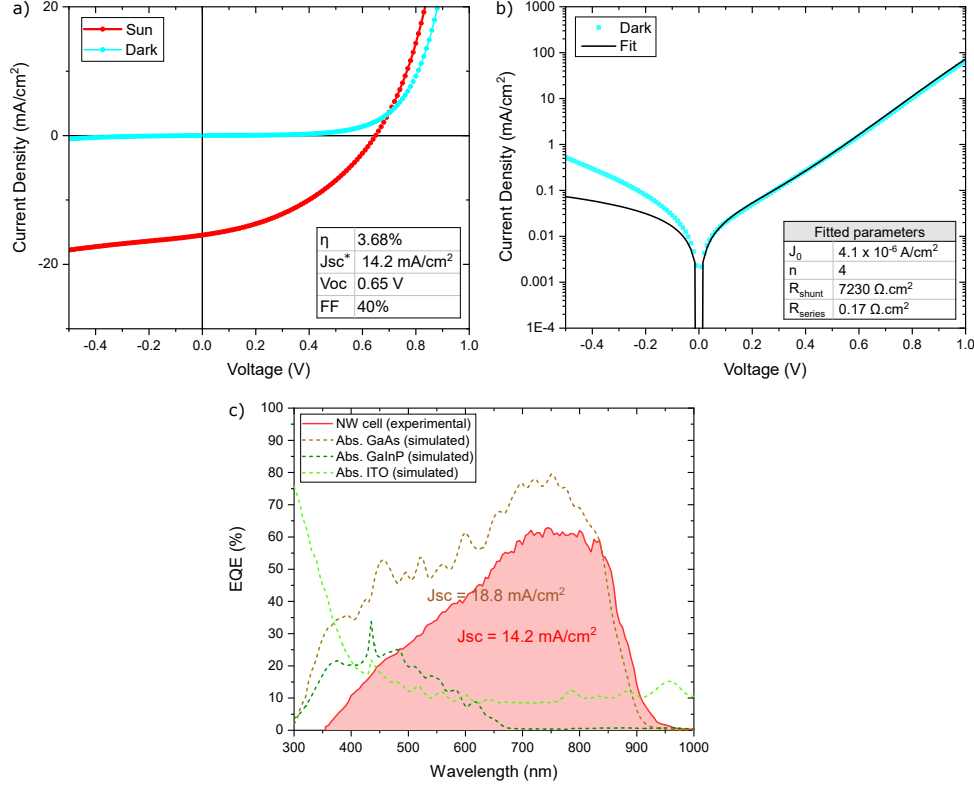


Figure 3.6: (a) J-V curves in the dark (blue) and under a 1 sun illumination using an AM1.5G spectrum (red). \* The  $J_{SC}$  value reported corresponds to the one determined from EQE integration (otherwise  $J_{SC(solar\ simulator)} = 15.5 \text{ mA cm}^{-2}$ ). (b) Semi-logarithmic plot of the J-V curve in the dark (blue), along with a one-diode fit (black). (c) EQE response of the champion cell (red) and simulated absorptions for GaAs, GaInP and ITO (dashed) using the simplified design shown in Figure 3.8a.

### 3.2.2 External quantum efficiency (EQE) response

A custom-built setup described in subsection 1.3.3 was used to measure the external quantum efficiency (EQE) of the NW solar cell. The resulting EQE spectrum is shown in Figure 3.6c (red). Between 700 and 800 nm the EQE remains relatively constant around 60% and is higher than the EQE values measured in other radial junction GaAs-based NW solar cells [Dastjerdi et al., 2016; Boulanger et al., 2016]. Below 700 nm the EQE decreases steadily, although experiments showed that a high-temperature annealing could increase the short wavelength part of the EQE by improving contact conductivity [de Lépinau, 2020].

Due to light scattering, specular reflectivity measurements could not be used to explicitly differentiate absorption issues from carrier collection issues, so EQE measurements were performed under forward and reverse biases to investigate carrier collection. Simulations of the absorption in the different regions of the NW solar cell were also carried out in subsection 3.2.3 to analyze potential absorption losses.



### EQE under applied voltage bias

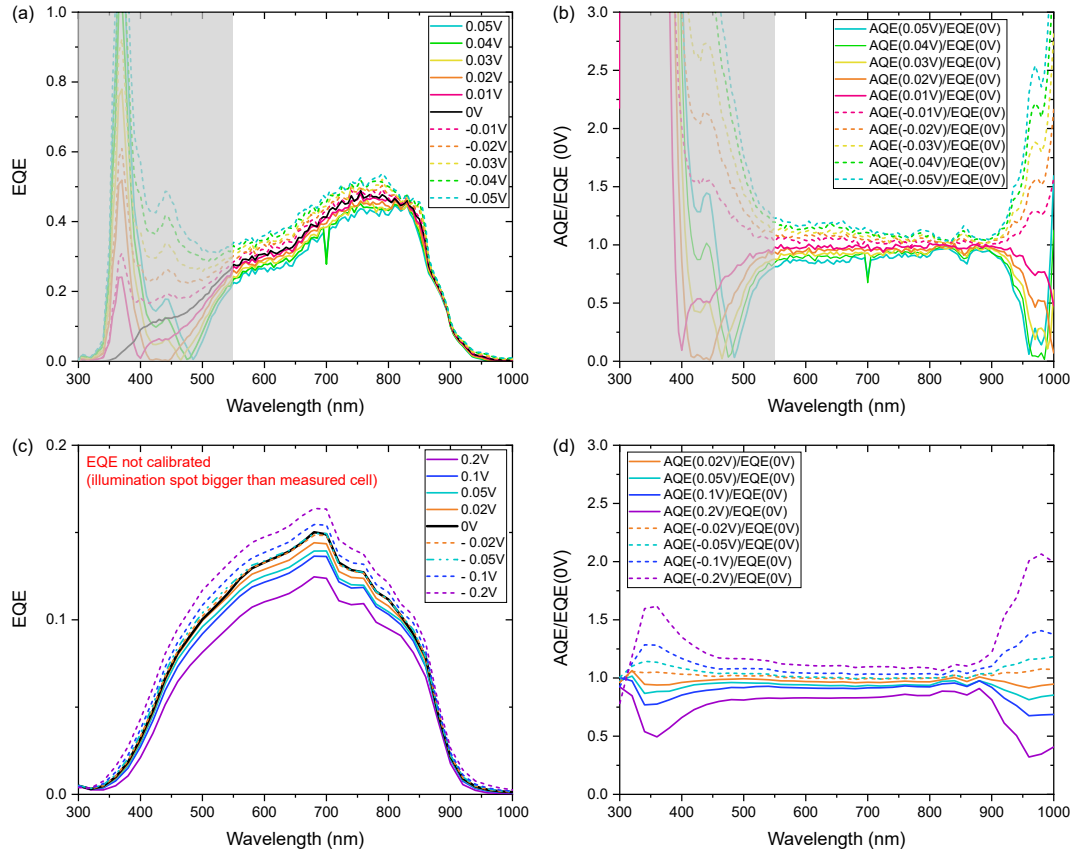


Figure 3.7: EQE response obtained under forward (solid lines) and reverse (dashed lines) biases, using a monochromator set-up located at (a) the C2N (see set-up description in subsection 1.3.3) and (c) the IPVF. The above unity EQEs observed in the grey region of (a) are artifacts arising from the absence of an optical chopper and lock-in amplifier system on the C2N monochromator set-up. The set-up at the IPVF uses an illumination spot size that is bigger than the measured cell, resulting in an uncalibrated EQE response. The ratios between the EQE response under bias and at 0 V are presented in (b) for the C2N measurements and (d) for the IPVF ones.

EQE measurements were performed under forward and reverse biases, on a NW solar cell from the aforementioned sample, with a  $V_{OC}$  of 0.53 V,  $J_{SC}$  of  $13.9 \text{ mA cm}^{-2}$  and FF of 43%, giving an overall efficiency of 2.9% (cell B276-20k-2c). These measurements were not performed on the champion cell (B276-18k-c) because at the time of this study the latter had already undergone surface damage caused by successive electrical measurements using contact probes. Figure 3.7 shows the EQE response recorded under forward (solid lines) and reverse (dashed lines) biases, between (a) -0.05 V and 0.05 V, using the monochromator set-up located at the C2N (described in subsection 1.3.3), and (c) -0.2 V and 0.2 V, using the monochromator set-up located at the IPVF, which has an illumination spot size bigger than the NW cell area, resulting in EQE responses that are not calibrated. The above unity EQEs observed in the grey region of Figure 3.7a are artifacts arising from the absence of an optical chopper and lock-in amplifier system on the C2N monochromator set-up. In fact, these artifacts are not observed in the measurements carried out using the IPVF set-up.

From Figure 3.7, the EQE response is seen to increase with reverse bias (carrier collection is enhanced) and decrease with forward bias, in such a way that the variation of the  $J_{SC}$  values obtained from the integration of the EQE curves in Figure 3.7c (not shown here) retraces the slope of the illuminated J-V curve near the short-circuit current point (Figure 3.6a). This indicates that the slope of the illuminated J-V curve near the short-circuit current point is a result of a voltage-dependent photocurrent (and hence collection function), rather than an illumination

dependent shunt path in the NW solar cell. A voltage-dependent photocurrent can arise due to several mechanisms, including variations with voltage of the SCR width, interface recombination, and photocurrent barrier [Scheer and Schock, 2011].

A voltage-dependent width of the SCR can be diagnosed by looking at the ratio between the EQE at different voltages and the EQE at 0 V (Figures 3.7b and d), and in particular its wavelength dependence. Typically, when the width of the SCR varies with voltage, the EQE/EQE(0V) ratio approaches unity at short wavelengths and increases (decreases) at longer wavelengths under reverse (forward) bias. Ignoring the artifacts at short and long wavelengths due to noise (background signal), this is not observed in our measurements. A voltage-dependent photocurrent arising from a voltage-dependent SCR width can thus be ruled out in these NW solar cells.

Both interface recombination and photocurrent barrier result in EQE variations under applied potential bias that are independent of wavelength, making the two mechanisms tougher to distinguish from one another. Charge carrier recombination at the absorber interface increases when the electric field at the junction decreases (under applied forward bias for instance), resulting in a photocurrent that typically decreases with forward bias and increases with reverse bias, as observed in the EQE measurements previously presented. In our NW solar cells, charge carriers may recombine at the dislocations near the i-GaAs/n-GaInP interface, introduced due to the GaInP shell composition variation along the NW axis (see discussion in subsection 3.1.1).

A photocurrent barrier arising from a CB offset at the absorber interface can also lead to a voltage-dependent photocurrent when a decrease (increase) in the electron concentration at the interface occurs under forward (reverse) bias. In our case, a small CB offset is indeed expected at the i-GaAs/n-GaInP interface (see CB spike in the simulated band diagram in Figure 3.11a), which could constitute a photocurrent barrier. It is likely that the voltage-dependent photocurrent (and hence EQE response) observed in our NW solar cells is a result of the presence of both interface recombinations and a photocurrent barrier.

After having reviewed carrier collection issues in the GaAs/GaInP NW solar cells, we will discuss absorption losses in the next section using optical simulations as support.

### 3.2.3 Nanowire absorption modelling

A frequency-domain modal method known as the Rigorous Coupled-Wave Analysis (RCWA) [Hugonin and Lalanne, 2005; Lalanne and Morris, 1996; Li, 1997; Lalanne and Jurek, 1998] was used to model absorption in the GaAs NWs, the GaInP contact and the ITO layer. A top view of the unit cell (hexagonal lattice) used to generate the NW array solar cell in the simulations is shown in Figure 3.8a (left). A cross-section view of the simulated NW solar cell along a single NW is also shown in Figure 3.8a (right). This simplified design incorporates the main elements of the NW solar cells previously presented, with the GaInP segment only present at the top of the NW as it is 6 times thicker than the GaInP shell, and is expected to be the main source of photon absorption in GaInP. A more refined design is not justified also due to the morphology dispersion between the different NWs of the NW array composing a cell. The absorption in each material (Figure 3.6c, dashed curves) was calculated using 20 Fourier orders, and the optical constants used for the RCWA simulations are plotted in Figure 3.8b.

The simulated absorption in the GaAs NWs (brown in Figure 3.6) is slightly higher than the experimentally measured EQE of the solar cell (red), although the general trend of the EQE is well reproduced by the simulations. The calculated short-circuit current, assuming that all the photo-generated carriers are collected, is  $18.77 \text{ mA cm}^{-2}$ . The difference of about  $4.5 \text{ mA cm}^{-2}$  with the experimentally obtained  $J_{SC}$  may be a result of a non-perfect carrier collection as previously discussed, or to an underestimation of the parasitic absorption inside the GaInP contact and/or the ITO. The parasitic absorption inside the GaInP contact is relatively high ( $2.84 \text{ mA cm}^{-2}$ ) even without considering the 34 nm-thick GaInP shell in the simulations.

The performances of the NW solar cell presented could thus be hindered by poor crystalline quality NWs, defective interfaces and contacts both at the foot (interface between the GaP stem and the Si substrate) and at the top of the NWs (contact between the GaInP shell and the ITO). As high optoelectronic quality NWs are essential for a performant solar cell, hyperspectral PL was used to assess the quasi-Fermi level (qFl) splitting developed in the NWs under illumination. The latter has been shown to represent the maximum  $V_{OC}$  that a solar cell can achieve [Feuerbacher

and Wurfel, 1990; Delamarre et al., 2012], and is discussed in the following section.

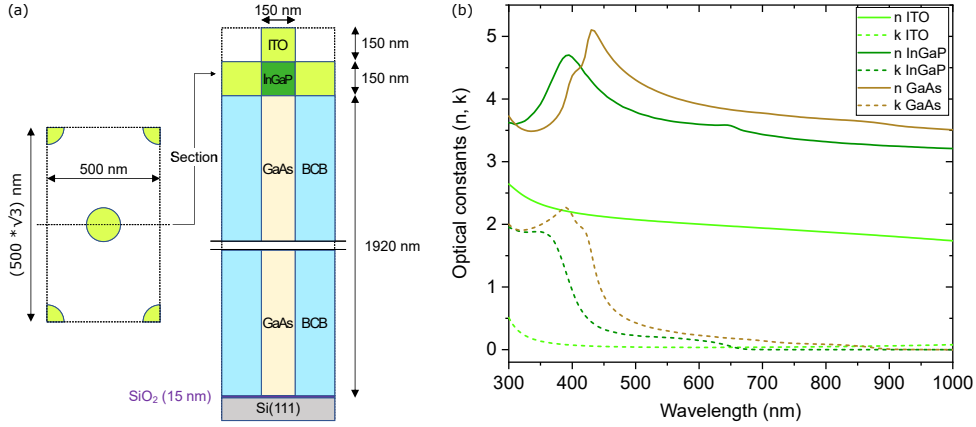


Figure 3.8: (a) Schematics of the NW solar cell model used in the RCWA simulations: (left) a top view of the unit cell (hexagonal) composing the NW array and (right) a cross-section view of the NW solar cell along a single NW. (b) Refractive indices ( $n$ ) and extinction coefficients ( $k$ ) used in the absorption simulations presented in Figure 3.6c.

The champion GaAs/GaInP core-shell NW solar cell demonstrated a high  $V_{OC}$  of 0.65 V, a  $J_{SC}$  of  $14.2 \text{ mA cm}^{-2}$  and a FF of 40%, resulting in a PCE of almost 3.7%. Although the latter is at the state-of-the-art of GaAs-based radial junction NW solar cells grown on Si, these performances are still far behind the ones of the best GaAs thin film solar cell. Current-voltage and EQE measurements under potential bias revealed carrier collection limitations, while optical simulations indicated absorption losses in the GaInP and ITO layers. In the next section, the intrinsic optoelectronic properties of the NWs will be investigated.

### 3.3 Absolute photoluminescence (PL) and quasi-Fermi level (qFl) splitting analysis

To better assess the optoelectronic properties of the NWs, a spatially and spectrally resolved hyperspectral imager set-up calibrated in absolute units was used (see subsection 1.3.2 for more details). LED excitation at 450 nm was carried out through a microscope objective with numerical aperture (NA) 0.6. Measurements were performed at illumination intensities varying from below 1 sun to 81 suns. The measurement at 12 suns was carried out with a 532 nm laser due to a set-up change.

According to the generalized Planck law presented in Equation (1.6), the absolute photon flux ( $\phi(\hbar\omega)$ ) emitted from a semiconductor under illumination into a hemisphere above its flat surface can be related to the carrier temperature ( $T$ ) and the qFl splitting ( $\Delta\mu$ ), assuming the latter is constant. For a semiconductor under quasi-thermal equilibrium with photon energies several  $k_B T$  larger than the separation of the quasi-Fermi levels, the Fermi distribution can be approximated by a Boltzmann distribution, giving:

$$\phi(\hbar\omega) = A(\hbar\omega) \frac{(\hbar\omega)^2}{4\pi^2 \hbar^3 c^2} \exp\left(\frac{-\hbar\omega}{k_B T}\right) \exp\left(\frac{E_{fc} - E_{fv}}{k_B T}\right). \quad (3.1)$$

This equation assumes an entirely collected Lambertian emission profile which has been shown to be an accurate description of the angular emission profile of non-optimized NW arrays [Cui et al., 2016]. The absorption probability  $A(\hbar\omega)$  in Equation (3.1) can be approximated by the experimentally measured EQE( $\hbar\omega$ ), such that:

$$\phi(\hbar\omega) = EQE(\hbar\omega) \frac{(\hbar\omega)^2}{4\pi^2 \hbar^3 c^2} \exp\left(\frac{-\hbar\omega}{k_B T}\right) \exp\left(\frac{\Delta\mu}{k_B T}\right). \quad (3.2)$$



We consider this approximation to be reasonable considering the good match between the experimentally measured EQE and the modeled  $A(\hbar\omega)$  in Figure 3.6c.

### 3.3.1 Hyperspectral PL maps and average PL spectra

Figure 3.9 shows the PL maps of the champion NW cell emission at 870 nm (1.43 eV), under an illumination of (a) 12 suns and (b) 81 suns. Note that the measurements at 12 suns and 81 suns were carried out in separate campaigns and hence not performed at the exact same cell location. Figures 3.9c and d present the corresponding qFl splitting maps obtained by fitting the absolute photon flux using the generalized Planck law (Equation (3.2)) between 1.43 and 1.52 eV, with a fixed carrier temperature of 330 K. Some qFl splitting variations can be observed across the maps due to spatial inhomogeneity which probably arose during device processing. However, this has not been further investigated as qFl splitting variations of less than  $\pm 30$  meV are observed, demonstrating in fact a relatively high qFl splitting homogeneity over the characterized device surface. The boxed areas in Figures 3.9a and b are roughly  $50 \times 50 \mu\text{m}^2$ , and present the cell surface from which an average PL spectrum was extracted. The semi-logarithmic plot in Figure 3.10a presents the average PL spectra under both illuminations (dotted lines). The solid curves correspond to the PL spectra divided by the cell's EQE (from Figure 3.6c), while the red lines are their generalized Planck law fit, from which qFl splittings of 0.95 eV (12 suns) and 1.01 eV (81 suns) were obtained. These two data points are indicated in light blue and cyan, respectively, in Figure 3.10b, and are comparable to the average qFl splitting values obtained in the red boxed areas of Figures 3.10c and d.

Due to lower signal-to-noise ratio at weaker illumination intensities ( $< 12$  suns), instead of directly measuring spectrally resolved images we measured simple luminescence images, that integrate all wavelengths above the 850 nm long-pass filter, therefore presenting more intense signals. This way we obtain the relative variation of the luminescence from the 81 suns illumination down to 0.7 sun, which is proportional to  $\exp(\frac{\Delta\mu}{k_B T})$  according to Equation (3.2). Since  $\Delta\mu$  was determined to be 1.01 eV at 81 suns,  $\Delta\mu$  for lower illuminations can be deduced, as displayed in Figure 3.10b (dark blue squares). After interpolation, a qFl splitting of 0.84 eV was determined for a 1 sun illumination. This qFl splitting value is considerably higher than the measured  $qV_{OC}$  at 1 sun (black squares in Figure 3.10b), and to the best of our knowledge constitutes a first-time quantification of the qFl splitting in NW array solar cells. As here the qFl splittings were determined by using a generalized Planck law fit in which the absorption probability  $A(\hbar\omega)$  was approximated by the EQE( $\hbar\omega$ ) (Equation (3.2)), the resulting qFl splitting values correspond to upper limits. Lower limits of the qFl splittings can be deduced by using a 30% higher absorption, as obtained from the optical simulations in subsection 3.2.3. The latter would translate into an 8 meV decrease in the qFl splitting values ( $kT \ln(1.3)$ , where  $T = 330$  K). The ideality factors  $n_{\Delta\mu}$  and  $n_{V_{OC}}$  indicated in Figure 3.10b were obtained by fitting the slope of the variation of  $\Delta\mu$  and  $V_{OC}$ , respectively, with illumination intensity, and they are discussed at the end of this section.

The high qFl splitting of 0.84 eV at 1 sun indicates a better optoelectronic quality than what could be deduced from electrical measurements and STEM observations alone. It also evidences significant room for device improvement, which can only be achieved if the mismatch between the qFl splitting and the  $qV_{OC}$  is clarified.

### 3.3.2 Investigating the mismatch between qFl splitting and $qV_{OC}$

A first reason for the lower measured  $qV_{OC}$  ( $V_{OC} = 0.65$  V,  $qV_{OC} = 0.65$  eV) as compared to qFl splitting (0.84 eV) could be inhomogeneous NW properties. Let us consider a situation where the NWs can be grouped into two distinct families: family 1 and family 2.

In family 1, the NWs sustain a qFl splitting  $\Delta\mu_1$ , and emit a luminescence signal  $A\phi_{bb}\exp(\frac{\Delta\mu_1}{k_B T})$ . In family 2, the NWs present a negligible qFl splitting  $\Delta\mu_2$ , and emit a negligible luminescence. Such a situation relies on two assumptions: (i) The effective carrier lifetimes of both NW families are significantly different. (ii) Resistances or current barriers must be present in between NWs, which could originate from processing issues, e.g. local incomplete BCB removal or inhomogeneous TCO deposition. Otherwise, the qFl splitting of each individual NW would equal its voltage, and the voltage of both NW families would equilibrate. It is possible that points (i) and (ii) are true for our solar cells, as they have been observed in similar NWs (VLS grown GaAs NWs on Si) by atomic force microscopy (AFM) [Mikulik et al., 2017] and electron beam induced current (EBIC) measurements [Barrigón et al., 2020], and in GaN/InGaIn core-shell NWs by scanning photocurrent

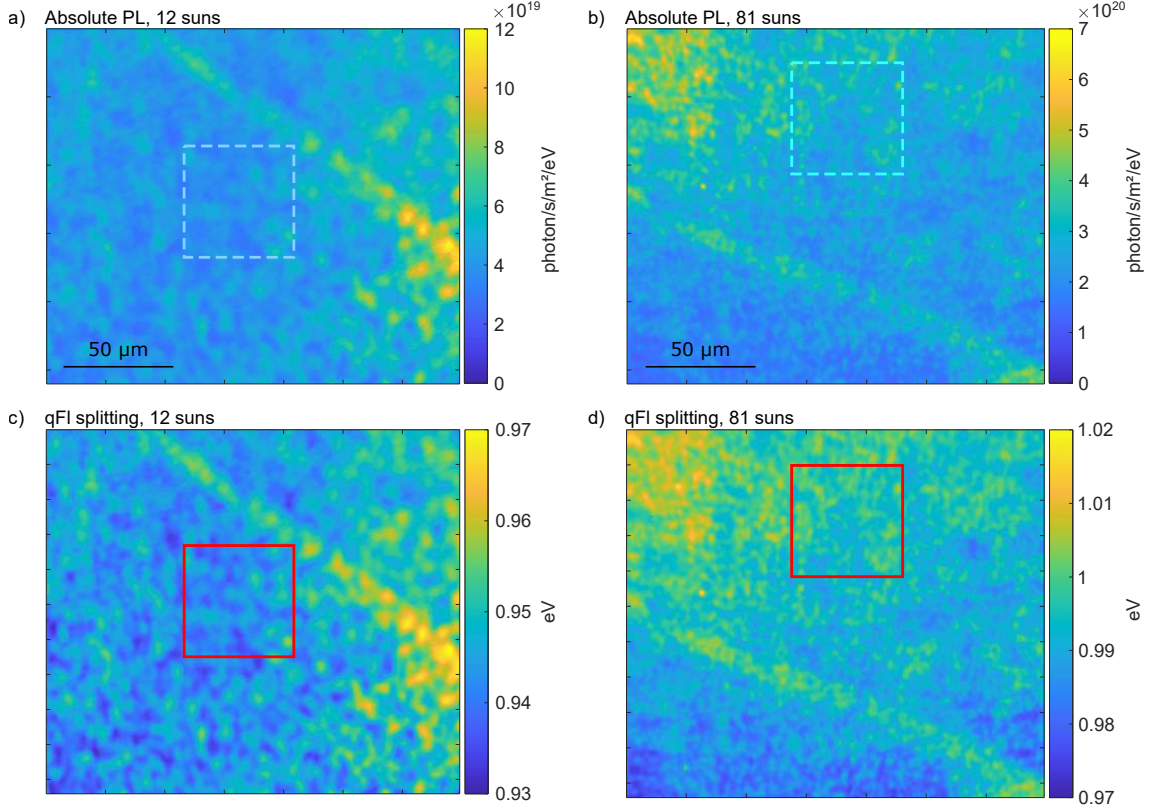


Figure 3.9: PL maps of the champion NW cell emission at 870 nm (1.43 eV) calibrated in absolute units, under an illumination of (a) 12 suns and (b) 81 suns. (c) and (d) show the qFl splitting maps of the same areas obtained by fitting the PL spectra using the generalized Planck law (Equation (3.2)) between 1.43 and 1.52 eV with a fixed carrier temperature of 330 K.

microscopy (SPCM) [Howell et al., 2013]. Therefore,  $\Delta\mu_1$  and  $\Delta\mu_2$  can differ, as well as their luminescence emissions. Nevertheless, they cannot be distinguished by luminescence imaging, since the NW-to-NW distance is in the order of the diffraction limit (500 nm). The luminescence density recorded on an area comprising an equal number of NWs from families 1 and 2 will be an average of their respective emission, i.e.  $A\phi_{bb}\exp(\frac{\Delta\mu_1}{k_B T}) \times 0.5 \approx A\phi_{bb}\exp(\frac{\Delta\mu_1 - 20 \text{ meV}}{k_B T})$ . This means that the determined qFl splitting (here  $\Delta\mu_1 - 20 \text{ meV}$ ) is close to its highest value. Simultaneously, the voltage can take any value in between  $\frac{\Delta\mu_1}{q}$  and  $\frac{\Delta\mu_2}{q}$ , depending on the local resistances. In the extreme situation where NWs 1 are totally disconnected and NWs 2 are connected without resistance, we have  $V = \frac{\Delta\mu_2}{q}$ . In the opposite case (NWs 1 connected, NWs 2 disconnected),  $V = \frac{\Delta\mu_1}{q}$ .

The fact that the qFl splitting obtained is higher than the measured  $qV_{OC}$  of the cell could also be attributed to additional recombinations at heterointerfaces. This has been observed in other types of solar cells, e.g. CIS [Elanzeery et al., 2019], CIGS [Lombez et al., 2014; Sood et al., 2021] or perovskites [Stolterfoht et al., 2019]. In our case, the efficient extraction of the majority charge carriers may be prevented by the p-Si/p-GaP/p-GaAs heterointerface at the foot and by the i-GaAs/n-GaInP/ITO heterointerface at the top, and they may recombine at the dislocations near the i-GaAs/n-GaInP interface introduced due to GaInP shell composition variation along the NW axis, as already mentioned previously. Although these were not investigated here, more details on charge generation, separation, recombination and collection could be obtained by using for example two-photon induced photocurrent [Parkinson et al., 2013].

The difference in the ideality factors obtained from the variation of  $\Delta\mu$  and  $V_{OC}$ , respectively, with illumination intensity (for more information on the determination of the ideality factors please refer to page 51 of the book by D. Abou-Ras et al. [Abou-Ras et al., 2016]) could also be explained by inhomogeneous NW properties and/or the presence of potential barriers at interfaces and recombination currents. As the ideality factor provides insight on the location of the dominat-

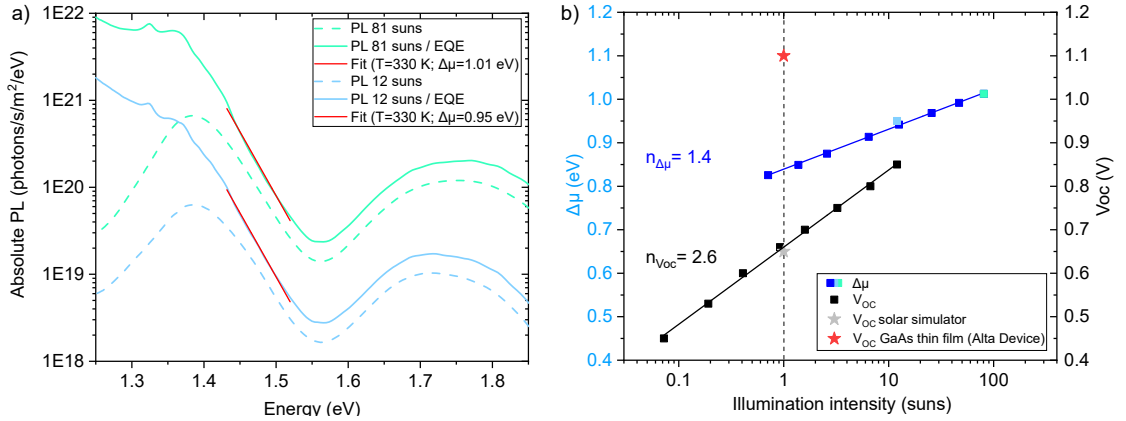


Figure 3.10: (a) Absolute PL spectrum of the champion cell from under an illumination of 12 suns and 81 suns (dashed curves). The PL spectra were averaged over a cell area of roughly  $50 \times 50 \mu\text{m}^2$ . The same spectra divided by the cell's EQE from Figure 3.6c are also shown (solid curves), along with their generalized Planck law fit carried out between 1.43–1.52 eV (red lines). (b) Evolution of the quasi-Fermi level splitting ( $\Delta\mu$ , blue) and the open-circuit voltage ( $V_{OC}$ , black) with illumination intensity. The light blue and cyan squares correspond to qFl splittings obtained from spectrally resolved luminescence images, while the dark blue squares are obtained from simple images that integrate all wavelengths. The record  $V_{OC}$  for planar GaAs cell (red star) corresponds to the one obtained by Alta Devices [Kayes et al., 2011].

ing recombination mechanism in a solar cell [Scheer and Schock, 2011], the higher ideality factor  $n_{V_{OC}} = 2.6$  compared to the optical ideality factor  $n_{\Delta\mu} = 1.4$  suggests the presence of an additional recombination channel at the GaAs absorber interfaces. However, these ideality factors are still lower than the one obtained from a one-diode model fit of the dark current-voltage characteristics of the cell ( $n = 4$ , Figure 3.6b), and further studies would be required to elucidate this matter.

The quasi-Fermi level splitting in GaAs/GaInP NW arrays composing a solar cell was assessed for the first time using hyperspectral PL measurements. A value of 0.84 eV was determined at 1 sun (up to 1.01 eV at 81 suns), which is considerably higher than  $qV_{OC}$  (0.65 eV) and indicates NWs of good optoelectronic quality, but device performances hindered by inhomogeneous NW properties and/or the presence of energy barriers and recombination channels at heterointerfaces.

### 3.4 Modelling hole transport at the p-type contact

The GaP stem introduced at the p-type contact of the NW structure (brown in Figure 3.1a) to enhance the vertical yield of the NWs is an additional heterostructure which could be a barrier for hole extraction [Gudovskikh et al., 2016]. To study the impact of this barrier, we simulated a simplified one-dimensional structure of the NW cell, using the solar cell device simulator SCAPS [Burgelman et al., 2000].

#### 3.4.1 Simplified 1D cell structure modelled using SCAPS

The modelled NW structure is illustrated at the top of Figure 3.11a. Since charges in core-shell NWs are separated radially, the modelled structure first follows the NW axis and then the direction perpendicular to the NW axis. Figure 3.11a presents the simulated band diagrams of the modelled structure under a 1 sun illumination and an applied bias corresponding to the maximum power point ( $V_{MPP}$ ), for different acceptor doping concentrations in the GaP stem, ranging from  $1 \times 10^{18}$ – $8 \times 10^{18} \text{ cm}^{-3}$ . All band diagrams have been shifted such that the conduction bands ( $E_C$ ) are aligned on the n-GaInP side. The parameters used in the SCAPS simulations are detailed in Table 3.1.

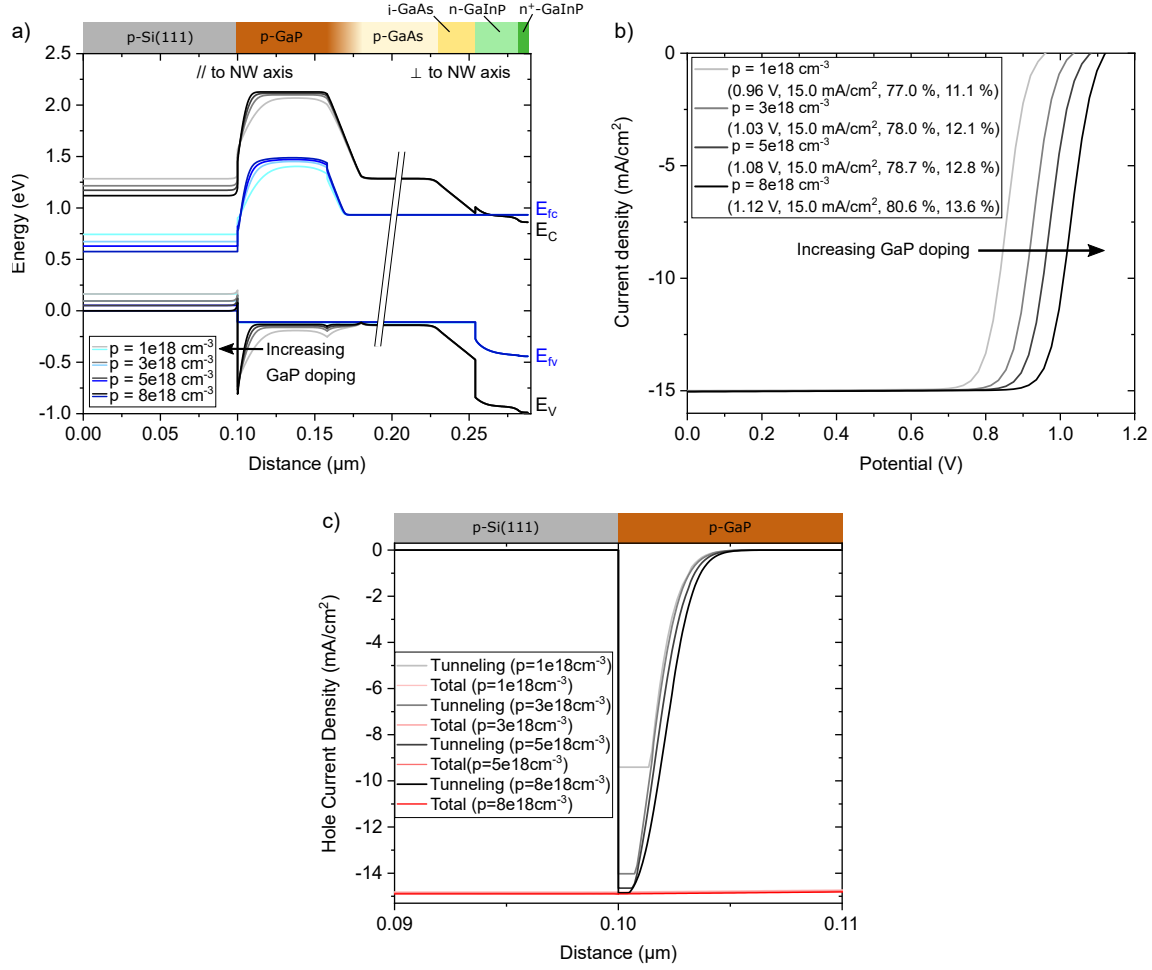


Figure 3.11: (a) Band diagrams obtained from 1D SCAPS simulations under 1 sun illumination and  $V_{MPP}$  bias for different GaP acceptor doping concentrations. (b) Current-voltage characteristics (values in brackets correspond to  $V_{OC}$ ,  $J_{SC}$ , FF, and  $\eta$ ), and (c) hole current densities obtained from the same SCAPS simulations.

### 3.4.2 A hole concentration-dependent potential barrier in the VB

As observed in Figure 3.11a, the increase of acceptor doping concentration in GaP brings about a narrowing of the VB potential barrier there. This is also evidenced by the current-voltage curves in Figure 3.11b through the improved  $V_{OC}$ , fill factor, and hence efficiency, with increased doping concentration. In fact, as the potential barrier width in GaP is decreased with increasing doping concentration, hole tunnelling becomes more efficient. This is illustrated in Figure 3.11c where the current density of intra-band tunnelling holes at  $V_{MPP}$  (grey/black curves) is almost doubled at the GaP/Si interface when the doping concentration changes from  $1 \times 10^{18} \text{ cm}^{-3}$  (light grey) to  $8 \times 10^{18} \text{ cm}^{-3}$  (black). For a doping concentration above  $5 \times 10^{18} \text{ cm}^{-3}$ , the hole tunnelling current densities (two darkest curves) become comparable to the total hole current density (red lines), indicating that a high doping concentration can help overcome the VB potential barrier in GaP thanks to intra-band tunnelling. The more efficient transport of holes via intra-band tunnelling at higher doping concentrations can also be observed in the band diagrams in Figure 3.11a, through a lower potential drop across the GaP/Si interface.

The threshold doping concentration required for holes to predominantly tunnel through the potential barrier depends however on the GaP/Si VB offset, which was found to vary considerably in the literature, as will be discussed in the next section.

Table 3.1: Parameters used in the 1D SCAPS simulations presented in Figure 3.11. The material parameters were extracted from references [Levinstein et al., 1999; Ioffe Institute, Gomez, 2018; Kao et al., 2019]. The acceptor doping concentration in p-GaP (in bold in the table) was varied between  $1 \times 10^{18}$ – $8 \times 10^{18} \text{ cm}^{-3}$  in the SCAPS simulations.

	p-Si	p-GaP	Graded GaAsP	p-GaAs	i-GaAs	n-GaInP	n <sup>+</sup> -GaInP
Thickness (nm)	100	58	22	50	24	28	6
Bandgap (eV)	1.12	2.26	linearly graded	1.424	1.424	1.85	1.85
Electron affinity (eV)	4.05	3.8	linearly graded	4.07	4.07	4.01	4.01
Dielectric permittivity	11.9	11.1	linearly graded	12.9	12.9	11.8	11.8
CB effective density of states (cm <sup>-3</sup> )	$2.8 \times 10^{19}$	$1.8 \times 10^{19}$	linearly graded	$4.7 \times 10^{17}$	$4.7 \times 10^{17}$	$6.24 \times 10^{17}$	$6.24 \times 10^{17}$
VB effective density of states (cm <sup>-3</sup> )	$1.04 \times 10^{19}$	$1.9 \times 10^{19}$	linearly graded	$9 \times 10^{18}$	$9 \times 10^{18}$	$1.46 \times 10^{19}$	$1.46 \times 10^{19}$
Electron thermal velocity (cm/s)	$2.3 \times 10^7$	$2 \times 10^7$	linearly graded	$4.4 \times 10^7$	$4.4 \times 10^7$	$3.9 \times 10^7$	$3.9 \times 10^7$
Hole thermal velocity (cm/s)	$1.65 \times 10^7$	$1.3 \times 10^7$	linearly graded	$1.8 \times 10^7$	$1.8 \times 10^7$	$1.4 \times 10^7$	$1.4 \times 10^7$
Electron mobility (cm <sup>2</sup> .V.s)	$1.5 \times 10^3$	$2.5 \times 10^2$	linearly graded	$8.5 \times 10^3$	$8.5 \times 10^3$	$5.0 \times 10^2$	$5.0 \times 10^2$
Hole mobility (cm <sup>2</sup> .V.s)	$4.5 \times 10^2$	$1.5 \times 10^2$	linearly graded	$4.0 \times 10^2$	$4.0 \times 10^2$	30	30
Doping concentration (cm <sup>-3</sup> )	(p) $1.0 \times 10^{19}$	<b>(p) <math>1.0 \times 10^{18}</math></b>	linearly graded	(p) $3.0 \times 10^{18}$	(n residual) $1.0 \times 10^{15}$	(n) $1.0 \times 10^{18}$	(n) $1.0 \times 10^{19}$
Radiative recombination coeff. (cm <sup>3</sup> /s)	$1.0 \times 10^{-15}$	$1.0 \times 10^{-13}$	linearly graded	$2.0 \times 10^{-10}$	$2.0 \times 10^{-10}$	$1 \times 10^{-10}$	$1 \times 10^{-10}$
Auger electron capture coeff. (cm <sup>6</sup> /s)	$3.0 \times 10^{-31}$	0	linearly graded	$5.0 \times 10^{-30}$	$5.0 \times 10^{-30}$	$4.7 \times 10^{-30}$	$4.7 \times 10^{-30}$
Auger hole capture coeff. (cm <sup>6</sup> /s)	$3.0 \times 10^{-31}$	0	linearly graded	$1.0 \times 10^{-31}$	$1.0 \times 10^{-31}$	$1.1 \times 10^{-30}$	$1.1 \times 10^{-30}$



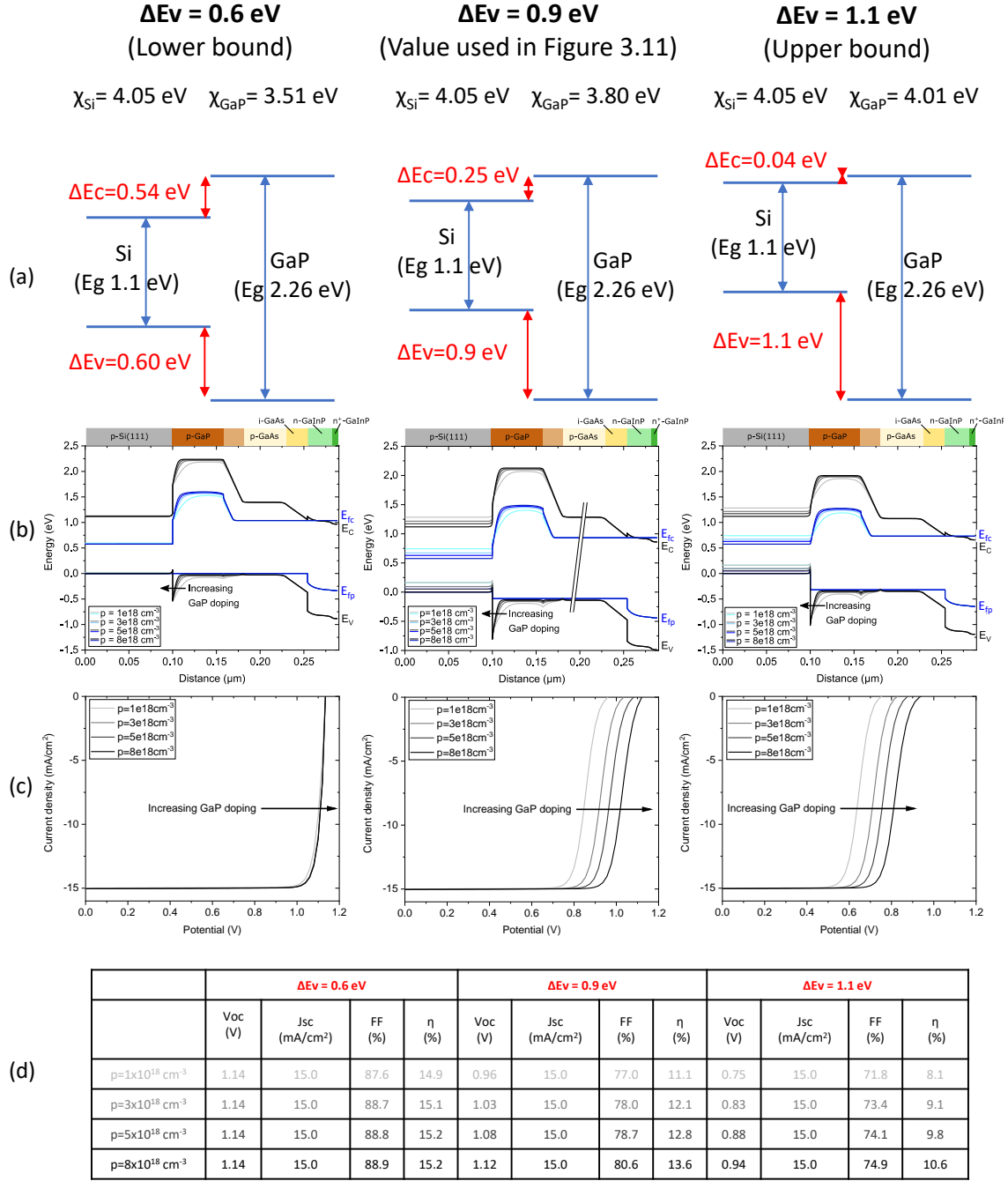


Figure 3.12: Impact of the VB offset ( $\Delta E_V$ ) at the GaP/Si interface on the SCAPS simulation results. (a) Comparison between the lower and upper bound GaP/Si VB offset values found in the literature ( $\Delta E_V = 0.6$  eV [Supplie et al., 2015] and  $\Delta E_V = 1.1$  eV [Roychowdhury et al., 2017], respectively) and the average value of  $0.9$  eV used in the simulations presented in the main article. The corresponding electron affinities for Si and GaP ( $\chi_{Si}$  and  $\chi_{GaP}$ ) are also indicated. (b) Band diagrams obtained from 1D SCAPS simulations under 1 sun illumination and  $V_{MPP}$  bias for different GaP acceptor doping concentrations. (c) Corresponding current-voltage characteristics under 1 sun illumination. The figures of merit  $V_{OC}$ ,  $J_{SC}$ , FF, and  $\eta$  are summarized in table (d).

### 3.4.3 Impact of the GaP/Si VB offset

The VB offset ( $\Delta E_V$ ) at the GaP/Si interface directly impacts the aforementioned simulation results, and its experimentally determined value varies from  $0.6$  eV to  $1.1$  eV in the literature [Supplie et al., 2015; Roychowdhury et al., 2017]. An average  $\Delta E_V$  of  $0.9$  eV was used in the simulations presented in the previous section (corresponding to a GaP electron affinity of  $3.8$  eV

[Ioffe Institute]). The simulation results obtained using the lower and upper bound VB offset values found in the literature are presented in Figure 3.12.

As we can see from the simulated J-V curves in Figure 3.12c, when the GaP/Si VB offset corresponds to the lower bound value of 0.6 eV, the solar cell performances do not vary much with increasing GaP doping concentration. However, as the GaP/Si VB offset increases, the cell performances degrade and become more impacted by the GaP doping concentration, as seen in Figures 3.12c and d.

The uncertainty on the VB offset value at the GaP/Si interface thus makes it difficult to determine a target threshold doping concentration in the GaP which would allow efficient transport of holes. Moreover, determining precisely the size of the actual GaP stem in the NW structure and its doping concentration is also a challenge. Previous CL studies have shown that the Be doping concentration in our GaAs NW cores, which are grown via the same VLS mechanism, can be superior to  $5 \times 10^{18} \text{ cm}^{-3}$  [Chen et al., 2021a]. It is reasonable to assume that the doping level in the GaP stem is similar, and hence that with a GaP/Si VB offset between 0.6–1.1 eV, the potential barrier in the VB does not significantly impact hole extraction at the p-type contact of our devices thanks to hole tunnelling.

Numerical 1D SCAPS simulations showed that while the GaP stem introduced at the p-type contact of the NW structure for vertical yield enhancement can indeed be a barrier for hole extraction, the latter can be overcome if the GaP stem is sufficiently doped. As we expect the hole concentration in the GaP stem to reach  $5 \times 10^{18} \text{ cm}^{-3}$ , we are confident that the performances of our NW solar cells are limited rather by recombination currents and potential barriers at the n-type contact (GaInP/ITO).

### 3.5 Chapter conclusions

Core-shell GaAs/GaInP NW solar cells directly grown on Si by MBE were successfully fabricated. The champion cell demonstrated an efficiency of almost 3.7% and a state-of-the-art  $V_{OC}$  of 0.65 V. A quasi-Fermi level splitting of 0.84 eV at 1 sun (up to 1.01 eV at 81 suns) was determined from hyperspectral PL measurements for the first time in NW array solar cells, which is considerably higher than  $qV_{OC}$ . This indicates NWs of good optoelectronic quality and significant room for the improvement of our devices, which is very encouraging information for the NW solar cells community! Numerical 1D simulations showed that the potential barrier at the p-type contact can be overcome if the GaP stem is sufficiently doped. As we expect the hole concentration in the GaP stem to reach  $5 \times 10^{18} \text{ cm}^{-3}$ , we are confident that our NW solar cells' performances can be further enhanced by improvements at the n-type contact (GaInP/ITO).

The n-type contact could be limited by recombinations at the i-GaAs/n-GaInP/ITO heterointerface, due to the presence of dislocations arising from the GaInP shell composition variation along the NW axis. Furthermore, electron extraction could also be hindered by the Schottky barrier formed at the GaInP/ITO interface. In fact, ITO ( $\text{In}_2\text{O}_3:\text{SnO}_2$ ) is a polycrystalline material considered as a wide bandgap ( $< 3.75 \text{ eV}$ ) degenerate semiconductor. Due to its high electron concentrations and mobilities, ITO has been widely used as transparent contact for thin film solar cells, but it is known to form an important Schottky barrier with GaAs and GaInP [Bachmann et al., 1979; Balasubramanian and Subrahmanyam, 1990; Morgan et al., 1992; Lee et al., 1998], and has been previously indicated as an interface limiting III-V NW solar cell performances [Otnes et al., 2018]. Encouragingly, high doping levels in the III-V layer have been shown to enable good conductivity at the GaInP/ITO contact [de Lépinau, 2020], however these are difficult to achieve using the commonly used Si dopant. In the next chapter, we will investigate the use of Te as an alternative to Si for high n-type doping levels in III-V NWs.



# Chapter 4

## Investigating Te as an Alternative n-type Dopant for GaAs Nanowires

### Chapter Contents

<b>4.1 Doping control in NWs</b>	<b>68</b>
4.1.1 Doping related challenges in GaAs NWs	68
Surface-driven effects	68
Non-uniform dopant distributions	68
Compensation effects	68
4.1.2 Characterizing carrier concentration in NWs	69
Electrical characterization techniques	69
Optical characterization techniques	69
Scanning characterization techniques	70
<b>4.2 Experimental methods</b>	<b>71</b>
4.2.1 Epitaxial growth of Te-doped GaAs thin films and NWs	71
4.2.2 Characterization	72
Electron microscopy observations of Te-NW1 and Te-NW2	72
Luminescence characterization methods	73
<b>4.3 Electron concentration determination in GaAs:Te thin film references</b>	<b>74</b>
<b>4.4 Electron concentration mapping in GaAs:Te nanowires</b>	<b>76</b>
4.4.1 NWs grown at 640°C (Te-NW1)	76
Room temperature CL analysis	76
Low temperature CL analysis	76
4.4.2 NWs grown at 620°C (Te-NW2)	77
Room temperature CL analysis	77
Low temperature CL analysis	78
4.4.3 Comparison	78
<b>4.5 Chapter conclusions</b>	<b>80</b>

The intentional introduction of foreign impurities into a semiconductor (doping) is key for tuning its electrical, optical, and structural properties. High doping levels are of particular importance in NWs to mitigate the effects of high surface recombination velocities and surface depletion. However, high doping levels are difficult to achieve in NWs due to non-uniform dopant distribution and compensation effects, especially in n-type GaAs NW shells doped with the commonly used silicon dopant. Tellurium (Te), as a group VI element, is an alternative n-type dopant which could enable higher electron concentrations to be achieved in GaAs NWs. During my PhD, I had the opportunity of collaborating with the Optoelectronics Research Center from Tampere University (Finland), to study the incorporation of Te in GaAs NWs using cathodoluminescence mapping. After an introduction on doping control in NWs, I will present in this chapter how we validated the room temperature and low temperature CL analysis methods previously developed in our group for Si-doped GaAs, using five Te-doped GaAs thin film samples. Then I will apply these methods to two Te-doped GaAs NW samples grown at 640°C and 620°C, respectively, in order to study the impact of the NW growth temperature on the Te incorporation efficiencies by vapor-solid and vapor-liquid-solid processes. The majority of the results presented in this chapter were published in [Tong et al., 2022a].

## 4.1 Doping control in NWs

In this section, I will first discuss some doping-related challenges observed in GaAs NWs, and then present a few commonly used doping characterization techniques which can help identify and mitigate the former. The specificities of cathodoluminescence spectroscopy, which was chosen for the study presented in this chapter, will also be highlighted.

### 4.1.1 Doping related challenges in GaAs NWs

#### Surface-driven effects

In high surface-to-volume structures such as nanowires, surface states can be detrimental due to Fermi level pinning and depletion of charge carriers. Surface states in the midgap of GaAs are known to pin the surface Fermi level and cause particularly high surface recombination velocities. While in moderately doped NWs, the depletion region consists of a cylindrical ring surrounding a central conducting channel, in poorly doped NWs the entire cross section can be depleted and hence insulating. For a 100 nm diameter GaAs NW, [Chang et al., 2012] found that doping concentrations below  $1 \times 10^{17} \text{ cm}^{-3}$  result in completely depleted NWs, and doping concentrations above roughly  $7 \times 10^{17} \text{ cm}^{-3}$  are required to generate a significant amount of free carriers. Heavy doping and surface passivation with a wide bandgap semiconductor are two ways of mitigating high surface recombination velocities and surface depletion [Chen et al., 2021a]. The introduction of an intrinsic region to form p-i-n NW junctions can also significantly reduce the depleted zone [Petronio, 2019].

#### Non-uniform dopant distributions

During NW growth, different dopant incorporation paths (VLS or VS) can lead to both axial and radial inhomogeneities in dopant distributions, especially when tapered growth occurs [Kim et al., 2021]. Due to the catalyst droplet acting as a secondary reservoir, a lack of sharpness in NW junctions grown by VLS has also been observed [Christesen et al., 2014; Darbandi et al., 2016]. Both tapering and reservoir effects can lead to not only non-uniform dopant distributions in single NWs, but also wire-to-wire inhomogeneity, directly impacting final device performance and its reproducibility.

Segregation of dopant atoms in GaAs NWs can also lead to inhomogeneities in dopant distributions. This has been observed in particular for Se- and Te-doped GaAs NWs [Oyama et al., 2000].

#### Compensation effects

Si is a widely used dopant in GaAs due to its high sticking coefficient, low diffusion length, and disinclination to surface segregation. However, as a group IV element, Si can either incorporate in Ga-sites and act as a donor (n-type dopant) or incorporate in As-sites and act as an acceptor (p-type dopant). This amphoteric behavior is not problematic for planar GaAs layers with (001) surface orientation, as Si incorporation in Ga-sites (n-type doping) is more favorable. In fact, electron concentrations up to  $7 \times 10^{18} \text{ cm}^{-3}$  have been achieved in Si-doped GaAs thin films [Neave et al., 1983]. At higher Si concentrations, increasing proportions of Si atoms occupy As sites to accommodate lattice strain, and the formation of Si donor-acceptor pairs reduces the doping efficiency through compensation effects (deactivation of the Si donors) [Chai et al., 1981; Neave et al., 1983; Domke et al., 1996].

In GaAs NWs, both n-type and p-type doping can be achieved using Si, depending on the primary incorporation mechanism (VLS or VS). For GaAs NWs grown by MBE in VLS mode, Si doping is usually p-type [Hijazi et al., 2019; Colombo et al., 2009; Dubrovskii et al., 2020], while NW shell doping by VS mode is typically n-type [Dimakis et al., 2012; Colombo et al., 2009]. Regardless of the doping type, strong level of compensation is often observed in Si-doped GaAs NWs [Hilse et al., 2010]. As a consequence, it is particularly difficult to obtain high n-type doping in GaAs NWs, although compensation effects can be attenuated by decreasing the growth temperature to below 490°C and using a high V/III flux ratio, both of which reduce the proportion of As vacancies [Dimakis et al., 2012].

The maximum electron concentration our group could achieve in Si-doped GaAs NW shells is  $5 \times 10^{17} \text{ cm}^{-3}$  at a growth temperature of  $475^\circ\text{C}$  [de Lépinau, 2020; Chen et al., 2021a]. This is an order of magnitude below the target electron concentration level. Furthermore, significant parasitic deposition was observed on the  $\text{SiO}_2$  mask as a result of the low growth temperature. To achieve higher electron concentrations in GaAs NWs, tellurium, as a group VI element, could be considered. Previous studies have already demonstrated the successful incorporation and activation of Te dopants in GaAs NWs [Suomalainen et al., 2015; Goktas et al., 2018; Hakkarainen et al., 2019], and [Orrù et al., 2016] reported electron concentrations up to the  $10^{19} \text{ cm}^{-3}$  range without compensation. However, both axial and radial Te doping gradients have been observed in Te-doped GaAs NWs [Hakkarainen et al., 2019], although the carrier concentration gradients could not be quantified. In the next section, I will present some of the most prominent NW doping characterization techniques, and explain why cathodoluminescence mapping was chosen in this study to probe the carrier concentration gradients in Te-doped GaAs NWs.

Due to the important surface-to-volume ratio in NWs, their properties are often degraded by high surface recombination velocities and surface depletion. High NW doping is one way of mitigating these phenomena, however the latter is difficult to achieve due to non-uniform dopant distribution and compensation effects, especially in n-type GaAs NW shells doped with the commonly used Si dopant.

#### 4.1.2 Characterizing carrier concentration in NWs

In order to obtain the desired electronic contribution from the dopant species, the latter need to be activated in the host semiconductor. Hence, more than the doping atom concentration, it is important to be able to quantify the carrier concentration. However, the small dimensions and complex geometry of NWs prevent the use of standard Hall effect measurements for carrier density assessment. Below I present the advantages and disadvantages of the most important NW carrier concentration characterization techniques based on electrical, optical, and scanning probe methods.

##### Electrical characterization techniques

The adaptation of standard electrical techniques to measure carrier concentration in NWs was enabled by recent progresses in the nanofabrication of good ohmic contacts at the extremities of individual NWs laid down on insulating substrates [Kim et al., 2021].

- **Field effect measurements:** The first quantification of doping levels in NWs was achieved by [Cui et al., 2000] using NW field-effect transistor (FET) devices, in which the measurement of the source-drain current variation as a function of the gate voltage enables the assessment of the charge type and carrier concentration [Kim et al., 2021]. However, the accuracy of such measurements is often questionable due to the number of assumptions made, and contact resistances that are often not considered [Wallentin, 2013; Kim et al., 2021].
- **Hall effect measurements:** An alternative to field effect measurements is Hall measurements, which enable a more direct assessment of the carrier concentration and were performed on NWs for the first time in 2012 [Storm et al., 2012; Blömers et al., 2012]. In Hall effect measurements, the interaction between the current flowing in the NW and a perpendicular magnetic field leads to the build-up of an electric potential from which the carrier concentration can be directly obtained.

Although these electrical methods have been widely used to determine carrier concentration in single GaAs NWs [Gutsche et al., 2009; Casadei et al., 2013; Wallentin et al., 2013; Hultin et al., 2016], they cannot map the variation of the carrier concentration in a NW. In addition, these electrical methods require the complex and time-consuming fabrication of localized contacts, which can be avoided by using optical characterization techniques.

##### Optical characterization techniques

Rapid and non-destructive characterization techniques like photoluminescence, Raman spectroscopy and optical pump-terahertz probe spectroscopy, are highly attractive for NW doping assessment.

However, due to the use of light as excitation source, the spatial resolution of these techniques is limited to the one of light diffraction, typically just below the micrometer scale (around 500 nm), making them more suited for the analysis of NW ensembles.

- **Photoluminescence (PL):** It is well known that heavy doping leads to changes in the band structure of semiconductors, which can be unveiled by analyzing the luminescence spectrum of the material [Casey and Stern, 1976; Lee et al., 1995]. A laser is typically used as a source of excitation in photoluminescence to generate minority charge carriers, whose radiative recombination is at the origin of the recorded emission spectrum. The carrier concentration dependent broadening and shift of the luminescence peaks then enable a quantitative determination of the carrier concentration through advanced line-shape analyses of the PL spectrum [Casey and Stern, 1976; Olego and Cardona, 1980; De-Sheng et al., 1982; Borghs et al., 1989]. When performed at low temperature, PL also allows to observe states with a small binding energy such as excitons, shallow energy impurities and defects, which can bring valuable information on the studied material.
- **Raman spectroscopy:** Resonant Raman spectroscopy relates the local vibrational modes of the semiconductor crystal with the concentration of dopants when the former are Raman active [Ketterer et al., 2010; Ojha et al., 2016]. It is widely used to study as-grown NW arrays [Kim et al., 2021], but a few analyses on single NWs can also be found [Mohajerani et al., 2016; Hakkarainen et al., 2019].
- **Optical pump-terahertz probe (OPTP):** Another established method is OPTP spectroscopy, in which a THz pulse is used to probe far-infrared absorption changes initiated by an ultrashort optical pulse [Němec et al., 2002]. The complex conductivity spectra recorded allow the measurement of a comprehensive set of electronic properties at room temperature, including dopant concentration, carrier lifetimes, mobilities and surface recombination velocities [Joyce et al., 2013, 2016]. OPTP can thus overcome the difficulties associated with standard contact-based electrical transport measurements, and the carrier concentration of several GaAs NW ensembles have been investigated by the Johnston group using this technique [Boland et al., 2015, 2016, 2017].

### Scanning characterization techniques

Scanning probe characterization techniques have higher spatial resolutions than the aforementioned techniques owing to the combination of nanometric probes (such as an electron beam) and scanning over macroscopic areas [Kim et al., 2021]. They thus respond to the need of investigating carrier concentration profiles in a large number of single NWs with very little nanofabrication required.

- **Electron beam induced current (EBIC):** EBIC measurements can be performed in a SEM or STEM configuration on semiconductors containing an internal electric field (i.e. p-n junction). Upon excitation by the scanning electron beam, electron-hole pairs are created in the semiconductor and collected in an external circuit, creating an induced current which can be correlated to the material's electronic band structure, and hence defects and minority carrier properties. Quantitative carrier concentration can be determined in NW p-n junctions using EBIC, with a limit of detection around  $10^{17} \text{ cm}^{-3}$  [Piazza et al., 2019].
- **Cathodoluminescence (CL):** CL also uses a scanning electron beam in an SEM or TEM environment, but unlike in EBIC measurements, neither electrical contacts nor a rectifying interface is required for carrier concentration determination. Similarly to PL, carrier concentrations can be obtained from CL spectra by advanced line-shape analyses. The detailed working principles of CL can be found in [subsection 1.3.1](#). The main advantage of CL compared to the characterization techniques previously presented is the high spatial resolution. With an electron beam spot size of around 10 nm, the spatial resolution is mainly limited by the interaction volume (10–100 nm) and the diffusion length of charge carriers, allowing to investigate the carrier concentration distribution in individual NWs. Compared to electrical characterization techniques in which complex sample fabrication is required, in CL individual NWs need only to be laid down on an external substrate for analysis. Furthermore, as it is a contactless method, contact resistances are not an issue and CL spectra can be acquired at both room- and low-temperature. The use of CL for carrier concentration determination in

NWs is however relatively new [Lindgren et al., 2015], and has not yet been applied to many different semiconductor/dopant systems. Our group has demonstrated rigorous methods for the quantitative assessment of carrier concentration in Be-doped (p-type) and Si-doped (n-type) GaAs thin films [Chen et al., 2021b] and NWs [Chen et al., 2017, 2021a]. In the next sections, I will validate the n-type methods for Te-doped GaAs, and use them to discuss the impact of NW growth temperature on the Te incorporation efficiency in GaAs NWs.

Advanced characterization methods are required to quantify carrier concentration in NWs due to their small dimensions and complex geometry. While optical techniques can avoid the sophisticated and time-consuming fabrication of localized contacts required in electrical techniques, the spatial resolution of the former is unfortunately limited to the one of light diffraction (around 500 nm), preventing the investigation of carrier concentration distribution in single NWs. Scanning probe characterization techniques like cathodoluminescence on the other hand require very little sample preparation while having at the same time higher spatial resolutions owing to the combination of nanometric probes (electron beam) and scanning over macroscopic areas. This is why cathodoluminescence was chosen herein to study the impact of NW growth temperature on the Te incorporation efficiency in GaAs NWs.

## 4.2 Experimental methods

### 4.2.1 Epitaxial growth of Te-doped GaAs thin films and NWs

All samples were grown by solid source MBE at Tampere University in Finland, in a reactor equipped with effusion cells for Ga and GaTe. As was provided by a valved cracker operating at 920°C to provide As<sub>2</sub> dimers.

A series of 1 µm thick planar Te-doped GaAs samples (labeled Te-TF1 to Te-TF5) were grown on semi-insulating GaAs wafers to be used as a reference for the CL measurements and to act as Hall measurement calibration samples for the GaTe cell temperatures. The growth temperature and V/III ratio used for these planar samples are summarized in Table 4.1. The electron concentration determined in the 5 thin film samples by Hall effect ranged from  $5 \times 10^{17}$ – $1 \times 10^{19}$  cm<sup>-3</sup>.

Two samples of self-catalyzed GaAs NWs (labeled Te-NW1 and Te-NW2) were grown on Si(111) substrates by using droplet-epitaxy mediated lithography-free oxide patterns as a template. Details of the template fabrication method are given in [Hakkarainen et al., 2015]. The NW growth was carried out at 620°C and 640°C for samples Te-NW1 and Te-NW2, respectively. For both samples, growth was initiated by a 40 s Ga pre-deposition and followed by simultaneous opening of the GaTe shutter and As needle valve. The Ga flux corresponded to a 0.3 µm/h planar (100) GaAs growth rate, and the GaTe flux corresponded to a  $2 \times 10^{19}$  cm<sup>-3</sup> doping level on planar GaAs, as calibrated by Hall measurements for the 0.3 µm/h growth rate. After 60 min, the NW growth was terminated by shutting all fluxes simultaneously and rapidly ramping down the substrate to preserve the Ga droplets.

Table 4.1: Epitaxial growth temperature ( $T_{\text{growth}}$ ) and V/III ratio of the 5 reference thin film samples (Te-TFx), and the 2 nanowire samples (Te-NWx).

Sample Name	$T_{\text{growth}}$ (°C)	V/III ratio
Te-TF1	520	10
Te-TF2	521	10
Te-TF3	580	15
Te-TF4	520	11
Te-TF5	571	15
Te-NW1	640	9
Te-NW2	620	9



### 4.2.2 Characterization

#### Electron microscopy observations of Te-NW1 and Te-NW2.

SEM images of the as-grown NW arrays can be found in [Figure 4.1](#). Their analysis, along with the results from [[Hakkarainen et al., 2019](#)], show that the NWs in Te-NW1 are on average 3700 nm long and have a uniform diameter of 170 nm throughout their length, whereas NWs in Te-NW2 are longer (4950 nm) and tapered with a bottom diameter of 220 nm and a top diameter of 160 nm.

Representative single NWs from samples Te-NW1 and Te-NW2 were also characterized by TEM (see [Figures 4.2](#) and [4.3](#)). The TEM analysis revealed that both NWs have predominantly ZB crystal structure with frequent twinning. In Te-NW1 the twinning increases towards the NW tip, where twinning superlattices are witnessed, whereas in Te-NW2, the most frequent twinning is found in the middle section of the NW. The tip region of Te-NW2 shows stacking faults and polytypism which evolve into longer WZ segments followed by a segment with mixed crystal phase and finally short ZB segment right below the droplet. Such microstructure can be explained by a gradual decrease of the droplet contact angle caused by lower As evaporation rate at the lower growth temperature of 620°C [[Panciera et al., 2020](#)]. Thus, based on the NW dimensions and the microstructure, we can conclude that Te-NW2 was grown with a higher As supersaturation than Te-NW1, and we will see in the next sections how the latter influences Te dopant incorporation.

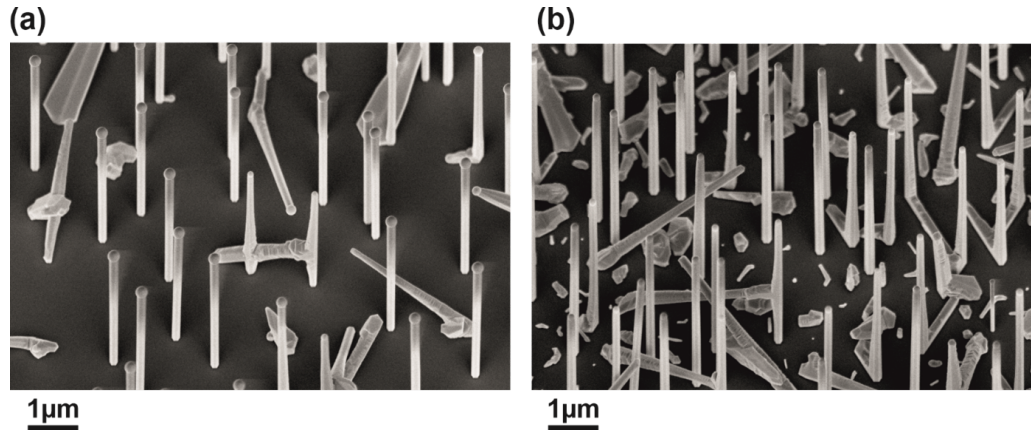


Figure 4.1: Tilted view (30°) SEM images of samples (a) Te-NW1 and (b) Te-NW2.

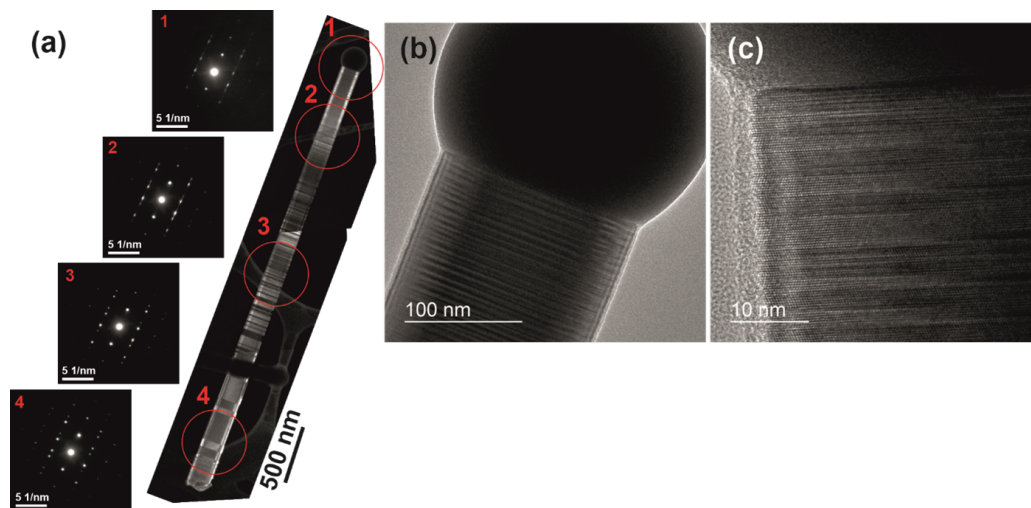


Figure 4.2: TEM images of a single NW from sample Te-NW1. (a) High resolution TEM overview and selected-area diffraction patterns measured from 4 different areas along the NW axis, showing twinned zinc blende crystal structure with frequent twinning. (b) and (c) show high-resolution TEM micrographs from area 1.



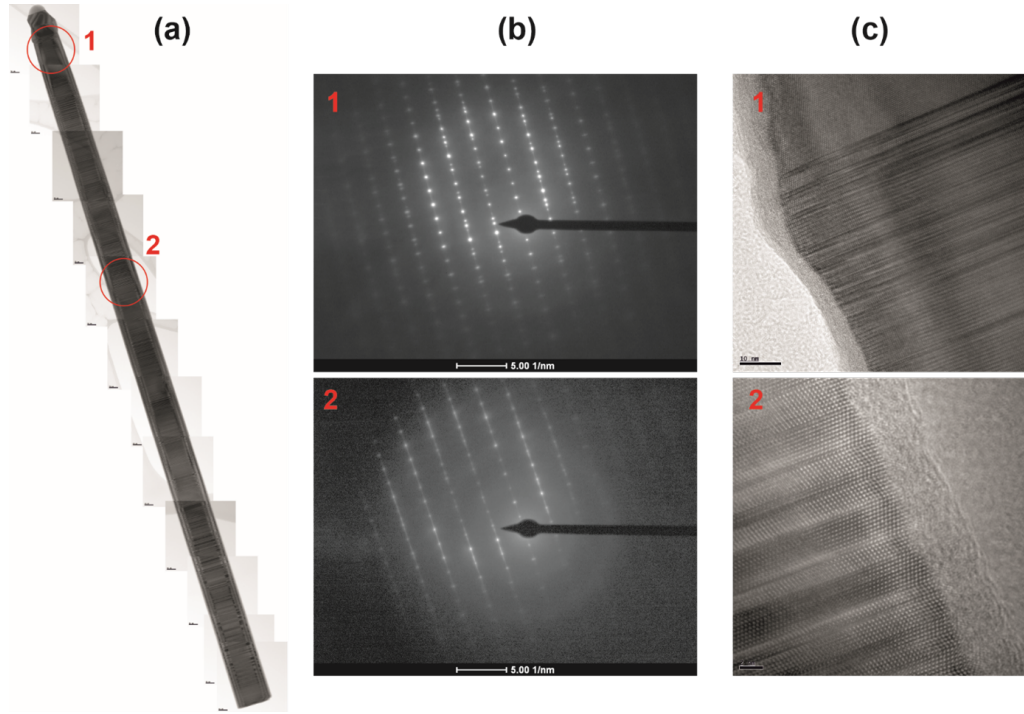


Figure 4.3: TEM data for a single NW from sample Te-NW2. (a) High resolution TEM overview of the NW. (b) Selected-area diffraction patterns from 2 different locations along the NW show polytypism, stacking faults and twinning. (c) High-resolution TEM micrographs from areas 1 and 2.

### Luminescence characterization methods

PL measurements were carried out at Tampere University at RT on all 5 thin film samples. A 532 nm laser was used as an excitation source and the PL signal was detected using a spectrometer and a CCD array.

For cathodoluminescence analysis in an Attolight Chronos cathodoluminescence microscope system located at the C2N, NWs were dispersed on Si substrates. The luminescence was collected by an achromatic reflective objective (numerical aperture of 0.72). The acceleration voltage of the electron beam was set to 6 kV, while the probe current of 2 nA was kept constant within less than  $\pm 5\%$ . As detailed in our previous work [Chen et al., 2021b], in these excitation conditions the CL injection level ( $< 10^{16} \text{ cm}^{-3}$ ) is expected to be more than one order of magnitude lower than the carrier concentrations studied. CASINO simulation showed that 75% and 95% of carriers are generated in a pear-shaped excitation volume within a radius/depth of approximately 30/95 nm and 110/185 nm, respectively. In the CL set-up, the luminescence spectra are dispersed with a diffraction grating (150 grooves/mm) in a Horiba iHR320 spectrometer and recorded with an Andor Newton CCD camera ( $1024 \times 256 \text{ pixel}^2$ , pixel width 26  $\mu\text{m}$ ). The corresponding spectral dispersion is 0.53 nm per pixel, and the image of a NW on the CCD (zero-order, no dispersion) is less than 3 pixels in length (NW length  $< 5 \mu\text{m}$ , magnification: 13), which results in a spectral resolution of about 2 nm. Luminescence spectra were corrected for the diffraction efficiency of the grating and the sensitivity of the CCD camera. The CL intensity spectra plotted hereafter correspond to a spectral density of photon flux per unit of energy ( $\text{counts s}^{-1} \text{ eV}^{-1}$ ) [Chen et al., 2017]. The scale of the panchromatic CL intensity maps correspond to a spectral density of photon flux integrated over all energies ( $\text{counts s}^{-1}$ ). LT spectra were recorded for a sample holder set at 10 K. For GaAs thin film samples, RT and LT CL spectra were averaged over hyperspectral maps ( $64 \times 64 \text{ pixel}^2$ ) measured over a  $31 \times 31 \mu\text{m}^2$  area. For sample Te-NW1, the RT CL hyperspectral map was recorded with an integration time of 500 ms per pixel. To limit the image drift, the exposure time was reduced for Te-NW2 down to 50 ms for the RT CL hyperspectral map, and 25 ms for the LT map. The narrow length distribution witnessed in similarly grown NWs [Koivusalo et al., 2017] strongly suggests that the dopant incorporation is uniform from NW to NW. Nevertheless, for each

NW sample presented in this chapter 3 NWs were measured, and similar results were obtained.

Five Te-doped GaAs thin film samples (Te-TF1 to Te-TF5) with electron concentration between  $5 \times 10^{17}$ – $1 \times 10^{19} \text{ cm}^{-3}$  were grown as reference for the CL measurements and to act as Hall measurement calibration samples. Electron microscopy observations of the two Te-doped GaAs NW samples (Te-NW1 and Te-NW2) grown at  $640^\circ\text{C}$  and  $620^\circ\text{C}$ , respectively, showed morphology and crystal structure differences arising from different Ga droplet supersaturation conditions during growth. The latter's impact on Te dopant incorporation in the NWs will be analyzed in the next sections.

### 4.3 Electron concentration determination in GaAs:Te thin film references

Our group has previously developed a method to quantitatively assess the electron concentration in Si-doped GaAs using cathodoluminescence [Chen et al., 2021b,a]. In the following, we extend this work to Te-doped GaAs thin films with different doping concentrations (growth parameters summarized in Table 4.1). Their luminescence spectra were measured at room and low temperature, and used to confirm the consistency between Te-doped and Si-doped results.

Figure 4.4a shows the RT PL (grey) and CL (black) spectra of the 5 GaAs:Te thin film samples from Table 4.1. Figure 4.4b shows their LT CL spectra (blue). The carrier concentration ( $n_{Hall}$ ) of each sample was determined using Hall effect measurements. The red curves correspond to the fits of the RT CL spectra obtained using the generalized Planck law as described in detail in [Chen et al., 2017] and [Chen et al., 2021b]. The fitted band gap ( $E_g$ ) and electron Fermi level ( $E_{fc}$ ) are indicated on the fits with circles and squares, respectively.

All the RT and LT CL spectra exhibit a distinct peak corresponding to GaAs band-to-band emission. A clear blueshift and broadening of this peak at both RT and LT can be observed with increasing electron concentration, as expected from conduction band filling (Burstein-Moss effect [Burstein, 1954; Moss, 1954]) and indirect recombinations between free electrons and localized holes acting as acceptor-like states [De-Sheng et al., 1982]. Sample Te-TF2 presents a low-energy shoulder on the GaAs emission peak, which is even more pronounced in Te-TF1 and has been previously attributed to donor-acceptor pair luminescence coming from the substrate region [De-Sheng et al., 1982]. Sample Te-TF1 also presents a distinct CL peak around 1.28 eV which has been previously attributed to sub-bandgap states [Chen et al., 2017]. Finally, a good correlation can be observed between the RT CL and PL spectra from Figure 4.4a. The small discrepancies between PL and CL at energies below the bandgap (sample Te-TF1) come from the higher injection level of CL which may partly saturate the defects.

The  $E_{fc}$  values obtained (with the bottom of the conduction band ( $E_C$ ) as zero-energy reference) from the RT CL spectra of samples Te-TF1 and Te-TF2 are plotted in Figure 4.4c and compared to the electron Fermi levels obtained previously from Si-doped GaAs thin film samples (green) [Chen et al., 2021b], as well as to a theoretical model (solid curve) relating the electron Fermi level to the electron concentration [Blakemore, 1982; Lee et al., 1995]. The model assumes a conduction band effective density of states of  $N_C = 4.2 \times 10^{17} \text{ cm}^{-3}$  [De-Sheng et al., 1982; Raymond et al., 1979] and accounts for the non-parabolicity of the conduction band. Like the Si-doped GaAs thin film samples, the data from Te-doped GaAs samples correlate well to the theoretical model. However, the  $E_{fc}$  values from this study are slightly lower than the ones from Si-doped GaAs samples. This could be explained by bandgap shrinkage due to non-negligible electron occupation in CB tail states [De-Sheng et al., 1982], surface depletion in GaAs or reabsorption effect [Chen et al., 2021b]. Since the CB only starts to be filled above a doping concentration of  $5 \times 10^{17} \text{ cm}^{-3}$  in GaAs [Burstein, 1954; Moss, 1954], the electron Fermi level cannot be determined below this doping concentration. Between  $5 \times 10^{17} \text{ cm}^{-3}$  and  $1 \times 10^{18} \text{ cm}^{-3}$ , the  $E_{fc}$  still cannot be accurately determined, which is why Te-TF3, Te-TF4 and Te-TF5 do not appear in Figure 4.4c and their electron Fermi level is indicated as negative in Figure 4.4a. Nevertheless, the results obtained in this study are consistent with previous results from Si-doped GaAs [Chen et al., 2021b] above  $1 \times 10^{18} \text{ cm}^{-3}$ . Figure 4.4d compares the FWHM values extracted from the LT CL spectra of the thin film samples (dark blue) to the relation (green) obtained by [Chen et al., 2021b] from

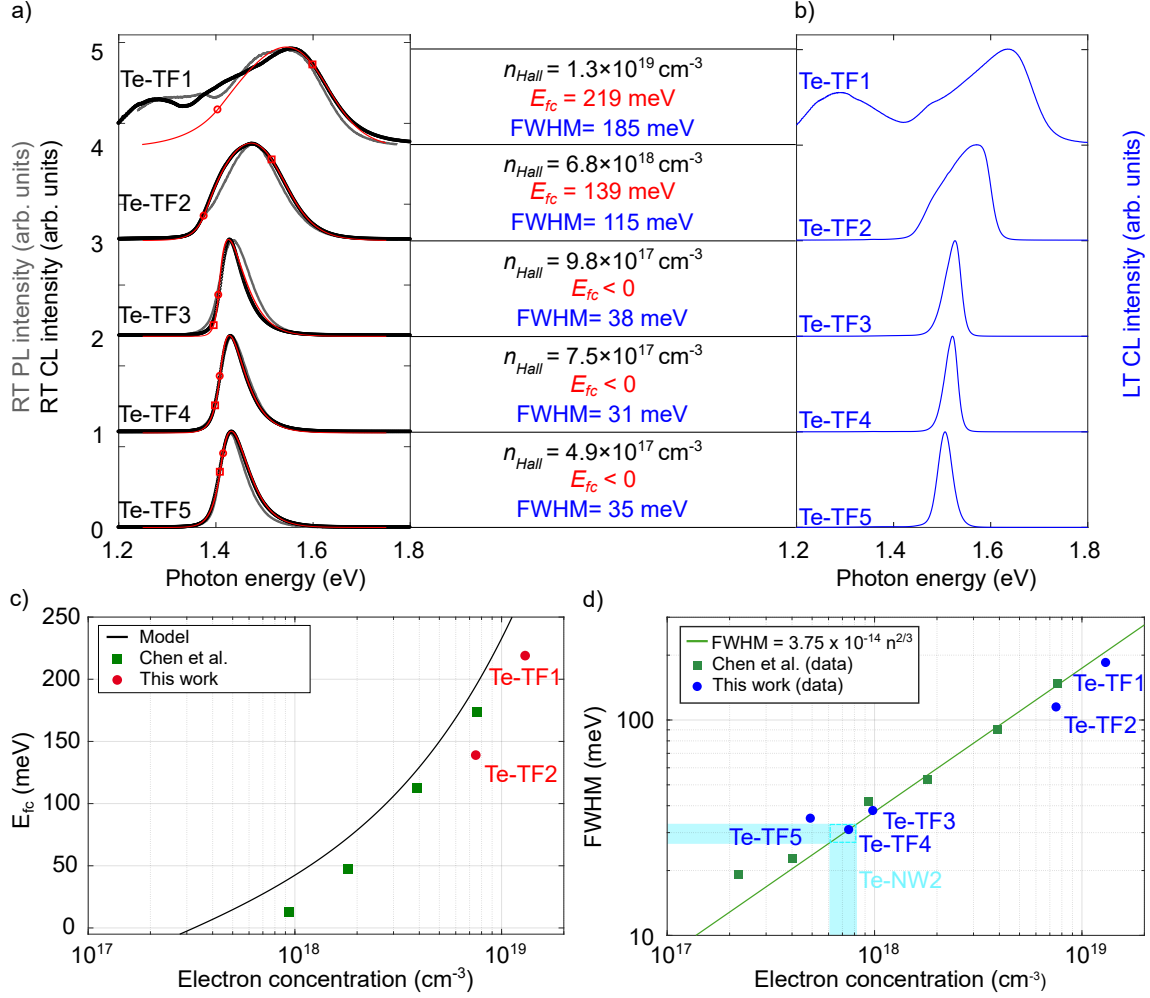


Figure 4.4: (a) Room temperature PL (grey) and CL (black) spectra of GaAs:Te thin films, and the fits of CL spectra (red). Red circles and squares correspond to the fitted bandgaps ( $E_g$ ) and electron Fermi levels ( $E_{fc}$ ), respectively. (b) Low temperature (10 K) CL spectra of the same samples. The Hall doping ( $n_{Hall}$ ),  $E_{fc}$  and FWHM measured at LT are reported. (c) Electron Fermi levels (with  $E_C$  as a zero reference) extracted from RT CL spectra fits (red) are compared to values obtained on Si-doped GaAs thin films [Chen et al., 2021b] (green) and a theoretical model accounting for the non-parabolicity of the conduction band [Blakemore, 1982; Lee et al., 1995; Chen et al., 2021b] (solid curve). (d) FWHM extracted from LT CL spectra of the thin film samples as a function of the electron concentration ( $n_{Hall}$ ). The green solid line is the relation derived by [Chen et al., 2021b] from Si-doped GaAs thin film samples. It is used to determine the electron concentration in Te-NW2 (light blue region). All electron concentrations ( $n_{Hall}$ ) in this figure were determined using Hall effect measurements.

Si-doped GaAs thin film samples, relating the peak FWHM to the electron concentration ( $n$ ) in cm<sup>-3</sup>:

$$FWHM(eV) = 3.75 \times 10^{-14} \times n^{2/3} \quad (4.1)$$

This relation enables the determination of doping concentrations between  $1 \times 10^{17}$  cm<sup>-3</sup> and  $1 \times 10^{19}$  cm<sup>-3</sup>. The LT FWHM values obtained from the Te-doped GaAs thin film samples are in very good agreement with this model.

Table 4.2: Summary of the carrier concentrations of GaAs:Te thin films obtained from CL spectra at RT and LT (10 K), compared to values obtained from Hall effect measurements at RT.

Sample	Carrier concentration CL from $E_{fc}$ (RT) $\text{cm}^{-3}$	Carrier concentration CL from FWHM (LT) $\text{cm}^{-3}$	Carrier concentration Hall effect (RT) $\text{cm}^{-3}$
Te-TF1	$9.1 \times 10^{18}$	$1.1 \times 10^{19}$	$1.3 \times 10^{19}$
Te-TF2	$4.5 \times 10^{18}$	$5.4 \times 10^{18}$	$6.8 \times 10^{18}$
Te-TF3	$< 1 \times 10^{18}$	$1 \times 10^{18}$	$9.8 \times 10^{17}$
Te-TF4	$< 1 \times 10^{18}$	$7.5 \times 10^{17}$	$7.5 \times 10^{17}$
Te-TF5	$< 1 \times 10^{18}$	$8.6 \times 10^{17}$	$4.9 \times 10^{17}$

Overall, both the RT and LT cathodoluminescence-based methods developed in our group for determining carrier concentrations in Si-doped GaAs can also provide an assessment of the electron concentration in Te-doped GaAs, with an accuracy comparable to Hall effect measurements. The results deduced from  $E_{fc}$  and FWHM applied to the reference models are summarized in Table 4.2. The RT and LT methods allow for the determination of electron concentrations above  $1 \times 10^{18} \text{ cm}^{-3}$  and  $4 \times 10^{17} \text{ cm}^{-3}$ , respectively. These methods will be used in the next section to determine the electron concentration in single NWs from samples Te-NW1 and Te-NW2.

## 4.4 Electron concentration mapping in GaAs:Te nanowires

Single NWs from the two NW samples described above were characterized using CL mapping in conditions similar to that of the thin film samples. Due to a small drift attributed to charge effects during the CL measurement of Te-NW1, the hyperspectral images shown in Figure 4.5b-d were drift corrected by 1 pixel (areas 1, 2 and 3 only).

### 4.4.1 NWs grown at 640°C (Te-NW1)

#### Room temperature CL analysis

From the liquid Ga droplet seen on the SEM image of Te-NW1 (Figure 4.5a), the top of the NW can be easily distinguished from the bottom. Figure 4.5b shows the panchromatic CL intensity map of Te-NW1 obtained at RT, from which an axial intensity gradient can be observed. We also note a blueshift and a broadening of the emission peak towards the top of the NW (Figures 4.5c and d), which is a signature of electron concentration gradient. In order to quantify the electron concentration, CL spectra were averaged over each of the 9 areas shown in Figure 4.5b ( $5 \times 6 \text{ pixel}^2$  each, or  $0.46 \times 0.55 \text{ }\mu\text{m}^2$ ) and plotted in Figure 4.5e. The CL spectra are dominated by band-to-band recombination around 1.43 eV, although sub-bandgap emission is also observed and can be attributed to shallow defects. The main emission peak blueshifts and broadens from the bottom to the top of the NW (areas 1 to 9). It is fitted using the generalized Planck law and an absorption model using the method previously described for the thin film samples and detailed in [Chen et al., 2017] and [Chen et al., 2021b]. The fitted electron Fermi levels (squares in Figure 4.5e) enabled the determination of electron concentrations ranging from  $1.6 \times 10^{18} \text{ cm}^{-3}$  (area 4) to  $3.3 \times 10^{18} \text{ cm}^{-3}$  (area 9), see Figure 4.5f. As previously explained, the RT method only allows the determination of electron concentrations above  $1 \times 10^{18} \text{ cm}^{-3}$ , preventing the quantification of the electron concentration in areas 1, 2 and 3.

#### Low temperature CL analysis

At LT, although defect bands dominate the CL spectra, the same blueshift of the GaAs CL emission peak can be observed from areas 1 to 9 (Figure 4.6c and e). The variations in FWHM are of the same order of magnitude as the RT FWHM values (Figure 4.6d), from 104 meV to 135 meV, and they further confirm the gradient of electron concentration along the NW axis. However, as the low-energy (defect) emission screens the GaAs band-to-band emission peak (Figure 4.6e), the

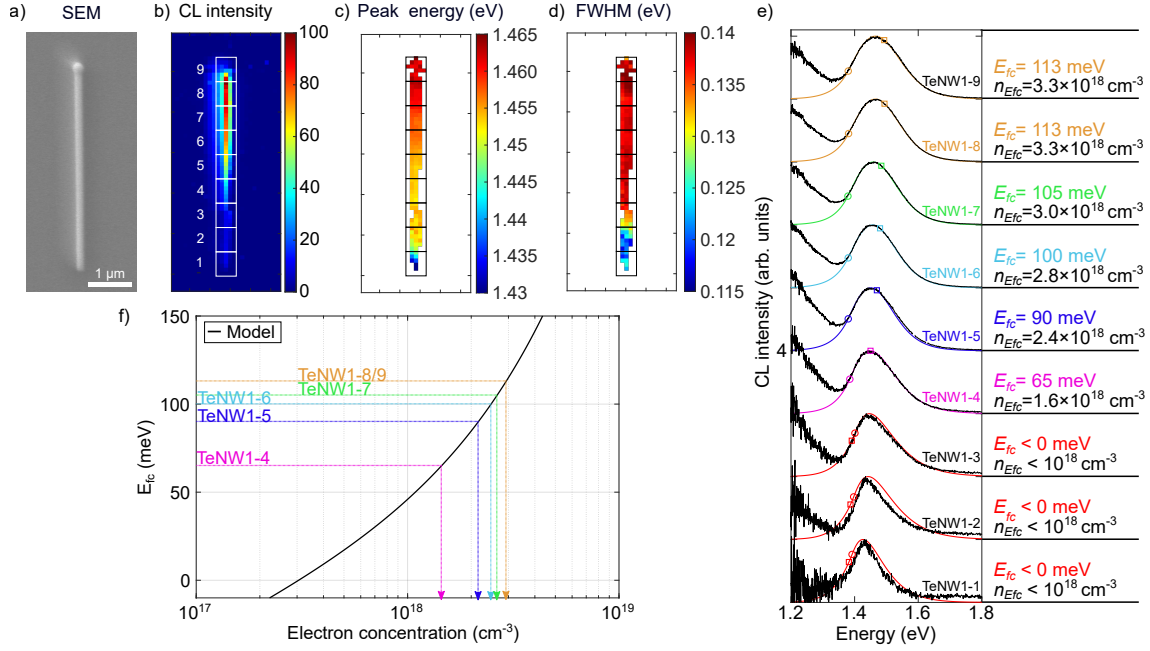


Figure 4.5: A single NW from sample Te-NW1 studied by RT cathodoluminescence. (a) SEM image, (b) RT panchromatic CL intensity map ( $27 \times 64$  pixel<sup>2</sup>). Corresponding (c) CL peak energy and (d) FWHM maps. (e) CL spectra averaged over the 9 different areas ( $5 \times 6$  pixel<sup>2</sup> each) shown in (b), and their respective fits with a generalized Planck law (colored curves). Circles and squares correspond to the fitted bandgaps and electron Fermi levels ( $E_{fc}$ ), respectively.  $E_{fc}$  values are also reported next to the CL spectra, along with the corresponding electron concentrations ( $n_{Efc}$ ) determined using the non-parabolic band model, as shown in (f).

LT CL results could not be used to corroborate the previously determined electron concentrations, or estimate the ones missing in areas 1, 2, and 3 of Te-NW1.

An axial electron concentration gradient ranging from below  $1 \times 10^{18} \text{ cm}^{-3}$  to  $3.3 \times 10^{18} \text{ cm}^{-3}$  was determined in Te-NW1 using RT CL results with a spatial resolution of 500 nm, corresponding to the height of each of the 9 rectangular areas chosen along the NW axis.

#### 4.4.2 NWs grown at 620°C (Te-NW2)

Sample Te-NW2 was grown at a temperature 20°C lower than Te-NW1, and as discussed in [subsection 4.2.2](#), higher As supersaturation in the Ga droplet resulted in longer and more tapered NWs.

##### Room temperature CL analysis

[Figure 4.7a](#) shows the SEM image of a single NW from Te-NW2, while [Figures 4.7b](#) and [c](#) present the RT and LT panchromatic CL intensity maps of this NW, respectively. At both RT and LT, the CL intensity is highest in areas 2 and 4, and lowest in areas 1 and 3, although the contrast between the different areas is more visible at LT. As seen from the TEM data in [Figure 4.3](#), Te-NW2 contains many defects arising from polytypism, stacking faults and twinning, which could act as non-radiative carrier recombination centres. The CL intensity variations may be the result of such bulk defects, but also depend on changes in the diffusion length and surface recombination. The CL maps suggest a higher density of such defects in areas 1 and 3. A slightly higher sub-bandgap emission is also observed in areas 1-3 ([Figure 4.7h](#)). The overall stronger CL intensity obtained from Te-NW2 compared to Te-NW1 can be understood by their different microstructures and dimensions. In order to quantify the carrier concentration in Te-NW2, an average RT CL spectrum was extracted from each of the 5 areas shown in [Figure 4.3b](#) ( $2 \times 8-9$  pixel<sup>2</sup> each, or



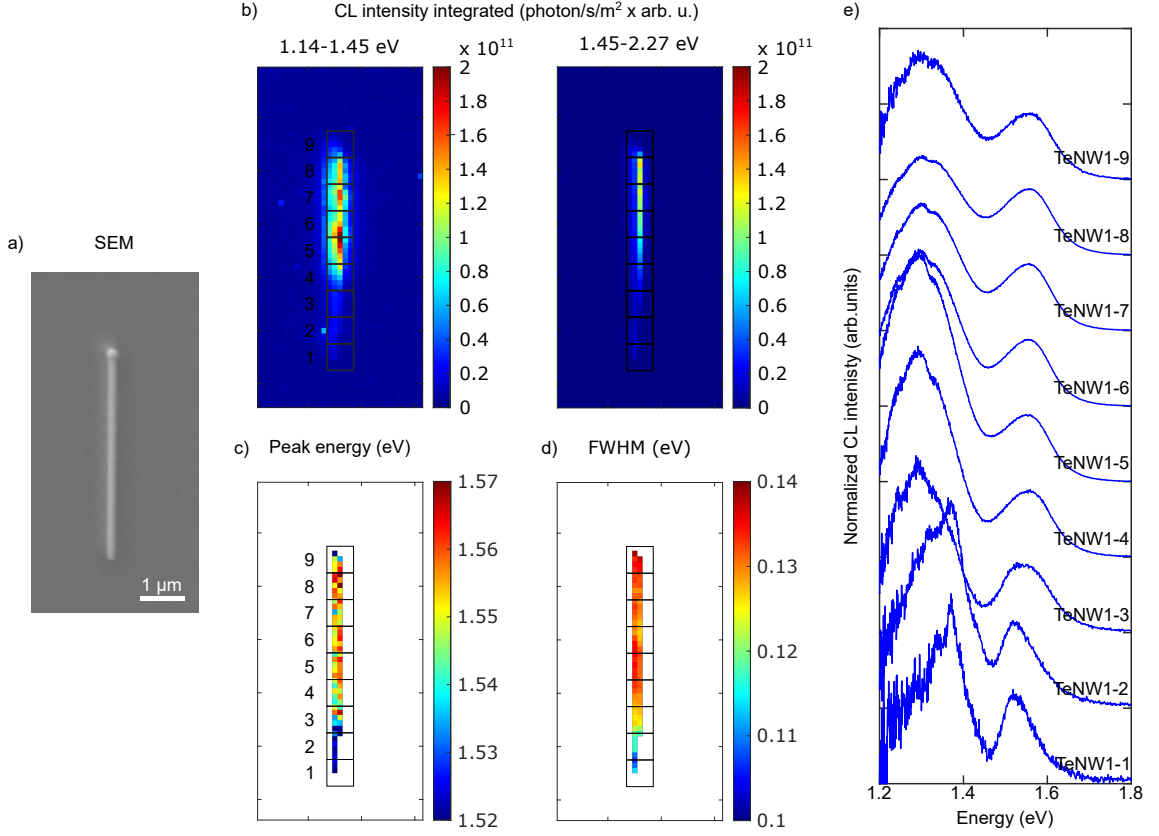


Figure 4.6: (a) SEM image of the NW from Figure 4.5 (Te-NW1) and its corresponding maps measured at LT: (b) panchromatic CL intensity, (c) CL peak energy and (d) FWHM ( $31 \times 64$  pixel<sup>2</sup>). The 9 areas indicated ( $5 \times 6$  pixel<sup>2</sup> each) correspond to the areas over which the CL spectra in (e) are averaged.

$0.28 \times 1 \mu\text{m}^2$ ). These 5 RT CL spectra were then normalized by their maximum and plotted in Figure 4.7h (black curves). The similarities in CL peak energy and FWHM for all averaged RT CL spectra (corresponding CL maps in Figures 4.7d and f) imply a relatively homogeneous axial electron concentration. This electron concentration could however not be quantified using the generalized Planck law method because the CL spectra could not be fitted accurately (red curve in Figure 4.7h,  $E_{fc} < 0$ ), suggesting an electron concentration below  $1 \times 10^{18} \text{ cm}^{-3}$ .

#### Low temperature CL analysis

The LT method based on the FWHM was then used to quantitatively determine the electron concentration in each of the 5 areas of Te-NW2 ( $3 \times 8$ - $9$  pixel<sup>2</sup> each, or  $0.41 \times 1 \mu\text{m}^2$ ). The FWHM values were extracted from each average LT CL spectra in Figure 4.7h (blue) and related to the electron concentrations according to Equation (4.1), as shown in Figure 4.4d (light blue region). The LT CL analysis confirms the homogeneous electron concentration along the NW axis with values between  $6.2 \times 10^{17} \text{ cm}^{-3}$  and  $8.2 \times 10^{17} \text{ cm}^{-3}$ .

Relatively homogeneous electron concentration values ( $6.2 \times 10^{17}$ – $8.2 \times 10^{17} \text{ cm}^{-3}$ ) were obtained along the axis of Te-NW2 from low temperature CL measurements, suggesting different Te incorporation efficiencies in samples Te-NW1 and Te-NW2. The reasons behind these discrepancies will be further discussed in the next section.

#### 4.4.3 Comparison

Figure 4.8 compares the electron concentrations determined in the two NW samples described above. The dotted lines serve as a guide to the eye to emphasize the inhomogeneous electron



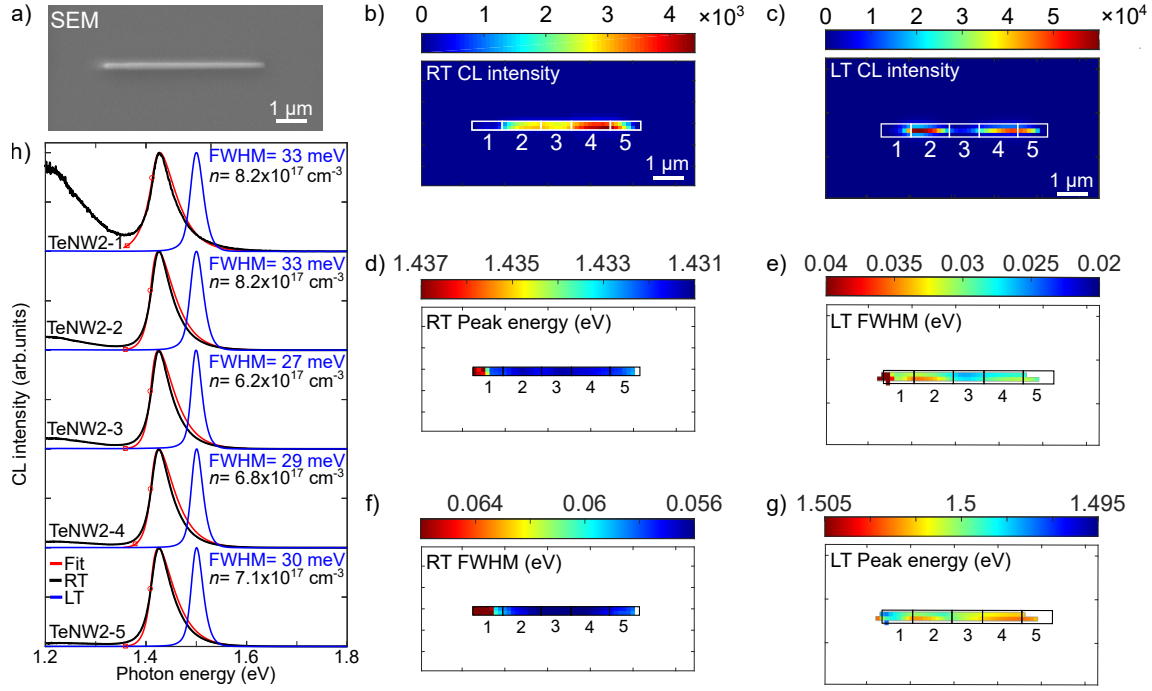


Figure 4.7: A single NW from sample Te-NW2 studied by RT and LT cathodoluminescence. (a) SEM image, (b) RT and (c) LT panchromatic CL intensity maps ( $26 \times 64 \text{ pixel}^2$  and  $31 \times 64 \text{ pixel}^2$  respectively for the intensity maps). Corresponding (d) RT and (e) LT FWHM maps, as well as (f) RT and (g) LT CL peak energy maps. The 5 areas indicated ( $2\text{-}3 \times 8\text{-}9 \text{ pixel}^2$ ) correspond to the areas over which the RT and LT CL spectra from (h) are averaged (black and blue, respectively). Red lines correspond to the fits of the RT CL spectra with the generalized Planck law, circles and squares indicate the fitted bandgaps ( $E_g = 1.41 \text{ eV}$ ) and electron Fermi levels ( $E_{fc} < 0$ ), respectively. The electron concentrations ( $n$ ) next to the spectra were obtained from the LT FWHM values indicated in blue, using the empirical model illustrated in Figure 4.4d.

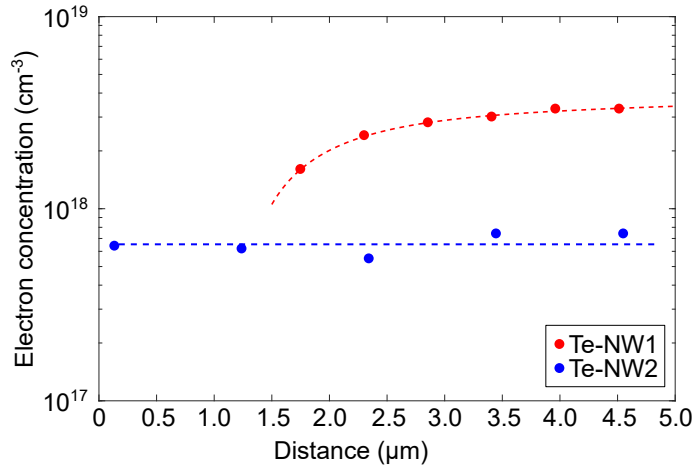


Figure 4.8: Spatial dependence of the electron concentration along the axis of the NW grown at  $640^\circ\text{C}$  (Te-NW1, red) and at  $620^\circ\text{C}$  (Te-NW2, blue). The bottom of the NW is at  $0 \mu\text{m}$ . The dotted lines serve as guides to the eye.

concentration in Te-NW1 as opposed to the homogeneous electron concentration in Te-NW2.

Generally, both Te-NW1 and Te-NW2 show around an order of magnitude lower electron concentration than the nominal dopant concentration calibrated by thin film growths. This is consistent with earlier reports on Te-incorporation in NW growth [Hakkarainen et al., 2019; Dubrovskii et al., 2020]. The electron concentration gradient obtained for Te-NW1 is in good agreement with

previous Raman spectroscopy results collected from the same sample [Hakkarainen et al., 2019], which indicated a carrier concentration of  $1.2 \times 10^{18} \text{ cm}^{-3}$  at the bottom and of  $4.1 \times 10^{18} \text{ cm}^{-3}$  at the top of the NW. In contrast, Te-NW2 exhibits lower maximum doping than Te-NW1, with no carrier concentration gradient observed. The reasons for these discrepancies are explained in the next paragraph.

As shown by [Hakkarainen et al., 2019], the primary incorporation mechanism of Te into self-catalyzed GaAs NWs at a growth temperature of  $640^\circ\text{C}$  is the VLS mechanism through the Ga droplet, as the Te incorporation via radial VS growth is inefficient at these elevated temperatures due to the high vapor pressure of Te [Collins et al., 1982]. The primary VLS incorporation of Te via the droplet actually leads to both axial and radial dopant gradients as follows: during NW growth, the droplet increases continuously in size, forming an inversely tapered NW core which has grown in VLS mode and thus has higher doping. Simultaneously, VS growth on the NW sidewalls compensates the inverse tapering, forming untapered NWs with a shell exhibiting lower doping (see schematics in Figure 2.1). Hence, at the bottom of Te-NW1, only a thin core of the NW is doped via the VLS mechanism, whereas the tip of Te-NW1 has grown fully via VLS growth. Te diffusion inside the NW mainly affects the radial gradients because of the high aspect ratio of the investigated NWs. Te-NW2 was grown at a lower temperature of  $620^\circ\text{C}$  and thus an increase of VS incorporation efficiency via the sidewalls is expected. On the other hand, Te incorporation by the VLS process is reduced by differences in the kinetics and shape of the droplet. In fact, Te-NW2 NWs have a smaller droplet contact angle and were grown with a larger axial growth rate. Both of these features show that the droplets have exhibited higher As supersaturation during the NW growth. Since Te incorporates to As lattice sites [Schubert, 1993], it is expected that the higher As supersaturation in the liquid phase weakens the Te incorporation via droplet. Simultaneously, the smaller effective droplet area for Te atom impingement in Te-NW2 reduces the collection rate of Te atoms from vapor phase to liquid phase when compared to Te-NW1. Therefore, the differences in the electron concentration levels and gradients between Te-NW1 and Te-NW2 can be explained by different Te incorporation efficiencies by VLS and VS processes.

## 4.5 Chapter conclusions

Cathodoluminescence was used to determine the electron concentration in Te-doped GaAs thin films and NWs. Measurements were first carried out on five GaAs:Te thin film references with electron concentrations between  $5 \times 10^{17} \text{ cm}^{-3}$  and  $1 \times 10^{19} \text{ cm}^{-3}$ . The correlation between CL spectrum and carrier concentration for GaAs:Te thin films was found to be consistent with previous work on GaAs:Si samples. This allowed the extension of the carrier concentration assessment method previously developed in our group for Si-doped GaAs at both room temperature and low temperature [Chen et al., 2017, 2021b,a] to Te-doped GaAs. Mapping of the electron concentration in single NWs from two GaAs:Te NW samples was then carried out. Both Te-NW1 (grown at  $640^\circ\text{C}$ ) and Te-NW2 (grown at  $620^\circ\text{C}$ ) showed an order of magnitude lower electron concentration than the nominal dopant concentration calibrated by thin film growths, in accordance with previous studies. An electron concentration gradient ranging from below  $1 \times 10^{18} \text{ cm}^{-3}$  to  $3.3 \times 10^{18} \text{ cm}^{-3}$  along the NW axis was determined for Te-NW1. In contrast, a homogeneous electron concentration of around  $6 - 8 \times 10^{17} \text{ cm}^{-3}$  was observed along the NW axis of Te-NW2, highlighting the possibility of obtaining homogeneous dopant distributions in Te-doped GaAs NWs. The differences in the electron concentration levels and gradients between Te-NW1 and Te-NW2 can be explained by different Te incorporation efficiencies via vapor-solid and vapor-liquid-solid processes.

Overall, this study evidences that cathodoluminescence with nanoscale spatial resolution is a powerful technique to characterize the actual carrier concentration of single GaAs:Te NWs, which can then be correlated to growth parameters (here the growth temperature). The control of the latter could then allow homogeneous dopant distributions and high carrier densities to be obtained in Te-doped GaAs NWs, overcoming the limitations of the commonly used Si dopant. It would be interesting in future experiments to study the incorporation efficiency of Te atoms in GaInP NW shells, in order to investigate whether the performance of the NW solar cell presented in Chapter 3 could be enhanced by replacing the

Si dopant with Te. In general, such improvement in the assessment and control of impurity doping, and hence properties in NWs, will undoubtedly help pave the way to the design of next-generation electronic devices.



## Chapter 5

# New Generation of Nanowire Solar Cells: GaAs/GaAsP Axial Heterojunctions

### Chapter Contents

<b>5.1 Axial vs. radial NW junctions</b>	<b>84</b>
5.1.1 Light absorption	84
5.1.2 Charge carrier separation and collection	84
5.1.3 Passivation	85
5.1.4 Evaluation of axial and radial junction NW solar cell performances	85
<b>5.2 Investigating the optoelectronic properties of GaAs/GaAsP axial junction NWs</b>	<b>86</b>
5.2.1 Growth recipe of the GaAs/GaAsP axial junction NWs	86
5.2.2 Growth recipe of the reference samples	87
5.2.3 Surface passivation assessment using luminescence	87
Photoluminescence	88
Cathodoluminescence	89
<b>5.3 Axial junction NW solar cell fabrication process</b>	<b>92</b>
5.3.1 <i>Ex-situ</i> removal of the Ga droplets	92
5.3.2 An organic/inorganic hybrid material for NW planarization	93
5.3.3 Improving the NW/ITO contact	94
<b>5.4 Performances of our first axial junction NW solar cells</b>	<b>96</b>
5.4.1 Current-voltage (J-V) characteristics	96
5.4.2 External quantum efficiency (EQE) response	97
EQE under bias	98
5.4.3 Modeling electron transport at the n-type contact	99
Simulated band diagrams	99
Simulated J-V curves and EQE responses	100
<b>5.5 Chapter conclusions</b>	<b>103</b>

The advantages and disadvantages of axial vs. radial NW junction geometries will first be discussed in this chapter to expose the still on-going debate in the community. Then, preliminary results on the optoelectronic characteristics of self-catalyzed GaAs/GaAsP axial-junction NWs, in which the catalyst droplet has not been consumed *in-situ*, will be presented. Finally, optimizations carried out on the axial junction NW solar cell fabrication process will be detailed, before showing the performances of the very first axial junction NW solar cells fabricated in our group.

## 5.1 Axial vs. radial NW junctions

NW p-n junctions can be formed in both the axial and radial direction, as illustrated in Figure 5.1. It is also common to see p-i-n NW junction designs, in which an intrinsic semiconductor region is inserted to reduce the extension of the depleted zone in the p- and n-regions [Colombo et al., 2009; Krogstrup et al., 2013; Yao et al., 2014, 2015; Nowzari et al., 2015; de Lépinau, 2020; Saket et al., 2020a]. Both axial and radial junction geometries have their own advantages and limitations for NW solar cell applications, which will be discussed in this section.

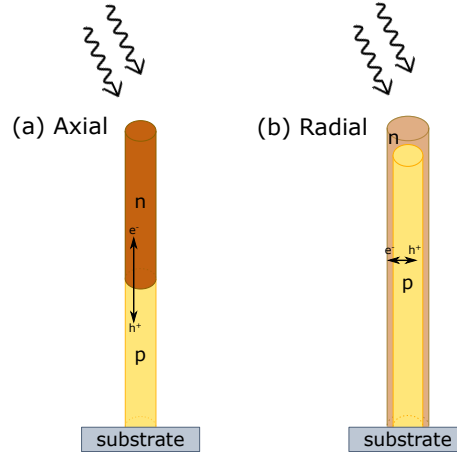


Figure 5.1: Schematic representation of a nanowire with (a) axial, and (b) radial p-n junction geometry. The wiggly arrows represent incoming photons while the double arrows indicate the charge separation axis in the NW.

### 5.1.1 Light absorption

Both radial and axial NW junctions can be tailored to benefit from resonant light absorption. In the case of homojunctions, light absorption in both junction geometries is comparable. In the case of heterojunctions however, optical absorption in the different materials need to be simultaneously optimized particularly in the radial configuration. In fact, the presence of a NW shell can significantly change the NW core absorption, due to mismatch in the materials' refractive indices and absorption coefficients, or to a combination of electric field confinement and passivation effects [Huang and Povinelli, 2014; Wu et al., 2016; Raj et al., 2019].

### 5.1.2 Charge carrier separation and collection

The main advantage of the radial NW junction geometry is the decoupling of the directions of light absorption and charge carrier separation, as indicated in Figure 5.1. In fact, since the NW diameter is typically much smaller than the minority carrier diffusion length, nearly all photogenerated carriers can be separated and effectively collected in a radial junction NW solar cell. In an axial junction NW solar cell however, like in a planar cell design, the junction position and depth are extremely important [Wallentin et al., 2013; Otnes et al., 2018; Gao et al., 2019]. In fact, while a certain NW length is required to absorb a sufficient amount of light, the top (emitter) and bottom (base) segments of the axial junction geometry must at the same time be kept thin enough to allow minority carrier diffusion to the junction before recombination. In other words, the axial NW junction geometry is more vulnerable to bulk defects than the radial junction geometry. From a device fabrication perspective, radial NW junctions also render the top contact fabrication easier, as the conducting material can be deposited conformally on the NW array without risking to shunt the device like it could happen in axial NW junctions if the contact is not formed solely at the top of the NWs.

While the radial NW junction geometry is more tolerant to bulk defects and facilitate top contact formation, it is however much more sensitive to doping levels. The latter need to be high in radial NW junction geometries in order to avoid fully depleted junctions, with drastic



consequences on the  $V_{OC}$ , majority carrier conduction, and contact formation [Chen, 2018]. As previously mentioned in Section 4.1, it is still very challenging to obtain homogeneously high n-type doping levels in NWs, preventing the advantages of the radial architecture in terms of charge carrier collection to be fully exploited. Furthermore, while the axial NW junction geometry reduces the lattice matching requirements for the growth of heterostructures, in the case of NW junctions formed in the radial direction lattice matching requirements become once again limiting above a certain shell thickness [Raychaudhuri and Yu, 2006; Aifantis et al., 2007; Haapamaki et al., 2012; Salehzadeh et al., 2013].

### 5.1.3 Passivation

Due to high surface-to-volume ratio in NWs, surface states are a major concern for device performances. While both axial and radial NW junctions experience a reduction of  $J_{SC}$  and  $V_{OC}$  in the presence of surface recombinations, the former is found to be more susceptible to high surface recombination rates [Huang et al., 2012; Yu et al., 2012]. With the same doping density and surface recombination velocity, the higher surface recombination rate in axial junctions is caused by higher surface minority carrier concentration resulting from the p-n junction being further away from the NW surface. Although radial NW junctions are less susceptible to the effects of surface recombination, surface passivation and p-n junction location are important factors in the design of NW solar cells based on both axial and radial junction geometries.

Several wide bandgap NW shells composed of AlGaAs [Titova et al., 2006; Perera et al., 2008; Tomioka et al., 2009; Parkinson et al., 2009; Zhou et al., 2009; Chang et al., 2012; Jiang et al., 2013; Vettori et al., 2019], GaInP [Sköld et al., 2005; Lin et al., 2012; Darbandi and Watkins, 2016], AlInP [Chia et al., 2012, 2013], GaAsP [Couto et al., 2012] or GaP [Darbandi et al., 2014; Haggren et al., 2014], have been shown to significantly improve the optical and electrical properties of GaAs NWs. However, the VS growth of a radial passivation shell around self-catalyzed GaAs NWs can only be carried out after Ga droplet consumption, which is known to induce crystal phase mixing and defects formation [Kim et al., 2012; Dastjerdi et al., 2016; Jacobsson et al., 2016]. Defects in the NW cores were found to degrade the shell morphology and crystal quality [Wallentin et al., 2011; Gorji Ghalestani et al., 2012; Haas et al., 2013; Zhang et al., 2017], limiting the final device performance. Furthermore, axial growth cannot be fully suppressed during radial shell growth, often resulting in a thicker layer at the top of the NWs that can lead to parasitic absorptions. In our GaAs/GaInP core-shell NWs presented in Chapter 3, a 6 times thicker GaInP layer was observed at the top of the NWs compared to the sidewalls, leading to a  $J_{SC}$  loss of  $2.84 \text{ mA cm}^{-2}$  as estimated from optical simulations (subsection 3.2.3).

To avoid crystal phase mixing and facilitate predominant radial growth, self-catalyzed NWs can be either taken out of the growth chamber to remove the catalyst droplet between core and shell growth [Heurlin et al., 2014], or passivated *ex-situ* [Mariani et al., 2011; Lin et al., 2012; Tajik et al., 2012; Gutsche et al., 2012; Alekseev et al., 2015]. However, removal of the NWs from the growth chamber exposes their surface to oxidation, deteriorating the interface properties. Hence, self-catalyzed NW passivation should ideally take place in the growth chamber, but without the need for catalyst droplet consumption. To the best of our knowledge, such a passivation scheme has not yet been explored in the literature, but could be achieved by precise control of the formation of the unintended radial shell during axial VLS NW growth (see schematics in Figure 2.1), as will be discussed in Section 5.2.

### 5.1.4 Evaluation of axial and radial junction NW solar cell performances

Performances of state-of-the-art III-V NW array solar cells are summarized in Table 1.1. While radial GaAs-based NW devices can achieve  $J_{SC}$  values comparable to those of the best axial ones, their  $V_{OC}$  and FF are still lingering behind, resulting in power conversion efficiencies that are almost 50% lower for radial junction NW solar cells. Hence, any advantage of the radial junction geometry has so far been overshadowed by other dominating factors, probably related to shell growth and insufficient doping levels, but which are not yet fully identified [Otnes and Borgström, 2017].

Despite advantages regarding charge carrier collection, surface recombinations and top contact fabrication in radial NW junctions, best performing NW array solar cells are so far still based on axial junction geometries. While the work presented in [Chapter 3](#) contributes to the understanding of the limitations in radial junction NW solar cells, the preliminary results that will be presented in this chapter aim at further improving the performances of axial junction solar cells by avoiding *in-situ* catalyst droplet consumption (and hence crystal phase mixing), and improving the solar cell fabrication process.

## 5.2 Investigating the optoelectronic properties of GaAs/GaAsP axial junction NWs

In VLS-grown NWs, an unintentional shell can form around the base part due to concurrent parasitic lateral growth by the VS mechanism (see schematics in [Figure 2.1](#)) [[Oehler et al., 2018](#); [Hakkarainen et al., 2019](#); [Saket et al., 2020a](#)]. In this section, we will use room temperature PL and CL to investigate whether a wide bandgap parasitic shell formed during VLS growth is enough to effectively passivate GaAs NWs in a GaAs/GaAsP axial junction configuration. Note that the aforementioned NW shell has not yet been characterized in any way, but its thickness is expected to be around 5 nm at the base of the NWs according to a previous study from our group [[Oehler et al., 2018](#)]. In this section, the luminescence of two NW samples with GaAs/GaAsP (sample D146) and GaAs/GaAsP/GaP (sample D137) axial junctions will be respectively characterized, and compared to reference samples, namely an unpassivated GaAs NW sample (sample D135), and one passivated by a intrinsic GaInP shell grown by the VS mechanism after catalyst droplet consumption (sample 76851).

### 5.2.1 Growth recipe of the GaAs/GaAsP axial junction NWs

Two 2-inch p-Si(111) substrates patterned and prepared according to the method described in [subsection 2.2.1](#) were used for the growths of samples D146 and D137. A standard N<sub>2</sub> drying was carried out on the substrates after the final HF dip because the samples presented here were grown before the Marangoni drying experiments detailed in [subsection 2.2.1](#) were carried out. Prior to growth, a 20 min *in-situ* high-temperature annealing was performed at 750°C. Then, the substrate temperature was brought down to the desired growth temperature of 600°C.

The self-catalyzed growth of GaAs NWs was initiated by a 2 min Ga pre-deposition step, in which a Ga flux corresponding to a two-dimensional GaAs equivalent growth rate of 0.71 ML/s (2 Å/s), was used to localize the Ga droplets in the holes of the patterned substrate. A Be flux corresponding to a hole concentration in planar GaAs of  $6 \times 10^{18} \text{ cm}^{-3}$  was also introduced for p-type doping. After Ga pre-deposition, the phosphorous valve was opened to begin the growth of a Be-doped GaP segment at a P<sub>2</sub>/Ga effective atomic flux ratio of 1.2. After 20 s of Be-doped GaP growth, the P valve is closed linearly while opening the one of As over the course of 30 s, resulting in a linearly graded GaP/GaAs transition which contributes to flatten the valence band offset between GaP and GaAs. GaAs NWs were then grown under an As<sub>4</sub>/Ga flux ratio of 1.2, and the same Be flux during 11 min (p-GaAs), before the 1 min growth of an intrinsic GaAs (i-GaAs) segment under no Be flux. The As valve was then closed linearly while opening the P valve under a Si flux corresponding to an electron concentration in planar GaAs of  $2 \times 10^{19} \text{ cm}^{-3}$ , over the course of 2 min and 3 min for samples D137 and D146, respectively, at a temperature decreasing from 600°C to 460°C and 490°C, respectively. The substrate temperature was lowered during the growth of the Si-doped GaAsP segments in an attempt to favor radial growth via the VS mechanism and limit potential compensation [[Dimakis et al., 2012](#)]. Although Si was reported to produce p-type doping in VLS-grown GaAs NWs, [[Saket et al., 2020b](#)] demonstrated that it can induce n-type conductivity in GaAs<sub>0.7</sub>P<sub>0.3</sub> NWs grown in conditions similar to ours. However, we did not assess the exact carrier concentration in our GaAsP NW segments. After the linearly graded GaAsP growth, a Si-doped GaP segment was grown for sample D137, at an effective V/III flux ratio of 1.2 and a constant growth temperature of 480°C. We assume that Si also acts as a donor in the GaP segment because it is routinely used as an n-type dopant in planar GaP layers [[Wang et al., 1996](#); [Feifel et al., 2016](#)]. However, no studies on Si-doped GaP NWs were found to confirm our hypothesis and we did not investigate this further.

### 5.2.2 Growth recipe of the reference samples

Sample D135 was grown in similar conditions to samples D146 and D137 in terms of growth rate and flux ratios, with also the same Ga pre-deposition step and GaP stem. However, the growth was terminated after a self-catalyzed Be-doped GaAs NW growth of 12 min.

Unlike the previous three samples, sample 76851 was grown in the Riber32 MBE set-up in 2017, at a growth temperature of 610°C, with a Ga pre-deposition step duration of 1 min and a 30 s GaP stem. The NWs consist of an i-GaAs core grown by VLS for 20 min, and i-GaAs and i-GaInP shells grown by VS for 20 min and 40 min, respectively, at growth temperatures of 580°C (i-GaAs) and 450°C (i-GaInP). Before growing the NW shells, the Ga droplet was consumed during 40 min under an As flux 16 times higher than the one used for GaAs NW growth.

SEM images of the as-grown NW arrays can be found in Figure 5.2. The former are from large-area patterns (spot patterns) with pitches of 360 nm (D146), 350 nm (D137), 350 nm (D135), and 500 nm (76851), respectively. The measured NW dimensions and vertical yields are summarized in Table 5.1. From high-magnification SEM images not shown here, the GaAsP segment in sample D146 is estimated to have a length of  $124 \pm 14$  nm. Schematics of the NW design in samples 76851, D137 and D146 can be found in Figure 5.4.

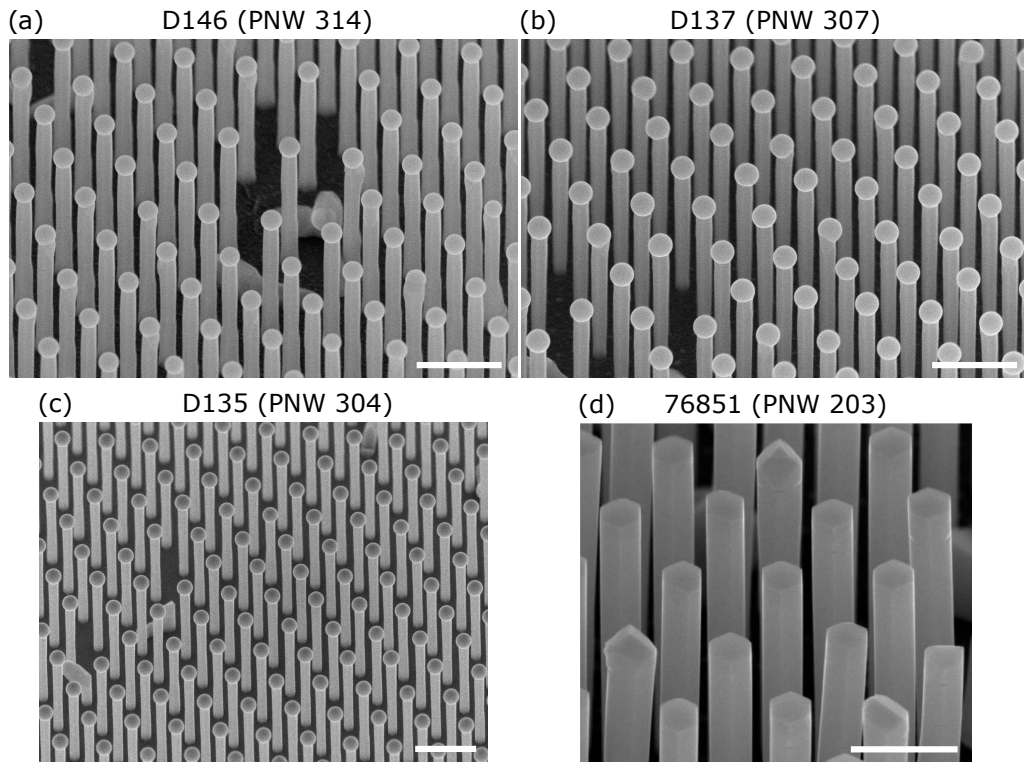


Figure 5.2: Tilted SEM images (45°) of as-grown NW arrays from large-area patterns of samples (a) D146, (b) D137, (c) D135, (d) 76851, with pitches of 350 nm, 360 nm, 350 nm, and 500 nm, respectively. Scale bar = 500 nm.

In the next section, we will use PL and CL measurements to evaluate the optoelectronic properties of the different NW samples, and try to correlate them to the NWs' surface passivation conditions.

### 5.2.3 Surface passivation assessment using luminescence

Optical methods based on luminescence have been widely used to assess the effect of different passivation strategies [Otnes and Borgström, 2017]. Here, photoluminescence and cathodoluminescence will be used to investigate the optoelectronic properties of axial-junction NW arrays and single NWs, respectively.

Table 5.1: Growth details of samples D146, D137, D135 and 76851, on which the passivation study is carried out.

Sample name	Growth mechanism	p-GaAs growth time (min)	i-GaAs growth time (min)	Passivation	Pitch (nm)	NW length (nm)	NW diameter (nm)	Yield (%)
D146	VLS	11	1	3min graded GaAsP:Si	360	726±16	91±2	92
D137	VLS	11	1	2min graded GaAsP:Si + 1min GaP:Si	350	778±7	94±4	94
D135	VLS	12	/	/	350	612±8	82±6	98
76851	VLS + VS	/	20 (VLS) + 20 (VS)	40min i-GaInP (VS)	500	1557±43	195±14	90

### Photoluminescence

NW arrays from samples D146, D137 and D135 were excited using a continuous wave laser with 532 nm wavelength,  $\sim 500$  nm spot size, and 1.7  $\mu$ W excitation power. For each sample, two measurements were carried out on different areas to monitor the sample homogeneity. The PL spectra obtained are plotted in Figure 5.3.

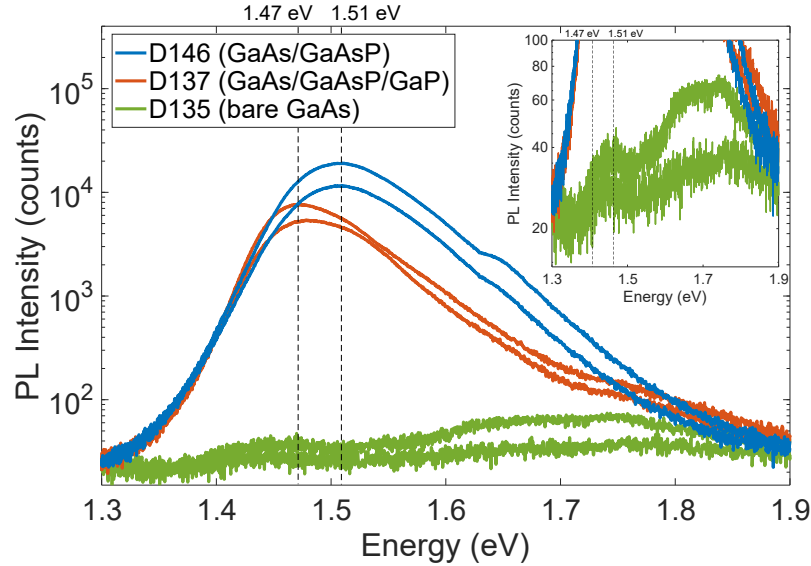


Figure 5.3: Semi-logarithmic plot of the PL spectra obtained from two different areas of samples D146 (blue), D137 (orange) and D135 (green), with pitches of 360 nm, 350 nm and 350 nm, respectively. The inset shows the same spectra with a scale more appropriate for sample D135.

The green curves in Figure 5.3 correspond to the PL spectra of sample D135 (bare Be-doped GaAs NWs). As observed, the latter exhibit low signal-to-noise ratio and maximum PL intensities more than two orders of magnitude lower than the ones from samples D146 (blue) and D137 (orange). Given the similar NW densities (Figure 5.2), this indicates a higher amount of non-radiative recombinations in sample D135, probably at surface states due to the absence of a passivation layer. The enhanced PL intensity in D146 and D137 can thus be attributed to the growth of the additional GaAsP and GaAsP/GaP segments, respectively, but not directly to a surface passivation effect. A possible interpretation of the aforementioned results is discussed in the next paragraph.

Given the top-view excitation configuration used in PL, most optical generation of carriers occurs at the top of the NWs [Wallentin et al., 2013; Yao et al., 2014]. The absorption depth can be estimated to be around 130 nm here using the Beer-Lambert law, assuming a GaAsP absorption coefficient similar to the GaAs absorption coefficient of  $7.72 \times 10^4 \text{ cm}^{-1}$  (534 nm) used in the absorption depth calculation. As previously mentioned, the GaAsP segment in D146 has a length of around 125 nm, which should be similar to the sum of the GaAsP and GaP segments in D137 since the overall NW lengths are comparable for the two samples (Table 5.1). Hence, most carriers should be photogenerated in the linearly graded GaAsP segment for both samples (the GaP segment in D137 is most likely not optically active due to its indirect wide bandgap and small



thickness), which has a bandgap varying from 1.42 eV (GaAs) to 2.25 eV (GaP). The fact that the emission peak energies of sample D146 (1.51 eV) and D137 (1.47 eV) are much closer to the band-to-band transition energy of GaAs than to the one of GaP, suggests that although carriers are generated throughout the linearly graded GaAsP segment, they diffuse and recombine radiatively close to the GaAs/GaAsP interface. The broad PL emission peaks observed in [Figure 5.3](#) further support the idea of carrier generation and recombination in the linearly graded GaAsP segments. A relatively short minority carrier diffusion length can thus be presumed at the top of the NWs ( $<$  GaAsP segment thickness of 125 nm), which could be a result of two factors. On one hand, the high n-type Si doping could lead to most generated minority carriers (holes) recombining rapidly with the large excess of majority carriers (electrons). On the other hand, a relatively short minority carrier diffusion length could result from a combination of potential barrier and recombination centers at the GaAs/GaAsP interface. This will be further discussed in [Section 5.4](#).

The slightly higher emission peak energy and PL intensity observed for D146 as compared to D137 could be explained by different carrier diffusion lengths, as well as absorbing material thicknesses, in the two samples. In fact, the GaAsP segment in D146 was grown for 3 min while the one in D137 was grown for 2 min, leading also to slightly different strain conditions and band structures at the top of the NWs from the two samples.

The high energy shoulder observed on one of the PL spectra of sample D146 is a measurement artifact, arising from spectral interval combination into a single PL spectrum. Overall, the spectra recorded on different areas of the same sample are comparable in both intensity and lineshape, indicating relatively good homogeneity in all 3 samples.

In the previous discussion, light absorption by the Ga droplets at the top of the NWs and light scattering effects were omitted for simplicity. However, in reality some photons should be scattered by the NW array and the metallic Ga droplets, enabling the generation of carriers also in GaAs. To further investigate carrier generation and recombination in the different NW segments, cathodoluminescence was carried out on single NWs.

The self-catalyzed growth of a GaAsP segment on top of GaAs NWs was found to increase the maximum PL intensity by more than two orders of magnitude compared to bare GaAs NWs of similar dimensions. However, given the top-view excitation configuration used in PL and its spatial resolution, it is difficult to attribute the higher PL intensity to any NW sidewall passivation effects. Next, cathodoluminescence results will be analyzed to investigate the optoelectronic properties of single NWs.

## Cathodoluminescence

Single NWs from samples 76851, D146 and D137 were laid down on an external substrate and probed by an electron beam accelerated at 6 kV, scanning the NWs with an impinging current of about 2 nA. More details on the CL set-up and signal acquisition can be found in [subsection 1.3.1](#) and [subsection 4.2.2](#). For each sample, 2 NWs were measured and results similar to the ones presented below were obtained.

Schematics of the probed NWs' architecture can be found in [Figures 5.4 \(a-c\)](#) (dimensions not to scale), while SEM images are shown in [Figures 5.4 \(d-f\)](#). Differentiating the top of the NW from the bottom using the SEM images is not straightforward, except for the NW from sample D146, in which the Ga droplet can be clearly identified ([Figure 5.4f](#)). For sample D137 ([Figure 5.4e](#)), we assume that the slanted extremity corresponds to the bottom of the NW where it was broken off during the substrate transfer. For sample 76851, the top of the NW is assumed to correspond to area 1 in [Figure 5.4g](#).

[Figures 5.4 \(g-i\)](#) present the panchromatic CL intensity maps of samples 76851, D146, and D137, respectively. Samples D146 and D137 are observed to exhibit maximum integrated CL intensities that are 8-300 times higher than the one of 76851, suggesting better GaAs intrinsic optoelectronic quality or more efficient surface passivation in the axial junction NWs. Lower intrinsic optoelectronic quality could indeed be expected in the radial NW junctions due to the presence of a lattice-mismatched shell straining the NW core. In fact, the GaInP shell in 76851 is known to vary in composition across the NW axis, and hence to not always be lattice-matched

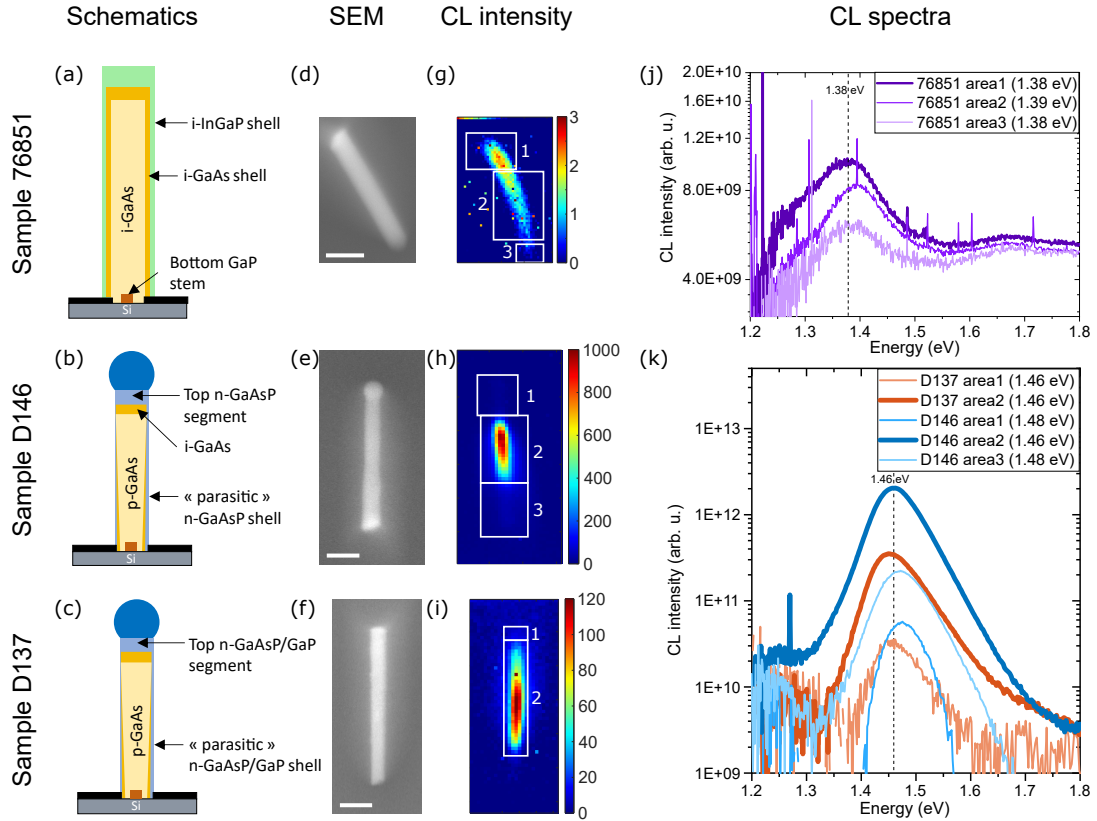


Figure 5.4: (a-c) Schematics, (d-f) SEM images, (g-i) panchromatic CL intensity maps of samples 76851, D146 and D137 respectively. (j-k) CL spectra averaged over the areas indicated by the white boxes on the CL intensity maps. The emission energy of the CL peaks obtained from a Gaussian fit is indicated in parenthesis in the legend. The scale bar in the SEM images is 200 nm.

to the GaAs core, potentially creating crystal defects at the interface which could act as non-radiative recombination centers (see discussion in [subsection 3.1.1](#)). In the axial junction samples D146 and D137, a parasitic shell of GaAsP and GaAsP/GaP is also expected to grow laterally during axial growth, but its thickness is predicted to be only a few nanometers (5 nm at most at the base of the NWs) based on a previous study from our group [[Oehler et al., 2018](#)], compared to over 30 nm for the GaInP shell in sample 76851 [[Bidaud, 2021](#)]. The critical thickness before the generation of misfit dislocations in GaP layers grown on GaAs was found to be less than 2 nm [[Mazuelas et al., 1993](#)]. However, the GaAsP segment linearly graded in composition between GaAs and GaP in samples D146 and D137, is expected to enable more efficient strain relaxation. A lower amount of non-radiative defects can be expected from the more efficient strain relaxation in the axial junction NWs, contributing to the higher CL intensity observed in samples D146 and D137. It is also important to keep in mind that sample 76851 was grown 5 years ago (2017) in the Riber32 MBE set-up, while samples D146 and D137 were grown recently in the Compact21 set-up, and that semiconductor quality can vary depending on the growth chamber conditions. Nonetheless, the high CL intensities observed in samples D146 and D137 suggest efficient GaAs surface passivation in the axial junction NWs, probably by a VS-grown phosphorous-based shell. Advanced TEM characterizations of single NWs from samples D146 and D137 would however be required to confirm the aforementioned hypothesis.

For all 3 samples, the CL intensity is observed to be non-uniform along the NW axis, with the central part luminescing the most. This is often observed in NWs probed by CL because their extremities are often of poor crystal quality. Defects at the bottom of the NW are typically created when the latter is broken off from its original substrate and transferred to another one for CL measurements. The top of the NW is often an undesired mixture of ZB and WZ crystal phases in radial junction NWs like the ones from sample 76851 due to the droplet consumption process [[Kim et al., 2012](#); [Dastjerdi et al., 2016](#); [Jacobsson et al., 2016](#)]. In the axial junction NWs however, the low CL intensity at the top of the NWs could be attributed to the presence of a metallic Ga



droplet (clearly seen in Figure 5.4e), and non-radiative defects in the GaAsP/GaP segments. From the CL intensity maps in Figures 5.4h and i, we see that the length of the top NW segment with low CL intensity in both D146 and D137 (around 100 nm if the Ga droplet in D146 is not taken into account) is comparable to the measured length of the GaAsP segment in D146 ( $124 \pm 14$  nm), and thus the sum of the GaAsP/GaP segments in D137. Hence the CL signal from area 1 of the NWs from samples D146 and D137 can be mainly attributed to the radiative recombination of carriers generated in their GaAsP and GaAsP/GaP segments, respectively.

Each probed NW was divided into different areas along its axis, over which CL spectra were averaged and plotted in Figures 5.4 (j-k). An emission peak around 1.38 eV can be observed for the most luminescent segment of the NW from sample 76851 (area 1). Its relatively low emission energy with respect to the GaAs band-to-band transition energy has been previously attributed to tensile strain [Signorello et al., 2013; Bidaud, 2021], supporting the idea that the GaInP shell induces strain on the GaAs NW core. As for the CL spectra obtained from samples D146 and D137, one can see from Figure 5.4k that area 1 from D146 luminesces twice as much as area 1 from D137. This luminescence intensity difference is similar to the one previously obtained from the PL measurements (Figure 5.3). On the other hand, area 2 of the NW from D146 demonstrates a 7 times higher CL intensity than area 2 from D137. These differences are overall relatively small, but a possible explanation for the observed trend will still be given in the next paragraph.

The main p-doped GaAs NW segments of samples D146 and D137 (area 2) were grown in identical conditions, while the top segments (area 1) differ (see Table 5.1). The fact that the central part of the NW from sample D146 presents a 7 times higher CL intensity than the one from sample D137 can thus neither be a result of different material composition nor higher crystal quality. In fact, the CL signal recorded from area 2 is centered around 1.46 eV for both samples, confirming the similar central NW segment composition. Instead, the CL intensity variation between area 2 of sample D146 and area 2 of sample D137 could be a consequence of different NW sidewall passivation efficiencies, arising from the different top NW segments. This hypothesis implies again an axial VLS NW growth that is accompanied by some extent of radial VS growth carrying a passivation effect. As for the slightly higher CL intensity observed in the top segment of the NW from sample D146 (area 1, cyan in Figure 5.3k), it should be a direct consequence of the varying final growth sequences in the two samples. As previously mentioned, the GaAsP segment in sample D137 is expected to be shorter and more strained than the one from sample D146, likely resulting in more recombining defects at the origin of the slightly lower luminescence intensity in area 1. It is worth highlighting once again that the same luminescence intensity difference was observed from the two samples' PL measurements (Figure 5.3), in which carriers were mainly generated at the top of the NWs (corresponding to area 1 in the CL intensity maps).

In the previous section on photoluminescence, we saw that upon top-view excitation, most carriers would be generated in the GaAsP segment in samples D146 and D137, and that given the PL emission energies (1.51 eV and 1.47 eV, respectively) the carriers must recombine close to the GaAs/GaAsP interface. From the identical CL peak energies (1.46 eV) observed for the spectra from areas 1 and 2 of the NW from sample D137 (orange in Figure 5.4k), it seems like carriers generated in the GaAsP can not only diffuse close to the GaAs/GaAsP interface, but even through it to recombine in GaAs. This could indicate a higher quality GaAs/GaAsP interface than anticipated from the PL results previously discussed, but is more likely due to the different excitation conditions in PL and CL measurements. In fact, the high excitation levels in CL could saturate the defect levels at the GaAs/GaAsP interface [Guthrey and Moseley, 2020; Bidaud, 2021], and allow some of the carriers generated in GaAsP to diffuse through the interface and recombine in GaAs. The latter would also explain the higher PL emission energy for sample D146 (1.51 eV) as compared to the CL emission energy obtained in area 1 of the NW from the same sample (1.48 eV, cyan in Figure 5.4k).

In summary, the GaAs/GaAsP axial junction NWs were found to exhibit two orders of magnitude higher maximum PL intensities than bare GaAs NWs, and 8-300 times higher integrated CL intensities than GaAs/GaInP radial junction NWs. These preliminary findings suggest that the self-catalyzed growth of GaAsP or GaAsP/GaP segments on top of GaAs NWs can enhance the optoelectronic properties of GaAs NWs. However, it is difficult to attribute the latter to some passivation effect from a potential GaAsP or GaAsP/GaP shell grown radially without TEM characterizations. Nevertheless, GaAs/GaAsP axial NW arrays were subsequently used to fabricate solar cells. Optimization of the NW solar cell fabrication process will be discussed in the next section, before presenting the performances of the very first axial junction NW solar cells fabricated in our group.

### 5.3 Axial junction NW solar cell fabrication process

After the observation of promising optoelectronic properties for the GaAs/GaAsP axial junction NWs, we decided to adapt the previous cell fabrication process developed for radial junction NWs to axial junction NWs. Given the absence of a standard passivation layer grown by the VS mechanism after Ga droplet crystallization in our axial junction NWs, *ex-situ* removal of the Ga droplet had to be investigated. Planarization tests using home-made organically-modified silica (ORMOSIL) solutions were also carried out in the aim of finding an alternative to the BCB polymer typically used for NW encapsulation. In fact, BCB was observed to not be thermally stable above 400°C, preventing a high-temperature annealing of the ITO contact which could significantly improve its conductivity. Finally, we also tried to optimize other processing steps to avoid the formation of gaps between the NW and the ITO layer.

#### 5.3.1 *Ex-situ* removal of the Ga droplets

The promising optoelectronic properties obtained for our axial junction NWs mean that there is no need for *in-situ* Ga droplet crystallization, which is known to introduce crystal phase mixing at the top of self-catalyzed NWs [Kim et al., 2012; Dastjerdi et al., 2016; Jacobsson et al., 2016]. However, it also means that the optically inactive Ga droplets need to be removed *ex-situ*. We investigated the use of hydrochloric acid (HCl) to selectively etch Ga, and found that immersing the sample in an HCl:H<sub>2</sub>O (1:2) bath for 4 min enables the complete etching of the Ga droplets. Figures 5.5a and b show tilted SEM images of a NW array from sample D137 before and after HCl etching, respectively. Figure 5.5c presents the PL spectra of the NW array before (solid curves) and after (dashed curves) HCl etching, obtained in the same conditions as the PL results presented in subsection 5.2.3. Two different areas were probed each time to account for array inhomogeneity.

As observed from Figure 5.5c, the PL spectra of the NW array after HCl etching (no Ga droplets) exhibit 2-3 times lower maximum PL intensities than that of the as-grown NW array (with Ga droplets), as well as slightly lower emission peak energies. These differences are not significant, but could be a result of NW surface damage by the HCl solution, although aqueous HCl solutions were reported to neither etch GaP nor GaAsP [Hong and Pearton, 1996; Kudryashov et al., 2018], which are expected to make up the outer most layers of the probed NWs (see detailed growth recipe in subsection 5.2.1). In fact, the chemical etching of GaP is actually quite complicated due to the strong Ga-P covalent bond, and typically requires the combination of strong oxidizers and a complex former [Kudryashov et al., 2018]. The higher PL intensity and emission peak energy observed for the as-grown NW array could then perhaps be related to light scattering effects induced by the metallic Ga droplets. In fact, [Park et al., 2012] also observed some modification of the optical properties (emission wavelength and luminescent area) of GaAs NWs with and without Ga droplets. Oxidation effects could also play a role in the differences observed, although more intense photoluminescence would have been expected from the deoxidized NW array obtained after HCl etching [Demichel et al., 2010; Couto et al., 2012].

To avoid any potential NW sidewall damage by the HCl etching, the Ga droplet removal step was subsequently carried out after the deposition of a thin layer of SiO<sub>2</sub>, and planarization of the NW array.

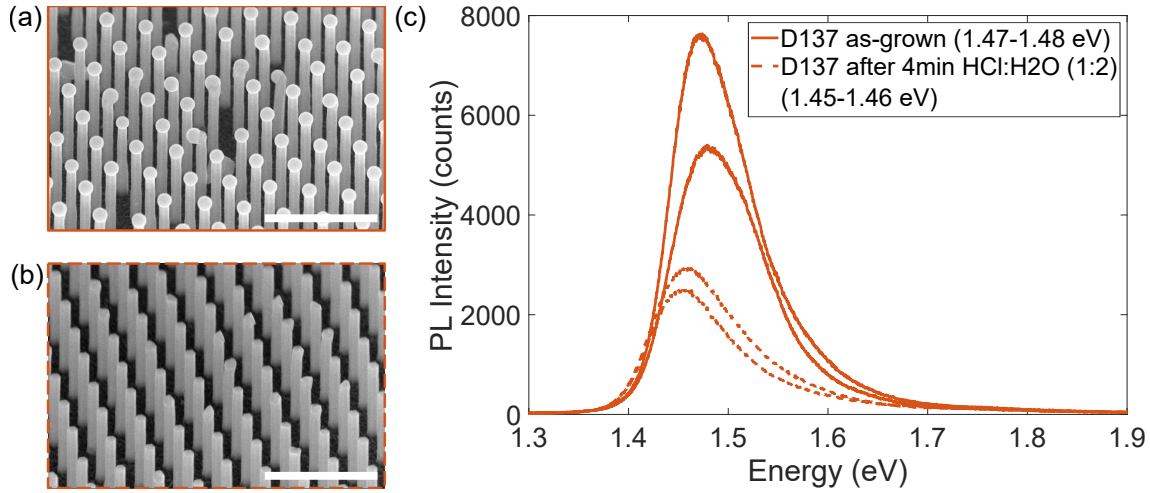


Figure 5.5: Tilted SEM images (45°) of the NW array from sample D137 with pitch 350 nm, (a) before and (b) after a 4 min HCl:H<sub>2</sub>O (1:2) bath. (c) Corresponding PL spectra obtained from two different areas of the NW array before and after HCl etching, represented by the solid and dashed curves, respectively.

### 5.3.2 An organic/inorganic hybrid material for NW planarization

Benzocyclobutene (BCB) is widely used in the NW community to planarize arrays and fulfill the role of transparent dielectric insulator, as it can be clearly seen from Table 1.1. However, in our radial junction NW solar cells, BCB's thermal stability was found to be limiting the top contact annealing temperature to 400°C, preventing further contact conductivity and hence cell performance improvement [de Lépinau, 2020]. This is why we looked into alternative planarization materials, and developed an organically modified silica (ORMOSIL) sol-gel.

ORMOSILs are produced by adding organosilane to a silica-derived gel, and the proportion of organic to inorganic compounds can be tailored to obtain the desired properties. The ideal NW array planarization material needs to be transparent, insulating, selectively etchable, and thermally stable above 450°C, without introducing any strain on the NWs. Its viscosity should also enable the complete filling of the NW array in a uniform manner. In order to develop a sol-gel with the aforementioned properties, several tests were carried out until the optimal ORMOSIL composition and deposition method were found.

Optimal NW array planarization was obtained by first depositing a thin layer of SiO<sub>2</sub> by PECVD around the NWs to promote ORMOSIL adhesion (as previously discussed it also provides NW sidewall protection during HCl etching of the Ga droplets). After a 1 min nitrogen plasma, an optimized ORMOSIL sol-gel composed of about 30 mol% organosilane is then spin-coated on the NW array. More precisely, the ORMOSIL sol-gel used was obtained by mixing 4 g of ethanol, 3.2 g of 0.1 M HCl, 4.32 g of tetraethyl orthosilicate (TEOS) and 2.08 g of triethoxyphenylsilane (phenylsilane). The presence of the organic phenylsilane compound in these proportions was found to be crucial to alleviate the stress induced during solvent evaporation, and to demonstrate better planarization properties than other planarization materials [Chia and LaPierre, 2011]. SEM images of embedded NW arrays can be found in Figures 5.6a and b, from which we can see that the synthesized ORMOSIL sol-gel homogeneously fills the NW array. The ORMOSIL can then be selectively etched by RIE using a mixture of SF<sub>6</sub> and CHF<sub>3</sub> gases in order to reveal the NW heads (Figure 5.6c). However, the etching rate of the ORMOSIL is much faster than the one of the SiO<sub>2</sub> layer deposited by PECVD around the NWs, resulting in an SiO<sub>2</sub> envelope surrounding the NWs, visible from Figure 5.6c. The impact of the latter on the NW/ITO physical contact will be discussed in the next section, along with the thermal stability of the ORMOSIL sol-gel.

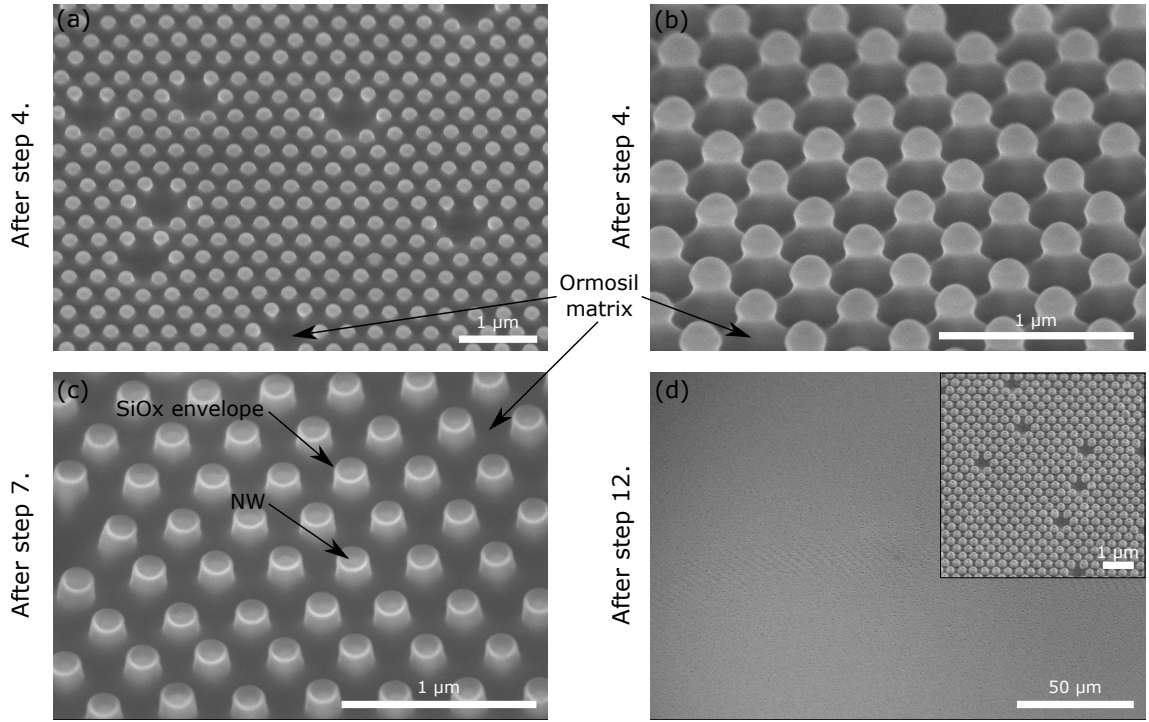


Figure 5.6: SEM images of a NW array (a-b) embedded in an ORMOSIL matrix (tilted at  $45^\circ$  and  $70^\circ$ , respectively), (c) after RIE etching of the ORMOSIL matrix and HCl etching of the Ga droplets, and (d) after a 150 nm-thick ITO layer deposition, followed by a 2 min rapid thermal annealing (RTA) at  $450^\circ\text{C}$ . The inset in (d) corresponds to a magnified view of the latter. The mentioned steps refer to the optimized process steps summarized at the end of the section.

### 5.3.3 Improving the NW/ITO contact

After planarizing the NW array, a negative lithography is performed before sputtering roughly 150 nm of ITO at room temperature. Then the spare ITO is lifted off in acetone in order to define the solar cells, before carrying out a 2 min rapid thermal annealing (RTA) at  $450^\circ\text{C}$  under an Ar/ $\text{H}_2$  flux. As observed from Figure 5.6d, no cracks were found on large sample areas, highlighting the good thermal stability of the synthesized ORMOSIL sol-gel up to  $450^\circ\text{C}$ . However, a closer look at the deposited ITO (inset Figure 5.6d, and Figure 5.7a) reveals that the latter forms doughnut-like shapes around the exposed NW heads, with the central gap making the NW/ITO contact physically difficult. To overcome this issue, a thinner  $\text{SiO}_2$  layer was deposited around the NWs (6 nm on planar Si substrates compared to 50 nm previously), and the length of the exposed NW heads was slightly reduced by performing a shorter RIE etching process. Furthermore, prior to the ITO sputtering the NW array was immersed in a pure HCl (37%) bath for 1 min to deoxidize the NW heads. All of these process changes resulted in the improved NW/ITO contact seen in Figure 5.7b. In fact, the hole previously observed in the ITO “doughnuts” now seems to be filled.

#### Summary of the optimized NW solar cell fabrication steps previously presented:

1. Thin  $\text{SiO}_2$  layer deposition by PECVD around the as-grown NWs (few nanometers) to promote ORMOSIL adhesion and protect the NW sidewalls from potential damage during the subsequent HCl etching.
2. Nitrogen plasma for 1 min just before ORMOSIL spin-coating.
3. ORMOSIL spin-coating at 2500 rpm for 20 s (needs to be adapted according to the NW length).
4. Baking at  $105^\circ\text{C}$  for 3 min.
5. Few minutes of RIE etching with a mixture of  $\text{SF}_6$  and  $\text{CHF}_3$  gases to reveal the NW heads (needs to be adapted according to the NW length).



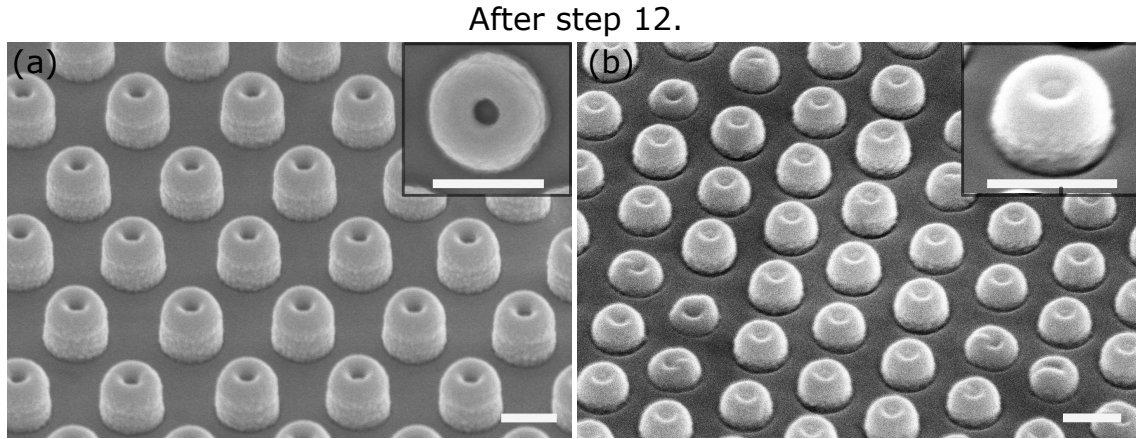


Figure 5.7: Tilted (45°) SEM images of a NW array with (a) poor NW/ITO contact due to the formation of ITO “doughnuts”, and (b) improved NW/ITO contact. The insets show magnified SEM images in either top view (a) or tilted view (b). The process differences between (a) and (b) are explained in the main text. The mentioned step number refers to the optimized process steps summarized at the end of the section. Scale bar = 250 nm.

6. SEM observation to make sure the NW heads come out of the ORMOSIL matrix, otherwise continue the RIE etching.
7. Ga droplet etching in an HCl:H<sub>2</sub>O (1:2) bath for 4 min.
8. Negative lithography to define cells.
9. Pure HCl bath (HCl 37%) for 1 min to deoxidize NW heads.
10. Sputtering of ITO (150 nm) at room temperature.
11. ITO lift-off in acetone.
12. RTA under Ar/H<sub>2</sub> flux at 450°C for 2 min.
13. Negative lithography to define the front contacts.
14. Ti/Au front contact deposition (20 nm/200 nm) by thermal evaporation.
15. Lift-off in acetone.
16. Al back-contact deposition (300 nm) by thermal evaporation after having cleaned the back surface with a 5% HF solution.

A 4 min HCl:H<sub>2</sub>O (1:2) bath was found to fully remove the optically inactive Ga droplets present on top of the axial junction NWs. However, the removal of the droplets by HCl etching was observed to impact the NWs' optical properties, requiring the former to be preferably performed after the deposition of a thin layer of SiO<sub>2</sub> and NW encapsulation in a planarization matrix. The home-made organically-modified silica (ORMOSIL) sol-gel was found to be a good alternative to the conventionally used BCB polymer for NW array planarization, with the additional advantage of good thermal stability up to 450°C (no cracks detected). The RIE etching rate of the ORMOSIL was however observed to be much slower than the one of the SiO<sub>2</sub> layer deposited around the NWs partly for enhanced matrix adhesion, calling for some process optimization to avoid the formation of ITO “doughnuts” that may not be in contact with the NWs. Using the optimized process steps discussed previously, axial junction NW solar cells were fabricated for the first time in our group. Their performances will be presented in the next section.

## 5.4 Performances of our first axial junction NW solar cells

Axial junction NW arrays similar to the ones from sample D137 (GaAs/GaAsP/GaP junctions, growth recipe in subsection 5.2.1) were successfully processed into solar cells as a proof-of-concept. Although from subsection 5.2.3 it was seen that GaAs/GaAsP axial junction NWs showed better optoelectronic properties than ones with GaAs/GaAsP/GaP junctions, the latter were used to make our first axial junction NW solar cells because they were the ones on which a successful fabrication process was initially obtained.

### 5.4.1 Current-voltage (J-V) characteristics

The electrical performances of 16 GaAs/GaAsP/GaP axial junction NW solar cells from sample D144 (PNW 313c) were measured using the set-up described in subsection 1.3.3. The box plots in Figure 5.8 show the distribution of the cells'  $V_{OC}$ ,  $J_{SC}$ , and FF. A high average  $V_{OC}$  of 0.62 V was obtained from a relatively narrow data distribution (all  $V_{OC}$  values are between 0.59–0.64 V). The  $J_{SC}$  and FF measurements are however more dispersed, with consistently low values (average of  $0.32 \text{ mA cm}^{-2}$  and 16%, respectively), suggesting a barrier for the photocurrent and potentially high recombination of photogenerated minority carriers at the absorber interface [Scheer and Schock, 2011].

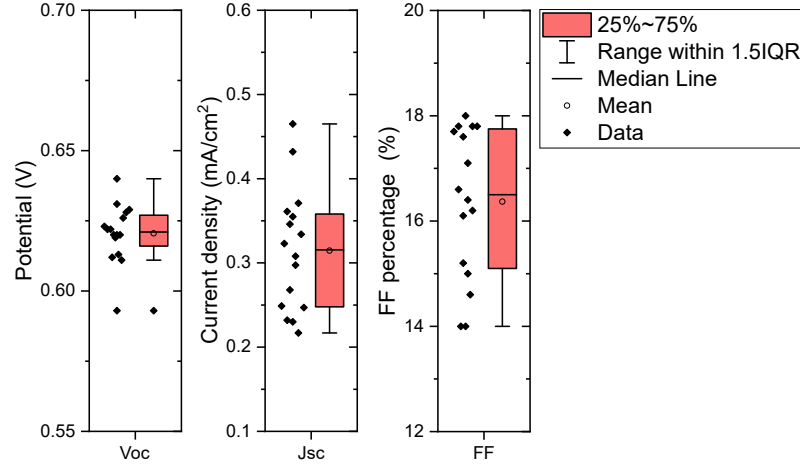


Figure 5.8: Box plots showing the  $V_{OC}$ ,  $J_{SC}$ , and FF measurements for 16 axial junction NW solar cells from sample D144 (PNW 313c).

The J-V curves of cell C16 from sample D144 (PNW 313c) were measured in the dark and under a 1 sun illumination, and plotted in Figure 5.9a (blue and red, respectively). A voltage-dependent photocurrent can be clearly noticed for the J-V curve under illumination, indicating indeed a barrier for the photocurrent which limits the  $J_{SC}$  and FF. The cross-over between the dark and illuminated J-V curves around 0.6 V points to an electron barrier in the conduction band, probably arising from a positive CB offset at the front (n-type) contact, as suggested by the current saturation at larger forward biases. The band alignment in our axial junction NW solar cells will be further investigated using numerical simulations in subsection 5.4.3.

Figure 5.9b presents the semi-logarithmic plot of the J-V curve in the dark along with its one-diode model fit. A high and unfittable reverse-current can be observed (similarly to the radial junction cell characteristics presented in Figure 3.6b), while the forward current is accurately fitted with a high ideality factor  $n$  of 5.8, a  $J_0$  of  $2.6 \times 10^{-8} \text{ mA cm}^{-2}$  and a satisfying shunt resistance  $R_{shunt}$  of  $1.2 \times 10^{11} \Omega \text{ cm}^2$ . A very high series resistance  $R_{series}$  of  $3824 \Omega \text{ cm}^2$  was also obtained from the forward current fit, which is coherent with the low FF recorded.

The effects of series resistance can be further evaluated using a pseudo-JV curve obtained from  $J_{sc}$ - $V_{oc}$  measurements. Each black data point from Figure 5.9c corresponds to a  $(V_{OC}, J_{sc})$  measurement at different incident light intensity, which was plotted with a vertical shift of the  $J_{SC}$  value measured at 1 sun. The fit of all the  $J_{sc}$ - $V_{oc}$  data points provides a pseudo-JV curve with a FF of 88% when an ideality factor ( $n$ ) of 0.6 is used (black curve), and a FF of 83.4%



when a fit with  $n=1$  is used (grey curve). The JV curve obtained using  $n=0.6$  (black) can be seen to better fit the experimental Jsc-Voc data points, suggesting that the one-diode fit model used cannot accurately describe the operation of our axial junction NW solar cells. The aforementioned FF values obtained from the fit of the pseudo-JV curve could be achieved experimentally only if  $R_{series}=0$ . In other words, a  $\sim 80\%$  FF diminution can be attributed to resistive losses in our axial junction NW solar cells, which given the excessively high values may also reduce the  $J_{SC}$ . The observed resistive losses could be due to relatively low n-type doping in the n-GaAsP/n-GaP NW segments (challenging to determine experimentally), and unoptimized ITO sheet resistance. Moreover, the physical contact between the NW and the ITO may still be problematic due to the formation of gaps, despite the optimization attempts presented in subsection 5.3.3.

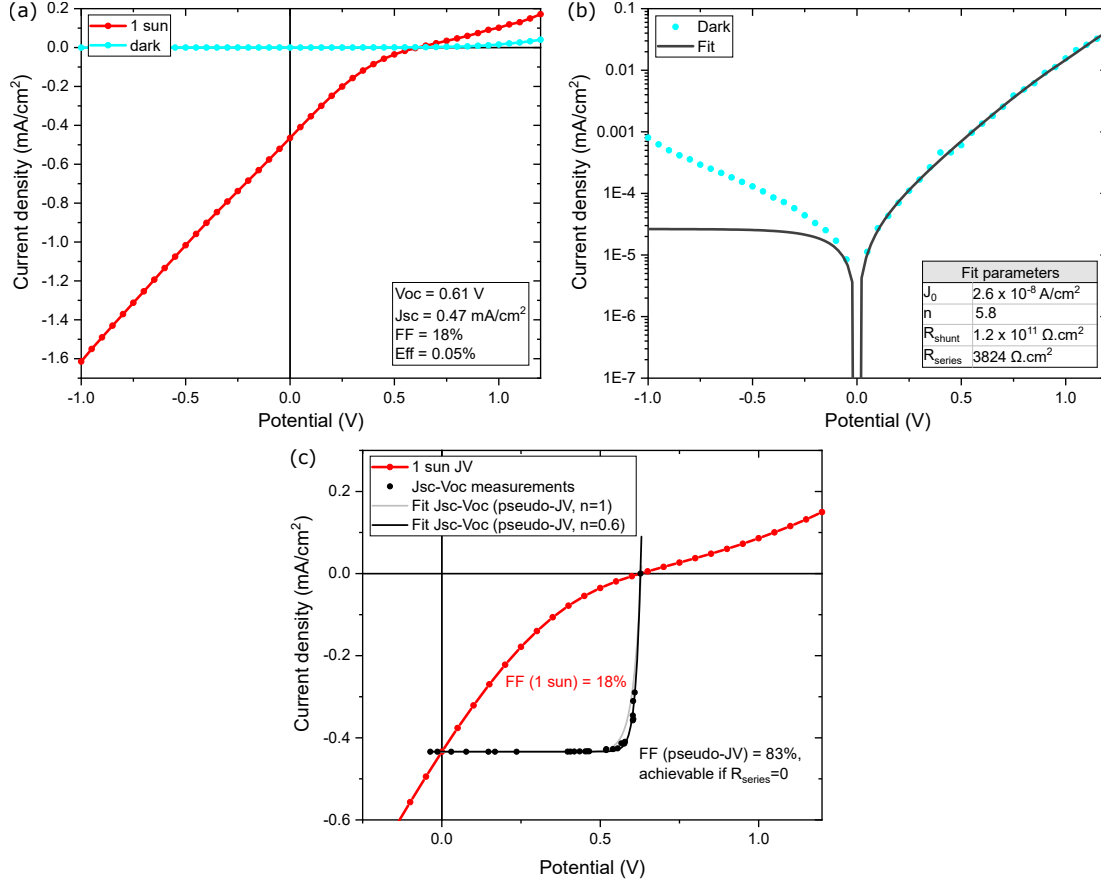


Figure 5.9: Characterization of cell C16 from sample D144 (PNW 313c). (a) J-V curves in the dark (blue) and under a 1 sun illumination (red). (b) Semi-logarithmic plot of the J-V curve in the dark (blue), along with a one-diode fit (black). (c) Comparison between the J-V curve measured under a 1 sun illumination and the pseudo J-V curve obtained from Jsc-Voc measurements.

#### 5.4.2 External quantum efficiency (EQE) response

The EQE response of cell C16 from sample D144 (PNW 313c) was investigated using the EQE set-up described in subsection 1.3.3. The EQE response of the cell recorded at zero potential bias is plotted in Figure 5.10 (black). The latter is observed to be low at all wavelengths, with a maximum value around 0.1 between 380–450 nm. This indicates a very low amount of electrons collected with respect to the incoming photons, more likely due to carrier collection issues rather than limited absorption. Above 450 nm, the EQE response decreases steadily reaching almost 0 around 700 nm (see black curve in the inset of Figure 5.10a). This indicates that most of the collected carriers were generated in the top GaAsP NW segment by the absorption of high-energy photons (short wavelengths), and hence that a potential barrier must be present for the transport of electrons generated in GaAs. Nonetheless, a distinct peak can be noticed in the EQE spectrum

of the cell around 850 nm, corresponding to the absorption range of GaAs and demonstrating the collection of a small amount of charge carriers generated in the GaAs NW segments.

A  $J_{SC}$  value of  $0.69 \text{ mA cm}^{-2}$  was obtained from EQE integration, which is 32% higher than the value of  $0.47 \text{ mA cm}^{-2}$  obtained from the illuminated J-V curve in Figure 5.9a. This points once again towards the presence of a photocurrent barrier, which can more or less impact the EQE measurement depending on the magnitude of the current density [Scheer and Schock, 2011]. EQE measurements under potential bias were also performed to further investigate the impact of the aforementioned photocurrent barrier.

### EQE under bias

EQE spectra obtained under reverse and forward biases between -1.0 V and 1.0 V can be found in Figures 5.10a and b, respectively. The above unity EQE values recorded at short wavelengths under forward biases (Figure 5.10b) are artifacts arising from the absence of an optical chopper and lock-in amplifier system on the monochromator set-up used at the C2N (also observed previously in Figure 3.7).

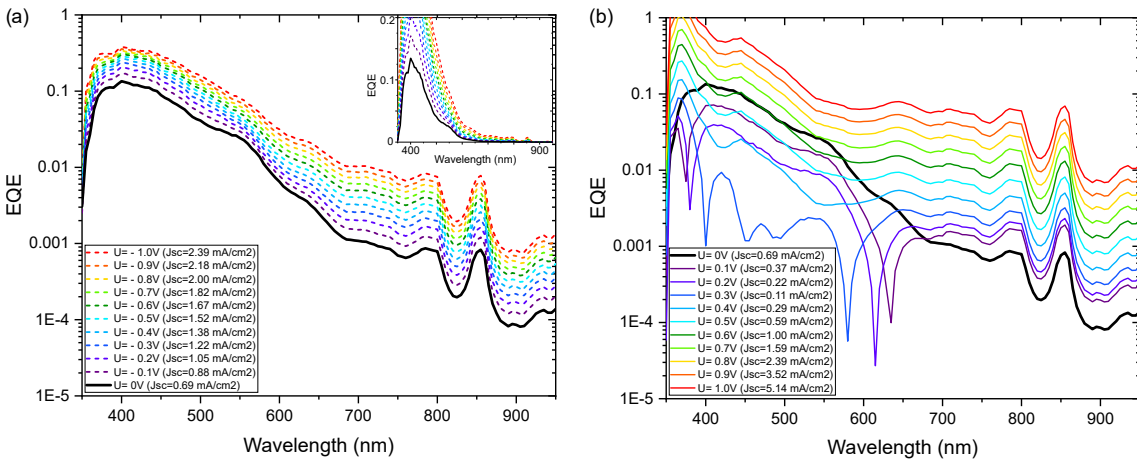


Figure 5.10: External quantum efficiency response of cell C16 from sample D144 (PNW313c), under (a) negative (reverse) bias, and (b) positive (forward) bias, plotted in a semi-logarithmic scale. The inset of (a) represents the EQE response under negative applied bias, plotted in a linear scale.

From Figure 5.10a, the EQE response of the cell is seen to clearly increase with reverse bias, highlighting carrier collection improvements. The behavior of the EQE response under forward bias (Figure 5.10b) is however more complex. At forward biases below 0.6 V, the cell's EQE response is observed to be lower than the one at zero applied potential between roughly 380 and 600-700 nm, and higher than the latter above 600-700 nm. At forward biases above 0.6 V, the cell's EQE response increases with applied positive potential across the full wavelength range of interest, indicating again carrier collection improvement. Please note however that the latter is difficult to interpret given that light emission from the NW solar cell and subsequent reabsorption are expected at such high forward biases. Similar trends were previously observed for the EQE response of the GaAs/GaInP radial junction NW solar cells (subsection 3.2.2), although much lower bias voltages were used. Overall, these observations point towards a voltage-dependent carrier collection function, and hence photocurrent, which could be attributed to a combination of interface recombination and photocurrent barrier.

Our very first axial junction NW solar cells demonstrated relatively high  $V_{OC}$  ( $> 0.6 \text{ V}$ ), but very low  $J_{SC}$  and FF due to significant resistive losses revealed by  $J_{SC}$ - $V_{OC}$  measurements. Analyses of J-V curves and EQE responses also indicated performance limitations coming from interface recombination and photocurrent barrier, probably arising from a positive conduction band offset at the front contact. In order to gain deeper insight into the conduction band alignment at the GaAs/GaAsP front interface, 1D numerical simulations were carried out using the solar cell device simulator SCAPS.

### 5.4.3 Modeling electron transport at the n-type contact

Two solar cell structures were modeled in 1D using the solar cell device simulator SCAPS, in the aim of better understanding the experimental results obtained from sample D144 (PNW 313c). The first modeled structure (schematized at the top of Figure 5.11a) closely follows the NW architecture expected from the growth sequence of sample D144 (PNW 313c). It contains an 85 nm thick GaAsP layer linearly graded in composition between GaAs and GaP (representing the GaAsP layer formed in sample D144 by linearly closing the As valve and opening the P valve), followed by a 45 nm thick GaP segment. In reality, the electronic and optical parameters of the GaAsP segment linearly graded in composition should not be equally graded linearly [Onno et al., 2016], but a linear gradient was still used for all GaAsP layer parameters for simplicity.

The second modeled structure (schematized at the top of Figure 5.11b) contains instead a GaAsP layer of fixed composition ( $\text{GaAs}_{0.3}\text{P}_{0.7}$ ), also followed by a 45 nm GaP segment. The GaAsP composition of  $\text{GaAs}_{0.3}\text{P}_{0.7}$  was chosen according to the bandgap wavelength of 630 nm determined from the inflection point of the EQE spectrum obtained experimentally (black in Figure 5.10), in the absorption threshold region between 600–700 nm [Almora et al., 2021]. The n-type doping level in the GaAsP and GaP segments was set to  $1 \times 10^{17} \text{ cm}^{-3}$  in both modeled structures, although for the structure with fixed  $\text{GaAs}_{0.3}\text{P}_{0.7}$  composition the n-type doping levels were varied between  $1 \times 10^{16} \text{ cm}^{-3}$  and  $1 \times 10^{17} \text{ cm}^{-3}$  to investigate its impact on the optoelectrical performances of the modeled solar cell.

For both modeled structures, the thickness of the GaAs layer was set to a value much lower than the length of the GaAs segment in the axial junction NWs because the aim here was to focus on the absorption and collection of charge carriers generated close to the top of the NWs. Details of the other parameters used in the SCAPS simulations can be found in Table 5.2. The results obtained from the simulations are shown in Figure 5.11, and will be discussed in the sections below. The discussion will be mainly qualitative with a focus on the general trends observed.

#### Simulated band diagrams

Figures 5.11a and b present the band diagrams of the two simulated solar cell structures under a 1 sun illumination and an applied bias corresponding to their maximum power point ( $V_{MPP}$ ). The VB offset observed at the p-Si/p-GaP interface has been previously discussed in Section 3.4, so the focus here will be on the band alignments at the i-GaAs/n-GaAsP and n-GaAsP/n-GaP interfaces. In the structure containing a graded n-GaAsP layer (Figure 5.11a), a gradual bandgap increase can be observed at the position of the layer due to its linearly graded composition. This gradual bandgap increase is achieved by lowering the VB edge and lifting the CB edge in n-GaAsP towards the n-GaP interface, in a smooth manner without any band offsets. Nevertheless, while the lowering of the VB edge is beneficial to repel holes from the n-type contact (right in Figure 5.11b), the lifting of the CB edge should to some extent impede electron transport. The behavior of the CB and VB edges in the outermost n-GaP layer (right in Figures 5.11a and b) is a result of the 4.7 eV metal work function imposed on the front contact in the aim of reproducing the Schottky barrier expected at the III-V/ITO interface. In the structure containing a n-GaAs<sub>0.3</sub>P<sub>0.7</sub> layer of fixed composition (Figure 5.11b), CB and VB offsets can be observed at both the i-GaAs/n-GaAs<sub>0.3</sub>P<sub>0.7</sub> and n-GaAs<sub>0.3</sub>P<sub>0.7</sub>/n-GaP interfaces. While the negative VB offset at these interfaces is once again beneficial for the transport of holes solely towards the p-type contact (left in Figure 5.11b), the positive CB offsets (0.4 eV and 0.2 eV at the i-GaAs/n-GaAs<sub>0.3</sub>P<sub>0.7</sub> and n-GaAs<sub>0.3</sub>P<sub>0.7</sub>/n-GaP interfaces, respectively) introduce a voltage barrier for the injection of electrons photogenerated in the GaAs absorber into the GaAsP hetero-contact, which is expected to impact both the FF and the short-circuit current. The band diagram of the same solar cell structure but with a lower electron concentration in the n-GaAsP and n-GaP layers ( $1 \times 10^{16} \text{ cm}^{-3}$  instead of  $1 \times 10^{17} \text{ cm}^{-3}$ ) is also illustrated in Figure 5.11b (thin lines). As expected, at the lower electron concentration of  $1 \times 10^{16} \text{ cm}^{-3}$ , the width of the potential barriers at the n-type contact (proportional to the curvature of the CB edge) becomes wider, making it more difficult for electrons to overcome the barrier. Next, we will qualitatively assess the performance of these different simulated solar cell structures.

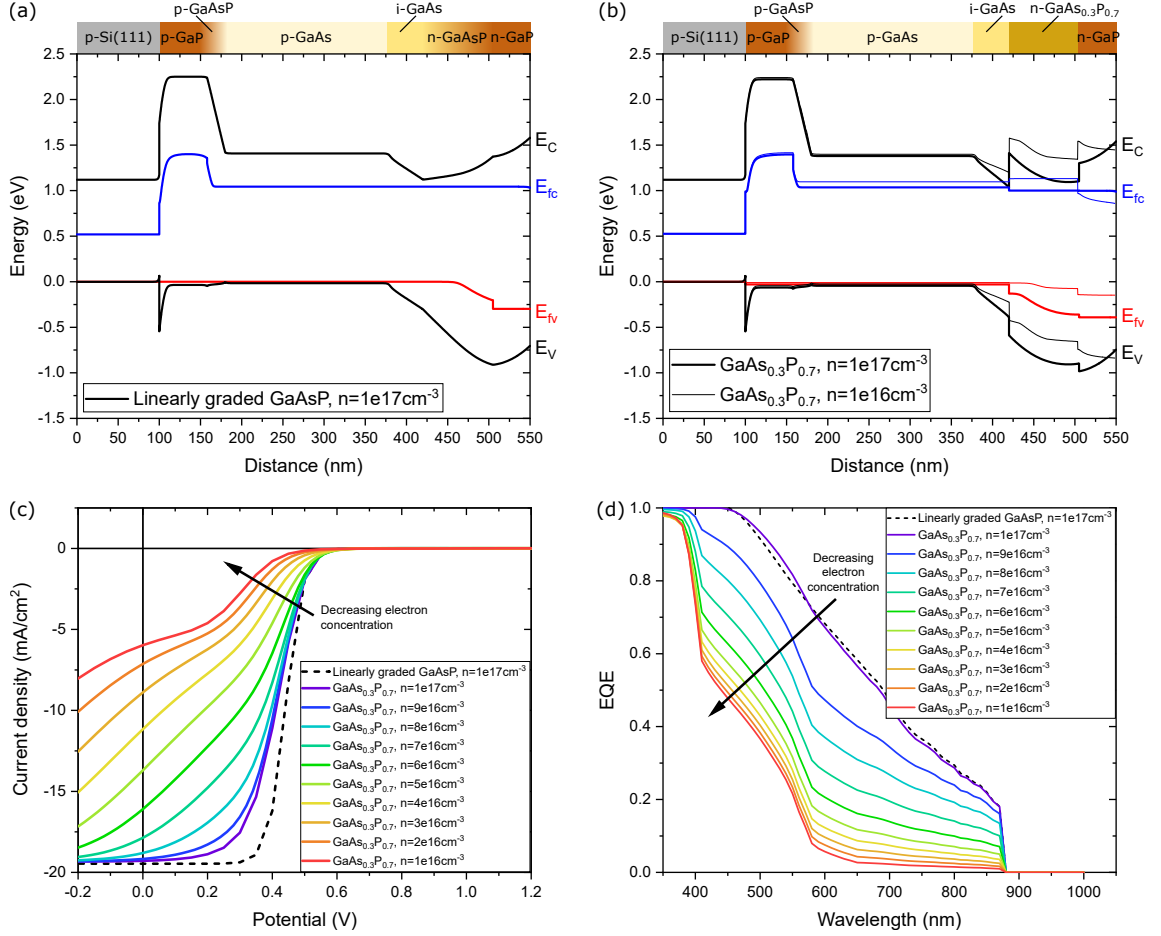


Figure 5.11: Band diagrams obtained from 1D SCAPS simulations under a 1 sun illumination and at  $V_{MPP}$ , for a p-i-n solar cell structure containing n-doped segments of (a) 85 nm linearly graded GaAsP followed by 45 nm GaP ( $n = 1 \times 10^{17} \text{ cm}^{-3}$ ), and (b) 85 nm GaAs<sub>0.3</sub>P<sub>0.7</sub>, followed by 45 nm GaP ( $n = 1 \times 10^{17} \text{ cm}^{-3}$  and  $1 \times 10^{16} \text{ cm}^{-3}$ ). (c) Corresponding J-V curves obtained under a 1 sun illumination. The black dashed J-V curve was obtained from the modeled structure containing a linearly graded GaAsP layer, while the colored curves were obtained from the modeled structure containing a GaAs<sub>0.3</sub>P<sub>0.7</sub> layer with varying n-doping levels. (d) Corresponding EQE responses obtained under an incident monochromatic power of  $1000 \text{ W m}^{-2}$ . The parameters used in the SCAPS simulations are detailed in Table 5.2.

### Simulated J-V curves and EQE responses

The simulated J-V curves obtained from the modeled solar cell structures can be found in Figure 5.11c. The black dashed curve corresponds to the J-V characteristics of the cell structure containing a linearly graded n-GaAsP layer, while the purple curve corresponds to the cell structure containing a n-GaAs<sub>0.3</sub>P<sub>0.7</sub> layer. The other colored curves were also obtained from the cell structure containing a n-GaAs<sub>0.3</sub>P<sub>0.7</sub> layer, by varying the electron concentration in the n-GaAs<sub>0.3</sub>P<sub>0.7</sub> and n-GaP layers. First, we can notice that all of the J-V curves from Figure 5.11c exhibit a saturation of the forward current at high forward bias. This rollover effect is typically the consequence of positive CB offsets [Scheer and Schock, 2011], like the ones observed in Figures 5.11a and b at the interfaces of the n-doped layers. The rollover effect observed in the simulated J-V curves reminds of the one obtained in the experimental J-V curve of cell C16 from sample D144 (PNW 313c) (Figure 5.9), confirming that unfavorable band alignment could be responsible for the modest cell parameters recorded. The more significant potential barrier observed in the cell structure containing a GaAs<sub>0.3</sub>P<sub>0.7</sub> layer, as compared to the one containing a linearly graded GaAsP layer, translates into slightly lower  $J_{SC}$  and FF values for a same electron doping concentration of  $1 \times 10^{17} \text{ cm}^{-3}$  (purple and dashed black curves, respectively). As the electron doping concentration decreases in the n-doped layers, the  $J_{SC}$  and FF values decrease significantly for the structure

containing a  $\text{GaAs}_{0.3}\text{P}_{0.7}$  layer (colored curves), with a voltage-dependent photocurrent arising at low n-type doping levels. On the contrary, the variation of the  $J_{SC}$  and FF values is negligible for the structure containing a linearly graded GaAsP layer when the electron doping concentration is decreased from  $1 \times 10^{16} \text{ cm}^{-3}$  to  $1 \times 10^{17} \text{ cm}^{-3}$  (not shown here). The electron concentration in the n-GaAsP and n-GaP segments of our axial junction NWs has not yet been quantified. Nevertheless, the shape of the experimental J-V curve and the low  $J_{SC}$  obtained (Figure 5.9a) strongly suggest a relatively low electron doping concentration in both the n-doped segments of our axial junction NWs, as well as the presence of at least one CB offset at the n-type contact. In fact, the perfectly linearly graded GaAsP layer modeled in Figure 5.11a is quite idealistic, and band offsets like the ones observed in Figure 5.11b are expected despite a nominally linear opening and closing of the P and As valves, respectively.

The EQE responses obtained from the simulated cell structures are presented in Figure 5.11d with the same color code as for Figure 5.11c. First, we can notice that the EQE spectra of both simulated cell structures (dashed black and purple curves) are very similar. In fact, they are both inclined towards long wavelengths (low red response), probably due to the small GaAs layer thicknesses in the modeled structures (240 nm). For the structure containing a n- $\text{GaAs}_{0.3}\text{P}_{0.7}$  layer, as the electron doping concentration decreases in the n-doped layers, the collection of electrons with short wavelengths is further reduced, until an EQE response with an absorption threshold at roughly 600 nm is obtained. On the contrary, for the structure containing a linearly graded GaAsP layer, the EQE response is not impacted by the variation of the electron doping concentration between  $1 \times 10^{17} \text{ cm}^{-3}$  and  $1 \times 10^{16} \text{ cm}^{-3}$  (not shown here). Given the similarity between the absorption threshold observed in the structure containing a n- $\text{GaAs}_{0.3}\text{P}_{0.7}$  layer and the one observed in the experimental EQE of cell C16 from sample D144 (Figure 5.10a inset), the presence of at least one CB offset, and relatively low electron concentrations in the n-doped segments are expected in our axial junction NWs. In fact, the cut-off of the EQE response around 600 nm indicates a voltage barrier for the collection of electrons photogenerated in the GaAs absorber, while the electrons photogenerated in the GaAsP layer can be collected. We can also deduce that the holes photogenerated in the GaAsP layer can however be easily injected into the GaAs absorber, and collected at the p-type contact. On the short wavelengths side, the EQE response of the simulated cell structures is observed to be much higher than the one of cell C16 from sample D144. This could be due to hindered carrier collection at the ITO contact resulting from unoptimized ITO sheet resistance or remaining issues regarding the physical contact between the NW and the ITO.

The axial junction NW solar cell characterized in Section 5.4 was modeled in 1D using the solar cell device simulator SCAPS. The simulated J-V curves and EQE responses obtained with low electron doping concentrations in the n-doped layers and the presence of CB offsets revealed characteristics similar to the ones recorded from experimental measurements on cell C16 from sample D144. This suggests that the performance of our axial junction NW solar cells could be hindered by low electron doping concentration in the n-GaAsP and n-GaP NW segments, as well as potential barriers at the n-type contact arising from at least one CB offset.

Table 5.2: Parameters used in the 1D SCAPS simulations presented in Figure 5.11. The material parameters were extracted from references [Levinstein et al., 1999; Ioffe Institute; Onno et al., 2016; Gomez, 2018; Kao et al., 2019]. The front contact metal work function was set to 4.7 eV to reproduce the Schottky barrier expected at the III-V/ITO interface.

	p-Si	p-GaP	Graded GaAsP	p-GaAs	i-GaAs	Graded GaAsP or GaAs <sub>0.3</sub> P <sub>0.7</sub>	n-GaP
Thickness (nm)	100	58	22	200	40	85	45
Bandgap (eV)	1.12	2.285	linearly graded	1.424	1.424	linearly graded or 2.001	2.285
Electron affinity (eV)	4.05	3.8	linearly graded	4.07	4.07	linearly graded or 3.693	3.494
Dielectric permittivity	11.9	11.1	linearly graded	12.9	12.9	linearly graded or 12.9	11.1
CB effective density of states (cm <sup>-3</sup> )	2.8 × 10 <sup>19</sup>	1.8 × 10 <sup>19</sup>	linearly graded	4.7 × 10 <sup>17</sup>	4.7 × 10 <sup>17</sup>	linearly graded or 9.996 × 10 <sup>17</sup>	1.8 × 10 <sup>19</sup>
VB effective density of states (cm <sup>-3</sup> )	1.04 × 10 <sup>19</sup>	1.9 × 10 <sup>19</sup>	linearly graded	9 × 10 <sup>18</sup>	9 × 10 <sup>18</sup>	linearly graded or 1.17 × 10 <sup>19</sup>	1.9 × 10 <sup>19</sup>
Electron thermal velocity (cm/s)	2.3 × 10 <sup>7</sup>	2 × 10 <sup>5</sup>	linearly graded	4.4 × 10 <sup>7</sup>	4.4 × 10 <sup>7</sup>	linearly graded or 2.5 × 10 <sup>5</sup>	2.5 × 10 <sup>5</sup>
Hole thermal velocity (cm/s)	1.65 × 10 <sup>7</sup>	1.3 × 10 <sup>5</sup>	linearly graded	1.8 × 10 <sup>7</sup>	1.8 × 10 <sup>7</sup>	linearly graded or 1.3 × 10 <sup>5</sup>	1.3 × 10 <sup>5</sup>
Electron mobility (cm <sup>2</sup> .V.s)	1.5 × 10 <sup>3</sup>	2.5 × 10 <sup>2</sup>	linearly graded	8.5 × 10 <sup>3</sup>	8.5 × 10 <sup>3</sup>	linearly graded or 2.5 × 10 <sup>2</sup>	2.5 × 10 <sup>2</sup>
Hole mobility (cm <sup>2</sup> .V.s)	4.5 × 10 <sup>2</sup>	1.5 × 10 <sup>2</sup>	linearly graded	4.0 × 10 <sup>2</sup>	4.0 × 10 <sup>2</sup>	linearly graded or 1.5 × 10 <sup>2</sup>	1.5 × 10 <sup>2</sup>
Doping concentration (cm <sup>-3</sup> )	(p) 1.0 × 10 <sup>19</sup>	(p) 5.0 × 10 <sup>18</sup>	(p) 5.0 × 10 <sup>18</sup>	(p) 5.0 × 10 <sup>18</sup>	(n residual) 1.0 × 10 <sup>15</sup>	(n) 1.0 × 10 <sup>17</sup>	(n) 1.0 × 10 <sup>17</sup>
Radiative recombination coeff. (cm <sup>3</sup> /s)	1.0 × 10 <sup>-15</sup>	1.0 × 10 <sup>-13</sup>	linearly graded	2.0 × 10 <sup>-10</sup>	2.0 × 10 <sup>-10</sup>	linearly graded or 0	0
Auger electron capture coeff. (cm <sup>6</sup> /s)	3.0 × 10 <sup>-31</sup>	0	linearly graded	5.0 × 10 <sup>-30</sup>	5.0 × 10 <sup>-30</sup>	linearly graded or 0	0
Auger hole capture coeff. (cm <sup>6</sup> /s)	3.0 × 10 <sup>-31</sup>	0	linearly graded	1.0 × 10 <sup>-31</sup>	1.0 × 10 <sup>-31</sup>	linearly graded or 0	0



## 5.5 Chapter conclusions

Self-catalyzed NW passivation should ideally take place in the growth chamber but without the need for catalyst droplet consumption, known to introduce crystal phase mixing and defects formation. Our aim here was to develop such a passivation scheme through the controlled formation of the unintended radial shell during axial VLS NW growth.

The growth of axial Si-doped GaAsP and GaAsP/GaP segments on top of GaAs NWs was found to significantly increase both the PL and CL intensities when compared to bare GaAs NWs or GaAs/GaInP radial junction NWs. The enhanced optoelectronic properties observed from these preliminary results suggest suppressed surface states in the axial junction NWs, but the latter could not be directly attributed to the formation of an unintentional radial shell during VLS axial growth. STEM-EDX would be required to confirm the correlation and assess the composition and thickness of the aforementioned radial shell, in order to help understand its effect on surface states.

Optoelectronic characterization of the GaAs/GaAsP/GaP axial junction NW cells revealed relatively high  $V_{OC}$  values ( $> 0.6$  V) but very limited  $J_{SC}$  and FF, partly due to high resistive losses in the devices. The high series resistance recorded could be a result of unoptimized doping in the n-GaAsP and n-GaP NW segments (the latter is challenging to quantify), issues with the physical contact between the NW and the ITO, and/or relatively low ITO sheet resistance despite the use of a more thermally stable planarization matrix (ORMOSIL) which enabled a rapid thermal annealing of the contact above 450°C. Numerical 1D simulations carried out using the solar cell device simulator SCAPS also indicated n-type doping level in the GaAsP and GaP layers as a critical parameter which could limit device performance. Furthermore, results obtained from the simulations suggested the presence of at least one CB offset in the GaAs/GaAsP/GaP solar cell structure, likely at the origin of potential barriers at the n-type contact.

To improve the performances of these NW array solar cells, the axial junction design and growth hence need to be optimized in order to enhance the doping levels in the n-doped NW segments, and achieve more favorable band alignments responsible for interface recombination and energy barriers.



## Chapter 6

# Conclusion and Perspectives

In order to achieve net zero greenhouse gas emissions and limit global warming effects, the share of solar photovoltaics in our electricity mix has to increase from 3% today to 33% by 2050. While the mature silicon-based PV technologies have already demonstrated high power conversion efficiencies (26.8% for lab-scale cells and 24.4% for modules), new materials and architectures are required to obtain efficiencies beyond the 30% threshold. In this PhD thesis, I focused on a strategy to integrate III-V solar cells on silicon using NW arrays grown by MBE, as a first step towards the fabrication of cost-efficient tandem solar cells with high performances. The main issues addressed in this PhD work had to do with the pre-growth and growth parameters required to obtain GaAs NW arrays with near-perfect vertical yields ([Chapter 2](#)), the origin of the limited efficiency in GaAs/GaInP core-shell NW solar cells ([Chapter 3](#)), the incorporation efficiency of tellurium in self-catalyzed GaAs NWs for n-type doping purposes ([Chapter 4](#)), and finally the potential of GaAs/GaAsP axial junction NW solar cells in which the catalyst droplet has not been consumed *in-situ* ([Chapter 5](#)). For detailed conclusions of each chapter, I invite the reader to refer to the “Chapter conclusions” sections, while the main findings obtained in this PhD work are reported below.

- The selectivity of a dielectric mask layer deposited by PECVD can be degraded due to contamination in the deposition chamber, resulting in poor NW growths. **A pre-conditioning of the deposition chamber can easily restore good mask selectivity** ([subsection 2.2.1](#)).
- NW vertical yield inhomogeneity across a sample surface could be a consequence of impurities introduced during water rinsing, and left there by standard N<sub>2</sub> flow drying. A **Marangoni drying** process with a N<sub>2</sub>/2-methoxyethanol flow at a substrate withdrawal speed of 2 mm/s can circumvent this problem and allow **near-perfect NW vertical yields** (average 99.5%) to be obtained homogeneously on large-area patterns spread across the sample surface ([subsection 2.2.1](#)).
- Such pristine substrate surfaces with oxide-less mask openings also result in near-perfect vertical yields across a wide-range of mask hole diameters in the matrix patterns. The latter enabled the observation of a **direct correlation between the NW diameter and mask hole size**, for two samples grown in different MBE reactors. This opens up new opportunities for the **precise control of the diameter of self-catalyzed NWs**. However, the sample for which Marangoni drying was used actually showed lower vertical yields in the matrix patterns (higher in the large-area patterns) compared to one sample for which standard N<sub>2</sub> drying was employed. We believe that this could be a result of the slightly different effective hole aspect ratios in the two samples ([subsection 2.2.2](#)), but further investigation is required to confirm this hypothesis.
- Our champion GaAs/GaInP core-shell NW solar cell demonstrated a **high  $V_{OC}$  of 0.65 V**, a  $J_{SC}$  of 14.2 mA cm<sup>-2</sup> and a FF of 40%, resulting in a **PCE of almost 3.7%** ([subsection 3.2.1](#)).
- Current-voltage and EQE measurements under potential bias revealed the presence of interface recombinations and a photocurrent barrier hindering carrier collection, while optical simulations indicated absorption losses in the top GaInP and ITO layers ([subsections 3.2.1 to 3.2.3](#)).

- A **first-time assessment of the quasi-Fermi level splitting in NW arrays** revealed a value of **0.84 eV at 1 sun** (up to 1.01 eV at 81 suns). The latter is considerably higher than  $qV_{OC}$  (0.65 eV) and indicates **NWs of good optoelectronic quality**, but device performances hindered by inhomogeneous NW properties and/or the presence of energy barriers and recombination channels at heterointerfaces (Section 3.3).
- Numerical 1D simulations indicated that the GaP stem introduced for NW vertical yield enhancement can be a barrier for hole extraction in our NW solar cells. Nevertheless, the simulations also showed that this energy barrier can be overcome if the stem is sufficiently doped, which we believe is our case. The exact doping threshold required however depends on the GaP/Si VB offset, the value of which varies significantly in the literature (Section 3.4).
- Given the above findings, we are confident that the **performances of our NW solar cells are rather hindered by the n-type contact (GaAs/GaInP/ITO)**. Relatively low n-type doping levels resulting from the amphoteric nature of the Si dopant used in the GaInP NW shell could be one of the limiting factors.
- The incorporation efficiency of Te as an alternative n-type dopant in self-catalyzed NWs was hence investigated. Cathodoluminescence measurements enabled the **determination of the electron concentration variation in single Te-doped GaAs NWs** with nanoscale spatial resolution, using the methods previously developed in our group for Si-doped GaAs (Sections 4.3 and 4.4).
- A difference in the electron concentration levels and gradients was observed in two Te-doped GaAs NW samples grown at 620°C and 640°C, respectively. The latter could be explained by different Te incorporation efficiencies via vapor-solid and vapor-liquid-solid processes. Controlling the growth temperature could hence allow **homogeneous dopant distributions and high carrier densities to be obtained in Te-doped GaAs NWs, overcoming the limitations of the commonly used Si dopant** (subsection 4.4.3).
- GaAs/GaAsP axial junction NWs were found to exhibit two orders of magnitude higher PL intensities than bare GaAs NWs, and 8-300 times higher CL intensities than GaAs/GaInP radial junction NWs. These preliminary findings suggest that for these axial junction NWs in which the Ga droplets have not been consumed *in-situ*, **additional surface passivation mechanisms may not be required**. This could offer an interesting alternative to conventional NW passivation techniques, although further investigation is still needed to fully understand these preliminary results (subsection 5.2.3).
- A 4 min HCl:H<sub>2</sub>O (1:2) bath was found to fully remove the Ga droplets present on top of self-catalyzed NWs. However, the HCl etching was observed to impact the NWs' optical properties, requiring the former to be preferably performed after NW encapsulation in a planarization matrix (subsection 5.3.1).
- Home-made **organically-modified silica (ORMOSIL)** sol-gel was found to be a good alternative to the conventionally used BCB polymer for NW array planarization, with the additional advantage of **good thermal stability up to 450°C** (no cracks identified) (subsection 5.3.2).
- The RIE etching rate of the ORMOSIL was however observed to be much slower than the one of the SiO<sub>2</sub> layer deposited around the NWs for mechanical stability and enhanced matrix adhesion, calling for some process optimization to avoid the formation of ITO "doughnuts" that are not in contact with the NWs (subsection 5.3.3).
- Our very **first GaAs/GaAsP axial junction NW solar cells** demonstrated relatively **high  $V_{OC}$  (>0.6 V)**, but **very low  $J_{SC}$  and FF** due to significant resistive losses revealed by Jsc-Voc measurements. Analyses of J-V curves and EQE responses also indicated performance limitations coming from interface recombination and photocurrent barrier, probably arising from a positive conduction band offset at the front contact (Section 5.4).

Overall, I presented advanced characterization experiments coupled to simulation results which shed a light on the potential and challenges of NW-based III-V-on-Si solar cells. In particular, I showed that the limited performances obtained so far for solar cells made of GaAs NWs directly

grown on Si by MBE are not a result of poorly controlled NW growth, nor low intrinsic NW optoelectronic quality, but rather a consequence of contact issues. Guidelines were given to overcome the latter and carry out further technological advances.

## Perspectives

In the short-term, the development of the NW top cell remains a priority towards III-V-on-Si tandem PV devices.

The best performing NW cell presented here has an efficiency of 3.7%. The factors limiting its performances have been identified as:

1. Dislocations at the GaAs/GaInP interface potentially acting as recombination centers due to inhomogeneous shell composition.  
*Theoretical calculations from the literature suggest that these dislocations could be avoided if shells with a uniform thickness of 15 nm could be grown with a composition maintained within  $\pm 5\%$  of the GaAs-matched composition. The formation of such a NW shell would require some growth optimizations, especially since it would also have to be heavily doped to prevent from carrier depletion.*
2. Low electron concentrations in the Si-doped GaInP shell are already suspected to be at the origin of a Schottky barrier at the GaInP/ITO contact. In order to grow a thinner and heavily doped NW shell, alternative doping techniques would need to be investigated.  
*The Te incorporation study carried out in this PhD work on self-catalyzed GaAs NWs showed promising results. Next, it would be interesting to investigate the incorporation efficiency of Te in GaInP NW shells, in order to see if higher electron concentrations could be obtained, and if the latter would lead to improved contact conductivity and hence cell performances. Modulation doping like the delta-doping technique employed during the growth of the sample presented in Chapter 3 could also be further investigated in the aim of increasing the n-type doping level in the Si-doped NW segments.*
3. Parasitic absorption by the thicker GaInP segment at the top of the NWs.  
*The growth of a thinner GaInP shell would also reduce the thickness of this top segment and hence limit parasitic absorption.*
4. Thermally unstable BCB planarization material preventing a high-temperature annealing which could improve n-contact conductivity.  
*The organically-modified silica (ORMOSIL) sol-gel developed in this PhD work showed good planarization properties, with in particular a better thermal stability than BCB. It would be interesting then to see whether the performances of the aforementioned cell could be improved by replacing the BCB with ORMOSIL for NW array planarization, and carrying out an annealing at a temperature of 450°C, or even above. However, the modification of the properties of the ITO layer upon such a high-temperature annealing would also have to be investigated.*
5. Inhomogeneous NW properties.  
*The substrate and growth conditions required to obtain NW arrays with near-perfect vertical yields and controlled diameters have been identified in this PhD work. The latter should help obtain more homogeneous NW properties. However, the reliable control of these conditions still needs to be verified on a higher number of samples. In this context, it would also be interesting to investigate whether the GaP stem really plays a role in the near-perfect vertical yields obtained for the GaAs NW arrays.*

Given the on-going debate on the NW junction geometries, I believe that in the short-term NW solar cells with p-n junctions formed in both the axial and radial directions should be developed in parallel. The luminescence results obtained in this PhD work on GaAs/GaAsP axial junction NWs in which the Ga droplets have not been consumed *in-situ* are very promising for axial junction cell performances improvement. However, further passivation studies coupled with transmission electron microscopy measurements are required to better understand the preliminary results obtained. In the near future, research efforts thus still have to be focused on binary compounds such as GaAs to limit complexity, before transitioning to ternary alloys such as GaAsP, with a bandgap tailored

for a tandem-on-Si PV device.

Finally, it is important to keep in mind that even in the optimal configuration, it is unlikely that NW solar cells will exceed the performances of planar devices. However, they can instead relax the requirements needed to reach high efficiencies, and open up the door to low-cost III-V/Si solar cells. In addition, the knowledge gained regarding the growth of vertical NW arrays, their characterization, dopant incorporation mechanisms, surface passivation, planarization, and contact formation, could also very well serve other fields of application. In fact, self-catalyzed III-V NWs are also widely studied for the fabrication of light-emitting diodes, lasers, transistors and photodetectors.



## Appendix A

# Impact of the RIE etching parameters on the Si/SiO<sub>2</sub> interface

This appendix serves as an explanation for the parameters (in particular bias) used in the reactive ion etching (RIE) processes (SF<sub>6</sub>-CHF<sub>3</sub> and O<sub>2</sub>) described in [subsection 2.2.1](#). As previously mentioned, during the transfer of the lithographically defined photoresist patterns into the SiO<sub>2</sub> mask layer using RIE with SF<sub>6</sub>-CHF<sub>3</sub> gases, care is taken to not completely etch open the mask holes. The few nm of SiO<sub>2</sub> remaining inside the mask holes are left there to prevent plasma-induced damage to the underlying Si. In fact, studies have established unambiguously that reactive ion etching of Si or SiO<sub>2</sub> could induce severe surface modifications, including the introduction of lattice damage in a near-surface region, and the penetration of impurities into a deep layer via ion implantation or diffusion effects [[Arora, 1987](#); [Oehrlein, 1989](#)]. As RIE is characterized by a large number of process parameters (etching gases, power, bias etc.) which can impact the character of the plasma-induced damage, our group decided a few years ago (before the start of this PhD work) to look into the influence of the RIE processes (SF<sub>6</sub>-CHF<sub>3</sub> and O<sub>2</sub>) on the Si/SiO<sub>2</sub> interface in our substrates. In particular, we wondered whether (1) the subsequent HF “development” could be impacted by the RIE processes, and if so, whether the extent of the impact would depend on (2) the applied plasma bias and the nature of the gases in the plasma (SF<sub>6</sub>-CHF<sub>3</sub> and O<sub>2</sub>), and/or (3) on the doping of the Si(111) substrate. As these effects could not be investigated directly in the nanoscale mask holes, an experiment based on the study of full 2-inch wafer surfaces was designed.

### Experimental methods

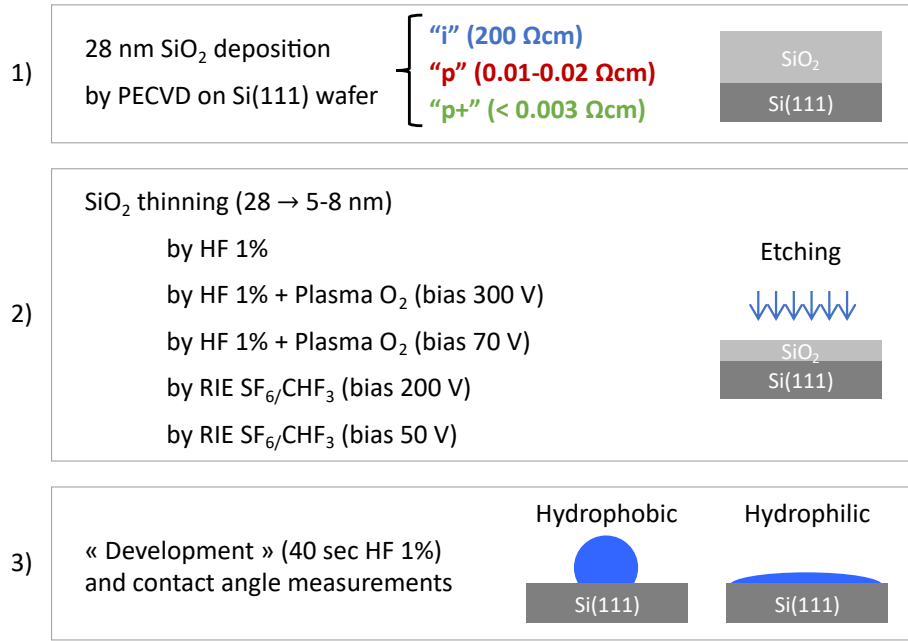
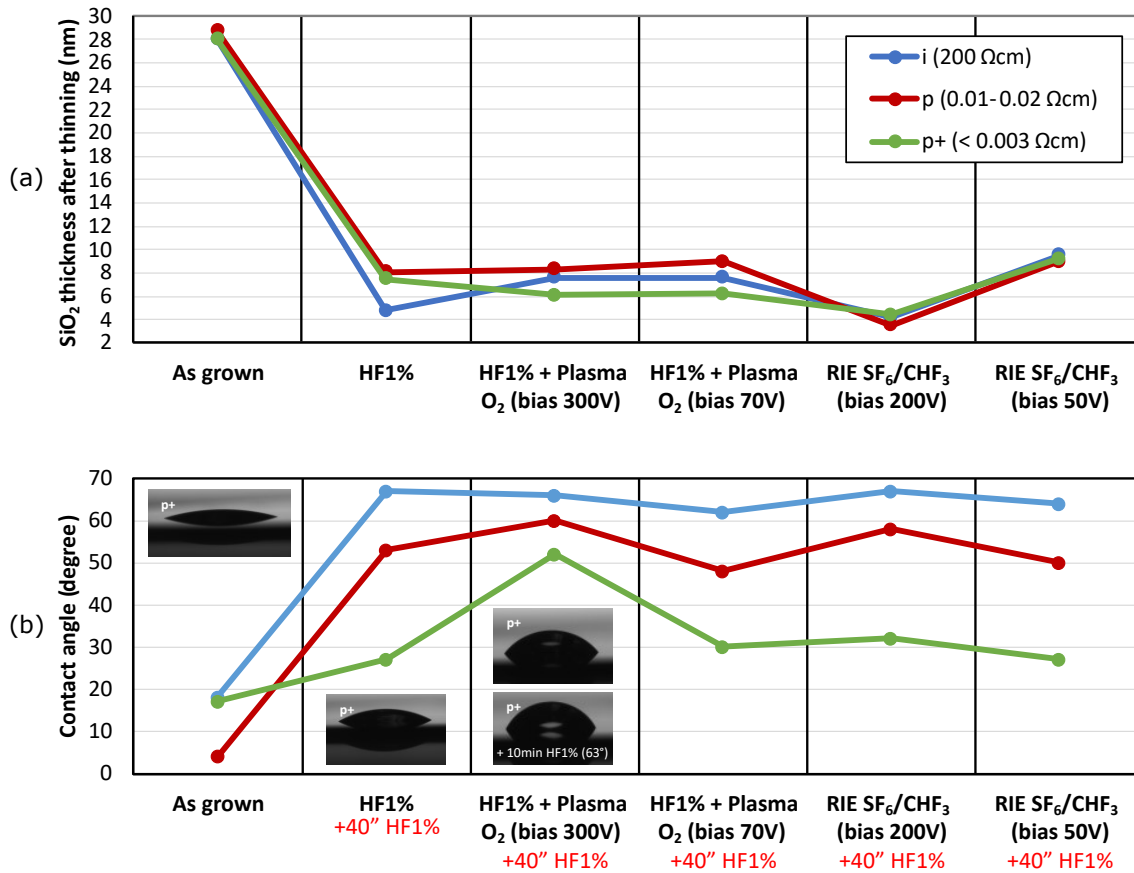
The experiment consisted in first depositing around 30 nm of SiO<sub>2</sub> (28 nm precisely) by PECVD on 3 types of Si(111) wafers: namely intrinsic (i), p-doped (p), and heavily p-doped (p<sup>+</sup>) wafers. This corresponds to step 1 of the experimental methods summarized in [Figure A.1](#). Then, the SiO<sub>2</sub> layer was etched to the nominal thickness expected in the mask holes (< 10 nm), using different processes indicated in step 2 of [Figure A.1](#). The sample etched solely by a 1% HF solution served as a reference sample. Despite the fact that both SF<sub>6</sub>-CHF<sub>3</sub> and O<sub>2</sub> plasmas are performed in our substrate preparation process (subsequently), their effect on the Si/SiO<sub>2</sub> interface was assessed independently in this study, with a focus placed on the bias applied in each of the plasma etching process. Finally, all samples were “developed” during 40 s in a 1% HF solution in order to remove the remaining SiO<sub>2</sub>. The surface-wetting characteristic of each Si wafer was then evaluated through contact angle measurements with water. Step 3 in [Figure A.1](#) reminds the reader that hydrophobic surfaces tend to repel water (high contact angles), whereas water tends to spread and adhere to hydrophilic surfaces (low contact angles).

### Results

[Figure A.2b](#) summarizes the contact angles recorded for the different samples. Intrinsic Si(111) wafers were observed to consistently exhibit higher contact angles (blue in [Figure A.2b](#)), while p<sup>+</sup> wafers (green) demonstrated the lowest contact angles regardless of the SiO<sub>2</sub> etching process. X-ray photoelectron spectroscopy (XPS) measurements not shown here, indicated that the aforementioned contact angle trend could be correlated to the amount of oxygen and carbon contamination remaining on the wafer surface after the etching processes. In fact, XPS spectra obtained from

i-Si(111), p-Si(111) and p<sup>+</sup>-Si(111) wafers having undergone a HF 1% + Plasma O<sub>2</sub> (both low and high bias) + 40 s 1% HF “development”, revealed that the intensity of the O1s and C1s peaks (proportional to oxygen and carbon surface contamination, respectively) followed the same order: i-Si(111) < p-Si(111) < p<sup>+</sup>-Si(111).

In addition, the water contact angle was observed to increase for all wafers having been exposed to a high bias plasma, regardless of the gases used. This is once again consistent with the XPS data (not shown), which indicated lower O1s and C1s contamination peaks for wafers having been exposed to a high bias (300 V) O<sub>2</sub> plasma. The cleaner surfaces obtained after a high bias plasma could be explained by either the formation of a more stoichiometric SiO<sub>2</sub> layer which is more easily etched in the 1% HF solution, and/or a stronger oxidizing power of the high bias plasma. In fact, the O<sub>2</sub> plasma at high bias may further oxidize (and hence trap) the residual carbon impurities on the SiO<sub>2</sub> surface, which will then be dissolved in the 1% HF solution.

Figure A.1: Summary of the experiment designed to study the impact of the RIE processes (SF<sub>6</sub>-CHF<sub>3</sub> and O<sub>2</sub>) on the Si/SiO<sub>2</sub> interface.Figure A.2: (a) SiO<sub>2</sub> layer thicknesses obtained after different etching processes, as measured by spectroscopic reflectometry. (b) Water contact angle measurements on the corresponding substrates after a 40 s “development” in a 1% HF solution.



# Appendix B

## Communication and Recognition

### Oral presentations

1. C. Tong, R. de Lépinau, T. Bidaud, A. Delamarre, B. Béranguier, J.-F. Guillemoles, G. Patriarche, F. Oehler, J.-C. Harmand, S. Collin, A. Cattoni, "MBE-grown GaAs/InGaP nanowires for solar cell applications", Seminar for the C2N Materials Department, December 2020, France.
2. C. Tong, R. de Lépinau, A. Scaccabarozzi, F. Oehler, G. Patriarche, T. Bidaud, B. Béranguier, L. Lombez, J.-F. Guillemoles, J.-C. Harmand, S. Collin, A. Cattoni, "Record Voc and quasi-Fermi level splitting in MBE-grown GaAs/InGaP nanowires on Si for tandem solar cells", Journées Nationales du PhotoVoltaire (JNPV), January 2021, *Online*.
3. C. Tong, R. de Lépinau, H. Xu, T. Bidaud, A. Delamarre, B. Béranguier, J.-F. Guillemoles, F. Oehler, A. Scaccabarozzi, S. Collin, A. Cattoni, "GaAs/InGaP on Si nanowire solar cells with high Voc and quasi-Fermi level splitting", European Materials Research Society (EMRS) Spring Meeting, May 2021, *Online*.
4. C. Tong, R. de Lépinau, A. Delamarre, A. Scaccabarozzi, F. Oehler, G. Patriarche, T. Bidaud, B. Béranguier, L. Lombez, J.-F. Guillemoles, J.-C. Harmand, S. Collin, A. Cattoni, "GaAs/InGaP on Si nanowire solar cells with high Voc and quasi-Fermi level splitting", C'Nano, November 2021, France.
5. C. Tong, R. de Lépinau, A. Delamarre, A. Scaccabarozzi, F. Oehler, G. Patriarche, T. Bidaud, B. Béranguier, L. Lombez, J.-F. Guillemoles, J.-C. Harmand, S. Collin, A. Cattoni, "State-of-the-Art Voc and Quasi-Fermi Level Splitting in GaAs/GaInP Nanowire Solar Cells directly Grown on Si", 8th World Conference on Photovoltaic Energy Conversion (WCPEC-8), September 2022, Italy.

### Peer-reviewed Publications

1. C. Tong, T. Bidaud, E. Koivusalo, M. Piton, M. Guina, H. Galeti, Y. Gobato, A. Cattoni, T. Hakkarainen, S. Collin, "Cathodoluminescence mapping of electron concentration in MBE-grown GaAs:Te nanowires", *Nanotechnology*, 33 (18), p185704, 2022.
2. C. Tong, A. Delamarre, R. De Lépinau, A. Scaccabarozzi, F. Oehler, J.-C. Harmand, S. Collin, A. Cattoni, "GaAs/GaInP nanowire solar cell on Si with state-of-the-art Voc and quasi-Fermi level splitting", *Nanoscale*, 14 (35), pp12722-12735, 2022.

### Recognition

1. C. Tong, A. Delamarre, T. Bidaud, R. de Lépinau, E. Koivusalo, M. Piton, M. Guina, F. Oehler, B. Béranguier, J.-C. Harmand, T. Hakkarainen, A. Cattoni, S. Collin, "Luminescence as a valuable characterization tool from single III-V NWs to complete solar cells", *Best Poster Award* at the Nanowire Week, April 2022, France.
2. C. Tong, A. Delamarre, R. De Lépinau, A. Scaccabarozzi, F. Oehler, J.-C. Harmand, S. Collin, A. Cattoni, "Selective-area growth of III-V nanowire arrays on Si and their application for tandem solar cells", *Invited Talk* at the Journées Nationales du PhotoVoltaire (JNPV), December 2022, France.





## Appendix C

# Summary in French / Résumé en langue française

### Introduction

Depuis la révolution industrielle (1850-1900), la température moyenne à la surface du globe a augmenté de 1.1°C. Il est désormais incontestable que ce réchauffement climatique est une conséquence des émissions de gaz à effet de serre d'origine humaine, et que si rien n'est fait les conséquences sur la planète et l'humanité seront dramatiques et irréversibles [IPCC, 2013]. Avec actuellement plus de 60% de la production mondiale d'électricité issue de combustibles fossiles, la production d'électricité reste le premier secteur émetteur de CO<sub>2</sub> dans le monde [Climate TRACE, 2022]. Avec l'augmentation de nos usages électriques, l'agence internationale de l'énergie (AIE) estime que nos besoins en électricité vont doubler d'ici 2050. Afin de limiter le réchauffement climatique et ses conséquences néfastes, il est alors impératif de déployer rapidement des sources de production d'électricité renouvelables et bas-carbones.

En 2020, la part des énergies renouvelables dans la production mondiale d'électricité s'élevait à 30% (3% pour le solaire photovoltaïque). Afin de réaliser les objectifs fixés lors de la 26<sup>ème</sup> Conférence des Parties (COP26) et d'atteindre la neutralité carbone d'ici 2050, 88% de notre électricité devra être d'origine renouvelable (33% d'origine solaire photovoltaïque) [International Energy Agency, 2021a]. Le solaire photovoltaïque (PV) permet de produire une énergie électrique à partir du rayonnement solaire grâce à des panneaux PV, constitués de cellules solaires. Le marché du PV pour la production terrestre d'électricité est aujourd'hui dominé à 95% par des technologies à base de silicium (Si). Ces dernières ont connu des améliorations significatives en termes de performances et de rentabilité au cours des dernières décennies, leur permettant d'être désormais compétitifs par rapport à d'autres sources de production d'électricité. Cependant, on approche aujourd'hui la limite fondamentale de l'efficacité de conversion des cellules solaires en Si (29% [Niewelt et al., 2022]), et d'autres technologies sont nécessaires pour atteindre des efficacités au-dessus de la barre des 30%.

Les technologies PV combinant plusieurs cellules à base de différents matériaux, superposées les unes aux autres, permettent d'aller au-delà de 30% d'efficacité de conversion en maximisant l'utilisation du spectre solaire. La forte complémentarité des cellules solaires à base de semiconducteurs III-V avec les cellules Si permettrait la formation d'une cellule tandem (deux cellules superposées) bénéficiant à la fois de la maturité technologique et industrielle des cellules en Si, et des meilleures performances des III-V. En effet, les semiconducteurs III-V comprennent une large gamme de composés connus notamment pour leurs bonnes propriétés opto-électroniques. Cependant, l'intégration de semiconducteurs III-V sur une cellule en Si est loin d'être triviale à cause du désaccord de maille et des différences d'expansion thermique entre les deux matériaux. En effet, lorsque des couches III-V planaires sont directement crues sur du Si, des dislocations s'y forment inévitablement, dégradant les performances du dispositif. Une alternative à la croissance directe de semiconducteurs III-V sur Si existe cependant. Elle consiste d'abord en la synthèse de couches III-V sur un substrat III-V. Puis, il s'agit de décoller cette couche pour la reporter sur une cellule en Si afin de former la structure tandem. Cette approche a déjà permis d'obtenir des efficacités de conversion de 35.9%, cependant sa complexité et le coût élevé des substrats III-V utilisés sont un frein pour un déploiement à l'échelle industrielle.

L'utilisation de semiconducteurs III-V sous forme de nanofils (NF) permet de contourner élégamment les problèmes découlant de la croissance directe de couches planaires sur Si. En effet,

de par leur faible diamètre, les NFs peuvent relaxer les contraintes mécaniques liées au désaccord de maille et aux différences d'expansion thermique, sans générer de défauts. Par ailleurs, disposés sur un plan vertical, les NFs agissent comme un entonnoir à lumière, et arrivent à absorber plus de photons incidents que leurs homologues planaires, tout en utilisant moins de matériau. La croissance directe de réseaux de NFs III-V sur Si devrait donc permettre la fabrication de cellules tandem hautes performances, à un coût raisonnable. Des modèles à base de NFs avec une bande interdite optimale de 1.7 eV ont montré une efficacité théorique de 33% pour une cellule tandem sur Si [Lapierre, 2011]. Seuls certains composés III-V ternaires comme le  $\text{In}_{0.65}\text{Ga}_{0.35}\text{P}$ ,  $\text{Al}_{0.19}\text{Ga}_{0.81}\text{As}$  ou  $\text{GaAs}_{0.77}\text{P}_{0.23}$  ont une bande interdite optimale de 1.7 eV, cependant leur composition est souvent difficile à maîtriser, et ce sont des systèmes qui ont beaucoup moins été étudiés que par exemple le GaAs. C'est pour cela que la plupart des efforts de recherche, dont ceux effectués dans cette thèse, ont pour l'instant été concentrés sur la croissance de NFs en GaAs. Des preuves de concepts ont déjà illustré le potentiel des cellules à base de NFs en GaAs, néanmoins celles crues sur Si ont pour l'instant des performances encore assez limitées (efficacité record de 7.7% [Mukherjee et al., 2021]).

La recherche effectuée dans le cadre de cette thèse a donc pour but ultime la fabrication d'une cellule solaire tandem à base de NFs III-V crues sur Si. Pour atteindre cet objectif, nous nous sommes concentrés dans un premier temps sur l'optimisation de la cellule supérieure de la structure tandem, c'est à dire la cellule à base de NFs en GaAs, crues par épitaxie par jets moléculaires (MBE) sur des substrats en Si inactifs, patternés pour former des réseaux organisés de NFs. J'ai notamment étudié les étapes de préparation du substrat étant critiques pour la croissance de NFs avec un haut taux de verticalité, ainsi que le contrôle du diamètre des NFs à partir de la taille des ouvertures du masque patterné (**Chapitre 2**). Dans un deuxième temps, des cellules solaires à base de NFs à jonctions GaAs/GaInP coeur-coquille ont été fabriqués et caractérisés. Le **Chapitre 3** présente les performances de ces cellules, qui ont démontré un  $V_{OC}$  de 0.65 V et un rendement de 3.7%, à l'état de l'art des cellules NFs en GaAs à jonctions radiales. Dans ce même chapitre est présentée une étude approfondie des propriétés opto-électroniques des cellules susmentionnées, basée sur la quantification de la séparation des quasi-niveaux de Fermi dans les NFs. Des simulations optiques et électroniques ont également été effectuées afin d'identifier les principales pertes d'absorption et pertes électriques. En particulier, des améliorations au niveau du contact de type n ont été jugées nécessaires pour favoriser l'extraction des électrons. Le **Chapitre 4** expose tout d'abord l'importance du contrôle du dopage dans les NFs, et souligne les difficultés pour obtenir des niveaux élevés de dopage de type n dans la coquille des NFs en GaAs lorsque le dopant Si est utilisé. Le tellure (Te), en tant qu'élément du groupe VI dans le tableau périodique, est un dopant de type n alternatif au Si qui pourrait permettre d'atteindre des concentrations d'électrons plus élevées dans les NFs en GaAs. Au cours de mon doctorat, j'ai eu l'opportunité de collaborer avec l'Université de Tampere (Finlande) pour étudier l'incorporation du Te dans des NFs de GaAs en utilisant la cartographie par cathodoluminescence (CL). Les méthodes de CL à température ambiante et à basse température développées dans notre groupe pour quantifier les concentrations d'électrons dans du GaAs dopé Si ont tout d'abord été validées sur des échantillons planaires de GaAs dopé Te. Ces méthodes ont ensuite été utilisées pour étudier l'impact de la température de croissance sur l'efficacité d'incorporation du dopant Te dans des NFs en GaAs. Enfin, le **Chapitre 5** évalue tout d'abord les avantages et désavantages des NFs à jonctions axiales par rapport aux NFs à jonctions radiales. Des résultats préliminaires portant sur les propriétés opto-électroniques de NFs à jonctions GaAs/GaAsP axiales y sont ensuite présentés. Ces NFs ont la particularité de posséder une gouttelette de catalyseur qui n'a pas été consommée in-situ à des fins de passivation. Cette dernière a plutôt été gravée ex-situ. Ensuite, les optimisations effectuées sur le processus de fabrication des cellules solaires NFs sont exposées, avant de présenter les performances de nos toutes premières cellules solaires NFs à jonction axiales. Ces dernières ont révélé des valeurs de  $V_{OC}$  relativement élevées ( $> 0.6$  V), mais de très faibles  $J_{SC}$  et FF, en partie due à de grandes pertes résistives dans les dispositifs et des barrières de potentiel au niveau du contact de type n.

## Croissance directe de réseaux de nanofils en GaAs sur Si

Afin d'obtenir des réseaux organisés de NFs avec un taux de verticalité élevé, la qualité du masque de silice est très importante. Cette dernière est en lien étroit avec la sélectivité du masque, qui au début de cette thèse a été dégradée par une contamination de la chambre de dépôt PECVD. Après

investigation, nous avons déterminé qu'un pré-conditionnement de la chambre de dépôt PECVD suffisait pour restaurer une bonne sélectivité du masque, ce qui à son tour a favorisé la croissance de réseaux de NFs avec de bons taux de verticalité. Néanmoins, nous avons remarqué des taux de verticalité inhomogènes sur la surface d'un même échantillon, probablement dus à des impuretés introduites sur la surface du substrat lors du rinçage et séchage finaux, à l'eau déionisée et à l'azote, respectivement. Un nouveau procédé de séchage connue sous le nom de séchage Marangoni a alors été exploré. Les surfaces les plus propres ont été obtenues en utilisant un flux de  $N_2/2$ -méthoxyéthanol et une vitesse de retrait du substrat de 2 mm/s, ce qui a permis d'obtenir des taux de verticalité quasi-parfaits (99,5% en moyenne), de façon homogène sur de grandes surfaces de l'échantillon, comme on peut le voir dans la [Figure C.1](#).

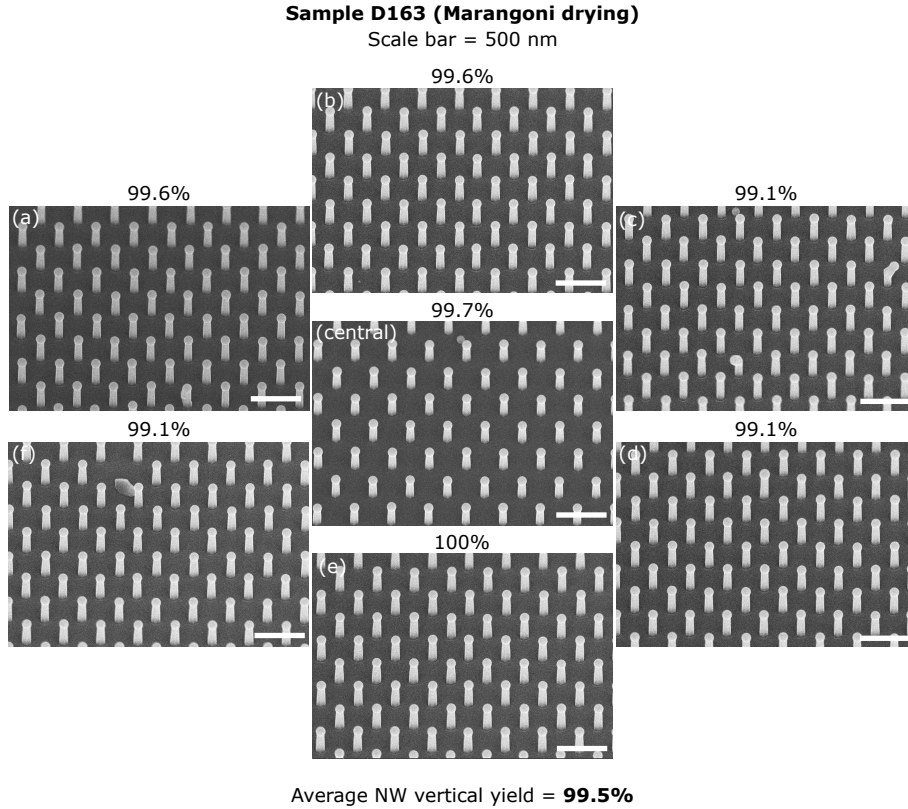


Figure C.1: Images MEB des 7 motifs de grande surface de l'échantillon D163 (carrés rouges à droite de la [Figure 2.9](#)), avec un espacement de 360 nm entre les NFs. Des taux de verticalité quasi-parfaits calculés sur des surfaces d'environ  $100 \mu m^2$  sont indiqués par les pourcentages.

Ces surfaces de substrats propres et dépourvues d'oxyde dans les ouvertures du masque ont également permis d'observer de très hauts taux de verticalité dans les motifs à matrices, sur une large gamme de taille d'ouvertures du masque. Ceci a alors rendu possible l'observation d'une corrélation directe entre le diamètre des NFs et la taille des trous du masque, pour deux échantillons crus dans des réacteurs MBE différents, comme indiqué dans la [Figure C.2](#). La corrélation susmentionnée laisse apparaître de nouvelles perspectives pour la maîtrise du diamètre des NFs auto-catalysés. Néanmoins, un plus faible taux de verticalité a été observé dans le motif à matrices de l'échantillon pour lequel un séchage Marangoni avait été réalisé (taux de verticalité plus élevés dans les motifs de grande surface) par rapport à l'échantillon pour lequel un séchage standard  $N_2$  avait été employé. Nous pensons que cela pourrait être le résultat de rapports d'aspect légèrement différents pour les ouvertures du masque des deux échantillons, mais une enquête plus approfondie serait nécessaire pour confirmer cette hypothèse.

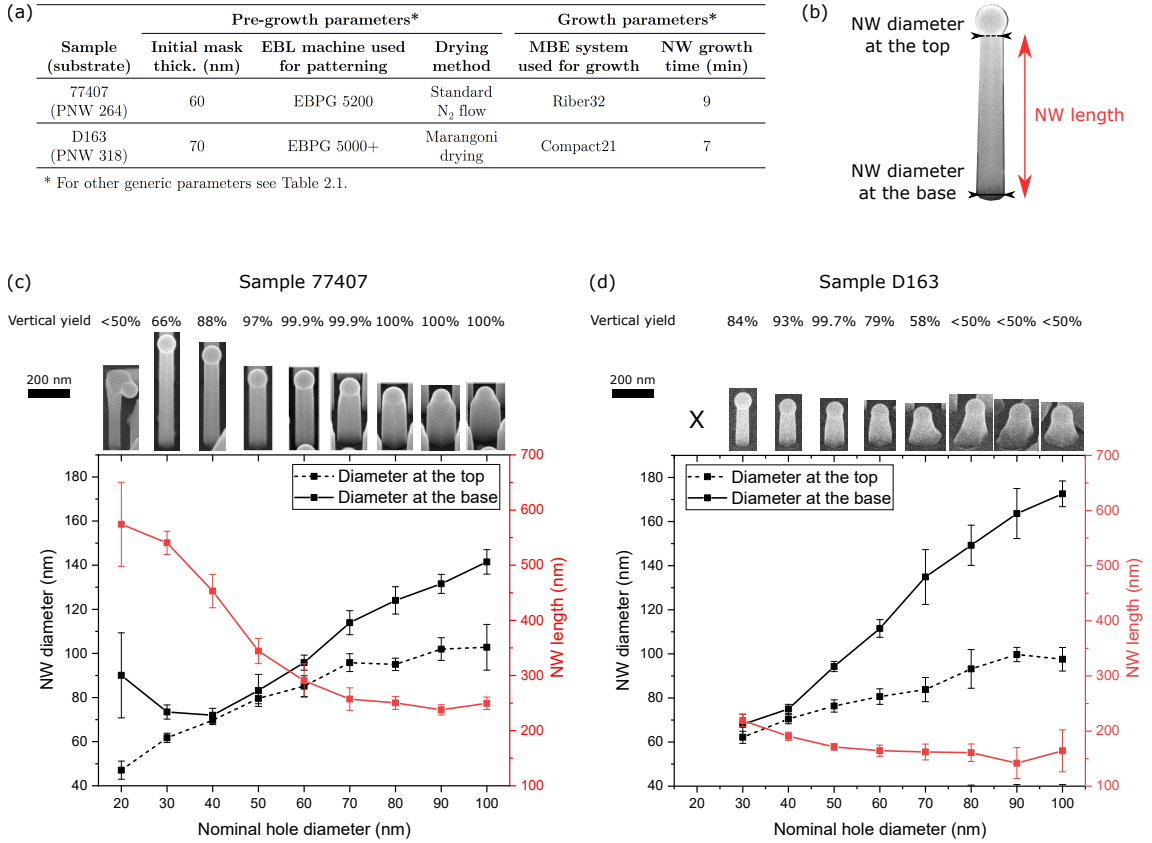


Figure C.2: (a) Tableau résumant les paramètres de croissance et de pré-croissance qui diffèrent pour les échantillons 77407 et D163. (b) Schéma illustrant la méthode de mesure des dimensions des NFs. (c) et (d): Évolution du diamètre (à la base et au sommet) et de la longueur des NFs des échantillons 77407 et D163, en fonction du diamètre nominal des ouvertures du masque, pour les matrices ayant un espacement de 250 nm entre les NFs. Une image MEB d'un NF représentatif de chaque réseau se trouve au-dessus des graphes, ainsi que le taux de verticalité calculé à partir de surfaces > 5 µm<sup>2</sup>. Les images MEB entières à partir desquelles les NFs représentatifs ont été extraits se trouvent dans la Figure 2.16.

## Fabrication et caractérisation de cellules solaires à base de nanofils à jonctions GaAs/GaInP radiales

L'architecture des cellules NFs à jonctions GaAs/GaInP radiales est présentée dans la Figure C.3a. Comme indiqué par les caractéristiques J-V de la Figure C.3b, la cellule record a démontré un  $V_{OC}$  élevé de 0,65 V, un  $J_{SC}$  de 14,2 mA cm<sup>-2</sup> et un FF de 40%, donnant un rendement de presque 3,7%. Combinées aux spectres d'EQE obtenus sous tension de polarisation (Figure 3.7), ces mesures révèlent la présence de recombinaisons d'interface et d'une barrière de photocourant empêchant la collecte des porteurs. Par ailleurs, les simulations optiques indiquent de l'absorption parasite dans les couches supérieures en GaInP et ITO (Figure C.3b).

Les propriétés opto-électroniques de ces cellules ont ensuite été évaluées à l'aide de mesures de photoluminescence (PL) hyperspectrales. La séparation des quasi-niveaux de Fermi a été quantifiée pour la première fois dans des réseaux organisés de NFs. Une valeur de 0,84 eV a été obtenue à 1 soleil (1,01 eV à 81 soleils) ce qui est considérablement plus élevée que le  $qV_{OC}$  et indique des NFs de bonne qualité opto-électronique, ainsi qu'une marge importante pour l'amélioration de nos dispositifs. L'augmentation du dopage de type n dans la coquille des NFs pourrait être une des pistes d'amélioration. Dans ce contexte, nous avons étudié l'efficacité de l'incorporation du tellure (Te) comme dopant de type n alternatif au Si dans les NFs en GaAs auto-catalysés.

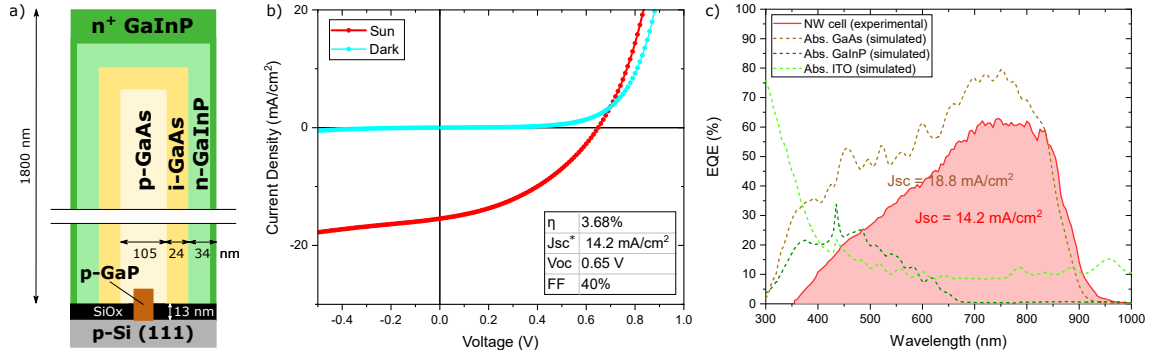


Figure C.3: (a) Représentation schématique des dimensions des NFs à hétéro-jonctions GaAs/GaInP radiales. (b) Courbes J-V mesurées dans l'obscurité (bleue) et sous un soleil (rouge). \* La valeur de  $J_{SC}$  présentée provient de l'intégration du spectre EQE. (c) Spectres EQE de la cellule record (rouge), ainsi que des absorptions simulées pour des couches de GaAs, GaInP et ITO (pointillés) en utilisant le modèle simplifié présenté dans la Figure 3.8a.

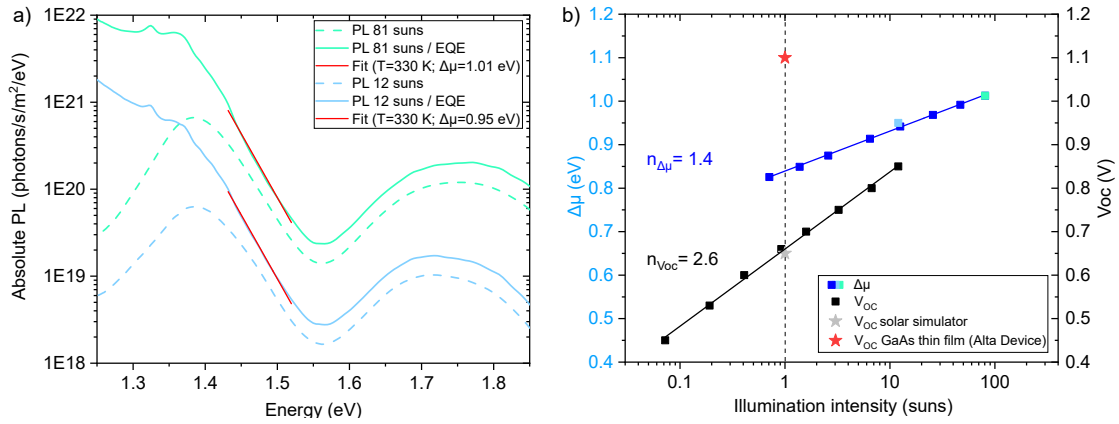


Figure C.4: (a) Spectres de PL calibrés en unités absolues de la cellule record, obtenus sous une illumination de 12 et 81 soleils (pointillés). Ces spectres sont le résultat d'une moyenne réalisée sur une surface d'environ  $50 \times 50 \mu\text{m}^2$ . Les mêmes spectres divisés par l'EQE de la cellule sont également présentés (traits pleins), ainsi que leur ajustement à la loi de Planck généralisée, entre 1,43-1,52 eV (rouge). (b) Évolution de la séparation des quasi-niveaux de Fermi ( $\Delta\mu$ , bleu), et de la tension de circuit ouvert ( $V_{OC}$ , noir), en fonction de l'intensité d'illumination. Les carrés bleus clairs et cyan correspondent à la séparation des quasi-niveaux de Fermi obtenus à partir d'images de PL résolues spectralement, tandis que les carrés bleus foncés ont été obtenus à partir d'images simples intégrant toutes les longueurs d'onde. Le  $V_{OC}$  record des cellules planaires en GaAs est indiqué par une étoile rouge (Alta Devices [Kayes et al., 2011]).

## Étude sur le dopage tellure dans des nanofils en GaAs

L'efficacité de l'incorporation des atomes de Te dans des NWs en GaAs auto-catalysés a été étudiée en utilisant la cathodoluminescence (CL). Les mesures de CL ont permis de déterminer la variation de la concentration d'électrons dans des NFs uniques avec une résolution spatiale à l'échelle nanométrique, en utilisant des méthodes précédemment développées dans notre groupe pour du GaAs dopé Si.

Les deux échantillons Te-NW1 (crû à  $640^\circ\text{C}$ ) et Te-NW2 (crû à  $620^\circ\text{C}$ ) ont montré une concentration d'électrons inférieure d'un ordre de grandeur à la concentration nominale calibrée par croissances planaires, conformément aux études précédentes. Un gradient de concentration d'électrons allant de moins de  $1 \times 10^{18} \text{ cm}^{-3}$  à  $3.3 \times 10^{18} \text{ cm}^{-3}$  a été déterminé le long de l'axe du NF de l'échantillon Te-NW1 (Figure C.5). En revanche, une concentration homogène d'électrons d'environ  $6-8 \times 10^{17} \text{ cm}^{-3}$  a été observée le long de l'axe du NF de l'échantillon Te-NW2 (Figure C.6), soulign-



nant la possibilité d'obtenir des distributions homogènes de dopants dans des NFs en GaAs dopés Te. Les différences de niveaux et de gradients de concentration d'électrons entre les échantillons Te-NW1 et Te-NW2 (Figure C.7) peuvent être expliquées par des efficacités d'incorporation de Te différentes via les processus vapeur-solide et vapeur-liquide-solide.

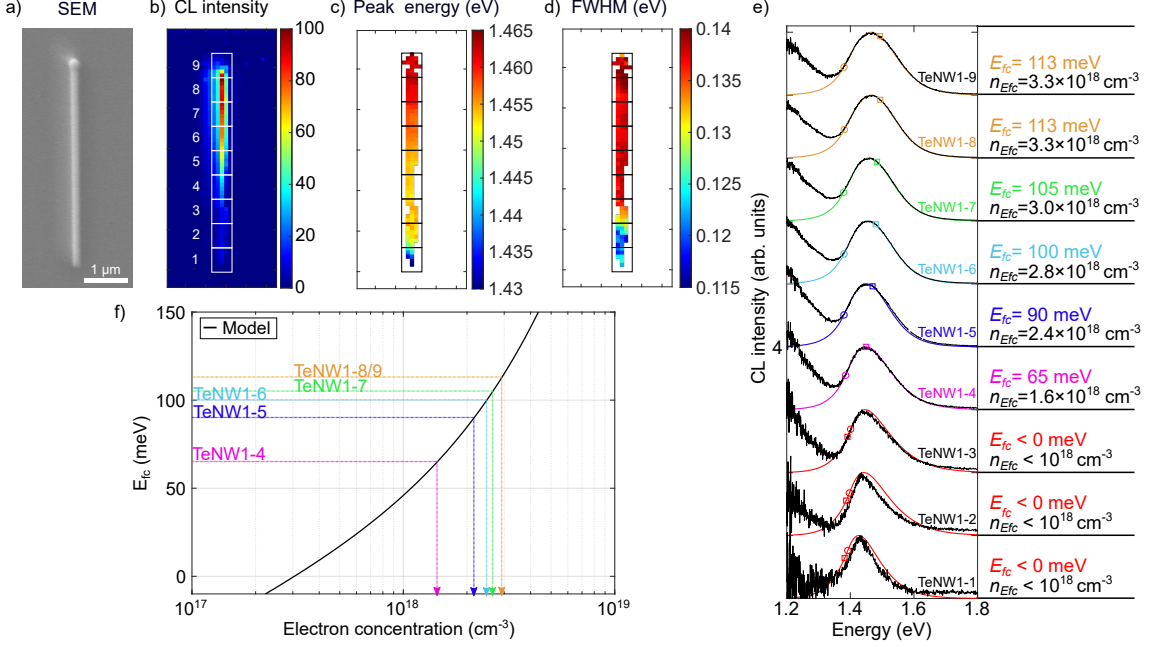


Figure C.5: (a) Image MEB d'un NF de l'échantillon Te-NW1 mesuré en CL à température ambiante. (b), (c) et (d): Cartographies de l'intensité de CL, de l'énergie du pic de CL, et de la largeur à mi-hauteur, respectivement. (e) Spectres de CL moyennés sur les 9 zones délimitées en (b), et leurs ajustements respectifs à la loi de Planck généralisée (courbes colorées). Les cercles et les carrés correspondent respectivement à la bande interdite et le quasi-niveau de Fermi des électrons ( $E_{fc}$ ), déterminés par les ajustements. Les valeurs de  $E_{fc}$  sont également indiquées à droite des spectres de CL, de même que les concentrations d'électrons correspondantes déterminées à l'aide d'un modèle de bandes non-paraboliques.

Dans l'ensemble, cette étude a démontré que la haute résolution spatiale de la cathodoluminescence fait d'elle une technique puissante pour caractériser la concentration réelle de porteurs dans des NFs uniques en GaAs. Cette concentration de porteurs peut ensuite être corrélée à certains paramètres de croissance (ici la température de croissance). Le contrôle de ces paramètres de croissance pourrait alors permettre d'obtenir des distributions de dopants homogènes et des densités d'électrons élevées dans des NFs en GaAs, surmontant ainsi les limitations liées au dopant Si couramment utilisé. Il serait intéressant, dans de futures expériences, d'étudier l'efficacité de l'incorporation d'atomes de Te dans la coquille GaInP de NFs, afin de déterminer si les performances de la cellule solaire NFs présentée dans la section précédente pourraient être améliorées en remplaçant le dopant Si par du Te. Plus généralement, une telle amélioration de l'évaluation et du contrôle du dopage et, par conséquent des propriétés, des NFs, contribuera sans aucun doute à la conception de dispositifs électroniques de nouvelle génération.

## Fabrication et caractérisation de cellules solaires à base de nanofils à jonctions GaAs/GaAsP axiales

La passivation de NFs auto-catalysés devrait idéalement avoir lieu dans la chambre de croissance, mais sans passer par la consommation des gouttelettes de catalyseur, connue pour induire un mélange de phases cristallines et la formation de défauts dans les NFs. Dans ce contexte, nous avons décidé d'étudier l'efficacité de passivation de la coquille formée non-intentionnellement pendant la croissance axiale des NFs. Des NFs à jonctions GaAs/GaAsP et GaAs/GaAsP/GaP axiales



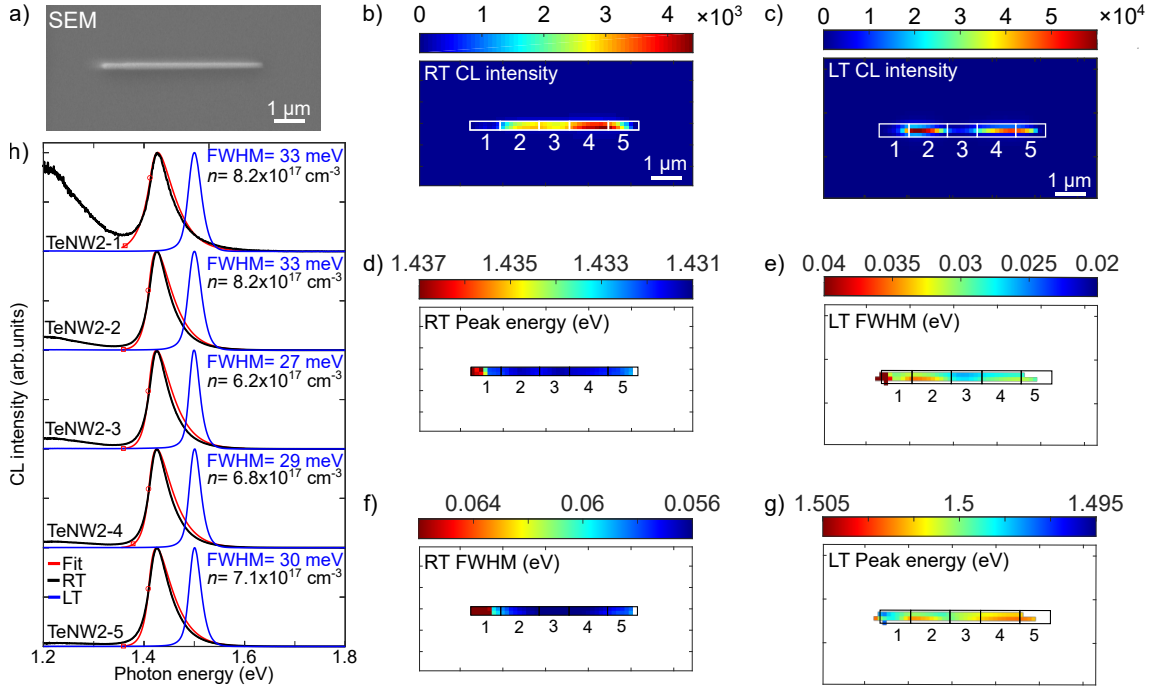


Figure C.6: (a) Image MBE d'un NF de l'échantillon Te-NW2 mesuré en CL. Cartographies panchromatiques de l'intensité de CL à (b) température ambiante, et (c) basse température. (d) et (e): Cartographies correspondantes de la largeur à mi-hauteur du pic de CL. (f) et (g): Cartographies correspondantes de l'énergie du pic de CL. Les 5 zones délimitées en (b) et (c) correspondent aux zones sur lesquelles les spectres de CL tracés en (h) ont été moyennés. Les spectres obtenus à température ambiante sont en noir, tandis que ceux obtenus à basse température sont en bleu. Les courbes rouges correspondent aux ajustements des spectres à température ambiante à la loi de Planck généralisée. Les cercles et les carrés correspondent respectivement à la bande interdite et au quasi-niveau de Fermi des électrons ( $E_{fc}$ ), déterminés par les ajustements. Les concentrations d'électrons ( $n$ ) indiquées à droite des courbes ont été obtenues à partir des valeurs de largeur à mi-hauteur à basse température, en utilisant un modèle empirique illustré dans la Figure 4.4d.

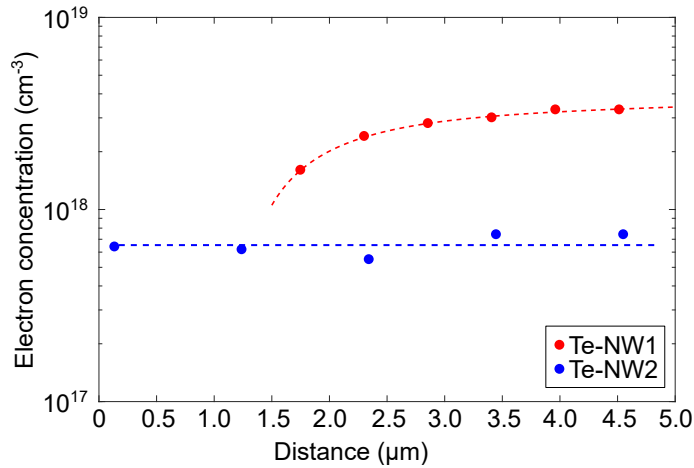


Figure C.7: Variation spatiale de la concentration d'électrons le long de l'axe du NF crû à 640°C (Te-NW1, rouge) et de celui crû à 620°C (Te-NW2, bleu). La base des NFs est à 0 μm. Les lignes pointillées servent de guides visuels.

ont été crus pour cette étude. La croissance de segments en GaAsP et GaAsP/GaP dopés Si a permis d'augmenter de manière significative les intensités de PL et CL par rapport à des NFs en GaAs non-passivés, et des NFs à jonctions GaAs/GaInP radiales. Ces résultats préliminaires suggèrent de bonnes propriétés opto-électroniques pour les NFs à jonctions axiales, mais ces derniers ne peu-

vent pas être directement attribués à la formation d'une coquille radiale crue pendant la croissance axiale VLS. Des mesures complémentaires de STEM-EDX seraient nécessaires pour confirmer cette corrélation et évaluer la composition, ainsi que l'épaisseur, de la coquille radiale susmentionnée, afin d'aider à comprendre son effet sur les états de surface.

Comme on peut le voir dans la Figure C.8, un bain de HCl:H<sub>2</sub>O (1:2) de 4 min a permis d'éliminer complètement les gouttelettes de Ga présentes sur le dessus des NFs auto-catalysés. Cependant, on a observé que la gravure au HCl avait un impact sur les propriétés optiques des NFs, incitant la gravure à être effectuée de préférence après l'encapsulation des NFs dans une matrice de planérisation.

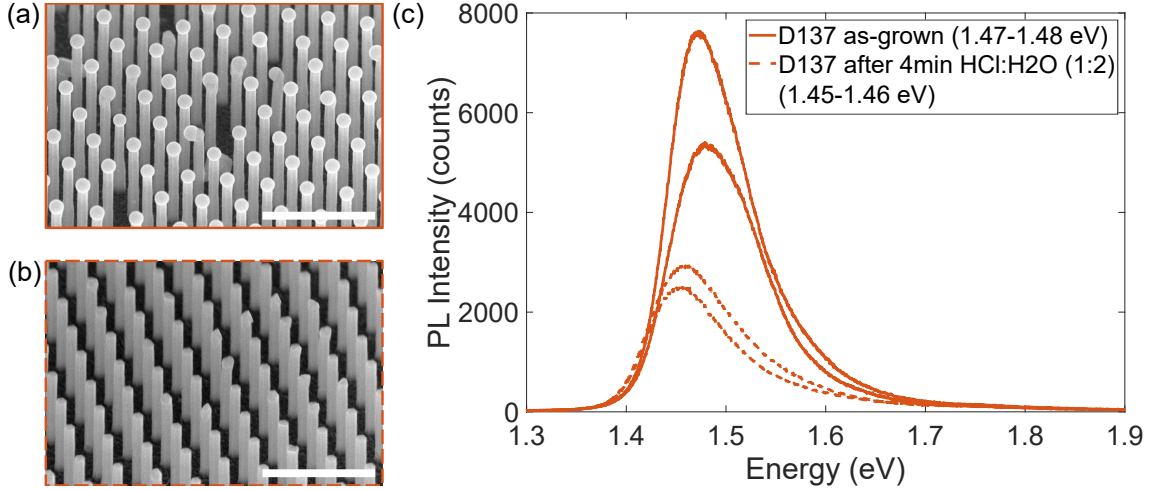


Figure C.8: Image MEB avec vue inclinée (45°) d'un réseau de NFs appartenant à l'échantillon D137, avec un espacement de 350 nm entre les NFs, (a) avant, et (b) après, un bain de HCl:H<sub>2</sub>O (1:2) de 4 min. (c) Spectres de PL correspondants, mesurés sur deux différentes zones du réseau de NFs.

Un sol-gel de silice modifié organiquement (ORMOSIL) a par la suite été synthétisé dans le but de trouver une alternative au polymère BCB communément utilisé pour l'encapsulation des NFs. Ce dernier a démontré de très bonnes propriétés de planérisation, avec l'avantage supplémentaire d'une bonne stabilité thermique jusqu'à 450°C (aucun fissure observée). Après de nouvelles optimisations du processus de gravure par RIE et de dépôt de la couche d'ITO, nos premières cellules à jonctions axiales ont été fabriquées. Les caractéristiques J-V d'une des cellules sont présentées dans la Figure C.9a. Cette dernière est représentative des autres cellules du même échantillon, et démontre un  $V_{OC}$  relativement élevé mais de très faibles  $J_{SC}$  et FF. Ceci a pu être en parti corrélé à d'importantes résistances séries révélées par des mesures de Suns-Voc (Figure C.9b). L'analyse des courbes J-V combinée à l'examen des spectres d'EQE indiquent également des limitations de performances liées à des recombinaisons d'interface, et des barrières de photocourant, probablement découlant d'alignements de bandes non-optimales au niveau du contact avant.

## Conclusion

En résumé, cette thèse a traité de différents aspects liés à la préparation des substrats de Si patternés, conduisant à la croissance de réseaux de NFs en GaAs présentant des taux de verticalité quasi-parfaits, de façon reproductible. Ceci a permis l'observation d'une corrélation entre les dimensions des ouvertures du masque et le diamètre des NFs, laissant apparaître de nouvelles perspectives pour la maîtrise du diamètre des NFs auto-catalysés. La caractérisation de cellules solaires NFs à base de jonctions GaAs/GaInP radiales a révélé des performances à l'état de l'art des cellules solaires à base de NFs à jonctions GaAs radiales crues sur Si ( $V_{OC}=0,65$  V;  $J_{SC} = 14,1$  mA cm<sup>-2</sup>; FF=0.4;  $\eta=3.7\%$ ). Par ailleurs, la quantification de la séparation des quasi-niveaux de Fermi dans les NFs ont indiqué de meilleures qualités opto-électroniques que celles auxquelles on aurait pu s'attendre par les mesures électriques ( $\Delta\mu$  élevé de 0,84 eV,  $> qV_{OC}$ ). Une marge importante

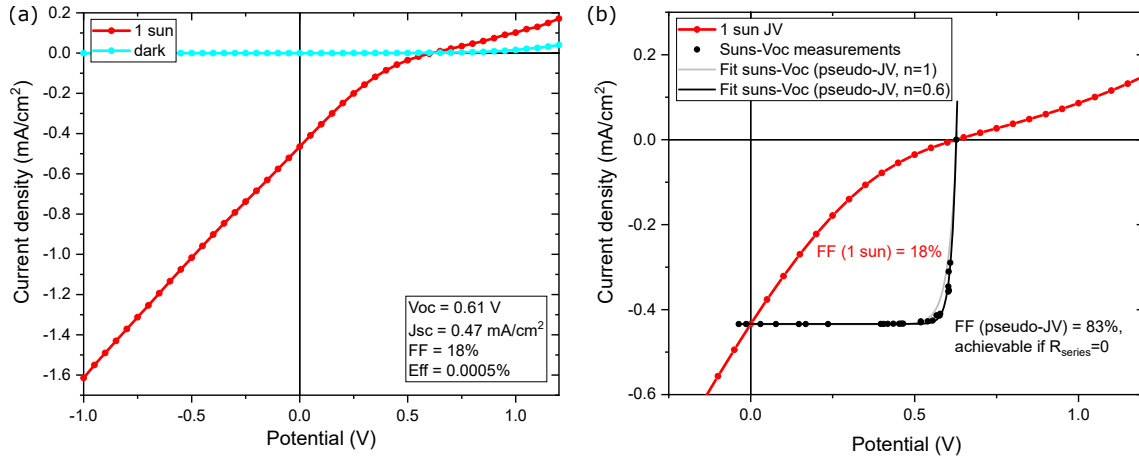


Figure C.9: Caractéristiques J-V de la cellule C16 de l'échantillon D144. (a) Courbes J-V mesurées dans l'obscurité (bleu) et sous 1 soleil (rouge). (b) Comparaison de la courbe J-V mesurée sous 1 soleil avec la pseudo-courbe J-V obtenue par des mesures de Suns-Voc.

demeure donc pour l'amélioration de ces dispositifs. L'augmentation du dopage de type n dans la coquille des NFs a été identifié comme une des pistes d'amélioration. Dans ce contexte, nous avons étudié l'efficacité de l'incorporation du tellure (Te) comme dopant de type n alternatif au Si dans les NFs en GaAs auto-catalysés. La caractérisation par cathodoluminescence a permis d'identifier la température de croissance comme un paramètre critique pour obtenir des distributions de dopants Te homogènes et des densités de porteurs élevés. L'utilisation du Te comme dopant de type n dans des NFs en GaAs permettrait alors potentiellement de surmonter les limitations liées au dopant Si couramment utilisé. La prochaine étape consisterait à étudier l'efficacité de l'incorporation des atomes de Te dans des coquilles de NFs en GaAs et GaInP. Enfin, la caractérisation par luminescence de NFs à jonctions GaAs/GaAsP/GaP et GaAs/GaAsP axiales a révélé des propriétés opto-électroniques prometteuses pour des NFs n'ayant pas été passivés avec des méthodes conventionnelles. Cependant, des mesures complémentaires seraient nécessaires pour évaluer les états de surface de ces NFs, tandis qu'une meilleure conception de l'architecture de ces NFs permettrait un alignement de bandes améliorant l'extraction des électrons au niveau du contact de type n.

Dans l'ensemble, ce travail de thèse a contribué à des avancées technologiques significatives, et les caractérisations avancées ainsi que les résultats de simulation présentés ont mis en lumière le potentiel et les défis des cellules solaires à base de NFs III-V sur Si. A court terme, l'élaboration de la cellule NFs supérieure reste donc une priorité pour les dispositifs tandem III-V sur Si. Compte tenu du débat en cours sur la géométrie des jonctions NFs, les cellules solaires NFs à jonctions radiales devraient continuer à être développées en parallèle de celles à jonctions axiales. Les efforts de recherche doivent pour l'instant encore se concentrer sur des NFs en GaAs pour limiter la complexité, avant de passer à des alliages ternaires comme le GaAsP, ayant une bande interdite optimale pour une cellule solaire tandem sur Si. Enfin, il est important de garder à l'esprit que même dans une configuration optimale, il est peu probable que les cellules solaires NFs dépassent les performances des dispositifs planaires. Néanmoins, elles peuvent assouplir les exigences nécessaires pour atteindre des efficacités élevées, et faire apparaître de nouvelles perspectives pour l'élaboration de cellules solaires III-V sur Si à bas coût. En outre, les connaissances acquises sur la croissance de réseaux verticaux de NFs, leur caractérisation, mécanismes de dopage, passivation de surface, planérisation et formation de contacts, pourraient également servir à d'autres domaines d'application. En effet, les NFs auto-catalysés à base de semiconducteurs III-V sont aussi largement étudiés pour la fabrication de diodes électroluminescentes, lasers, transistors et photo-détecteurs.



# Bibliography

- Aberg, I., Vescovi, G., Asoli, D., Naseem, U., Gilboy, J. P., Sundvall, C., Dahlgren, A., Svensson, K. E., Anttu, N., Bjork, M. T., and Samuelson, L. A GaAs nanowire array solar cell with 15.3% efficiency at 1 sun. *IEEE Journal of Photovoltaics*, 6(1):185–190, 2016. ISSN 21563381. doi: 10.1109/JPHOTOV.2015.2484967. (Cited on page [18](#), [19](#))
- Abou-Ras, D., Kirchartz, T., and Rau, U. *Advanced Characterization Techniques for Thin Film Solar Cells: Second Edition*, volume 1-2. Wiley-VCH, 2016. ISBN 9783527699025. doi: 10.1002/9783527699025. (Cited on page [61](#))
- Aifantis, K. E., Kolesnikova, A. L., and Romanov, A. E. Nucleation of misfit dislocations and plastic deformation in core/shell nanowires. *Philosophical Magazine*, 87(30):4731–4757, 2007. ISSN 14786435. doi: 10.1080/14786430701589350. (Cited on page [53](#), [85](#))
- Alekseev, P. A., Dunaevskiy, M. S., Ulin, V. P., Lvova, T. V., Filatov, D. O., Nezhdanov, A. V., Mashin, A. I., and Berkovits, V. L. Nitride surface passivation of GaAs nanowires: Impact on surface state density. *Nano Letters*, 15(1):63–68, 2015. ISSN 15306992. doi: 10.1021/nl502909k. (Cited on page [85](#))
- Almora, O., Cabrera, C. I., Garcia-Cerrillo, J., Kirchartz, T., Rau, U., and Brabec, C. J. Quantifying the Absorption Onset in the Quantum Efficiency of Emerging Photovoltaic Devices. *Advanced Energy Materials*, 11(16), 2021. ISSN 16146840. doi: 10.1002/aenm.202100022. (Cited on page [99](#))
- Angermann, H., Henrion, W., Röseler, A., and Rebien, M. Wet-chemical passivation of Si(111)- and Si(100)-substrates. *Materials Science and Engineering B: Solid-State Materials for Advanced Technology*, 73(1):178–183, 2000. ISSN 09215107. doi: 10.1016/S0921-5107(99)00457-2. (Cited on page [37](#))
- Anttu, N. and Xu, H. Q. Efficient light management in vertical nanowire arrays for photovoltaics. *Optics Express*, 21(S3):A558–A575, 2013. ISSN 10944087. doi: 10.1364/oe.21.00a558. (Cited on page [19](#))
- Arora, B. M. Reactive ion-etching-induced damage in silicon using SF<sub>6</sub> gas mixtures. *Journal of Vacuum Science & Technology B: Microelectronics and Nanometer Structures*, 5(4):876, 1987. ISSN 0734211X. doi: 10.1116/1.583683. (Cited on page [39](#), [109](#))
- Ashcroft, N. W. and Mermin, N. D. *Solid State Physics*. Harcourt College Publishers, 1976. doi: 10.1063/1.3022632. (Cited on page [14](#))
- Bachmann, K. J., Schreiber, H., Sinclair, W. R., Schmidt, P. H., Thiel, F. A., Spencer, E. G., Pasteur, G., Feldmann, W. L., and Sreeharsha, K. Solar-cell characteristics and interfacial chemistry of indium-tin-oxide/indium phosphide and indium-tin-oxide/gallium arsenide junctions. *Journal of Applied Physics*, 50(5):3441–3446, 1979. ISSN 00218979. doi: 10.1063/1.326337. (Cited on page [66](#))
- Bahrami, D., Mostafavi Kashani, S. M., Al Hassan, A., Davtyan, A., and Pietsch, U. High yield of self-catalyzed GaAs nanowire growth on silicon (111) substrate templated by focused ion beam patterning. *Nanotechnology*, 31(18):185302, 2020. ISSN 13616528. doi: 10.1088/1361-6528/ab6d99. (Cited on page [34](#), [35](#))
- Balasubramanian, N. and Subrahmanyam, A. Schottky diode properties and the photovoltaic behaviour of indium tin oxide (ITO)/n-GaAs junctions-effect of arsenic deficient GaAs surface. *Semiconductor Science and Technology*, 5(8):871–876, 1990. ISSN 02681242. doi: 10.1088/0268-1242/5/8/012. (Cited on page [66](#))

- Barrigón, E., Heurlin, M., Bi, Z., Monemar, B., and Samuelson, L. Synthesis and Applications of III–V Nanowires. *Chemical Reviews*, 119(15):9170–9220, 2019. ISSN 0009-2665. doi: 10.1021/acs.chemrev.9b00075. (Cited on page 33)
- Barrigón, E., Zhang, Y., Hrachowina, L., Otnes, G., and Borgström, M. T. Unravelling processing issues of nanowire-based solar cell arrays by use of electron beam induced current measurements. *Nano Energy*, 71(2007):104575, 2020. ISSN 22112855. doi: 10.1016/j.nanoen.2020.104575. (Cited on page 60)
- Becquerel, E. Comptes rendus hebdomadaires des séances de l’Académie des sciences. *Comptes rendus Académie des Sciences*, (July):561–567, 1839. (Cited on page 5, 11)
- Bercegol, A. *Transport de charge dans le photovoltaïque par imagerie multidimensionnelle de luminescence*. PhD thesis, PSL Research University, 2020. (Cited on page 23, 24)
- Bett, A. W., Dimroth, F., Stollwerck, G., and Sulima, O. V. III-V compounds for solar cell applications. *Applied Physics A: Materials Science and Processing*, 69(2):119–129, 1999. ISSN 09478396. doi: 10.1007/s003390050983. (Cited on page 14)
- Bidaud, T. *Characterization of nanomaterials by cathodoluminescence for photovoltaic applications*. PhD thesis, Université Paris-Saclay, 2021. (Cited on page 21, 90, 91)
- Blakemore, J. S. Semiconducting and other major properties of gallium arsenide. *Journal of Applied Physics*, 53(10):123–181, 1982. ISSN 00218979. doi: 10.1063/1.331665. (Cited on page 22, 74, 75)
- Blömers, C., Grap, T., Lepsa, M. I., Moers, J., Trellenkamp, S., Grützmacher, D., Lüth, H., and Schäpers, T. Hall effect measurements on InAs nanowires. *Applied Physics Letters*, 101:152106, 2012. ISSN 00036951. doi: 10.1063/1.4759124. (Cited on page 69)
- Boland, J. L., Conesa-Boj, S., Parkinson, P., Tütüncüoglu, G., Matteini, F., Rüffer, D., Casadei, A., Amaduzzi, F., Jabeen, F., Davies, C. L., Joyce, H. J., Herz, L. M., Fontcuberta I Morral, A., and Johnston, M. B. Modulation doping of GaAs/AlGaAs core-shell nanowires with effective defect passivation and high electron mobility. *Nano Letters*, 15(2):1336–1342, 2015. ISSN 15306992. doi: 10.1021/nl504566t. (Cited on page 70)
- Boland, J. L., Casadei, A., Tütüncüoglu, G., Matteini, F., Davies, C. L., Jabeen, F., Joyce, H. J., Herz, L. M., Fontcuberta i Morral, A., and Johnston, M. B. Increased Photoconductivity Lifetime in GaAs Nanowires by Controlled n-Type and p-Type Doping. *ACS Nano*, 10(4):4219–4227, 2016. ISSN 1936086X. doi: 10.1021/acsnano.5b07579. (Cited on page 70)
- Boland, J. L., Tütüncüoglu, G., Gong, J. Q., Conesa-Boj, S., Davies, C. L., Herz, L. M., Fontcuberta Morral, A., and Johnston, M. B. Towards higher electron mobility in modulation doped GaAs/AlGaAs core shell nanowires. *Nanoscale*, 9(23):7839–7846, 2017. ISSN 20403372. doi: 10.1039/c7nr00680b. (Cited on page 70)
- Borghs, G., Bhattacharyya, K., Deneffe, K., Van Mieghem, P., and Mertens, R. Band-gap narrowing in highly doped n- and p-type GaAs studied by photoluminescence spectroscopy. *Journal of Applied Physics*, 66(9):4381–4386, 1989. ISSN 00218979. doi: 10.1063/1.343958. (Cited on page 70)
- Bosmans, J. H., Dammeier, L. C., and Huijbregts, M. A. Greenhouse gas footprints of utility-scale photovoltaic facilities at the global scale. *Environmental Research Letters*, 16(9), 2021. ISSN 17489326. doi: 10.1088/1748-9326/ac1df9. (Cited on page 16)
- Boulanger, J. P., Chia, A. C., Wood, B., Yazdi, S., Kasama, T., Aagesen, M., and LaPierre, R. R. Characterization of a Ga-Assisted GaAs Nanowire Array Solar Cell on Si Substrate. *IEEE Journal of Photovoltaics*, 6(3):661–667, 5 2016. ISSN 21563381. doi: 10.1109/JPHOTOV.2016.2537547. URL <http://ieeexplore.ieee.org/document/7434568/>. (Cited on page 18, 36, 43, 52, 56)
- Burgelman, M., Nollet, P., and Degraeve, S. Modelling polycrystalline semiconductor solar cells. *Thin Solid Films*, 361:527–532, 2000. ISSN 00406090. doi: 10.1016/S0040-6090(99)00825-1. (Cited on page 62)



- Burstein, E. Anomalous optical absorption limit in InSb [4]. *Physical Review*, 93(3):632–633, 1954. ISSN 0031899X. doi: 10.1103/PhysRev.93.632. (Cited on page 74)
- Capper, P., Irvine, S., and Joyce, T. Epitaxial Crystal Growth: Methods and Materials. In Kasap, S. and Capper, P., editors, *Springer Handbook of Electronic and Photonic Materials*, chapter 14, pages 271–303. Springer Science & Business Media, 2007. ISBN 9780387260594. doi: [https://doi.org/10.1007/978-0-387-29185-7{\\\_}14](https://doi.org/10.1007/978-0-387-29185-7{\_}14). (Cited on page 29, 30)
- Casadei, A., Krogstrup, P., Heiss, M., Röhr, J. A., Colombo, C., Ruelle, T., Upadhyay, S., Sørensen, C. B., Nygård, J., and Fontcuberta I Morral, A. Doping incorporation paths in catalyst-free Be-doped GaAs nanowires. *Applied Physics Letters*, 102(1), 2013. ISSN 00036951. doi: 10.1063/1.4772020. (Cited on page 69)
- Casey, H. C. and Stern, F. Concentration-dependent absorption and spontaneous emission of heavily doped GaAs. *Journal of Applied Physics*, 47(2):631–643, 1976. ISSN 00218979. doi: 10.1063/1.322626. (Cited on page 70)
- Chai, Y. G., Chow, R., and Wood, C. E. The effect of growth conditions on Si incorporation in molecular beam epitaxial GaAs. *Applied Physics Letters*, 39(10):800–803, 1981. ISSN 00036951. doi: 10.1063/1.92562. (Cited on page 68)
- Chang, C. C., Chi, C. Y., Yao, M., Huang, N., Chen, C. C., Theiss, J., Bushmaker, A. W., Lalumondiere, S., Yeh, T. W., Povinelli, M. L., Zhou, C., Dapkus, P. D., and Cronin, S. B. Electrical and optical characterization of surface passivation in GaAs nanowires. *Nano Letters*, 12(9):4484–4489, 2012. ISSN 15306984. doi: 10.1021/nl301391h. (Cited on page 68, 85)
- Chapin, D. M., Fuller, C. S., and Pearson, G. L. Solar Energy Conversion Apparatus, 1957. (Cited on page 5)
- Chen, H.-L., Himwas, C., Scaccabarozzi, A., Rale, P., Oehler, F., Lemaitre, A., Lombez, L., Guillemoles, J.-F., Tchernycheva, M., Harmand, J.-C., Cattoni, A., and Collin, S. Determination of n-Type Doping Level in Single GaAs Nanowires by Cathodoluminescence. *Nano Letters*, 17: 6667–6675, 2017. (Cited on page 21, 71, 73, 74, 76, 80)
- Chen, H. L., De Lépinau, R., Scaccabarozzi, A., Oehler, F., Harmand, J. C., Cattoni, A., and Collin, S. Quantitative Assessment of Carrier Density by Cathodoluminescence. II. GaAs nanowires. *Physical Review Applied*, 15(2):024007, 2021a. ISSN 23318422. doi: 10.1103/physrevapplied.15.024007. URL <https://doi.org/10.1103/PhysRevApplied.15.024007>. (Cited on page 54, 66, 68, 69, 71, 74, 80)
- Chen, H. L., Scaccabarozzi, A., Lepinau, R. D., Oehler, F., Lemaitre, A., Harmand, J. C., Cattoni, A., and Collin, S. Quantitative Assessment of Carrier Density by Cathodoluminescence. I. GaAs Thin Films and Modeling. *Physical Review Applied*, 15(2):024006, 2021b. ISSN 23318422. doi: 10.1103/physrevapplied.15.024006. URL <https://doi.org/10.1103/PhysRevApplied.15.024006>. (Cited on page 21, 54, 71, 73, 74, 75, 76, 80)
- Chen, M. H.-l. *Ultrathin and nanowire-based GaAs solar cells*. PhD thesis, Université Paris-Saclay, 2018. (Cited on page 21, 85)
- Cheng, Y. and Ding, L. Perovskite/Si tandem solar cells: Fundamentals, advances, challenges, and novel applications. *SusMat*, 1(3):324–344, 2021. ISSN 2692-4552. doi: 10.1002/sus2.25. (Cited on page 17)
- Chia, A. C., Tirado, M., Li, Y., Zhao, S., Mi, Z., Comedi, D., and Lapierre, R. R. Electrical transport and optical model of GaAs-AlInP core-shell nanowires. *Journal of Applied Physics*, 111(9), 2012. ISSN 00218979. doi: 10.1063/1.4716011. (Cited on page 85)
- Chia, A. C., Tirado, M., Thouin, F., Leonelli, R., Comedi, D., and Lapierre, R. R. Surface depletion and electrical transport model of AlInP-passivated GaAs nanowires. *Semiconductor Science and Technology*, 28(10), 2013. ISSN 02681242. doi: 10.1088/0268-1242/28/10/105026. (Cited on page 85)

- Chia, A. C. E. and LaPierre, R. R. Contact planarization of ensemble nanowires. *Nanotechnology*, 22(24):245304, 6 2011. ISSN 0957-4484. doi: 10.1088/0957-4484/22/24/245304. URL <https://iopscience.iop.org/article/10.1088/0957-4484/22/24/245304>. (Cited on page 93)
- Christesen, J. D., Pinion, C. W., Zhang, X., McBride, J. R., and Cahoon, J. F. Encoding abrupt and uniform dopant profiles in vapor-liquid-solid nanowires by suppressing the reservoir effect of the liquid catalyst. *ACS Nano*, 8(11):11790–11798, 2014. ISSN 1936086X. doi: 10.1021/nm505404y. (Cited on page 68)
- Chuang, L. C., Moewe, M., Chase, C., Kobayashi, N. P., Chang-Hasnain, C., and Crankshaw, S. Critical diameter for III-V nanowires grown on lattice-mismatched substrates. *Applied Physics Letters*, 90(4):043115, 1 2007. ISSN 0003-6951. doi: 10.1063/1.2436655. URL <http://aip.scitation.org/doi/10.1063/1.2436655>. (Cited on page 19)
- Climate TRACE. Tracking Real-time Atmospheric Carbon Emissions, 2022. (Cited on page 5, 115)
- Collins, D. M., Miller, J. N., Chai, Y. G., and Chow, R. Sn and Te doping of molecular beam epitaxial GaAs using a SnTe source. *Journal of Applied Physics*, 53(4):3010–3018, 1982. ISSN 00218979. doi: 10.1063/1.331042. (Cited on page 80)
- Colombo, C., Spirkoska, D., Frimmer, M., Abstreiter, G., and Fontcuberta I Morral, A. Ga-assisted catalyst-free growth mechanism of GaAs nanowires by molecular beam epitaxy. *Physical Review B - Condensed Matter and Materials Physics*, 77(15):155326, 2008. ISSN 10980121. doi: 10.1103/PhysRevB.77.155326. (Cited on page 34)
- Colombo, C., Heiß, M., Grätzel, M., and Fontcuberta I Morral, A. Gallium arsenide p-i-n radial structures for photovoltaic applications. *Applied Physics Letters*, 94(17):13–16, 2009. ISSN 00036951. doi: 10.1063/1.3125435. (Cited on page 29, 68, 84)
- Couto, O. D., Sercombe, D., Puebla, J., Otubo, L., Luxmoore, I. J., Sich, M., Elliott, T. J., Chekhovich, E. A., Wilson, L. R., Skolnick, M. S., Liu, H. Y., and Tartakovskii, A. I. Effect of a GaAsP shell on the optical properties of self-catalyzed GaAs nanowires grown on silicon. *Nano Letters*, 12(10):5269–5274, 2012. ISSN 15306984. doi: 10.1021/nl302490y. (Cited on page 29, 85, 92)
- Cui, Y., Duan, X., Hu, J., and Lieber, C. M. Doping and electrical transport in silicon nanowires. *Journal of Physical Chemistry B*, 104(22):5215–5216, 2000. ISSN 15206106. doi: 10.1021/jp0009305. (Cited on page 69)
- Cui, Y., Van Dam, D., Mann, S. A., Van Hoof, N. J., Van Veldhoven, P. J., Garnett, E. C., Bakkers, E. P., and Haverkort, J. E. Boosting Solar Cell Photovoltage via Nanophotonic Engineering. *Nano Letters*, 16(10):6467–6471, 2016. ISSN 15306992. doi: 10.1021/acs.nanolett.6b02971. (Cited on page 59)
- Dabrowski, J. and Müssig, H.-J. *Silicon surfaces and formation of interfaces : basic science in the industrial world*. World Scientific, River Edge, N.J, 2000. ISBN 978-981-02-3286-3. (Cited on page 5)
- Darbandi, A. and Watkins, S. P. Measurement of minority carrier diffusion lengths in GaAs nanowires by a nanoprobe technique. *Journal of Applied Physics*, 120(1), 2016. ISSN 10897550. doi: 10.1063/1.4955136. URL <http://dx.doi.org/10.1063/1.4955136>. (Cited on page 85)
- Darbandi, A., Salehzadeh, O., Kuyanov, P., Lapierre, R. R., and Watkins, S. P. Surface passivation of tellurium-doped GaAs nanowires by GaP: Effect on electrical conduction. *Journal of Applied Physics*, 115(23), 2014. ISSN 10897550. doi: 10.1063/1.4883960. (Cited on page 85)
- Darbandi, A., McNeil, J. C., Akhtari-Zavareh, A., Watkins, S. P., and Kavanagh, K. L. Direct measurement of the electrical abruptness of a nanowire p-n junction. *Nano Letters*, 16(7):3982–3988, 2016. ISSN 15306992. doi: 10.1021/acs.nanolett.6b00289. (Cited on page 68)

- Dastjerdi, M. H. T., Boulanger, J. P., Kuyanov, P., Aagesen, M., and LaPierre, R. R. Methods of Ga droplet consumption for improved GaAs nanowire solar cell efficiency. *Nanotechnology*, 27(47):475403, 2016. ISSN 0957-4484. doi: 10.1088/0957-4484/27/47/475403. URL <http://iopscience.iop.org/0957-4484/27/47/475403><http://stacks.iop.org/0957-4484/27/i=47/a=475403?key=crossref.db5d965b092ca9c57327d1398844019d>. (Cited on page 18, 35, 36, 56, 85, 90, 92)
- de Lépinau, R. *GaAs-on-Si solar cells based on nanowire arrays grown by molecular beam epitaxy*. PhD thesis, Université Paris-Saclay, 2020. (Cited on page 20, 33, 36, 37, 39, 48, 51, 53, 54, 56, 66, 69, 84, 93)
- De-Sheng, J., Makita, Y., Ploog, K., and Queisser, H. J. Electrical properties and photoluminescence of Te-doped GaAs grown by molecular beam epitaxy. *Journal of Applied Physics*, 53(2): 999–1006, 1982. ISSN 00218979. doi: 10.1063/1.330581. (Cited on page 22, 70, 74)
- Delamarre, A. *Development of luminescence based characterisation methods for solar cells*. PhD thesis, Université Pierre et Marie Curie, 2013. (Cited on page 24)
- Delamarre, A., Lombez, L., and Guillemoles, J. F. Contactless mapping of saturation currents of solar cells by photoluminescence. *Applied Physics Letters*, 100(13):131108, 2012. ISSN 00036951. doi: 10.1063/1.3697704. (Cited on page 59)
- Demichel, O., Heiss, M., Bleuse, J., Mariette, H., and Fontcuberta Morral, I. A. Impact of surfaces on the optical properties of GaAs nanowires. *Applied Physics Letters*, 97(20):201907, 2010. ISSN 00036951. doi: 10.1063/1.3519980. (Cited on page 92)
- Dimakis, E., Ramsteiner, M., Tahraoui, A., Riechert, H., and Geelhaar, L. Shell-doping of GaAs nanowires with Si for n-type conductivity. *Nano Research*, 5(11):796–804, 11 2012. ISSN 1998-0124. doi: 10.1007/s12274-012-0263-9. URL <https://link-springer-com.proxy.scd.u-psud.fr/content/pdf/10.1007https://link.springer.com/10.1007/s12274-012-0263-9>. (Cited on page 68, 86)
- Domke, C., Ebert, P., Heinrich, M., and Urban, K. Microscopic identification of the compensation mechanisms in Si-doped GaAs. *Physical Review B - Condensed Matter and Materials Physics*, 54(15):10288–10291, 1996. ISSN 1550235X. doi: 10.1103/PhysRevB.54.10288. (Cited on page 68)
- Drouin, D., Couture, A. R., Joly, D., Tastet, X., Aimez, V., and Gauvin, R. CASINO V2.42 - A fast and easy-to-use modeling tool for scanning electron microscopy and microanalysis users. *Scanning*, 29(3):92–101, 2007. ISSN 01610457. doi: 10.1002/sca.20000. (Cited on page 21)
- Dryzek, J. S., Norgaard, R. B., and Schlosberg, D. *Climate Change and Society: Approaches and Responses*. Oxford University Press, USA, 2011. ISBN 9780191735271. doi: 10.1093/oxfordhb/9780199566600.003.0001. (Cited on page 5)
- Dubrovskii, V. G. *Nucleation Theory and Growth of Nanostructures*. Springer Berlin Heidelberg, 2014. ISBN 3642396593. (Cited on page 28)
- Dubrovskii, V. G., Xu, T., Álvarez, A. D., Plissard, S. R., Caroff, P., Glas, F., and Grandidier, B. Self-Equilibration of the Diameter of Ga-Catalyzed GaAs Nanowires. *Nano Letters*, 15(8): 5580–5584, 2015. ISSN 15306992. doi: 10.1021/acs.nanolett.5b02226. (Cited on page 45, 47)
- Dubrovskii, V. G., Hijazi, H., Goktas, N. I., and Lapierre, R. R. Be, Te, and Si Doping of GaAs Nanowires: Theory and Experiment. *Journal of Physical Chemistry C*, 124(31):17299–17307, 2020. ISSN 19327455. doi: 10.1021/acs.jpcc.0c04061. (Cited on page 68, 79)
- Efazi, E. T., Rhaman, M. M., Al Imam, S., Bashar, K. L., Kabir, F., Mourtaza, M. E., Sakib, S. N., and Mozahid, F. A. A review of primary technologies of thin-film solar cells. *Engineering Research Express*, 3(3), 2021. ISSN 26318695. doi: 10.1088/2631-8695/ac2353. (Cited on page 16)
- Elanzeery, H., Melchiorre, M., Sood, M., Babbe, F., Werner, F., Brammertz, G., and Siebentritt, S. Challenge in Cu-rich CuInSe<sub>2</sub> thin film solar cells: Defect caused by etching. *Physical Review Materials*, 3(5):55403, 2019. ISSN 24759953. doi: 10.1103/PhysRevMaterials.3.055403. URL <https://doi.org/10.1103/PhysRevMaterials.3.055403>. (Cited on page 61)

- Eperon, G. E., Hörantner, M. T., and Snaith, H. J. Metal halide perovskite tandem and multiple-junction photovoltaics. *Nature Reviews Chemistry*, 1(12), 2017. ISSN 23973358. doi: 10.1038/S41570-017-0095. (Cited on page 17)
- Farrow, R. F. C. *Molecular Beam Epitaxy - Applications to Key Materials*. Noyes Publications, New Jersey, 1995. ISBN 3904144987. (Cited on page 30)
- Feifel, M., Rachow, T., Benick, J., Ohlmann, J., Janz, S., Hermle, M., Dimroth, F., and Lackner, D. Gallium phosphide window layer for silicon solar cells. *IEEE Journal of Photovoltaics*, 6(1): 384–390, 2016. ISSN 21563381. doi: 10.1109/JPHOTOV.2015.2478062. (Cited on page 86)
- Feifel, M., Lackner, D., Schön, J., Ohlmann, J., Benick, J., Siefer, G., Predan, F., Hermle, M., and Dimroth, F. Epitaxial GaInP/GaAs/Si Triple-Junction Solar Cell with 25.9% AM1.5g Efficiency Enabled by Transparent Metamorphic Al<sub>x</sub>Ga<sub>1-x</sub>As<sub>y</sub>P<sub>1-y</sub> Step-Graded Buffer Structures. *Solar RRL*, 5(5):2000763, 2021. ISSN 2367198X. doi: 10.1002/solr.202000763. (Cited on page 17)
- Feuerbacher, B. and Wurfel, P. Verification of a generalised Planck law by investigation of the emission from GaAs luminescent diodes. *Journal of Physics: Condensed Matter*, 2(16):3803–3810, 1990. ISSN 09538984. doi: 10.1088/0953-8984/2/16/010. (Cited on page 58)
- Fontcuberta i Morral, A., Dayeh, S. A., and Jagadish, C. *Semiconductor Nanowires I - Growth and Theory*, volume 93. Elsevier Inc., 2015. ISBN 9780128030271. URL <http://www.sciencedirect.com/science/article/pii/S0080878415000368>. (Cited on page 28)
- Fournier, O. *Synthèse par ALD et caractérisation de couches extractrices d ’ électrons pour application dans les cellules solaires à base de pérovskite*. PhD thesis, Université Paris sciences et lettres, 2021. (Cited on page 24)
- Fraunhofer Institute for Solar Energy Systems. Photovoltaics Report. Technical Report July, ISE, 2021. (Cited on page 6)
- Fraunhofer ISE. Photovoltaics Report. Technical Report December, Fraunhofer ISE, 2022. (Cited on page 15)
- Gao, Q., Dubrovskii, V. G., Caroff, P., Wong-Leung, J., Li, L., Guo, Y., Fu, L., Tan, H. H., and Jagadish, C. Simultaneous Selective-Area and Vapor-Liquid-Solid Growth of InP Nanowire Arrays. *Nano Letters*, 16(7):4361–4367, 2016. ISSN 15306992. doi: 10.1021/acs.nanolett.6b01461. (Cited on page 28)
- Gao, Q., Li, Z., Li, L., Vora, K., Li, Z., Alabadla, A., Wang, F., Guo, Y., Peng, K., Wenas, Y. C., Mokkapati, S., Karouta, F., Tan, H. H., Jagadish, C., and Fu, L. Axial p-n junction design and characterization for InP nanowire array solar cells. *Progress in Photovoltaics: Research and Applications*, 27(3):237–244, 2019. ISSN 1099159X. doi: 10.1002/pip.3083. (Cited on page 84)
- Garnett, E., Brongersma, M., Cui, Y., and McGehee, M. Nanowire solar cells. *Annu. Rev. Mater. Res.*, 41:269–295, 2011. ISSN 21622701. doi: 10.1146/annurev-matsci-062910-100434. (Cited on page 19)
- Ghahfarokhi, O. M., Anttu, N., Samuelson, L., and Åberg, I. Performance of GaAs Nanowire Array Solar Cells for Varying Incidence Angles. *IEEE Journal of Photovoltaics*, 6(6):1502–1508, 2016. ISSN 21563381. doi: 10.1109/JPHOTOV.2016.2604564. (Cited on page 19)
- Glas, F., Harmand, J. C., and Patriarche, G. Why does wurtzite form in nanowires of III-V zinc blende semiconductors? *Physical Review Letters*, 99(14):146101, 2007. ISSN 00319007. doi: 10.1103/PhysRevLett.99.146101. (Cited on page 28)
- Goktas, N. I., Fiordaliso, E. M., and LaPierre, R. R. Doping assessment in GaAs nanowires. *Nanotechnology*, 29(23):234001, 2018. ISSN 0957-4484. doi: 10.1088/1361-6528/aab6f1. URL <https://iopscience.iop.org/article/10.1088/1361-6528/aab6f1>. (Cited on page 69)
- Gomez, M. O. *TCAD Modelling, simulation and characterization of III-V multijunction solar cells*. PhD thesis, Universidad Politécnica de Madrid, Escuela Técnica Superior de Ingenieros de Telecomunicación, 2018. (Cited on page 64, 102)

- Gorji Ghalamestani, S., Heurlin, M., Wernersson, L. E., Lehmann, S., and Dick, K. A. Growth of InAs/InP core-shell nanowires with various pure crystal structures. *Nanotechnology*, 23(28), 2012. ISSN 09574484. doi: 10.1088/0957-4484/23/28/285601. (Cited on page 85)
- Green, M. A., Dunlop, E. D., Hohl-Ebinger, J., Yoshita, M., Kopidakis, N., Bothe, K., Hinken, D., Rauer, M., and Hao, X. Solar cell efficiency tables (Version 60). *Progress in Photovoltaics: Research and Applications*, 30(7):687–701, 2022. ISSN 1099159X. doi: 10.1002/pip.3595. (Cited on page 16, 17)
- Gudiksen, M. S. and Lieber, C. M. Diameter-selective synthesis of semiconductor nanowires. *Journal of the American Chemical Society*, 122(36):8801–8802, 2000. ISSN 00027863. doi: 10.1021/ja002008e. (Cited on page 47)
- Gudovskikh, A. S., Zelentsov, K. S., Baranov, A. I., Kudryashov, D. A., Morozov, I. A., Nikitina, E. V., and Kleider, J. P. Study of GaP/Si Heterojunction Solar Cells. *Energy Procedia*, 102 (May):56–63, 2016. ISSN 18766102. doi: 10.1016/j.egypro.2016.11.318. URL <http://dx.doi.org/10.1016/j.egypro.2016.11.318>. (Cited on page 62)
- Guillemoles, J.-f., Kirchartz, T., Cahen, D., and Rau, U. Guide for the perplexed to the Shockley – Queisser model for solar cells. *Nature Photonics*, 13(August):501–508, 2019. (Cited on page 14)
- Güniat, L., Caroff, P., and Fontcuberta I Morral, A. Vapor Phase Growth of Semiconductor Nanowires: Key Developments and Open Questions. *Chemical Reviews*, 119(15):8958–8971, 2019. ISSN 15206890. doi: 10.1021/acs.chemrev.8b00649. (Cited on page 29)
- Guthrey, H. and Moseley, J. A Review and Perspective on Cathodoluminescence Analysis of Halide Perovskites. *Advanced Energy Materials*, 10(26):1903840, 2020. ISSN 16146840. doi: 10.1002/aenm.201903840. (Cited on page 91)
- Gutsche, C., Regolin, I., Blekker, K., Lysov, A., Prost, W., and Tegude, F. J. Controllable p -type doping of GaAs nanowires during vapor-liquid-solid growth. *Journal of Applied Physics*, 105(2), 2009. ISSN 00218979. doi: 10.1063/1.3065536. (Cited on page 69)
- Gutsche, C., Niepelt, R., Gnauck, M., Lysov, A., Prost, W., Ronning, C., and Tegude, F. J. Direct determination of minority carrier diffusion lengths at axial GaAs nanowire p-n junctions. *Nano Letters*, 12(3):1453–1458, 2012. ISSN 15306984. doi: 10.1021/nl204126n. (Cited on page 85)
- Haapamaki, C. M., Baugh, J., and Lapierre, R. R. Critical shell thickness for InAs-AlxIn1-xAs(P) core-shell nanowires. *Journal of Applied Physics*, 112(12), 2012. ISSN 00218979. doi: 10.1063/1.4769735. (Cited on page 53, 85)
- Haas, F., Sladek, K., Winden, A., Von Der Ahe, M., Weirich, T. E., Rieger, T., Lüth, H., Grütz-macher, D., Schäpers, T., and Hardtdegen, H. Nanoimprint and selective-area MOVPE for growth of GaAs/InAs core/shell nanowires. *Nanotechnology*, 24(8), 2013. ISSN 09574484. doi: 10.1088/0957-4484/24/8/085603. (Cited on page 85)
- Haggren, T., Jiang, H., Kakko, J. P., Huhtio, T., Dhaka, V., Kauppinen, E., and Lipsanen, H. Strong surface passivation of GaAs nanowires with ultrathin InP and GaP capping layers. *Applied Physics Letters*, 105(3), 2014. ISSN 00036951. doi: 10.1063/1.4891535. (Cited on page 85)
- Hakkarainen, T., Piton, M. R., Fiordaliso, E. M., Leshchenko, E. D., Koelling, S., Bettini, J., Vinicius, H., Galeti, A., Koivusalo, E., Gobato, Y. G., Rodrigues, A. D. G., Lupo, D., Koenraad, P. M., Leite, E. R., Dubrovskii, V. G., and Guina, M. Te incorporation and activation as n -type dopant in self-catalyzed GaAs nanowires. *Physical Review Materials*, 3(8):086001, 2019. doi: 10.1103/PhysRevMaterials.3.086001. (Cited on page 69, 70, 72, 79, 80, 86)
- Hakkarainen, T. V., Schramm, A., Mäkelä, J., Laukkanen, P., and Guina, M. Lithography-free oxide patterns as templates for self-catalyzed growth of highly uniform GaAs nanowires on Si(111). *Nanotechnology*, 26(27):275301, 2015. ISSN 13616528. doi: 10.1088/0957-4484/26/27/275301. (Cited on page 71)



- Heiss, M., Russo-Averchi, E., Dalmau-Mallorquí, A., Tütüncüoğlu, G., Matteini, F., Rüffer, D., Conesa-Boj, S., Demichel, O., Alarcon-Lladó, E., and Fontcuberta I Morral, A. III-V nanowire arrays: Growth and light interaction. *Nanotechnology*, 25(1), 2014. ISSN 09574484. doi: 10.1088/0957-4484/25/1/014015. (Cited on page 34, 35)
- Heurlin, M., Hultin, O., Storm, K., Lindgren, D., Borgström, M. T., and Samuelson, L. Synthesis of doped InP core-shell nanowires evaluated using hall effect measurements. *Nano Letters*, 14(2):749–753, 2014. ISSN 15306984. doi: 10.1021/nl404039d. (Cited on page 85)
- Hijazi, H., Monier, G., Gil, E., Trassoudaine, A., Bougerol, C., Leroux, C., Castellucci, D., Robert-Goumet, C., Hoggan, P. E., André, Y., Isik Goktas, N., Lapierre, R. R., and Dubrovskii, V. G. Si doping of vapor-liquid-solid gaas nanowires: N-Type or p-Type? *Nano Letters*, 19(7):4498–4504, 2019. ISSN 15306992. doi: 10.1021/acs.nanolett.9b01308. (Cited on page 68)
- Hilse, M., Ramsteiner, M., Breuer, S., Geelhaar, L., and Riechert, H. Incorporation of the dopants Si and Be into GaAs nanowires. *Applied Physics Letters*, 96(19):193104, 2010. ISSN 0003-6951. doi: 10.1063/1.3428358. URL [https://www.researchgate.net/profile/Maria-Hilse/publication/234855797\\_Incorporation\\_of\\_the\\_dopants\\_Si\\_and\\_Be\\_into\\_GaAs\\_nanowires/links/00b7d537470dab2246000000.pdf](https://www.researchgate.net/profile/Maria-Hilse/publication/234855797_Incorporation_of_the_dopants_Si_and_Be_into_GaAs_nanowires/links/00b7d537470dab2246000000.pdf)<http://aip.scitation.org/doi/10.1063/1.3428358>. (Cited on page 68)
- Hong, J. and Pearton, S. J. Selective and Non-Selective Wet Chemical Etching of GaAs(0.93)P(0.07). *Solid State Electronics*, 39(11):1675–1677, 1996. (Cited on page 92)
- Honsberg, C. B. and Bowden, S. G. Photovoltaics Education Website, 2019. URL [www.pveducation.org](http://www.pveducation.org). (Cited on page 12)
- Howell, S. L., Padalkar, S., Yoon, K., Li, Q., Koleske, D. D., Wierer, J. J., Wang, G. T., and Lauhon, L. J. Spatial mapping of efficiency of GaN/InGaN nanowire array solar cells using scanning photocurrent microscopy. *Nano Letters*, 13(11):5123–5128, 2013. ISSN 15306984. doi: 10.1021/nl402331u. (Cited on page 61)
- Huang, N. and Povinelli, M. L. Design of passivation layers on axial junction GaAs nanowire solar cells. *IEEE Journal of Photovoltaics*, 4(6):1511–1517, 2014. ISSN 21563381. doi: 10.1109/JPHOTOV.2014.2351624. (Cited on page 84)
- Huang, N., Lin, C., and Povinelli, M. L. Limiting efficiencies of tandem solar cells consisting of III-V nanowire arrays on silicon. *Journal of Applied Physics*, 112(6), 2012. ISSN 00218979. doi: 10.1063/1.4754317. (Cited on page 19, 85)
- Hugonin, J. P. and Lalanne, P. RETICOLO CODE 1D for the diffraction by stacks of lamellar 1D gratings (classical diffraction). Technical report, Institut d’Optique/CNRS, 2005. (Cited on page 58)
- Hultin, O., Otnes, G., Borgström, M. T., Björk, M., Samuelson, L., and Storm, K. Comparing Hall Effect and Field Effect Measurements on the Same Single Nanowire. *Nano Letters*, 16(1): 205–211, 2016. ISSN 15306992. doi: 10.1021/acs.nanolett.5b03496. (Cited on page 69)
- Ikejiri, K., Noborisaka, J., Hara, S., Motohisa, J., and Fukui, T. Mechanism of catalyst-free growth of GaAs nanowires by selective area MOVPE. *Journal of Crystal Growth*, 298(SPEC. ISS):616–619, 2007. ISSN 00220248. doi: 10.1016/j.jcrysgro.2006.10.179. (Cited on page 28)
- International Energy Agency. Net Zero by 2050: A Roadmap for the Global Energy Sector. Technical report, IEA, 2021a. (Cited on page 115)
- International Energy Agency. World Energy Outlook 2021. Technical report, IEA, 2021b. URL [www.iea.org/weo](http://www.iea.org/weo). (Cited on page 5)
- Ioffe Institute. New Semiconductor Materials. Characteristics and Properties. (Cited on page 64, 66, 102)
- IPCC. Climate change 2013: The Physical Science Basis. Contribution of Working Group I to the Fifth Assessment Report of the Intergovernmental Panel on Climate Change. Technical report, IPCC, 2013. (Cited on page 5, 115)



- IPCC. Climate Change 2021: The Physical Science Basis. Contribution of Working Group I to the Sixth Assessment Report of the Intergovernmental Panel on Climate Change. Technical report, IPCC, 2020. (Cited on page 5)
- Jacobsson, D., Panciera, F., Tersoff, J., Reuter, M. C., Lehmann, S., Hofmann, S., Dick, K. A., and Ross, F. M. Interface dynamics and crystal phase switching in GaAs nanowires. *Nature*, 531(7594):317–322, 2016. ISSN 14764687. doi: 10.1038/nature17148. URL <http://dx.doi.org/10.1038/nature17148>. (Cited on page 85, 90, 92)
- Jiang, N., Gao, Q., Parkinson, P., Wong-Leung, J., Mokkapati, S., Breuer, S., Tan, H. H., Zheng, C. L., Etheridge, J., and Jagadish, C. Enhanced minority carrier lifetimes in GaAs/AlGaAs core-shell nanowires through shell growth optimization. *Nano Letters*, 13(11):5135–5140, 2013. ISSN 15306984. doi: 10.1021/nl4023385. (Cited on page 85)
- Joyce, H. J., Docherty, C. J., Gao, Q., Tan, H. H., Jagadish, C., Lloyd-Hughes, J., Herz, L. M., and Johnston, M. B. Electronic properties of GaAs, InAs and InP nanowires studied by terahertz spectroscopy. *Nanotechnology*, 24(21), 2013. ISSN 13616528. doi: 10.1088/0957-4484/24/21/214006. (Cited on page 70)
- Joyce, H. J., Boland, J. L., Davies, C. L., Baig, S. A., and Johnston, M. B. A review of the electrical properties of semiconductor nanowires: Insights gained from terahertz conductivity spectroscopy. *Semiconductor Science and Technology*, 31(10), 2016. ISSN 13616641. doi: 10.1088/0268-1242/31/10/103003. (Cited on page 70)
- Kaneka Corporation. World’s Highest Conversion Efficiency of 24.37 % Achieved in a Crystalline Silicon Solar Cell Module, 2016. (Cited on page 15)
- Kao, Y. C., Chou, H. M., Hsu, S. C., Lin, A., Lin, C. C., Shih, Z. H., Chang, C. L., Hong, H. F., and Horng, R. H. Performance comparison of III–V//Si and III–V//InGaAs multi-junction solar cells fabricated by the combination of mechanical stacking and wire bonding. *Scientific Reports*, 9(1):4308, 2019. ISSN 20452322. doi: 10.1038/s41598-019-40727-y. (Cited on page 64, 102)
- Katahara, J. K. and Hillhouse, H. W. Quasi-fermi level splitting and sub-bandgap absorptivity from semiconductor photoluminescence. *Journal of Applied Physics*, 116(17), 2014. ISSN 10897550. doi: 10.1063/1.4898346. (Cited on page 22)
- Kavanagh, K. L. Misfit dislocations in nanowire heterostructures. *Semiconductor Science and Technology*, 25(2):024006, 2010. ISSN 02681242. doi: 10.1088/0268-1242/25/2/024006. (Cited on page 19)
- Kayes, B. M., Nie, H., Twist, R., Spruytte, S. G., Reinhardt, F., Kizilyalli, I. C., and Hgashi, G. S. 27.6% Conversion efficiency, a new record for single-junction solar cells under 1 sun illumination. *2011 37th IEEE Photovoltaic Specialists Conference*, pages 000004–000008, 2011. ISSN 01608371. doi: 10.1109/PVSC.2011.6185831. (Cited on page 16, 18, 19, 62, 119)
- Ketterer, B., Mikheev, E., Uccelli, E., and Fontcuberta I Morral, A. Compensation mechanism in silicon-doped gallium arsenide nanowires. *Applied Physics Letters*, 97(22):223103, 2010. ISSN 00036951. doi: 10.1063/1.3517254. (Cited on page 70)
- Kim, H., Ren, D., Farrell, A. C., and Huffaker, D. L. Catalyst-free selective-area epitaxy of GaAs nanowires by metal-organic chemical vapor deposition using triethylgallium. *Nanotechnology*, 29(8):085601, 2018. ISSN 13616528. doi: 10.1088/1361-6528/aaa52e. (Cited on page 28)
- Kim, W., Güniat, L., Fontcuberta I Morral, A., and Piazza, V. Doping challenges and pathways to industrial scalability of III-V nanowire arrays. *Applied Physics Reviews*, 8(1):011304, 2021. ISSN 19319401. doi: 10.1063/5.0031549. URL <https://doi.org/10.1063/5.0031549>. (Cited on page 68, 69, 70)
- Kim, Y. H., Park, D. W., and Lee, S. J. Gallium-droplet behaviors of self-catalyzed GaAs nanowires : A transmission electron microscopy study. *Applied Physics Letters*, 100(3):033117, 2012. doi: 10.1063/1.3678185. (Cited on page 85, 90, 92)

- Koivusalo, E. S., Hakkarainen, T. V., Guina, M. D., and Dubrovskii, V. G. Sub-Poissonian Narrowing of Length Distributions Realized in Ga-Catalyzed GaAs Nanowires. *Nano Letters*, 17(9):5350–5355, 2017. ISSN 15306992. doi: 10.1021/acs.nanolett.7b01766. (Cited on page 73)
- Krogstrup, P., Jørgensen, H. I., Heiss, M., Demichel, O., Holm, J. V., Aagesen, M., Nygard, J., and Fontcuberta i Morral, A. Single-nanowire solar cells beyond the Shockley–Queisser limit. *Nature Photonics*, 7(4):306–310, 4 2013. ISSN 1749-4885. doi: 10.1038/nphoton.2013.32. URL <http://www.nature.com/doifinder/10.1038/nphoton.2013.32><http://www.nature.com/articles/nphoton.2013.32>. (Cited on page 19, 84)
- Kudryashov, D. A., Gudovskikh, A. S., and Baranov, A. I. Precision Chemical Etching of GaP(NAs) Epitaxial Layers for the Formation of Monolithic Optoelectronic Devices. *Semiconductors*, 52(13):1775–1781, 2018. ISSN 10637826. doi: 10.1134/S1063782618130092. (Cited on page 92)
- Küpers, H., Tahraoui, A., Lewis, R. B., Rauwerdink, S., Matalla, M., Krüger, O., Bastiman, F., Riechert, H., and Geelhaar, L. Surface preparation and patterning by nano imprint lithography for the selective area growth of GaAs nanowires on Si(111). *Semiconductor Science and Technology*, 32(11):115003, 2017. ISSN 13616641. doi: 10.1088/1361-6641/aa8c15. (Cited on page 34, 35)
- Küpers, H., Lewis, R. B., Tahraoui, A., Matalla, M., Krüger, O., Bastiman, F., Riechert, H., and Geelhaar, L. Diameter evolution of selective area grown Ga-assisted GaAs nanowires. *Nano Research*, 11(5):2885–2893, 2018. ISSN 19980000. doi: 10.1007/s12274-018-1984-1. (Cited on page 35, 45, 47)
- Lalanne, P. and Jurek, M. P. Computation of the near-field pattern with the coupled-wave method for transverse magnetic polarization. *Journal of Modern Optics*, 45(7):1357–1374, 1998. ISSN 13623044. doi: 10.1080/09500349808230634. (Cited on page 58)
- Lalanne, P. and Morris, G. M. Highly improved convergence of the coupled-wave method for TM polarization. *Journal of the Optical Society of America A*, 13(4):779–784, 1996. (Cited on page 58)
- Lang, D. V., Grimmeiss, H. G., Meijer, E., and Jaros, M. Complex nature of gold-related deep levels in silicon. *Physical Review B*, 22(8):3917–3934, 1980. ISSN 01631829. doi: 10.1103/PhysRevB.22.3917. (Cited on page 28)
- Lang, R., Schon, J., Dimroth, F., and Lackner, D. Optimization of GaAs solar cell performance and growth efficiency at MOVPE growth rates of 100  $\mu\text{m}/\text{h}$ . *IEEE Journal of Photovoltaics*, 8(6):1596–1600, 2018. ISSN 21563381. doi: 10.1109/JPHOTOV.2018.2868021. (Cited on page 30)
- Lang, R., Habib, F., Dauelsberg, M., Dimroth, F., and Lackner, D. MOVPE growth of GaAs with growth rates up to 280  $\mu\text{m}/\text{h}$ . *Journal of Crystal Growth*, 537(December 2019):125601, 2020. ISSN 00220248. doi: 10.1016/j.jcrysgro.2020.125601. URL <https://doi.org/10.1016/j.jcrysgro.2020.125601>. (Cited on page 30)
- Lapierre, R. R. Theoretical conversion efficiency of a two-junction III-V nanowire on Si solar cell. *Journal of Applied Physics*, 110(1):014310, 2011. ISSN 00218979. doi: 10.1063/1.3603029. (Cited on page 19, 116)
- Lapierre, R. R., Chia, A. C., Gibson, S. J., Haapamaki, C. M., Boulanger, J., Yee, R., Kuyanov, P., Zhang, J., Tajik, N., Jewell, N., and Rahman, K. M. III-V nanowire photovoltaics: Review of design for high efficiency. *Physica Status Solidi - Rapid Research Letters*, 7(10):815–830, 2013. ISSN 18626254. doi: 10.1002/pssr.201307109. (Cited on page 19)
- Lee, C. T., Fu, C. H., Tsai, C. D., and Lin, W. Performance characterization of InGaP schottky contact with ITO transparent electrodes. *Journal of Electronic Materials*, 27(9):1017–1021, 1998. ISSN 03615235. doi: 10.1007/s11664-998-0155-7. (Cited on page 66)

- Lee, N. Y., Lee, K. J., Lee, C., Kim, J. E., Park, H. Y., Kwak, D. H., Lee, H. C., and Lim, H. Determination of conduction band tail and fermi energy of heavily Si-doped GaAs by room-temperature photoluminescence. *Journal of Applied Physics*, 78(5):3367–3370, 1995. ISSN 00218979. doi: 10.1063/1.359963. (Cited on page 70, 74, 75)
- Leenaars, A. F., Huethorst, J. A., and Van Oekel, J. J. Marangoni Drying: A New Extremely Clean Drying Process. *Langmuir*, 6(11):1701–1703, 1990. ISSN 15205827. doi: 10.1021/la00101a014. (Cited on page 41)
- Levinshtein, M., Rumyantsev, S., and Shur, M. *Handbook series on semiconductor parameters*. World Scientific, 1999. ISBN 981-02-1420-0. (Cited on page 64, 102)
- Li, L. New formulation of the Fourier modal method for crossed surface-relief gratings. *Journal of the Optical Society of America A*, 14(10):2758–2767, 1997. ISSN 14644258. doi: 10.1088/1464-4258/4/5/358. (Cited on page 58)
- Lin, A., Shapiro, J. N., Senanayake, P. N., Scofield, A. C., Wong, P. S., Liang, B., and Huffaker, D. L. Extracting transport parameters in GaAs nanopillars grown by selective-area epitaxy. *Nanotechnology*, 23(10), 2012. ISSN 09574484. doi: 10.1088/0957-4484/23/10/105701. (Cited on page 85)
- Lindgren, D., Hultin, O., Heurlin, M., Storm, K., Borgström, M. T., Samuelson, L., and Gustafsson, A. Study of carrier concentration in single InP nanowires by luminescence and Hall measurements. *Nanotechnology*, 26(4):045705, 2015. ISSN 13616528. doi: 10.1088/0957-4484/26/4/045705. (Cited on page 71)
- Lombez, L., Soro, M., Delamarre, A., Naghavi, N., Barreau, N., Lincot, D., and Guillemales, J. F. Revisiting the interpretation of biased luminescence: Effects on Cu(In,Ga)Se<sub>2</sub> photovoltaic heterostructures. *Journal of Applied Physics*, 116(6):064504, 2014. ISSN 10897550. doi: 10.1063/1.4891525. (Cited on page 61)
- LONGi. At 26.81%, LONGi sets a new world record efficiency for silicon solar cells, 2022. URL <https://www.longi.com/en/news/propelling-the-transformation/>. (Cited on page 15)
- Madiomanana, K., Bahri, M., Rodriguez, J. B., Largeau, L., Cerutti, L., Mauguin, O., Castellano, A., Patriarche, G., and Tournié, E. Silicon surface preparation for III-V molecular beam epitaxy. *Journal of Crystal Growth*, 413:17–24, 2015. ISSN 00220248. doi: 10.1016/j.jcrysgro.2014.12.004. URL <http://dx.doi.org/10.1016/j.jcrysgro.2014.12.004>. (Cited on page 37)
- Marangoni, C. *Sull’espansione delle gocce d’un liquido galleggianti sulla superficie di altro liquido*. PhD thesis, Università degli Studi di Pavia, 1865. (Cited on page 41)
- Mariani, G., Wong, P. S., Katzenmeyer, A. M., Léonard, F., Shapiro, J., and Huffaker, D. L. Patterned radial GaAs nanopillar solar cells. *Nano Letters*, 11(6):2490–2494, 2011. ISSN 15306984. doi: 10.1021/nl200965j. (Cited on page 85)
- Mariani, G., Zhou, Z., Scofield, A., and Huffaker, D. L. Direct-Bandgap Epitaxial Core–Multishell Nanopillar Photovoltaics Featuring Subwavelength Optical Concentrators. *Nano Letters*, 13(4):1632–1637, 4 2013. ISSN 1530-6984. doi: 10.1021/nl400083g. URL <http://pubs.acs.org.proxy.scd.u-psud.fr/doi/pdf/10.1021/nl400083g><http://pubs.acs.org/doi/10.1021/nl400083g>. (Cited on page 18)
- Mårtensson, T., Svensson, C. P. T., Wacaser, B. A., Larsson, M. W., Seifert, W., Deppert, K., Gustafsson, A., Wallenberg, L. R., and Samuelson, L. Epitaxial III-V nanowires on silicon. *Nano Letters*, 4(10):1987–1990, 2004. ISSN 15306984. doi: 10.1021/nl0487267. (Cited on page 19)
- Matteini, F., Tütüncüoğlu, G., Mikulik, D., Vukajlovic-Plestina, J., Potts, H., Leran, J. B., Carter, W. C., and Morral, A. F. Impact of the Ga Droplet Wetting, Morphology, and Pinholes on the Orientation of GaAs Nanowires. *Crystal Growth and Design*, 16(10):5781–5786, 2016. ISSN 15287505. doi: 10.1021/acs.cgd.6b00858. (Cited on page 36)
- Mazuelas, A., González, L., Ponce, F. A., Tapfer, L., and Briones, F. Critical thickness determination of InAs, InP and GaP on GaAs by X-ray interference effect and transmission electron microscopy. *Journal of Crystal Growth*, 131(3-4):465–469, 1993. ISSN 00220248. doi: 10.1016/0022-0248(93)90197-5. (Cited on page 90)

- Mikulik, D., Ricci, M., Tutuncuoglu, G., Matteini, F., Vukajlovic, J., Vulic, N., Alarcon-Llado, E., and Fontcuberta i Morral, A. Conductive-probe atomic force microscopy as a characterization tool for nanowire-based solar cells. *Nano Energy*, 41(October):566–572, 2017. ISSN 22112855. doi: 10.1016/j.nanoen.2017.10.016. URL <http://dx.doi.org/10.1016/j.nanoen.2017.10.016>. (Cited on page 60)
- Mohajerani, M. S., Khachadorian, S., Schimpke, T., Nenstiel, C., Hartmann, J., Ledig, J., Avramescu, A., Strassburg, M., Hoffmann, A., and Waag, A. Evaluation of local free carrier concentrations in individual heavily-doped GaN:Si micro-rods by micro-Raman spectroscopy. *Applied Physics Letters*, 108(9):09112, 2016. ISSN 00036951. doi: 10.1063/1.4943079. URL <http://dx.doi.org/10.1063/1.4943079>. (Cited on page 70)
- Morgan, D. V., Aliyu, Y., and Bunce, R. W. The Thermal Stability of Indium-Tin-Oxide/n-GaAs Schottky Contacts. *Physica Status Solidi (a)*, 133(1):77–93, 1992. ISSN 1521396X. doi: 10.1002/pssa.2211330110. (Cited on page 66)
- Morita, M., Ohmi, T., Hasegawa, E., Kawakami, M., and Ohwada, M. Growth of native oxide on a silicon surface. *Journal of Applied Physics*, 68(3):1272–1281, 1990. ISSN 00218979. doi: 10.1063/1.347181. (Cited on page 37)
- Moss, T. S. The interpretation of the properties of indium antimonide. *Proceedings of the Physical Society. Section B*, 67(10):775–782, 1954. ISSN 03701301. doi: 10.1088/0370-1301/67/10/306. (Cited on page 74)
- Motohisa, J., Noborisaka, J., Takeda, J., Inari, M., and Fukui, T. Catalyst-free selective-area MOVPE of semiconductor nanowires on (111)B oriented substrates. *Journal of Crystal Growth*, 272(1-4):180–185, 2004. ISSN 00220248. doi: 10.1016/j.jcrysgro.2004.08.118. (Cited on page 28)
- Mukherjee, A., Ren, D., Vullum, P.-E., Huh, J., Fimland, B.-O., and Weman, H. GaAs/AlGaAs Nanowire Array Solar Cell Grown on Si with Ultrahigh Power-per-Weight Ratio. *ACS Photonics*, 8(8):2355–2366, 2021. ISSN 2330-4022. doi: 10.1021/acsp Photonics.1c00527. (Cited on page 18, 19, 35, 36, 116)
- Munshi, A. M., Dheeraj, D. L., Fauske, V. T., Kim, D. C., Huh, J., Reinertsen, J. F., Ah-tapodov, L., Lee, K. D., Heidari, B., van Helvoort, A. T. J., Fimland, B. O., and Weman, H. Position-Controlled Uniform GaAs Nanowires on Silicon using Nanoimprint Lithography. *Nano Letters*, 14(2):960–966, 2 2014. ISSN 1530-6984. doi: 10.1021/nl404376m. URL <http://www.ncbi.nlm.nih.gov/pubmed/24467394><http://pubs.acs.org/doi/abs/10.1021/nl404376m><https://pubs.acs.org/doi/10.1021/nl404376m>. (Cited on page 34, 35, 36)
- Nakai, E., Yoshimura, M., Tomioka, K., and Fukui, T. GaAs / InGaP Core – Multishell Nanowire-Array-Based Solar Cells. *Japanese Journal of Applied Physics*, 52:055002, 2013. (Cited on page 18)
- Neave, J. H., Dobson, P. J., Harris, J. J., Dawson, P., and Joyce, B. A. Silicon doping of MBE-grown GaAs films. *Applied Physics A Solids and Surfaces*, 32(4):195–200, 1983. ISSN 07217250. doi: 10.1007/BF00820260. (Cited on page 68)
- Nelson, J. *The physics of Solar Cells*. Imperial College Press, 2003. ISBN 13978860943409. URL <https://fuelrfuture.com/energy/physicsOfSolarCellsNelson.pdf>. (Cited on page 11, 12)
- Němec, H., Kadlec, F., and Kužel, P. Methodology of an optical pump-terahertz probe experiment: An analytical frequency-domain approach. *Journal of Chemical Physics*, 117(18):8454–8465, 2002. ISSN 00219606. doi: 10.1063/1.1512648. (Cited on page 70)
- Niewelt, T., Steinhauser, B., Richter, A., Veith-Wolf, B., Fell, A., Hammann, B., Grant, N. E., Black, L., Tan, J., Youssef, A., Murphy, J. D., Schmidt, J., Schubert, M. C., and Glunz, S. W. Reassessment of the intrinsic bulk recombination in crystalline silicon. *Solar Energy Materials and Solar Cells*, 235:111467, 2022. ISSN 09270248. doi: 10.1016/j.solmat.2021.111467. URL <https://doi.org/10.1016/j.solmat.2021.111467>. (Cited on page 7, 16, 115)

- Nowzari, A., Heurlin, M., Jain, V., Storm, K., Hosseinnia, A., Anttu, N., Borgström, M. T., Pettersson, H., and Samuelson, L. A comparative study of absorption in vertically and laterally oriented InP core-shell nanowire photovoltaic devices. *Nano Letters*, 15(3):1809–1814, 2015. ISSN 15306992. doi: 10.1021/nl504559g. (Cited on page 84)
- Oehler, F., Cattoni, A., Scaccabarozzi, A., Patriarche, G., Glas, F., and Harmand, J.-C. Measuring and modeling the growth dynamics of self-catalyzed GaP nanowire arrays. *Nano Letters*, 18(2): 701–708, 2018. (Cited on page 28, 29, 86, 90)
- Oehrlein, G. S. Dry etching damage of silicon: A review. *Materials Science and Engineering B*, 4(1-4):441–450, 1989. ISSN 09215107. doi: 10.1016/0921-5107(89)90284-5. (Cited on page 39, 109)
- Oh, T. and Choi, C. K. Comparison between SiOC thin films fabricated by using plasma enhance chemical vapor deposition and SiO<sub>2</sub> thin films by using fourier transform infrared spectroscopy. *Journal of the Korean Physical Society*, 56(4):1150–1155, 2010. ISSN 03744884. doi: 10.3938/jkps.56.1150. (Cited on page 38)
- Ohring, M. *Materials Science of Thin Films*. Academic Press, 2nd editio edition, 2001. ISBN 9780080491783. (Cited on page 31)
- Ojha, S. K., Kasanaboina, P. K., Lewis Reynolds, C., Rawdanowicz, T. A., Liu, Y., White, R. M., and Iyer, S. Incorporation of Be dopant in GaAs core and core-shell nanowires by molecular beam epitaxy. *Journal of Vacuum Science & Technology B, Nanotechnology and Microelectronics: Materials, Processing, Measurement, and Phenomena*, 34(2):02L114, 2016. ISSN 2166-2746. doi: 10.1116/1.4943600. URL <http://dx.doi.org/10.1116/1.4943600>. (Cited on page 70)
- Olego, D. and Cardona, M. Photoluminescence in heavily doped GaAs. I. Temperature and hole-concentration dependence. *Physical Review B*, 22(2):886–893, 1980. ISSN 01631829. doi: 10.1103/PhysRevB.22.886. (Cited on page 70)
- Onno, A., Harder, N. P., Oberbeck, L., and Liu, H. Simulation study of GaAsP/Si tandem solar cells. *Solar Energy Materials and Solar Cells*, 145:206–216, 2016. ISSN 09270248. doi: 10.1016/j.solmat.2015.10.028. URL <http://dx.doi.org/10.1016/j.solmat.2015.10.028>. (Cited on page 99, 102)
- Orrù, M., Repiso, E., Carapezzi, S., Henning, A., Roddaro, S., Franciosi, A., Rosenwaks, Y., Cavallini, A., Martelli, F., and Rubini, S. A Roadmap for Controlled and Efficient n-Type Doping of Self-Assisted GaAs Nanowires Grown by Molecular Beam Epitaxy. *Advanced Functional Materials*, 26(17):2836–2845, 2016. ISSN 16163028. doi: 10.1002/adfm.201504853. (Cited on page 69)
- Orton, J. and Foxon, T. *Molecular Beam Epitaxy: A Short History*. Oxford University Press, 2015. ISBN 0199695822. (Cited on page 30)
- Otnes, G. and Borgström, M. T. Towards high efficiency nanowire solar cells. *Nano Today*, 12:31–45, 2017. doi: 10.1016/j.nantod.2016.10.007. URL [https://ac-els-cdn-com.proxy.scd.u-psud.fr/S1748013216303024/1-s2.0-S1748013216303024-main.pdf?\\_tid=9a071692-a41e-11e7-904b-00000aabb0f6c&acdnat=1506583880\\_ff1f4a294faa92fed5ea1a1f07802475](https://ac-els-cdn-com.proxy.scd.u-psud.fr/S1748013216303024/1-s2.0-S1748013216303024-main.pdf?_tid=9a071692-a41e-11e7-904b-00000aabb0f6c&acdnat=1506583880_ff1f4a294faa92fed5ea1a1f07802475). (Cited on page 85, 87)
- Otnes, G., Barrigón, E., Sundvall, C., Svensson, K. E., Heurlin, M., Siefer, G., Samuelson, L., Åberg, I., and Borgström, M. T. Understanding InP Nanowire Array Solar Cell Performance by Nanoprobe-Enabled Single Nanowire Measurements. *Nano Letters*, 18(5):3038–3046, 2018. ISSN 15306992. doi: 10.1021/acs.nanolett.8b00494. (Cited on page 18, 66, 84)
- Oyama, Y., Nishizawa, J. i., Seo, K., and Suto, K. Electrical activation of Te and Se in GaAs at extremely heavy doping up to  $5 \times 10^{20} \text{ cm}^{-3}$  prepared by intermittent injection of TEG/AsH<sub>3</sub> in ultra-high vacuum. *Journal of Crystal Growth*, 212(3):402–410, 2000. ISSN 00220248. doi: 10.1016/S0022-0248(00)00206-2. (Cited on page 68)
- Paek, J. H., Nishiwaki, T., Yamaguchi, M., and Sawaki, N. MBE-VLS growth of GaAs nanowires on (111)Si substrate. *Physica Status Solidi (c)*, 5(9):2740–2742, 2008. doi: 10.1002/pssc.200779248. (Cited on page 34)



- Panciera, F., Baraissov, Z., Patriarche, G., Vladimir, G., Glas, F., Travers, L., Mirsaidov, U., Christophe, J., Panciera, F., Baraissov, Z., Patriarche, G., Dubrovskii, V. G., and Glas, F. Phase Selection in Self-catalyzed GaAs Nanowires. *Nano Letters*, 20:1669–1675, 2020. (Cited on page 72)
- Park, D. W., Lee, C. R., Kim, J. S., Lee, S. J., Kim, Y. H., Noh, S. K., Oh, H. M., Kim, Y. H., Leem, J. Y., Jeong, M. S., and Ryou, J. H. Formation characteristics of a self-catalyzed GaAs nanowire without a Ga droplet on Si(111). *Journal of the Korean Physical Society*, 61(12): 2017–2021, 2012. ISSN 03744884. doi: 10.3938/jkps.61.2017. (Cited on page 92)
- Parkinson, P., Joyce, H. J., Gao, Q., Tan, H. H., Zhang, X., Zou, J., Jagadish, C., Herz, L. M., and Johnston, M. B. Carrier lifetime and mobility enhancement in nearly defect-free core-shell nanowires measured using time-resolved terahertz spectroscopy. *Nano Letters*, 9(9):3349–3353, 2009. ISSN 15306984. doi: 10.1021/nl9016336. (Cited on page 85)
- Parkinson, P., Lee, Y. H., Fu, L., Breuer, S., Tan, H. H., and Jagadish, C. Three-dimensional in situ photocurrent mapping for nanowire photovoltaics. *Nano Letters*, 13(4):1405–1409, 2013. ISSN 15306984. doi: 10.1021/nl304170q. (Cited on page 61)
- Pelzel, R. A comparison of MOVPE and MBE growth technologies for III-V epitaxial structures. In *2013 International Conference on Compound Semiconductor Manufacturing Technology, CS MANTECH 2013*, pages 105–108, 2013. ISBN 1893580210. (Cited on page 30)
- Perera, S., Fickenscher, M. A., Jackson, H. E., Smith, L. M., Yarrison-Rice, J. M., Joyce, H. J., Gao, Q., Tan, H. H., Jagadish, C., Zhang, X., and Zou, J. Nearly intrinsic exciton lifetimes in single twin-free GaAs/AlGaAs core-shell nanowire heterostructures. *Applied Physics Letters*, 93(5):053110, 2008. ISSN 00036951. doi: 10.1063/1.2967877. (Cited on page 85)
- Perez-Lopez, P., Jolivet, R., Blanc, I., Besseau, R., Douziech, M., Gschwind, B., Tannous, S., Schlesinger, J., Brière, R., Prieur-Vernat, A., and Clavreul, J. PROJET INCER-ACV : Incertitudes dans les méthodes d’évaluation des impacts environnementaux des filières de production énergétique par ACV. Technical report, ADEME, 2020. (Cited on page 7)
- Petronio, F. *III-V nanowires on Si for high-efficiency tandem solar cells*. PhD thesis, ENSTA Paris, Politecnico di Milano, 2019. (Cited on page 68)
- Piazza, V., Wirths, S., Bologna, N., Ahmed, A. A., Bayle, F., Schmid, H., Julien, F., and Tchernycheva, M. Nanoscale analysis of electrical junctions in InGaP nanowires grown by template-assisted selective epitaxy. *Applied Physics Letters*, 114(10), 2019. ISSN 00036951. doi: 10.1063/1.5085405. URL <http://dx.doi.org/10.1063/1.5085405>. (Cited on page 70)
- Plissard, S., Dick, K. A., Larrieu, G., Godey, S., Addad, A., Wallart, X., and Caroff, P. Gold-free growth of GaAs nanowires on silicon: arrays and polytypism. *Nanotechnology*, 21(38):385602, 2010. ISSN 0957-4484. doi: 10.1088/0957-4484/21/38/385602. URL <http://stacks.iop.org/0957-4484/21/i=38/a=385602?key=crossref.29efab006d496c3dc6a979d4152de318>. (Cited on page 34)
- Plissard, S., Larrieu, G., Wallart, X., and Caroff, P. High yield of self-catalyzed GaAs nanowire arrays grown on silicon via gallium droplet positioning. *Nanotechnology*, 22(27):275602, 2011. ISSN 0957-4484. doi: 10.1088/0957-4484/22/27/275602. URL <http://stacks.iop.org/0957-4484/22/i=27/a=275602?key=crossref.e418a6ee239cea8ea3fb8caa0269d769>. (Cited on page 34, 35, 36)
- Pohl, U. W. *Epitaxy of Semiconductors*. Springer, 2013. ISBN 9783319610870. (Cited on page 29)
- Priante, G., Ambrosini, S., Dubrovskii, V. G., Franciosi, A., and Rubini, S. Stopping and resuming at will the growth of GaAs nanowires. *Crystal Growth and Design*, 13(9):3976–3984, 2013. ISSN 15287483. doi: 10.1021/cg400701w. (Cited on page 47)
- Qiu, Z., Mei, A., Hu, Y., Rong, Y., and Han, H. Aiming at the industrialization of perovskite solar cells: Coping with stability challenge. *Applied Physics Letters*, 119(25), 2021. ISSN 00036951. doi: 10.1063/5.0069697. (Cited on page 16)



- Raj, V., Fu, L., Tan, H. H., and Jagadish, C. Design Principles for Fabrication of InP-Based Radial Junction Nanowire Solar Cells Using an Electron Selective Contact. *IEEE Journal of Photovoltaics*, 9(4):980–991, 2019. ISSN 21563403. doi: 10.1109/JPHOTOV.2019.2911157. (Cited on page 84)
- Raychaudhuri, S. and Yu, E. T. Critical dimensions in coherently strained coaxial nanowire heterostructures. *Journal of Applied Physics*, 99(11), 2006. ISSN 00218979. doi: 10.1063/1.2202697. (Cited on page 53, 85)
- Raymond, A., Robert, J. L., and Bernard, C. The electron effective mass in heavily doped GaAs. *Journal of Physics C: Solid State Physics*, 12(12):2289–2293, 1979. ISSN 00223719. doi: 10.1088/0022-3719/12/12/014. (Cited on page 74)
- Robinson, R. E., Sandberg, R. L., Allred, D. D., Jackson, A. L., Johnson, J. E., Evans, W., Doughty, T., Baker, A. E., Adamson, K., and Jacquier, A. 47th Annual Technical Conference Proceedings: Removing Surface Contaminants from Silicon Wafers. *Society of Vacuum Coaters*, pages 368–376, 2004. (Cited on page 37)
- Roychowdhury, R., Kumar, S., Wadikar, A., Mukherjee, C., Rajiv, K., Sharma, T. K., and Dixit, V. K. Role of surface energy on the morphology and optical properties of GaP micro & nano structures grown on polar and non-polar substrates. *Applied Surface Science*, 419(October): 957–967, 2017. ISSN 01694332. doi: 10.1016/j.apsusc.2017.05.026. URL <http://dx.doi.org/10.1016/j.apsusc.2017.05.026>. (Cited on page 65)
- Russo-Averchi, E., Vukajlovic Plestina, J., Tütüncüoglu, G., Matteini, F., Dalmau-Mallorquí, A., De La Mata, M., Rüffer, D., Potts, H. A., Arbiol, J., Conesa-Boj, S., and Fontcuberta I. Morral, A. High yield of GaAs nanowire arrays on Si mediated by the pinning and contact angle of Ga. *Nano Letters*, 15(5):2869–2874, 2015. ISSN 15306992. doi: 10.1021/nl504437v. (Cited on page 34, 35)
- Saket, O., Himwas, C., Cattoni, A., Oehler, F., Bayle, F., Collin, S., Travers, L., Babichev, A., Julien, F. H., Harmand, J. C., and Tchernycheva, M. Influence of surface passivation on the electrical properties of p-i-n GaAsP nanowires. *Applied Physics Letters*, 117(12), 2020a. ISSN 00036951. doi: 10.1063/5.0022157. (Cited on page 84, 86)
- Saket, O., Himwas, C., Piazza, V., Bayle, F., Cattoni, A., Oehler, F., Patriarche, G., Travers, L., Collin, S., Julien, F. H., Harmand, J. C., and Tchernycheva, M. Nanoscale electrical analyses of axial-junction GaAsP nanowires for solar cell applications. *Nanotechnology*, 31(14), 2020b. ISSN 13616528. doi: 10.1088/1361-6528/ab62c9. (Cited on page 86)
- Salehzadeh, O., Kavanagh, K. L., and Watkins, S. P. Geometric limits of coherent III-V core/shell nanowires. *Journal of Applied Physics*, 114(5), 2013. ISSN 00218979. doi: 10.1063/1.4816460. (Cited on page 53, 85)
- Scaccabarozzi, A., Cattoni, A., Patriarche, G., Travers, L., Collin, S., Harmand, J.-C., Glas, F., and Oehler, F. Stable and high yield growth of GaP and In 0.2 Ga 0.8 As nanowire arrays using In as a catalyst. *Nanoscale*, 12(35):18240–18248, 2020. ISSN 2040-3364. doi: 10.1039/d0nr04139d. (Cited on page 35, 36)
- Scheer, R. and Schock, H.-W. Chalcogenide Photovoltaics. In *Chalcogenide Photovoltaics*, chapter 2.6. Wiley-VCH, 2011. ISBN 9783527326471. doi: 10.1002/9783527633708. (Cited on page 25, 58, 62, 96, 98, 100)
- Schroth, P., Al Humaidi, M., Feigl, L., Jakob, J., Al Hassan, A., Davtyan, A., Küpers, H., Tahraoui, A., Geelhaar, L., Pietsch, U., and Baumbach, T. Impact of the Shadowing Effect on the Crystal Structure of Patterned Self-Catalyzed GaAs Nanowires. *Nano Letters*, 19(7):4263–4271, 2019. ISSN 15306992. doi: 10.1021/acs.nanolett.9b00380. (Cited on page 34, 35, 47)
- Schubert, E. F. Delta doping of III–V compound semiconductors: Fundamentals and device applications. *Journal of Vacuum Science & Technology A: Vacuum, Surfaces, and Films*, 8(3): 2980–2996, 1990. ISSN 0734-2101. doi: 10.1116/1.576617. (Cited on page 54)
- Schubert, E. F. *Doping in III-V Semiconductors*. Cambridge University Press, 1993. ISBN 9780521419192. (Cited on page 80)

- Seeger, K. *Semiconductor Physics*. Springer-Verlag, 9th edition, 2004. ISBN 9781119130536. (Cited on page 15)
- Senichev, A., Corfdir, P., Brandt, O., Ramsteiner, M., Breuer, S., Schilling, J., Geelhaar, L., and Werner, P. Electronic properties of wurtzite GaAs: A correlated structural, optical, and theoretical analysis of the same polytypic GaAs nanowire. *Nano Research*, 11(9):4708–4721, 2018. ISSN 19980000. doi: 10.1007/s12274-018-2053-5. (Cited on page 13)
- Shockley, W. and Queisser, H. J. Detailed balance limit of efficiency of p-n junction solar cells. *Journal of Applied Physics*, 32(3):510–519, 1961. ISSN 00218979. doi: 10.1063/1.1736034. (Cited on page 14)
- Shun'ko, E. V. and Belkin, V. S. Cleaning properties of atomic oxygen excited to metastable state  $2s\ 2\ p\ 4$  ( $S\ 1\ 0$ ). *Journal of Applied Physics*, 102(8):083304, 2007. ISSN 00218979. doi: 10.1063/1.2794857. (Cited on page 37)
- Sibirev, N. V., Tchernycheva, M., Timofeeva, M. A., Harmand, J. C., Cirlin, G. E., and Dubrovskii, V. G. Influence of shadow effect on the growth and shape of InAs nanowires. *Journal of Applied Physics*, 111(10), 2012. ISSN 00218979. doi: 10.1063/1.4718434. (Cited on page 47)
- Siffert, P. and Krimmel, E. Preface. In *Silicon: Evolution and Future of a Technology*. Springer Science & Business Media, 2013. ISBN 978-3-662-09897-4. (Cited on page 5)
- Signorello, G., Karg, S., Björk, M. T., Gotsmann, B., and Riel, H. Tuning the light emission from GaAs nanowires over 290 meV with uniaxial strain. *Nano Letters*, 13(3):917–924, 2013. ISSN 15306984. doi: 10.1021/nl303694c. (Cited on page 91)
- Sköld, N., Karlsson, L. S., Larsson, M. W., Pistol, M. E., Seifert, W., Trägårdh, J., and Samuelson, L. Growth and optical properties of strained GaAs-GaxIn 1-xP core-shell nanowires. *Nano Letters*, 5(10):1943–1947, 2005. ISSN 15306984. doi: 10.1021/nl051304s. (Cited on page 85)
- Smets, A., Jager, K., Isabella, O., Van Swaaij, R., and Zeman, M. *Solar Energy: The Physics and Engineering of Photovoltaic Conversion, Technologies and Systems*. UIT Cambridge, 2016. ISBN 1853330566. (Cited on page 11)
- Sood, M., Lumisco, A., Werner, F., Nikolaeva, A., Dale, P., Melchiorre, M., Guillot, J., Abou-Ras, D., and Siebentritt, S. Passivating Surface Defects and Reducing Interface Recombination in CuInS<sub>2</sub> Solar Cells by a Facile Solution Treatment. *Solar RRL*, 5(4):2100078, 2021. (Cited on page 61)
- Stolterfoht, M., Caprioglio, P., Wolff, C. M., Márquez, J. A., Nordmann, J., Zhang, S., Rothhardt, D., Hörmann, U., Amir, Y., Redinger, A., Kegelmann, L., Zu, F., Albrecht, S., Koch, N., Kirchartz, T., Saliba, M., Unold, T., and Neher, D. The impact of energy alignment and interfacial recombination on the internal and external open-circuit voltage of perovskite solar cells. *Energy and Environmental Science*, 12(9):2778–2788, 2019. ISSN 17545706. doi: 10.1039/c9ee02020a. (Cited on page 61)
- Storm, K., Halvardsson, F., Heurlin, M., Lindgren, D., Gustafsson, A., Wu, P. M., Monemar, B., and Samuelson, L. Spatially resolved Hall effect measurement in a single semiconductor nanowire. *Nature Nanotechnology*, 7(11):718–722, 2012. ISSN 17483395. doi: 10.1038/nnano.2012.190. (Cited on page 69)
- Suomalainen, S., Hakkarainen, T. V., Salminen, T., Koskinen, R., Honkanen, M., Luna, E., and Guina, M. Te-doping of self-catalyzed GaAs nanowires. *Applied Physics Letters*, 107(1):1–5, 2015. ISSN 00036951. doi: 10.1063/1.4926494. URL <http://dx.doi.org/10.1063/1.4926494>. (Cited on page 69)
- Supplie, O., May, M. M., Steinbach, G., Romanyuk, O., Grosse, F., Nägelein, A., Kleinschmidt, P., Brückner, S., and Hannappel, T. Time-resolved in situ spectroscopy during formation of the GaP/Si(100) heterointerface. *Journal of Physical Chemistry Letters*, 6(3):464–469, 2015. ISSN 19487185. doi: 10.1021/jz502526e. (Cited on page 65)
- Sze, S. M. and Ng, K. K. Semiconductor Physics. In *Physics of Semiconductor Devices*, chapter 1. John Wiley & Son, 3rd edition, 2007a. (Cited on page 11, 13)

- Sze, S. M. and Ng, K. K. Device Building Blocks. In *Physics of Semiconductor Devices*, chapter 2. John Wiley & Son, 3rd edition, 2007b. (Cited on page 15)
- Tajik, N., Chia, A. C., and Lapierre, R. R. Improved conductivity and long-term stability of sulfur-passivated n-GaAs nanowires. *Applied Physics Letters*, 100(20):10–13, 2012. ISSN 00036951. doi: 10.1063/1.4719675. (Cited on page 85)
- Tavendale, A. J. and Pearton, S. J. Deep level, quenched-in defects in silicon doped with gold, silver, iron, copper or nickel. *Journal of Physics C: Solid State Physics*, 16(9):1665–1673, 1983. ISSN 00223719. doi: 10.1088/0022-3719/16/9/011. (Cited on page 28)
- Tiedje, T. O. M., Yablonovitch, E. L. I., Cody, G. D., and Brooks, B. G. Limiting Efficiency of Silicon Solar Cells. *IEEE Transactions on Electron Devices*, 31(5):711–716, 1984. (Cited on page 14)
- Tierney, J. E., Zhu, J., King, J., Malevich, S. B., Hakim, G. J., and Poulsen, C. J. Glacial cooling and climate sensitivity revisited. *Nature*, 584(7822):569–573, 2020. ISSN 14764687. doi: 10.1038/s41586-020-2617-x. URL <http://dx.doi.org/10.1038/s41586-020-2617-x>. (Cited on page 5)
- Titova, L. V., Hoang, T. B., Jackson, H. E., Smith, L. M., Yarrison-Rice, J. M., Kim, Y., Joyce, H. J., Tan, H. H., and Jagadish, C. Temperature dependence of photoluminescence from single core-shell GaAs-AlGaAs nanowires. *Applied Physics Letters*, 89(17):14–17, 2006. ISSN 00036951. doi: 10.1063/1.2364885. (Cited on page 85)
- Tomioka, K., Kobayashi, Y., Motohisa, J., Hara, S., and Fukui, T. Selective-area growth of vertically aligned GaAs and GaAs/AlGaAs core-shell nanowires on Si(111) substrate. *Nanotechnology*, 20(14):145302, 2009. ISSN 09574484. doi: 10.1088/0957-4484/20/14/145302. (Cited on page 85)
- Tong, C., Bidaud, T., Koivusalo, E., Piton, M. R., Guina, M., Galeti, H. V. A., Gobato, Y. G., Cattoni, A., Hakkarainen, T., and Collin, S. Cathodoluminescence mapping of electron concentration in MBE-grown GaAs:Te nanowires. *Nanotechnology*, 33(18):185704, 2022a. ISSN 0957-4484. doi: 10.1088/1361-6528/ac4d58. (Cited on page 67)
- Tong, C., Delamarre, A., De Lépinau, R., Scaccabarozzi, A., Oehler, F., Harmand, J.-C., Collin, S., and Cattoni, A. GaAs/GaInP nanowire solar cell on Si with state-of-the-art Voc and quasi-Fermi level splitting. *Nanoscale*, 14(35):12722–12735, 2022b. doi: 10.1039/D2NR02652J. (Cited on page 44, 51, 53, 54)
- UN Climate Change Conference UK. COP26 The Glasgow Climate Pact. Technical report, United Nations, 2021. (Cited on page 5)
- van Dam, A. D. *Nanowire Photonics for Photovoltaics*. PhD thesis, Eindhoven University of Technology, 2016. (Cited on page 19)
- Van Dam, D., Van Hoof, N. J., Cui, Y., Van Veldhoven, P. J., Bakkers, E. P., Gómez Rivas, J., and Haverkort, J. E. High-Efficiency Nanowire Solar Cells with Omnidirectionally Enhanced Absorption Due to Self-Aligned Indium-Tin-Oxide Mie Scatterers. *ACS Nano*, 10(12):11414–11419, 2016. ISSN 1936086X. doi: 10.1021/acsnano.6b06874. (Cited on page 18, 19)
- van der Heide, P. A. M., Baan Hofman, M. J., and Ronde, H. J. Etching of thin SiO<sub>2</sub> layers using wet HF gas. *Journal of Vacuum Science & Technology A: Vacuum, Surfaces, and Films*, 7(3): 1719–1723, 1989. ISSN 0734-2101. doi: 10.1116/1.576033. (Cited on page 40)
- VanSant, K. T., Tamboli, A. C., and Warren, E. L. III-V-on-Si Tandem Solar Cells. *Joule*, 5(3): 514–518, 2021. ISSN 25424351. doi: 10.1016/j.joule.2021.01.010. URL <https://doi.org/10.1016/j.joule.2021.01.010>. (Cited on page 16)
- Vettori, M., Piazza, V., Cattoni, A., Scaccabarozzi, A., Patriarche, G., Regreny, P., Chauvin, N., Botella, C., Grenet, G., Penuelas, J., Fave, A., Tchernycheva, M., and Gendry, M. Growth optimization and characterization of regular arrays of GaAs/AlGaAs core/shell nanowires for tandem solar cells on silicon. *Nanotechnology*, 30(8), 2019. ISSN 13616528. doi: 10.1088/1361-6528/aaf3fe. (Cited on page 29, 34, 35, 47, 85)

- Vukajlovic-Plestina, J., Kim, W., Ghisalberti, L., Varnavides, G., Tütüncüoglu, G., Potts, H., Friedl, M., Güniat, L., Carter, W. C., Dubrovskii, V. G., and Fontcuberta i Morral, A. Fundamental aspects to localize self-catalyzed III-V nanowires on silicon. *Nature Communications*, 10(1):869, 12 2019. ISSN 2041-1723. doi: 10.1038/s41467-019-08807-9. URL <http://www.nature.com/articles/s41467-019-08807-9>. (Cited on page 34, 35, 36)
- Wagner, R. S. and Ellis, W. C. Vapor-liquid-solid mechanism of single crystal growth. *Applied Physics Letters*, 4(5):89–90, 1964. ISSN 00036951. doi: 10.1063/1.1753975. (Cited on page 28)
- Wallentin, J. *Doping of semiconductor nanowires*. PhD thesis, Lund University, 2013. (Cited on page 69)
- Wallentin, J., Messing, M. E., Trygg, E., Samuelson, L., Deppert, K., and Borgström, M. T. Growth of doped InAsP<sub>1-y</sub> nanowires with InP shells. *Journal of Crystal Growth*, 331(1):8–14, 2011. ISSN 00220248. doi: 10.1016/j.jcrysgro.2011.07.002. (Cited on page 85)
- Wallentin, J., Anttu, N., Asoli, D., Huffman, M., Aberg, I., Magnusson, M. H., Siefer, G., Fuss-Kailuweit, P., Dimroth, F., Witzigmann, B., Xu, H. Q., Samuelson, L., Deppert, K., and Borgstrom, M. T. InP Nanowire Array Solar Cells Achieving 13.8% Efficiency by Exceeding the Ray Optics Limit. *Science*, 339(6123):1057–1060, 3 2013. ISSN 0036-8075. doi: 10.1126/science.1230969. URL <http://www.sciencemag.org/cgi/doi/10.1126/science.1230969>. (Cited on page 69, 84, 88)
- Wang, X. L., Wakahara, A., and Sasaki, A. Si and Zn doping of GaP grown by OMVPE using tertiarybutylphosphine. *Journal of Crystal Growth*, 158(1-2):49–52, 1996. ISSN 00220248. doi: 10.1016/0022-0248(95)00341-X. (Cited on page 86)
- Wilson, D. P., Dubrovskii, V. G., and LaPierre, R. R. Improving the yield of GaAs nanowires on silicon by Ga pre-deposition. *Nanotechnology*, 32(26):265301, 2021. ISSN 0957-4484. doi: 10.1088/1361-6528/abef93. (Cited on page 34, 35, 36, 45, 47)
- Wood, B. *Fabrication and Characterization of GaAsP Nanowire-on-Silicon Tandem Photovoltaic Cells*. PhD thesis, McMaster University, 2017. URL [https://macsphere.mcmaster.ca/bitstream/11375/22251/2/Wood\\_Brendan\\_A\\_2017August\\_MASc.pdf](https://macsphere.mcmaster.ca/bitstream/11375/22251/2/Wood_Brendan_A_2017August_MASc.pdf). (Cited on page 18)
- Wu, D., Tang, X., Wang, K., and Li, X. Effective coupled optoelectrical design method for fully infiltrated semiconductor nanowires based hybrid solar cells. *Optics Express*, 24(22):A1336, 2016. ISSN 10944087. doi: 10.1364/oe.24.0a1336. (Cited on page 84)
- Wu, D., Tang, X., Wang, K., He, Z., and Li, X. An Efficient and Effective Design of InP Nanowires for Maximal Solar Energy Harvesting. *Nanoscale Research Letters*, 12(1):604, 12 2017a. ISSN 1931-7573. doi: 10.1186/s11671-017-2354-8. URL <https://nanoscalereslett.springeropen.com/articles/10.1186/s11671-017-2354-8>. (Cited on page 43)
- Wu, D., Tang, X., Wang, K., and Li, X. An Analytic Approach for Optimal Geometrical Design of GaAs Nanowires for Maximal Light Harvesting in Photovoltaic Cells. *Scientific Reports*, 7(1):46504, 6 2017b. ISSN 2045-2322. doi: 10.1038/srep46504. URL <http://www.nature.com/articles/srep46504>. (Cited on page 43)
- Würfel, P. and Würfel, U. *Physics of Solar Cells: From Basic Principles to Advanced Concepts*. Wiley-VCH, 3rd editio edition, 2016. ISBN 9783527413126. (Cited on page 11)
- Yao, M., Huang, N., Cong, S., Chi, C.-Y., Seyedi, M. A., Lin, Y.-T., Cao, Y., Povinelli, M. L., Dapkus, P. D., and Zhou, C. GaAs Nanowire Array Solar Cells with Axial p-i-n Junctions. *Nano Letters*, 14(6):3293–3303, 6 2014. ISSN 1530-6984. doi: 10.1021/nl500704r. URL <http://pubs.acs.org/doi/10.1021/nl500704r>. (Cited on page 18, 84, 88)
- Yao, M., Cong, S., Arab, S., Huang, N., Povinelli, M. L., Cronin, S. B., Dapkus, P. D., and Zhou, C. Tandem Solar Cells Using GaAs Nanowires on Si: Design, Fabrication, and Observation of Voltage Addition. *Nano Letters*, 15(11):7217–7224, 2015. ISSN 15306992. doi: 10.1021/acs.nanolett.5b03890. (Cited on page 18, 19, 28, 84)

- Yoshimura, M., Nakai, E., Tomioka, K., and Fukui, T. Indium phosphide core-shell nanowire array solar cells with lattice-mismatched window layer. *Applied Physics Express*, 6(5):1–5, 2013. ISSN 18820778. doi: 10.7567/APEX.6.052301. (Cited on page 18)
- Yu, S., Roemer, F., and Witzigmann, B. Analysis of surface recombination in nanowire array solar cells. *Journal of Photonics for Energy*, 2(1):028002–1, 2012. ISSN 1947-7988. doi: 10.1117/1.jpe.2.028002. (Cited on page 85)
- Zeng, H., Yu, X., Fonseca, H. A., Boras, G., Jurczak, P., Wang, T., Sanchez, A. M., and Liu, H. Preferred growth direction of III-V nanowires on differently oriented Si substrates. *Nanotechnology*, 31(47), 2020. ISSN 13616528. doi: 10.1088/1361-6528/abafd7. (Cited on page 33)
- Zhang, A., Zheng, G., and M. Lieber, C. *Nanowires*. Springer, 2016. ISBN 978-3-319-41979-4. (Cited on page 28)
- Zhang, Y., Wu, J., Aagesen, M., Holm, J., Hatch, S., Tang, M., Huo, S., and Liu, H. Self-Catalyzed Ternary Core-Shell GaAsP Nanowire Arrays Grown on Patterned Si Substrates by Molecular Beam Epitaxy. *Nano Letters*, 14(8):4542–4547, 8 2014. ISSN 1530-6984. doi: 10.1021/nl501565b. URL <http://pubs.acs.org/doi/10.1021/nl501565b>. (Cited on page 34, 35, 36)
- Zhang, Y., Fonseca, H. A., Aagesen, M., Gott, J. A., Sanchez, A. M., Wu, J., Kim, D., Jurczak, P., Huo, S., and Liu, H. Growth of pure zinc-blende GaAs(P) core-shell nanowires with highly regular morphology. *Nano Letters*, 17(8):4946–4950, 2017. ISSN 15306992. doi: 10.1021/acs.nanolett.7b02063. (Cited on page 85)
- Zhou, H. L., Hoang, T. B., Dheeraj, D. L., Van Helvoort, A. T., Liu, L., Harmand, J. C., Fimland, B. O., and Weman, H. Wurtzite GaAs/AlGaAs core-shell nanowires grown by molecular beam epitaxy. *Nanotechnology*, 20(41), 2009. ISSN 09574484. doi: 10.1088/0957-4484/20/41/415701. (Cited on page 85)